Purdue University
Purdue e-Pubs

Open Access Dissertations | Theses and Dissertations

4-2016

Coupled resonator based wireless power transfer for bioelectronics

Henry Mei
Purdue University

Follow this and additional works at: https://docs.lib.purdue.edu/open_access_dissertations

Part of the Biomedical Engineering and Bioengineering Commons, and the Electromagnetics and Photonics Commons

Recommended Citation
Mei, Henry, "Coupled resonator based wireless power transfer for bioelectronics" (2016). *Open Access Dissertations*. 678.
https://docs.lib.purdue.edu/open_access_dissertations/678

This document has been made available through Purdue e-Pubs, a service of the Purdue University Libraries. Please contact epubs@purdue.edu for additional information.

Graduate School Form
30 Updated 12/26/2015

PURDUE UNIVERSITY
GRADUATE SCHOOL
Thesis/Dissertation Acceptance

This is to certify that the thesis/dissertation prepared

By Henry Mei

Entitled
COUPLED RESONATOR BASED WIRELESS POWER TRANSFER FOR BIOELECTRONICS

For the degree of Doctor of Philosophy

Is approved by the final examining committee:

Pedro Irazoqui
Chair

Eugenio Culurciello

Zhongming Liu

Jennifer Bernhard

To the best of my knowledge and as understood by the student in the Thesis/Dissertation Agreement, Publication Delay, and Certification Disclaimer (Graduate School Form 32), this thesis/dissertation adheres to the provisions of Purdue University's "Policy of Integrity in Research" and the use of copyright material.

Approved by Major Professor(s): Pedro Irazoqui

Approved by: George R. Wodicka 4/5/2016
Head of the Departmental Graduate Program Date

COUPLED RESONATOR BASED WIRELESS POWER TRANSFER FOR BIOELECTRONICS

A Dissertation

Submitted to the Faculty

of

Purdue University

by

Henry Mei

In Partial Fulfillment of the

Requirements for the Degree

of

Doctor of Philosophy

May 2016

Purdue University

West Lafayette, Indiana

I dedicate this dissertation to my wife, Jocelyne, who has provided her undying love and unwavering support from which this most selfish endeavor would never have been possible. May we forever conquer life's precious gifts and unexpected challenges.

To my mother, Betty, who taught me, from the very beginning, the meaning of love, sacrifice, and strength. You continue to inspire me and I am forever grateful. To my father, Gregg, who gave me the perspective on what it means and takes to become a great man. Thank you for accepting me for who I am. You both have always been in my corner.

And finally to my little son, Harrison, may you know that through hard work and dedication anything is possible. I will always be there for you.

ACKNOWLEDGEMENTS

The work conducted in this dissertation would not have been possible if it were not for the incredible people that I have been so lucky to work with throughout my graduate career. I am indebted to my advisor, Professor Pedro P. Irazoqui, who provided the support, guidance, environment, ideas, and patience to see this work develop into what you hold in this dissertation. Thank you for introducing the wonderful world of electromagnetics to me, thank you for pushing me, and thank you for believing in me. I would like to thank Professor John Jefferys. Our collaborative work, which began at the University of Birmingham in the United Kingdom, helped define some of the specifications necessary to make the cavity resonator based wireless power transfer arena a competitive piece of technology. I would like to thank Professor William Chappell and Dr. Dohyuk Ha for providing the filter synthesis foundation from which the analysis and optimization methodologies presented in this work were developed. I would also like to thank and acknowledge my PhD committee members, Professor Jennifer T. Bernhard, Professor Eugenio Culurciello, and Professor Zhongming Liu, for serving as members on my committee, reviewing, supporting, and providing suggestions for this work.

Indeed, during my time at Purdue, I was afforded the special opportunity to work with a hardworking and gifted group of peers. To the entire Center for Implantable Devices, thank you all for making this a fun and special journey. To Dr. Steven T. Lee

and Dr. Kurt Qing, thank you both for listening and providing feedback throughout the growth of my research. To Dr. Matthew Ward, Dr. Oren Gall, and Dr. David Jaroch, thank you for showing me what good research looks like. To Kyle Thackston, thank you for learning, believing in, and advancing this work. To Becky Bercich, Grant Wang, Jack Williams, Dan Pederson, Hansraj Bhamra, Chris Quinkert, Yu-Wen Huang, Jesse Somman thank you for providing unique perspectives and various expertise within the wide breadth of engineering art that is Biomedical Engineering. To Gabriel Albors and Henry Zhang, thank you for providing technical support and teaching me how to fabricate clean “working” electronics. Finally, I would like to thank my family: Jocelyne, Harrison, Mom and Gregg, you have all always been there for me and pushed me to go for it.

TABLE OF CONTENTS

Page

LIST OF TABLES ix

LIST OF FIGURES xi

ABSTRACT xx

CHAPTER 1. INTRODUCTION 1

1.1 A Prelude to Wireless Power Transfer 1

1.2 Motivation 3

1.3 Definition of WPT Technology Requirements 5

1.4 Review of WPT Technologies 6

1.4.1 Far-field WPT 7

1.4.2 Mid-Field WPT 11

1.4.3 Near-field (Coupled resonator) WPT 12

1.5 Thesis Objectives, Key Contributions, and Organization 15

CHAPTER 2. ANALYSIS, DESIGN, AND OPTIMIZATION OF MAGNETIC RESONANT COUPLING WIRELESS POWER TRANSFER USING MICROWAVE NETWORK AND BANDPASS FILTER THEORY 19

2.1 Introduction 19

2.2 Derivation of Bandpass Filter Model for MRC WPT Systems 20

2.2.1 Description of Impedance Inverter (K-inverter) Networks 22

2.2.2 Model Modification to Account for Lossy Resonators 27

2.2.3 Model Modification to Accommodate Detuning Effects of Complex Port Impedances 28

2.2.4 Final Generalized BPF Model for MRC WPT System 32

2.3 Synthesis and Derivation of the Generalized Coupling Matrix 32

Page

2.4 Determination of System Transfer Response and Derivation of Optimal KiP..... 37
2.5 Investigation of Optimal PTE Responses and PTE Control Through k12opt 40
2.6 Lumped element K-Inverter Design to Exhibit KS1opt, K2Lopt, and XFIRi..... 46
2.7 Experimental Results and Theory Validation 50
2.7.1 Experimental Design 50
2.7.2 Measurement of Resonator Parameters 52
2.7.3 CCP Control and PTE Response Optimization for Tx to Rx1 (Non-Complex Source and Load Impedance) 55
2.7.4 CCP Control and PTE Response Optimization for Tx to Rx2 (Non-Complex Source and Load Impedance) 60
2.7.5 Demonstration of Complex Load Impedance Accommodation (Tx to Rx1) 60
2.7.6 Summary of PTE/CCP Response Control and Optimization Methodology.. 64
2.7.7 Additional Coupling Maps and Corresponding Coupling Matrices 66
2.8 Conclusion..... 68
CHAPTER 3. NOVEL MRC WPT ARRANGEMENT FOR A MYOELECTRIC SENSING SYSTEM 69
3.1 Introduction 69
3.2 The MRC WPT Arrangement 70
3.2.1 Anti-Helmholtz Coil 72
3.2.2 Anti-Helmholtz Coil and Rx coil Fabrication 73
3.2.3 Equal Power Distribution Optimization 77
3.3 Human sEMG Acquisition 82
3.4 Safety Considerations..... 84
3.5 Conclusion..... 86
CHAPTER 4. CAVITY RESONATOR BASED WIRELESS POWER TRANSFER SYSTEM..... 88
4.1 Introduction 88
4.2 General Overview of Cavity Resonator Structures 89
4.3 Cavity Resonator MRC WPT BPF Model 93

Page

4.4 Synthesis of Cavity Resonator WPT System Coupling Matrix 98
4.5 Determination of System Transfer Response and Derivation of Optimal JiP..... 101
4.6 Symmetry of PTE Response and Behavior 101
4.7 Network Configuration for JiPopt and BFISi..... 102
4.8 Experimental Validation 105
4.8.1 Cavity and Receive Resonator Construction 105
4.8.2 Extraction of Resonator Parameters 107
4.8.2.1 Extraction of Cavity Resonator Parameters..... 107
4.8.2.1.1 Comment on Measured versus Theoretically Predicted Quality Factor . ……..……111
4.8.2.1.2 Determination of Cavity R, L, C..... 112
4.8.2.1.3 Determination of Cm and Cprobe Corresponding to lprobe..... 112
4.8.2.2 Extraction of Receive Resonator Parameters and k12 113
4.8.3 Measured, Circuit Simulated and Theory Predicted Optimal PTE Response 115
4.9 In-Vivo Experiment with Porcine Ocular Tissue 117
4.9.1 Experimental Design and Measured PTE..... 117
4.9.2 Application Demonstration..... 122
4.10 Conclusion 124
CHAPTER 5. SMALL ANIMAL CAVITY RESONATOR WIRELESS POWER TRANSFER SYSTEM 126
5.1 Introduction 126
5.2 Cavity Resonator Design and Construction 130
5.2.1 Material Selection..... 130
5.2.2 Cavity Dimensions and Resonant Frequency 132
5.2.3 H-field Distribution in the TM_{110} Excitation Mode..... 133
5.2.4 Cavity Slots and Animal Viewing 133
5.2.5 Removable Lid Design and Excitation Probe..... 135
5.3 Animal Housing Cavity Resonator WPT Optimization and Characterization..... 135

Page

5.3.1 Characterization of lprobe to Cprobe and Cm 136
5.3.2 PTE Measurements (Aluminum Cavity, No Animal) 136
5.3.3 Copper Cavity PTE Capability (No Animal)..... 142
5.3.4 Accounting for the Presence of the Small Animal and PTE Measurements 142
5.4 Custom Designed Implantable Device for the Chronic *In-Vivo* Experiment..... 148
5.4.1 The Bionode..... 149
5.4.2 Biaxial Powernode System 150
5.4.3 Packaging Design 155
5.5 Chronic *In-Vivo* Experiment 156
5.5.1 Surgical Procedure..... 156
5.5.2 *In-vivo* Experimental Setup and Validation..... 156
5.5.3 Evaluation of Powering Fidelity 157
5.5.4 Specific Absorption Rate Considerations 160
5.5.5 Electromagnetic Interference (EMI) Considerations..... 161
5.6 Conclusion..... 162
CHAPTER 6. CONCLUSION AND FUTURE WORK 165
6.1 Conclusion..... 165
6.2 Future Work 167
6.2.1 Cavity Resonator WPT Systems for Freely-Behaving Small Animal Experiments 167
6.2.2 Cavity Resonator WPT System for Potential Human Clinical Applications 169
6.2.2.1 Evanescent Coupling into Biological Tissue..... 169
6.2.2.2 Experimental Demonstration..... 171
6.2.2.3 Qualitative Demonstration using a Human Arm 174
LIST OF REFERENCES 176
VITA 185
PUBLICATIONS..... 189

LIST OF TABLES

Table Page

Table 1.1 Survey of simulated ESA performances in various tissue replicated body phantoms 10

Table 2.1 Coil Design for coil Tx, Rx1, and Rx2 52

Table 2.2 Measured Resonator Parameters 53

Table 2.3 Calculated Optimal Capacitance Values for Tx to Rx1 56

Table 2.4 Predicted and Measured FOM for Tx to Rx1 Optimization Examples 57

Table 3.1 Measured Resonator Parameters (forearm) 77

Table 3.2 Implemented K-inverter Capacitance Values and Power Budget 84

Table 3.3 RF Exposure Limits by ICNIRP and FCC (100 kHz – 10 MHz) 85

Table 4.1 Measured Resonator Parameters 114

Table 4.2 Summary of $JS1opt$, $J2Lopt$, and Corresponding Optimal and Actual Capacitance Values at $\omega = \omega 0$ and $k12opt = 0.0025$ 114

Table 4.3 Measured Resonator Parameters with Porcine Eye 119

Table 4.4 Summary of $JS1opt$, $J2Lopt$, and Corresponding Optimal and Actual Capacitance Values at $\omega = \omega 0$ and $k12opt = 0.0015$ (For Porcine Eye Experiment, 50 Ohm source and load) 121

Table 4.5 Wireless PTE Comparison to Biologically Implanted Systems with 2 mm diameter receive coils 121

Table Page

Table 5.1 Relevant Dimensions of the Constructed Animal Housing Cavity Resonator Structure 132

Table 5.2 Measured Resonator Parameters 138

Table 5.3 Summary of $JS1opt$, $J2Lopt$, and Corresponding Optimal and Actual Capacitance Values at $\omega = \omega 0$ and $k12opt = 0.002$ 139

Table 5.4 Rat Tuning Conditions for Figure 5.10 146

Table 6.1 Wireless PTE Comparison using 2 mm diameter receive coils 173

LIST OF FIGURES

Figure Page

Figure 1.1 Characterization of the far-field, mid-field, and near-field regions. The mechanism of WPT are dependent on the region at which energy is captured. 7

Figure 1.2 The fundamental minimum limit of radiation Q factor plotted as a function of *kr* for a linearly polarized antenna. Antenna Q increases exponentially as the electrical size of the antenna decreases. Indeed, ESAs tend to exhibit low radiating performance. Figure reprinted and modified from [17]. Note that *a* in the figure corresponds to *r*..... 9

Figure 1.3 Comparison of miniaturization and safe power delivery capabilities between far-field, mid-field, and near-field (coupled resonator) based WPT technologies. A new WPT technology is necessary to improve miniaturization capability while maintaining the capability to safely deliver power requirements of sophisticated bioelectronics. 16

Figure 2.1 Traditional two resonator coupled MRC system. Each resonator is driven by externally coupled source and load coils. 21

Figure 2.2 Equivalent circuit of original system. T-network circuits are substituted in place to represent mutual inductances. Critically, each T-network is equivalent to an impedance inverter (K-inverter). 22

Figure 2.3 Function of an impedance inverter (K-inverter)..... 23

Figure 2.4 Example of an *ABCD* network parameter derivation for a K-inverter formed of a T-network of inductors. (a) Equivalent two-port network derivation. (b) Impedance tracking of input impedance (blue line in smith chart) as a function of inductance, L, at $\omega = \omega 0$. At $L = ZLZL * \omega 0$ the input impedance is inverted across the real axis and is equivalent to the complex conjugate of load impedance ZL. 24

Figure 2.5 BPF network formed of K-inverters and series resonators 25

Figure 2.6 External coupling K-inverter generalization method for resonator 2 and load. K-inverter $K2L$ is formed from the absorption of load coil LL and formation of $L2$. The generalization procedure is applied to the source side..... 26

Figure 2.7 Generic BPF model for a 2 resonator MRC WPT system..... 27

Figure Page

Figure 2.8 Series resonator modified to exhibit finite $Q0i$. 28

Figure 2.9 Complex load accommodation. (a) Unaccommodated BPF requiring extraneous IM networks for complex port impedance matching. (b) Accommodated BPF inherently matched to complex port impedances. Complex impedance accommodation removes the need for extra IM networks. 29

Figure 2.10 Impedance, Zi, seen by resonator i, when connected to external coupling K-inverter, KiP, terminated with port impedance, ZP..... 30

Figure 2.11 Modified resonator network incorporating a frequency invariant reactance element. 31

Figure 2.12 Final Generalized BPF model for MRC WPT 33

Figure 2.13 (a) Coupling map for 2 resonator BPF modeled MRC WPT system and (b) equivalent impedance matrix Z representation 33

Figure 2.14 Impedance matrix normalization procedure using impedance ($1/RP$)and resonator ($1/\omega 0Li$) scaling factors. 34

Figure 2.15 Normalized impedance matrix for 2 resonator BPF modeled MRC WPT System. 35

Figure 2.16 Map of $S21\omega = \omega 02$ (PTE at $\omega = \omega 0$) as a function of external coupling characteristic impedances $KS1$ and $K2L$. Note the locations of maximum power transfer at $KS1opt$ and $K2Lopt$. The example system design parameters are given. 39

Figure 2.17 Plot of theoretically predicted $S21opt2$ as a function $k12$ and frequency ratio, $ff0$, with clearly defined under, critical, and over-coupling PTE regions. Plot was created using the same example system design parameters used to generate Figure 2.16 (a) Full-view and (b) Top down view. 41

Figure 2.18 Plot of theoretically predicted $S21opt2$ as a function $k12$ for varying values of $k12opt$. The PTE at the CCP and $k12opt$ for each curve is given. Except for design parameter $k12opt$, the example design parameters for generating each curve is given in Figure 2.16. 43

Figure 2.19 Capacitive K-inverter network connected to port impedance ZP. 47

Figure 2.20 Simple and practically realizable 2 resonator BPF modeled MRC WPT system. (a) all individual lumped element components and (b) all lumped components with total series capacitor, Cti, representing the total absorbed capacitance. 49

Figure Page

Figure 2.21 (a) Experimental Set-up between transmit (Tx) and receive (Rx) coils with linear guide rail and (b) photograph of experimental set-up..... 51
Figure 2.22 Measured $k12$ range for (a) Tx to Rx1 and (b) Tx to Rx2..... 54

Figure 2.23 Measured and theory predicted PTE responses at $f0 = 13.56$ MHz as a function of $k12$ as a result of five different $k12opt$ optimization points. The predicted and measured FOM are also given..... 56

Figure 2.24 Example frequency response, at $k12$ locations representing UC, CC, and OC regions, for the $k12opt = 0.01$ optimized Tx to Rx1 system..... 58

Figure 2.25 Example $S11$ responses at $k12$ locations representing UC, CC, and OC regions, for the $k12opt = 0.01$ optimized Tx to Rx1 system..... 58

Figure 2.26 Measured (dotted line) and Simulated PTE responses for Tx to Rx2. Critical coupling can never be achieved in this system. However, as large as an 11% increase in PTE can be achieved by choosing an ideal $k12opt$ optimization point..... 61

Figure 2.27 Measured input impedance ($f0$=13.56 MHz, Pin = 15 dBm) for (a) rectifier and voltage regulator circuit connected to a custom designed medical device (Bionode) and (b) input impedance replication circuit for enabling 2-port VNA measurement. 62

Figure 2.28 Experimental validation of complex load impedance accommodation. (a) Comparison of Inter-resonator coupling PTE response for Tx to Rx1 optimized at $k12opt = 0.01$. The complex load accommodated system achieves the same PTE response predicted and measured for a non-complex load impedance system. (b) Measured and circuit simulated $S11$ and $S22$ responses at inter-resonator coupling location $k12 = k12opt = 0.01$. 63

Figure 2.29 Generalized procedure for BPF modeled MRC WPT control and optimization. 65

Figure 2.30 Example BPF modeled MRC WPT coupling arrangements: (a) serial power "hopper", (b) cross-coupled parallel power "hopper", and (c) multi-load power distribution arrangement. 67

Figure 3.1 MRC WPT arrangement for operating multiple Myoelectric sensing devices. (a) Intended placement of the AHH arm band coil around a human body model in ANSYS HFSS®. (b) AHH coil dimensions. (c) Illustration of magnetic field vectors. (d) Rx coil fabricated on a flexible polyimide substrate with 2oz. copper deposition and insulting polyimide overlay. Coil footprint is 15 mm x 15 mm and a thickness of 0.13 mm. (e) HFSS® model of the AHH arm band coil and relative positioning of the 8 flexible printed Rx coils. Equal inter-resonator coupling is achieved to enable optimum

Figure Page

simultaneous wireless power distribution to eight devices wrapped circumferentially around a subject's forearm. (f) Adjustable forearm cuff designed to house eight pairs of dry metal dome electrodes for sEMG recording on the interior lining. Electrode interface with the microelectronics platform on the exterior surface through snap joint and flexible extension spring leads. 71

Figure 3.2 Anti-Helmholtz coil arrangement. Note the equal and opposite current, i, directions between top and bottom coils. 72

Figure 3.3 HFSS simulated H-field distribution for an AHH arranged coil. Opposite currents are achieved by connecting oppositely wound coils. (a) magnitude of H-field distribution. The AHH system produces a quadrupole field. (b) vector H-field distribution. Note the high density of radially directed fields within the cylindrical window between coils. (Red, large magnitude; Blue, small magnitude) 73

Figure 3.4 (a) Fabricated AHH arm coil and (b) placement on a subject's forearm. 74

Figure 3.5 Measured AHH system inductor Q and comparison between an AHH system formed of top and bottom coils with 1 cm inter-winding spacing and an AHH system with top and bottom coils that were tightly wound. Inductor Q is improved by 272% (90 to 245 at 8 MHz) by implementing a 1 cm space in between windings in the top and bottom coils. 75

Figure 3.6 Individual flexible Rx coil (a) design: gw = 0.25 mm, tw = 0.35 mm, $L1 = L2 = 15$ mm, N = 4 turns. (b) Fabricated coil 75

Figure 3.7 Measured Rx coil Q on and off the forearm. 76

Figure 3.8 (a) Coupling configuration, (b) coupling map, and (c) general coupling matrix for the AHH MRC powering arrangement (1 source resonator and 8 receive resonators and loads). See Figure 2.29 for coupling map key. 78

Figure 3.9 Coupling matrix for the single source and 8 resonator/load AHH MRC powering arrangement. 79

Figure 3.10 Individual receive resonator and power management system. 81

Figure 3.11 Predicted (theory) and circuit simulated PTE response between each receive system and the AHH arm band coil coupled to 8 receive systems. At $k12 = k12opt$, equal power distribution and optimal PTE is achieved. 81

Figure 3.12 Demonstration of the novel MRC arrangement integrated around the arm of an able-bodied subject. Eight devices, wrapped circumferentially around the arm, were simultaneously wirelessly powered enabling the control of a virtual arm. 83

Figure Page

Figure 3.13 HFSS simulated SAR distribution for the forearm with AHH armband coil excited with 1 W power and 8 MHz operation. A peak value of 0.0005 W/kg whole body average. Inset shows peak SAR of 0.3 W/kg averaged over 10 g of tissue. 86
Figure 4.1 Illustration of commonly shaped EM cavity resonators. (a) Rectangular cavity resonator and associated dominant mode (TM_{110}) EM field distribution and (b) cylindrical cavity resonator and associated dominant mode (TM_{010}) EM field distribution. 91

Figure 4.2 Illustration of a cavity resonator MRC WPT system concept. An excitation probe is fed by an external signal generator to excite the cavity at $f010$. The induced fields are resonantly coupled to an internal receive resonator within. The internal receive resonator is formed by a coil and shunt capacitor. External coupling from the receive resonator to load is configured by an admittance inverter. 94

Figure 4.3 Circuit representation and BPF model transformation of the cavity resonator MRC WPT system. (a) standard circuit model, (b) standard circuit model with equivalent external and inter-resonator coupling networks, and (c) BPF model form. 95

Figure 4.4 Generalized cavity resonator BPF model, with complex port admittance (impedance) accommodation, for a rectangular or cylindrical cavity resonator (excited in the dominant TM mode) WPT system. 98

Figure 4.5 Representative Y for the BPF modeled cavity resonator WPT system. Resonator and impedance scaling factors are shown. 99

Figure 4.6 Normalized admittance matrix 99
Figure 4.7 Lumped element representation of external coupling J-inverters. (a) Capacitive coupling between excitation probe and cavity resonator. (b) half-pi J-inverter network. 103

Figure 4.8 Simplified and generalized cavity resonator BPF model. Capacitor $CFIS1$ is small relative to $C1$ and is thus removed from the transmit side. The parallel combination $C2$, $-Cp2$, and $CFIS2$ forms a single parallel capacitor, Cpt, on the receive resonator system. 105

Figure 4.9 Image of the constructed cylindrical cavity and receive resonator WPT system. Physical dimensions: $r1 = 30$ cm, $h1 = 25.4$ cm, $Lprobe = 5.76$ cm, $r2 = 2.5$ mm, receive coil thickness = 0.70 mm. Cavity volume = 0.072 m^3; 106

Figure 4.10 One port reflection cavity resonator measurement. (a) Illustration of one-port measurement set-up. (b) Equivalent circuit. (c) Measured $S11$ response of copper cylindrical cavity. The excitation probe length was set to 57.6 cm 109

Figure Page

Figure 4.11 Curve fitting method to determine Cm and $Cprobe$ for a corresponding excitation probe, $lprobe$ (a) Circuit simulation set-up, Cm and $Cprobe$ are varied in circuit simulation until the simulated $S11$ response matches the measured response. (b) circuit simulation shows close match to the measured response ($lprobe = 57.6$ cm) when Cm and $Cprobe$ are tuned to 8.65 pF and 1.6 pF, respectively. 113

Figure 4.12 (a) Theoretically predicted, circuit simulated, and measured $S212$ responses (measured includes optimal IM and non-optimal IM results). Inset shows a comparison of peak PTE. (b) Measured (optimal and no IM) and circuit simulated $S11$ and $S22$ responses. The receive resonator was oriented perpendicular to the TM_{010} distributed magnetic fields located 10 cm within the cavity and a height of 15 cm. 116

Figure 4.13 Experimental set-up to measure optimal cavity resonator WPT with porcine eye tissue. (A) shows location of porcine eye tissue and cavity resonator system. (B) shows the coil located in the eye for two-port VNA measurements. (C) shows a close up view of the porcine eye with embedded silicone epoxied 2 mm diameter receive resonator coil..... 118

Figure 4.14 Measured PTE between the optimally tuned 2 mm diameter coil made resonator and cavity resonator system in air and in the anterior chamber of the Porcine Eye. In the eye tissue, the 2 mm diameter receive coil achieved a peak PTE of 6.11% 120

Figure 4.15 Ultra-miniature device circuit schematic. The fabricated device was implanted into porcine eye tissue. 123

Figure 4.16 Fabricated miniature LED device. Left: Device fully implanted in the anterior chamber of the ocular tissue and right: zoomed in view of the optimally tuned miniature device. The device was packaged in silicone epoxy to isolate the electronics from the biological tissue. 123

Figure 4.17 Peek-hold view inside the cavity resonator demonstrating wireless powering to the miniature LED device operating within the implant environment. 124

Figure 5.1 Summarized illustration of a cavity resonator WPT arena. The magnetic field density of the TM_{110} resonant mode is illustrated (Magnitude legend: Red, large; Blue, small). A small animal with a packaged implanted device is housed within the cavity resonator volume. A biaxial arranged power receive resonator system is used to promote orientation insensitivity. The in package bioelectric system consists of a custom designed "Powernode" and "Bionode" system. 129

Figure 5.2 Photograph of the constructed cavity resonator small animal housing unit. (a) Full perspective view with lid attached. (b) Underside of lid unattached to cavity. The excitation probe with length, lprobe, is located at the center of the lid. The lips of the lid

Figure Page

are lined with Copper Beryllium RF gasket. This provides electrical connection and minimizes field leakage. Copper tape is utilized to reinforce electrical connections. (c) Side view of cavity resonator with detail view of the cut out slots. (d) full perspective view without lid. Interior magnetic field "blind-spot" barriers (center and four corners) are shown. 131
Figure 5.3 Simulated H-field distribution in the TM_{110} excitation mode. 134

Figure 5.4 Simulated surface J-field distribution in the TM_{110} excitation mode. 134

Figure 5.5 Relationship between $lprobe$ and model capacitances $Cprobe$ and Cm. (a) Circuit model used for circuit simulation. $Cprobe$ and Cm were dynamically tuned in simulation until the simulated $S11$ response matched to the measured response. (b) example of circuit simulation matching for measured responses with $lprobe$ at 110 mm, 80 mm, and 50 mm. (c) Plot of $Cprobe$ and Cm as a function of $lprobe$ from 50mm to 130 mm for the small animal housing constructed rectangular cavity resonator structure. 137

Figure 5.6 Experimental set-up of cavity resonator WPT characterization. (a) Diagram illustration of measurement set-up and labeled positions. The receive resonator is placed through slot 4 and moved in the x-direction. (b) Closed lid inside view highlighting excitation probe and receive resonator system within the plastic guide tube. (c) 7 mm diameter receive coil connected to optimized tuning PCB for measurement. 139

Figure 5.7 Summary of measured PTE response within the cavity. Location of measurements are in reference to the coordinates provided in Figure 5.6. (a) Peak PTE as a function of x-direction position. (b) Measured, circuit simulated, and theoretically predicted frequency response at $k12 = k12opt = 0.002$. 140

Figure 5.8 Estimated peak obtainable PTE (inferred from measured data) in the x-y plane at a height of 15 cm. Note the lower values of PTE at the slot locations. 141

Figure 5.9 Copper cavity resonator provides drastic improvement in WPT performance. (a) Full perspective view of the constructed rectangular copper cavity with dimensions of 60.96 cm x 60.96 cm x 30.0 cm (L x W x H). (b) Full perspective view of the copper cavity lid and attached excitation probe (lprobe = 50 mm). The copper cavity exhibits a measured Q0 of 12,157 and f110 = 344.60 MHz. (c) 2 mm diameter receive coil coil (L = 16.73 nH at f110) connected to tuning circuit PCB (Cs2 = 1.8 pF, -Cp2+C2 = 12.4 pF). (d) 5 mm diameter receive coil (L = 48.23 nH at f110) connected to tuning circuit PCB (Cs2 = 1.2 pF, -Cp2+C2 = 4.1 pF). (e) Measured peak PTE as a function of radial position within the cavity. The measurement set-up and coil locations were conducted identically with the experimental set-up shown in Fig. 8(a). Constructing the cavity out of copper and utilizing our optimal IM methodology, we achieve a maximum peak PTE of 51% for a 5 mm diameter receive coil and a maximum peak PTE of 7.7%

Figure Page

with a 2 mm diameter coil. In comparison, a maximum PTE of 14% is achieved with a 7 mm diameter coil in the aluminum cavity of same dimensions..... 143

Figure 5.10 Cavity $Q0$ and $f110$ as a function of rat position within the cavity (moved incrementally through center of cavity). Note that the excitation probe length was 84.0 mm. 144

Figure 5.11 Measured peak PTE (frequency tracked) as a function of radial position (through Slot 4) for various re-tuning conditions (summarized in Table 5.4)..... 146

Figure 5.12 Measured peak PTE (frequency tracked) as a function of radial position (through Slot 4) for various re-tuning conditions (summarized in Table 5.4)..... 148

Figure 5.13 Block diagram of implantable microelectronics and external base station used to record bioelectric events in untethered, freely behaving animals within the cavity resonator. The bioelectric recording device utilizes all COTS integrated circuits and incorporates two analog front-end channels having a combined peak sample rate of 25 kHz and a current-controlled stimulating output channel having a voltage headroom of 10.5 V. Device logic and tasks are facilitated by a SoC with an integrated 2.4 GHz transceiver. The power needed to run the microelectronics come from the Powernode, which coupled and rectifies RF energy and supplies regulated DC voltages to the bioelectric recording device. 151

Figure 5.14 Biaxial Powernode System. (a) Schematic diagram of biaxial RF-to-DC conversion circuitry. (b) Photograph of fabricated Powernode device PCB. The Powernode is stacked on top of and electrically connected to the bionode..... 152

Figure 5.15 Simulated power receive performance as a function of angular performance of the biaxial arranged Powernode system. (a) Orientation and coordinate reference. (b) Normalized (0 to 1) simulated PTE as a function of angular rotation (theta and phi).... 154

Figure 5.16 Full system and packaging. (a) Pre-packaged and (b) fully packaged wireless implantable device with biaxial powering capability. 155

Figure 5.17 *In-vivo* experimental setup. (a) An external view showing the signal generator, PA, cavity resonator, external basestation, and corresponding PC. (b) Inside view of the cavity with a freely behaving rat within (post-operative day 43). The green light on the external base station indicates that the implanted device is on and transmitting data..... 158

Figure 5.18 Wirelessly acquired rat ECG signal from within the cavity. (a) 60 s window and (b) 2 second zoomed in view (segment between dashed lines). 159

Figure Page

Figure 5.19 Power fidelity distribution for rat R200 over nine separate recording sessions taken over a period of nine weeks. The recording session length is provided in each bar. 159

Figure 5.20 EMI testing results. (a) Reconstructed signal (from ADC input, AFE output) under 3 powering and operating conditions. Input signal (into AFE) = 100 Hz sin wave, 2 mVpp, AFE gain = 100. (b) FFT of the 3 powering and operating conditions. 162

Figure 5.21 Comparison of this work to prior state-of-the-art WPT systems used for small animal experiments. WPT system approaching the upper right corner exhibit the largest operating volume with greatest device miniaturization capability. See Table 5.5 for a description of arena volume calculations for each reference. Circles with an "X" represent references which did not describe or demonstrate wireless powering of a bioelectronics device. 163

Figure 6.1 Key contribution framework of this research. This research provides a robust and new analytical understanding and optimization methodology of filter synthesized coupled resonator WPT system. The same framework can be extended to cavity resonator WPT systems which were also developed within this research. 168

Figure 6.2 Simulations of evanescent field coupling into biological tissue. (a) side view of cavity resonator structure with meshed top. (b) top view showing mesh top. With a radius of 7.3 cm, the dominant mode excitation frequency is 1.57 GHz. (c) Simulation model with cylindrical muscle tissue and bone. A 5 mm air gap exists between the tissue model and cavity mesh. (d) Simulated H-field distribution within the human arm model. The simulation results indicate that a z-dir. propagating mode can be induced into tissue at 1.57 GHz by evanescent field coupling. Note the attenuation of H-field in the cortical bone structure. 170

Figure 6.3 Experimental Demonstration. (a) Experimental setup with constructed cavity resonator structure and receive resonator system (2 mm diameter coil connected to tuning PCB, $Cpt = 0.2$ pF, $Cs2 = 0.2$ pF) located at a height, h, above the surface of the cavity mesh. (b) Experimental setup with a liquid tissue phantom (replicating electrical properties of muscle at 1.6 GHz) on the surface of the mesh. (c) Measured PTE results at h = 6 cm and h = 3 cm with and without the liquid tissue phantom. 171

Figure 6.4 Evanescent field coupling demonstration with and without coupling into a human arm. In both experiments, the input power to the cavity was 6 W at 1.55 GHz. (a) Without the presence of a human arm, wireless power transfer efficiency decays rapidly resulting in the LED being off at a height of approximately 6.0 cm. (b) Acting as a dielectric waveguide, energy is coupled into the human arm and wireless power transfer efficiencies are maintained at a level high enough to operate the LED at > 3 times the height. 175

ABSTRACT

Mei, Henry. Ph.D., Purdue University, May 2016. Coupled Resonator Based Wireless Power Transfer for Bioelectronics. Major Professor: Pedro Irazoqui.

Implantable and wearable bioelectronics provide the ability to monitor and modulate physiological processes. They represent a promising set of technologies that can provide new treatment for patients or new tools for scientific discovery, such as in long-term studies involving small animals. As these technologies advance, two trends are clear, miniaturization and increased sophistication i.e. multiple channels, wireless bi-directional communication, and responsiveness (closed-loop devices). One primary challenge in realizing miniaturized and sophisticated bioelectronics is powering. Integration and development of wireless power transfer (WPT) technology, however, can overcome this challenge.

In this dissertation, I propose the use of coupled resonator WPT for bioelectronics and present a new generalized analysis and optimization methodology, derived from complex microwave bandpass filter synthesis, for maximizing and controlling coupled resonator based WPT performance. This newly developed set of analysis and optimization methods enables system miniaturization while simultaneously achieving the necessary performance to safely power sophisticated bioelectronics. As an application example, a novel coil to coil based coupled resonator arrangement to wirelessly

operate eight surface electromyography sensing devices wrapped circumferentially around an able-bodied arm is developed and demonstrated.

In addition to standard coil to coil based systems, this dissertation also presents a new form of coupled resonator WPT system built of a large hollow metallic cavity resonator. By leveraging the analysis and optimization methods developed here, I present a new cavity resonator WPT system for long-term experiments involving small rodents for the first time. The cavity resonator based WPT arena exhibits a volume of 60.96 x 60.96 x 30.0 cm^3. In comparison to prior state of the art, this cavity resonator system enables nearly continuous wireless operation of a miniature sophisticated device implanted in a freely behaving rodent within the largest space.

Finally, I present preliminary work, providing the foundation for future studies, to demonstrate the feasibility of treating segments of the human body as a dielectric waveguide resonator. This creates another form of a coupled resonator system. Preliminary experiments demonstrated optimized coupled resonator wireless energy transfer into human tissue. The WPT performance achieved to an ultra-miniature sized receive coil (2 mm diameter) is presented. Indeed, optimized coupled resonator systems, broadened to include cavity resonator structures and human formed dielectric resonators, can enable the effective use of coupled resonator based WPT technology to power miniaturized and sophisticated bioelectronics.

CHAPTER 1. INTRODUCTION

1.1 A Prelude to Wireless Power Transfer

In 1865, James Clerk Maxwell published his profound manuscript, "A Dynamical Theory of the Electromagnetic Field," [1] helping to set in motion mankind's transition into the modern technological world. In that work, Maxwell described the physically intimate connection between electricity and magnetism. Through his mathematics, he helped unify the electric and magnetic phenomena observed prior by scientific greats such as Alessandro Volta, Hans Christian Ørsted, André-Mariè Ampere, and Michael Faraday, among others. Today, Maxwell's electromagnetic (EM) unification are encoded in his four (Maxwell's original formulation contained 20 equations, but was simplified by Oliver Heaviside) equations (differential form):

$$\nabla \cdot \vec{D} = \rho \tag{1.1}$$

$$\nabla \cdot \vec{B} = 0 \tag{1.2}$$

$$\nabla \times \vec{E} = -\frac{\partial \vec{B}}{\partial t} \tag{1.3}$$

$$\nabla \times \vec{H} = \vec{J} + \frac{\partial \vec{D}}{\partial t} \tag{1.4}$$

Intrinsic to Maxwell's equations are the formulations for calculating EM fields and the formulations proving the existence of propagating EM waves—and that light itself is an EM wave. Indeed, Maxwell's equations and natural EM phenomena form the theoretical

basis for the transfer of energy without physical conduits, better known as wireless power transfer (WPT).

The development and deliberate use of WPT technology was popularized later toward the end of the 19th century when Nikola Tesla carried out his grandiose and technically incredible high frequency and high voltage experiments [2]. Indeed, Tesla spent a considerable amount of energy trying to establish and share his vision of creating a world where both energy and communication could reach the far reaches of the world without the need for wires. As Tesla wrote [3]:

> "Our senses enable us to perceive only a minute portion of the outside world. Our hearing extends to a small distance. Our sight is impeded by intervening bodies and shadows. To know each other we must reach beyond the sphere of our sense perceptions. We must transmit our intelligence, travel, transport the materials and transfer the energies necessary for our existence."

Unfortunately, due to financial difficulties and lacking support, his global reaching endeavors to bring WPT capability to the world never reached fruition. However, his work helped provide the foundation for wireless communication which, from the early to mid-20th century, became a primary research and development focus within the wireless technology sector. And as high frequency and microwave engineering techniques advanced, interest in WPT as a means for deliberately sourcing power re-emerged. In the 1970's, William C. Brown gained notoriety for his work developing and demonstrating far-field based radiofrequency (RF) energy transfer systems; highlighting its useful potential as an alternative method of power delivery [4-6]. Today, WPT technology continues to gain significant attention as it represents the final frontier from which we can

fully detach from the cord. Of major significance is the adoption and advancement of WPT technologies for use in bioelectronics.

1.2 Motivation

Since the first pacemaker was implanted over 50 years ago [7], bioelectronics have seen rapid growth, becoming smaller, more capable, and less invasive for patients. These advances have paved the way for the development of medical devices that are able to provide therapy for a wide range of pathologies and disorders. Some examples include: retinal and cochlear implants, which have helped introduce visual or auditory perception to the blind or deaf; Vagus nerve and deep brain stimulators, which have reduced seizures in epileptic patients, minimized motor control symptoms in patients with Parkinson's disease, and reduced depression; pacemakers, which pace the heart; brain-machine interface systems, which have enabled amputees to regain control of their environment; and a host of others. Indeed, the push to develop new devices and therapies continues to strengthen. For example, the electroceutical initiative, introduced through collaborative efforts between industry, government, and academic institutions, have incentivized the development for a new class of sophisticated and miniature bioelectronic devices that could be utilized for precise and adaptive modulation of individual circuits of neural systems [8]. These electroceutical based devices could tap directly into single or multiple neuronal fibers, modulate action potentials, and deliver specific and smart therapies for conditions that were once ineffectively treated through other avenues [9]. Indeed, the path forward requires the advent of new bioelectronics that can be constructed in small form

factors while still incorporating high sophistication i.e. multi-channel recording and simulation capability, bi-directional wireless communication, and responsiveness.

The electroceutical initiative has also incentivized research to extensively understand the mechanisms and language of neural systems. Consequently, miniature bioelectronics are not only needed for clinical applications in humans, but are also required for scientific discovery involving small animals such as rodents. Long-term electrophysiological recording and neural stimulation (electrical or optical) experiments conducted with freely behaving small animals help provide understanding of the central and peripheral nervous systems and the effect neural modulation may have on physiology, behavior, and emotion. Consequently, the bioelectronics which interface with the small animal and the environment in which the small animal is housed must be designed in such a manner so as to not interfere with any of the natural processes incurred in the animal by the controlled experiment. Indeed, device miniaturization and long-term housing in a large and unrestrictive experimental environment are required to facilitate the natural processes of the small animal and improve experimental outcomes.

In both clinical and scientific discovery based applications, device miniaturization represents a key need. One major obstacle towards miniaturization, however, comes from the commonly utilized power source, the battery. Integrated batteries are able to power bioelectronics for extended periods of time but often occupy greater than 90% of the overall device volume. To some extent, decreasing power consumptions as a result of advances in device microelectronics have decreased needs, but advances in bioengineering and the need for device sophistication have largely reversed such gains [10]. Consequently, alternative powering methods are necessary. Energy harvesting

systems, which utilize anatomical function such as vibrational energy from the beating heart and expansion of lungs have been explored [11]. Although highly advanced, such energy harvesting systems currently exhibit power densities too low (time-average power density of 0.12 and 0.18 $\mu W/cm^2$) to adequately power sophisticated miniaturized bioelectronics. More practical, however, is wireless power, which is capable of yielding high power densities when adequately designed. Utilizing WPT technology, sophisticated implantable devices could operate with smaller batteries and be recharged wirelessly from an external source. In devices designed for small spaces or to be implanted in small rodents, the battery could be removed altogether. Consequently, WPT technology would enable untethered operation of fully implanted miniature bioelectronics in small animals and minimize external factors which may confound the experimental results.

1.3 Definition of WPT Technology Requirements

In order for WPT technology to become a practical and advantageous power delivery method for sophisticated bioelectronics, it must exhibit two critical criteria: First, the WPT technology must exhibit the capability to safely (i.e. within EM energy exposure limits imposed by government agencies) transfer adequate energy to operate sophisticated bioelectronics. In this work, sophisticated bioelectronics refers to the power operating conditions of a state-of-the-art and custom designed electrophysiological recording and stimulating device named the Bionode. The Bionode is a comprehensive, adaptable, responsive (i.e. closed-loop), fully wireless (bi-directional communication with wireless programming), and batteryless bioelectric recording and stimulating (electrical or optical) system, custom designed at the Center for Implantable Devices at

Purdue University. Depending on operating conditions, average power consumptions of the Bionode can range from 6.1 mW to 13 mW, with peak power consumptions (from on board processing and radio) exceeding 20 mW. Secondly, the WPT technology must be amenable to miniaturization to enable fully implanted chronic rodent (rats and mice) animal experiments. In this work, WPT technology miniaturization capability refers to the ability to utilize wireless energy receive structures (inductor coils, antennas, etc.) with max dimensions that correspond to or are less than the physical dimensions of the miniature sized Bionode system. The Bionode is approximately 8 mm in width and 15 mm in length.

1.4 Review of WPT Technologies

Current WPT technologies are based on three mechanisms: far-field, mid-field, and near-field (coupled resonator systems). These three WPT modalities are distinguished by the behavior of the EM energy transfer mechanism which are strongly dependent on the frequency of operation and relative distance between the energy source and energy receive element (Figure 1.1). Far-field WPT occurs from the capture of radiated EM waves. Radiated EM fields are captured by a receive (Rx) antenna in the region where the field distribution of the radiated field is independent of distance [12]. In reference to Figure 1.1, this occurs at a radial distance (R) of approximately $R > 2D^2/\lambda$, where D is the largest dimension of the transmit (Tx) antenna and λ is the wavelength at the frequency of operation. In the near-field, wireless delivery of power occurs from the capture of stored energy (electric, magnetic, or mixed) in close vicinity to the source. This region extends to a radial distance of approximately $R = \lambda/2\pi$ from the source. The region

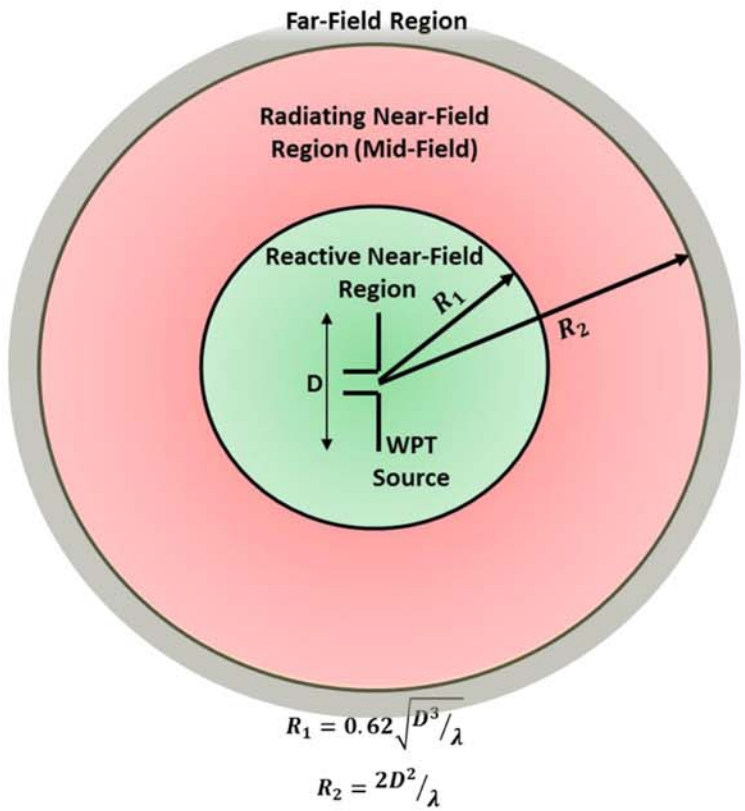

Figure 1.1 Characterization of the far-field, mid-field, and near-field regions. The mechanism of WPT are dependent on the region at which energy is captured.

between the reactive near-field and far-field is known as the radiating mid-field. In this region, radiation fields dominate and the angular distribution of phase cannot be ignored [12]. In the following sub-sections, an exploration on the capabilities for each WPT modality to achieve the criteria described in the previous section (i.e. safely power sophisticated wearable or implantable bioelectronics in a miniature form factor) are explored.

1.4.1 Far-field WPT

Far-field methods operate on the principle of radiation, where propagating EM fields are captured at distances far from the source. Antenna performance is optimal when

its physical dimensions are comparable to the wavelength (λ) at its designed operating frequency (*f*), of which they are inversely proportional, i.e.. $\lambda \propto f^{-1}$ [13]. Higher frequencies lead to shorter wavelengths and therefore smaller Rx antennas. As a consequence, frequencies in the gigahertz (GHz) ranges are typically used in order to achieve sufficient miniaturization of the receive element. However, high frequency EM fields rapidly degrade as they impinge upon and travel through tissue. This is a result of losses due to tissue conductivity and boundary reflections at the interface between heterogeneous layers of tissue. As an example, far-field radiofrequency (RF) energy is attenuated by ~37% at depths ranging from ~100 mm at 433 MHz to ~ 10mm at 5.8 GHz [14]. Thus, a fundamental trade-off exists between developing far-field systems that enable device miniaturization and far-field systems that can safely power sophisticated bioelectronics in implanted spaces. To address this, significant research has been conducted on the optimization of electrically small antennas for capturing far-field RF energy at low frequencies.

Antennas with physical dimensions operating at a frequency satisfying the condition of $kr < 0.5$ are termed electrically small antennas (ESAs), where k is the free-space wave number ($k = \frac{2\pi}{\lambda}$) and r is the radius of the minimum size sphere that encloses the antenna [13]. ESAs tend to store energy rather than dissipate it through radiation. As a consequence, they exhibit high radiation quality (Q) factors; defined as the ratio of stored reactive energy to energy dissipated through radiation [15, 16]. Due to a tendency to store rather than radiate energy, ESA's exhibit low radiative performance and thus low antenna gain, a key parameter describing an antennas radiative performance which relates the antennas directivity and radiation efficiency [12]. Figure 1.2 illustrates the

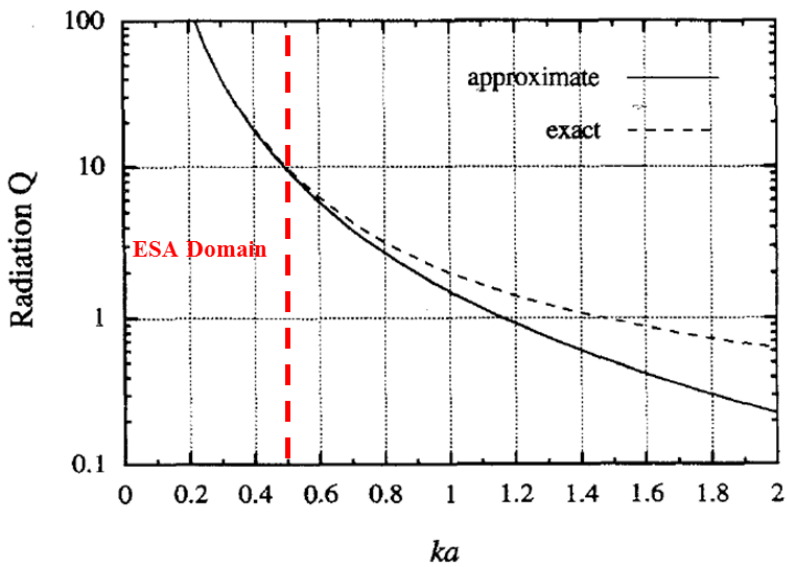

Figure 1.2 The fundamental minimum limit of radiation Q factor plotted as a function of *kr* for a linearly polarized antenna. Antenna Q increases exponentially as the electrical size of the antenna decreases. Indeed, ESAs tend to exhibit low radiating performance. Figure reprinted and modified from [17]. Note that *a* in the figure corresponds to *r*.

fundamental limit of minimum achievable radiation Q factor as a function of the antennas electrical size (*kr*). Within the ESA domain, radiation Q factor increases rapidly and radiation performance degrades accordingly. This fundamental limitation of achieving high antenna gain highlights the key trade-off between miniaturization and performance in far-field WPT systems. Among the literature, ESAs designed for free space applications have illustrated various ESA optimization strategies. Novel ESA designs utilizing spherical current distributions have resulted in radiation Q factor performance approaching the fundamental limits [18-20]. This has provided an excellent foundation for the design of ESAs for operation in the tissue space. However, due to the conductive nature of biological tissue, optimized ESA designs are still challenged by poor antenna efficiency performance. Table 1.1 summarizes characteristics of optimized ESAs and

Table 1.1 Survey of simulated ESA performances in various tissue replicated body phantoms

Reference	Resonant Frequency (MHz)	Body Phantom	Wavelength at frequency of operation (mm)	Radius of Minimum Sphere enclosing antenna (mm)	*kr**	Implanted Peak Simulated Antenna Gain (dBi)	Rad. Pattern
Izdebski et al. [21]	1400	Small Intestine	214.3	7.8	0.228	-30	Omni
Abadia et al. [22]	402	Muscle	746.0	20.0	0.168	-28.5	Omni
Karacolak et al. [23]	402	Skin	746.0	16.0	0.134	-26	Omni
Soontornpipit et al. [24]	402	Muscle	746.0	15.7	0.132	-35	Omni
Merli et al. [25]	402	Muscle	746.0	13.3	0.112	-29	Omni
Chien et al. [26]	402	Skin	746.0	12.2	0.103	-19	Omni
Yang et al. [27]	402	Human Oral Cavity	746.0	8.0	0.068	-38	Omni
Lee et al. [28]	402	Skin	746.0	7.0	0.059	-26	Omni
Gosalia et al. [29]	2450	Eye	122.4	4.2	0.22	NR	NR

*Calculated from dimensions and operating frequency from respective reference; NR = Not Reported

performance in tissue replicated body phantoms. It is clear from Table 1.1 that implanted ESAs suffer from extremely low antenna gain. Consequently, it has been shown that the average usable power received by an implant located 2 cm deep in muscle achieved only microwatt (μW) capability with values of 20.7 μW at 915 MHz, 1.40 μW at 2.40 GHz, and 0.000638 μW at 5.80 GHz [30]. That study imposed frequency specific maximum permissible exposure (defined by the federal communications committee) limits at the air-tissue interface of a three layered finite element simulation model, assumed an implanted antenna with peak gain of -20 dBi, a matching network efficiency of 100%, and a rectifier conversion circuit efficiency of 20%.

Consequently, far-field WPT using ESAs, in its current state, would be insufficient to sustain and operate sophisticated bioelectronics devices, especially in an implanted environment. Instead, far-field WPT may be most promising for non-implanted ultra-low power (< 1 mW peak power consumption) systems such as contact lenses and active sub-corneal implants for intraocular pressure sensing or wearable electronics and sensor nodes [31-34]. Overall, the significant energy losses incurred by the high frequency electrical properties of tissues, coupled with the very inefficient capture capability of electrically small receive antennas due to the conductive nature of the implant environment, result in far-field WPT efficiencies unsuitable for powering implanted devices in clinical and scientific based applications.

1.4.2 Mid-Field WPT

Mid-field WPT is based on the energy capture of induced EM energy propagation by coupling evanescent waves between an optimized energy source and heterogeneous layers of biological tissue. Developed by Ho et al. [35], this methodology enabled the wireless operation of a tiny (about the size of single grain of rice) pacemaker device (2 mW power consumption) implanted in the chest of a rabbit. To achieve that feat, the researchers utilized their previous bodies of work which provided the optimal frequencies (1.5 GHz to 1.6 GHz) at which evanescent coupling of EM energy would be most efficient through heterogeneous layers of tissue [36] and provided the development method for an optimized evanescent generating field antenna [35, 37]. As another application example, the same group utilized mid-field powering principles for building a small WPT arena for operating simple and passive optogenetic devices implanted in mice

[38-40]. Indeed, the mid-field WPT methodology has garnered significant attention. However, clear challenges must be overcome in order for the technology to become a practical methodology as a means to wirelessly power more sophisticated bioelectronics with higher power consumptions than the devices utilized in their work. For example, to provide the 2 mW necessary to operate the pacemaker device, the power output of the transmitter was set to 6.3 W which resulted in tissue specific absorption rate (SAR) levels reaching the maximum allowable level (determined by federal guidelines and explained in more detail in Chapter 3, Section 3.4). Indeed, mid-field WPT would be unsuitable for safely operating sophisticated bioelectric devices, which can exhibit typical peak power consumptions exceeding 2 mW, implanted in humans. Additionally, to operate the implanted optogenetic device in mice, the power output from the energy source was set to 16 W (20% duty cycle). This power level far exceeded the 4 W limit the same group previously described as the maximum power that could be sent into the small animal arena transmitter without breaking SAR regulations [40]. Although no SAR limitation guidelines for small animals exists, staying below SAR limits will minimize behavioral changes in the animal, ensure safety for the user, and promote use across the scientific community. Although ultra-miniaturization was achievable, Mid-field WPT technology, as reported in the current literature, has been shown to only safely operate passive ultra-low-power systems.

1.4.3 Near-field (Coupled resonator) WPT

Faraday's Law states that the voltage induced on a closed circuit is proportional to the magnitude (1/distance^3 dependence) and rate of change of magnetic flux in a given area

through a closed circuit [41]. The wireless delivery of power is therefore accomplished by coupling non-radiative magnetic energy between Tx and Rx coils. The types of coils used to transmit and receive near-field energies typically fall into two main categories: short solenoids and spiral inductors. Commonly, the conductor lengths of these coils are $< 1/10^{th}$ of the wavelength at the frequency of operation which typically range from kilohertz (kHz) to low megahertz (MHz) levels [42]. Therefore, near-field coils operate in the electrically small domain. In this domain, radiation losses are negligible and current is distributed uniformly in the conductors allowing the coils to be treated as lumped element inductors [43]. Consequently, most efficient magnetic coupling occurs in the reactive near-field, defined as the region between the Tx (primary) and Rx (secondary) coils where the separation distance is much smaller than the wavelength at the operating frequency [12].

A highly efficient form of near-field WPT is magnetic resonance coupling (MRC). In the bioelectronics sector, MRC has been explored for use in powering ventricular assist devices [44] and as platforms for small animal WPT arenas [45-47]. Energy is transferred through coupling of magnetic fields using resonant circuits (electric fields could also be used, but due to the non-magnetic nature of biological tissue, magnetic field coupling is more practical for implanted bioelectronics). It is important to note that the principle mechanism of magnetic energy transfer does not differ from traditional inductive powering. However, the primary difference between traditional inductive powering and MRC is the implementation of optimizable impedance match conditions [48]. By carefully designing and optimizing the impedance matching (IM) conditions, system performance can be drastically increased over traditional inductive methods. In the highly

publicized work of Kurs et al., high efficiencies were achieved at distances several times the diameter of the powering coils [49]. Consequently, much of the literature has focused on the optimization methods of MRC systems which meet IM conditions by physically varying parameters of MRC systems constructed using 4 coils (source: drive and Tx coil; load: Rx coil and load coil) [49-53]. In those systems, IM was conducted by physically switching the coils used for WPT or varying the physical distances between resonators and respective source/load coils of the four coil system. However, in bioelectronics applications, physically manipulating a four coil system to achieve an IM condition would be impractical. Greatly simplifying this process, however, has been the design of MRC systems using microwave filter synthesis techniques [54-60]. In these systems, optimal IM conditions can be obtained to maximize power transfer with minimal components, drastically reducing size and system complexity. The foundation of MRC optimization developed by the filter synthesis perspective has shown significant promise for practical application for powering bioelectronics. However, severely lacking yet is the robust analytical understanding of performance control in filter synthesized MRC systems. Without insight into parameter relationships and their influence on system performance, the methodology for maximizing WPT performance to sophisticated and miniature bioelectronics would remain elusive. With robust analytical understanding and optimization methodologies, filter synthesized MRC systems based on traditional coil to coil coupling may become effective for clinical based applications. However, coil to coil based MRC systems utilized in non-clinical applications such as long term small rodent experimental studies are challenged by an ineffectiveness to wirelessly transfer energy to small devices implanted in a freely behaving small animal within a large volume (see

Chapter 5 for a brief literature review). This is simply due to the fundamental 2-dimensional nature of coil to coil based magnetic coupling. Consequently, for this application, a new coupled resonator based technology would be necessary.

1.5 Thesis Objectives, Key Contributions, and Organization

Figure 1.3 summarizes the power delivery and miniaturization capabilities of far-field, mid-field, and near-field (coupled resonator) WPT technologies. Some miniaturization can be achieved in far-field but power delivery to sophisticated bioelectronics remains non-existent. Mid-field WPT technologies are capable of ultra-miniaturization with higher power delivery capabilities than far-field but still not at the performance to safely power sophisticated bioelectronics. On the other hand, coupled resonator based WPT exhibits high potential for delivering the necessary power requirements for operating sophisticated bioelectronics. In traditional coil to coil based MRC systems, miniaturization still represents a primary challenge (as indicated by the coil to coil boundary). With careful optimization standard coil to coil based coupled resonator WPT systems would become more practical for human clinical applications where ultra-miniaturization may not be a critical factor. However new coupled resonator technologies are required to obtain the miniaturization capability of mid-field methods while maximizing safe power delivery to operate sophisticated bioelectronics for use in small rodent studies.

Consequently, the main objectives of this thesis are twofold: 1.) derive a robust analytical framework and methodology for filter synthesized MRC performance optimization and control and 2.) develop new coupled resonator based WPT systems for

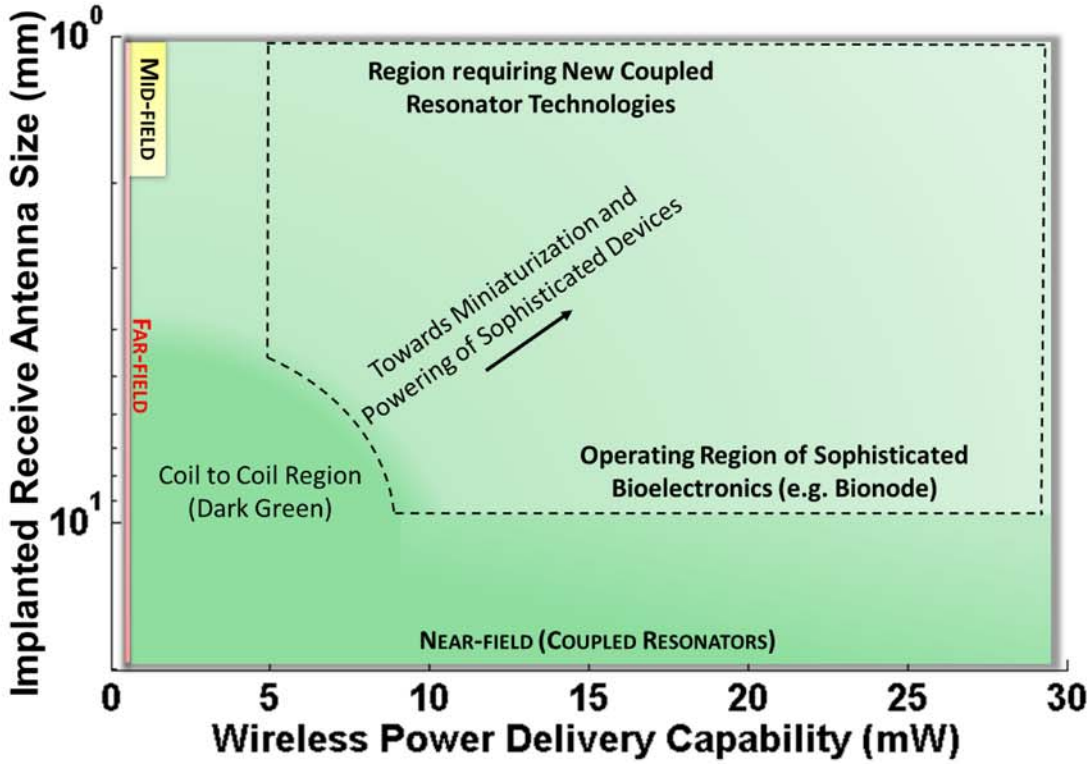

Figure 1.3 Comparison of miniaturization and safe power delivery capabilities between far-field, mid-field, and near-field (coupled resonator) based WPT technologies. A new WPT technology is necessary to improve miniaturization capability while maintaining the capability to safely deliver power requirements of sophisticated bioelectronics.

scientific discovery applications that achieves device miniaturization while simultaneously enables the safe delivery of power to operate fully implanted sophisticated bioelectronics. To address the first objective, an exhaustive mathematical analysis on filter synthesized coupled resonators is conducted. As a result, I present new optimization methods, system behavior, and performance prediction and control methodologies for coupled resonator systems. Using the derived analytical framework and optimization methodologies, a novel MRC WPT arrangement is designed to successfully operate a myoelectric sensing system. To address the second objective, I introduce a novel cavity resonator WPT system and optimization methodology for the

first time. As a result, a large small animal experimental arena for powering miniaturized sophisticated devices is developed and demonstrated with a set of chronic small animal experiments. To the best knowledge of the author, this novel system is capable of safely delivering the necessary power to operate fully implanted sophisticated bioelectronics using receive coils approaching the miniature sizes of mid-field WPT systems within the largest freely behaving operating volume. Overall, within the framework of near-field resonator WPT systems, this research provides the general optimization methodology for coupled resonator WPT systems and introduces a new cavity resonator WPT system. I also present preliminary work demonstrating the feasibility of a new cavity resonator WPT system technology which is predicated on treating parts of the human body as dielectric resonators from which energy can be extracted and delivered wirelessly to ultra-miniature (2 mm diameter) receive coils.

The organization of this thesis is as follows. In chapter 1, I present the motivation of this work, a review of WPT technologies, and the objectives of this research. In chapter 2, I present an exhaustive analytical derivation of filter synthesized MRC systems resulting in new system optimization and performance control capabilities. Experimental validation methods and results are presented. In chapter 3, I present a novel MRC WPT arrangement and utilize the optimization methodology and analytical framework developed in chapter 2 to demonstrate the fully wireless powering of multiple myoelectric sensing devices simultaneously. In chapter 4, I present the full cavity resonator WPT system, filter model, and optimization methodology. Proof-of-concept application experiments utilizing porcine eye and a custom designed ultra-miniature LED device are utilized to demonstrate *in-vivo* powering capabilities for biological objects

within the cavity resonator. In chapter 5, I present the design, construction, optimization, and utilization of a large (60.96 cm x 60.96 cm x 30.0 cm) small animal housing cavity resonator system. A chronic study using rats implanted with the Bionode is showcased. Finally, in chapter 6, I provide a summary of this thesis and provide the framework for future work that will continue to improve the capabilities of the systems developed in this research. Additionally, I provide preliminary results demonstrating the feasibility of treating the human arm as a dielectric waveguide resonator. Through evanescent field interaction with a novel cavity resonator structure, a phenomenon of induced coupled resonator based energy transfer into human tissue is verified. This system may exhibit utility for future clinical applications requiring the need for wirelessly powering ultra-miniature and sophisticated bioelectronics.

CHAPTER 2. ANALYSIS, DESIGN, AND OPTIMIZATION OF MAGNETIC RESONANT COUPLING WIRELESS POWER TRANSFER USING MICROWAVE NETWORK AND BANDPASS FILTER THEORY

2.1 Introduction

In this chapter, I develop a new MRC design, analysis, and optimization methodology. The methodologies described in this chapter were motivated by techniques employed in the development of complex microwave filter systems [61-64]. Specifically, I create a bandpass filter (BPF) model where impedance matching (IM) to attain optimal power transfer efficiency (PTE) at a single resonant frequency is achieved by creating a network which exhibits optimally calculated characteristic impedances of external coupling impedance inverters (K-inverters). Two unique elements are incorporated into the BPF model, a parasitic resistive element to account for the effects of finite Q_0 and a frequency invariant reactance (FIR) element for complex source and/or load impedance accommodation. Importantly, this IM methodology accommodates complex source and load impedances without distorting a pre-designed optimal power transfer efficiency (PTE) system response. This removes the necessity for additional IM networks which add complexity and additional losses. Previously published MRC models lack both of these elements and are designed based on 50 Ω source and load impedances [54, 55, 57, 58, 60]. Thus, these systems are unable to provide the optimal IM criteria for finite Q_0 MRC systems connected to complex impedances such as an RF-to-DC rectifier circuit.

Additionally, many previously published MRC IM design methods lack insight on the effect finite Q_0 resonators have on critical coupling point (CCP) control i.e. controlling the inter-resonator coupling location where peak PTE can be achieved at a single frequency [65-70]. To shed light on these effects and provide the methodology for determining optimal IM criteria, I develop a general coupling matrix synthesis method and employ network analysis to derive simple and useful analytical methods to predict PTE responses and control the CCP. The capabilities presented in this work are crucial for achieving optimal PTE behavior in MRC systems where coil sizes and powering distances are highly restricted such as in miniaturized implantable medical devices where sizes are constrained by the available volume of the body location. The novel contributions of this work are:

1. New modifications to the coupled resonator BPF model which enable analyses involving resonators of finite Q_0 and complex port impedance accommodation
2. Critical coupling point behavior and control in BPF modeled MRC systems
3. Systematic analytical derivations to predict full system response.

2.2 Derivation of Bandpass Filter Model for MRC WPT Systems

Figure 2.1 shows the generic form, originally proposed in [49], of a two resonator coupled MRC system. Each LC resonator is driven externally through coupled oscillating magnetic fields generated by a source or load coil. Magnetic energy generated from the excited resonator is magnetically transferred to the second resonator. This inter-resonator magnetic coupling interaction represents the primary mechanism of WPT. Since the

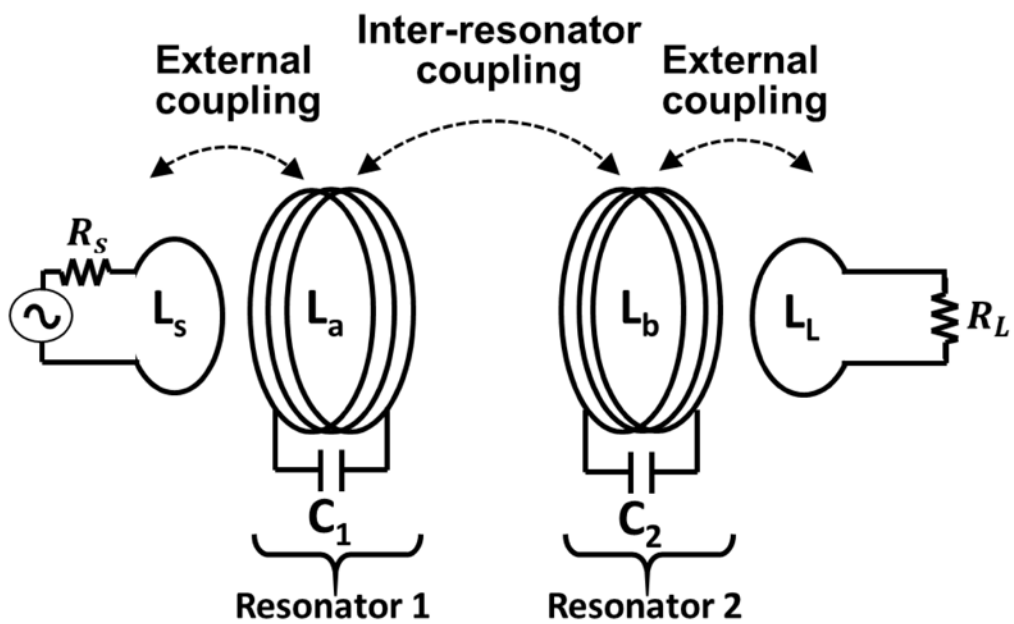

Figure 2.1 Traditional two resonator coupled MRC system. Each resonator is driven by externally coupled source and load coils.

external and inter-resonator couplings are magnetic, a circuit representation of this system can be formed through T-network representations of all mutual inductances. Therefore, the system in Figure 2.1 is transformed into the circuit described in Figure 2.2. In Figure 2.2, L_{Sa} represents the mutual inductance in external coupling between source and resonator 1 inductors. Likewise, L_{bL} represents the mutual inductance in external coupling between resonator 2 and load inductors. Inductance, L_{ab} represents the mutual inductance of the inter-resonator coupling. Importantly, the T-network representation of mutual inductances constitutes an impedance inverter (K-inverter), exhibiting a characteristic impedance, K. The resulting system in Figure 2.2 is analogous to a BPF made of series resonant elements and inter-resonating coupling structures. To generalize Figure 2.2 as a generic BPF, a cursory analysis of impedance inverters is necessary.

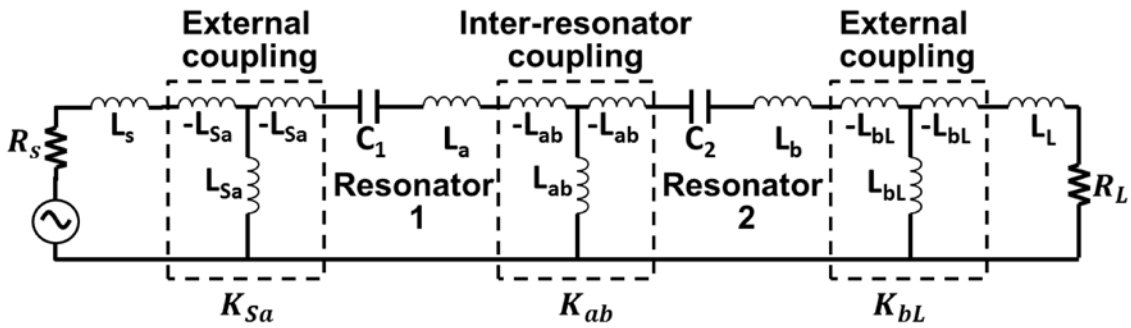

Figure 2.2 Equivalent circuit of original system. T-network circuits are substituted in place to represent mutual inductances. Critically, each T-network is equivalent to an impedance inverter (K-inverter).

2.2.1 Description of Impedance Inverter (K-inverter) Networks

In bandpass or bandstop filter design, impedance inverters are utilized to conveniently configure filter impedance matching (IM) characteristics or convert filter elements into desirable series or shunt configurations i.e. filters consisting of either only series or only shunt elements [62]. Additionally, impedance inverters accurately model the load inversion and 90° phase shift behavior of coupled resonating structures in RF filters; for example the inter-resonator couplings between adjacent cavities in high frequency cavity resonator BPFs [71, 72]. The operation of a K-inverter network is illustrated in Figure 2.3. K-inverters are 2-port networks exhibiting the unique property of

$$Z_1 = \frac{K^2}{Z_2} \tag{2.1}$$

where Z_1 is the impedance seen looking into the K-inverter network, Z_2 is the port termination impedance, and K is real and defined as the characteristic impedance of the inverter [62]. Based on the inversion property shown in (2.1), a capacitive/inductive

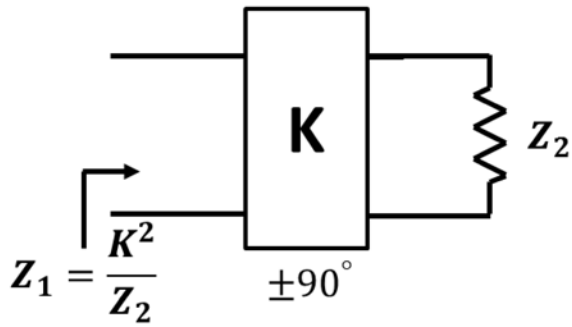

Figure 2.3 Function of an impedance inverter (K-inverter)

termination impedance would appear as an inductive/capacitive input impedance. Therefore, K-inverters also exhibit the property of a $\mp 90^\circ$ phase shift [62]. The *ABCD* matrix of a K-inverter is given as

$$\begin{bmatrix} A & B \\ C & D \end{bmatrix} = \begin{bmatrix} 0 & \pm jK \\ \mp \frac{j}{K} & 0 \end{bmatrix} \tag{2.2}$$

Equation (2.2) is easily verified through derivation of the *ABCD* matrix for a quarter-wave transmission line, a commonly utilized distributed element form of a K-inverter network. Figure 2.4(a) describes the two-port network representation of the T circuit of mutual inductances. Using standard *ABCD* network parameter derivation [61], the *ABCD* parameters for the T-network model of mutual inductances between series resonators is given by

$$\begin{bmatrix} A & B \\ C & D \end{bmatrix} = \begin{bmatrix} 0 & -j\omega L \\ \frac{1}{j\omega L} & 0 \end{bmatrix} \tag{2.3}$$

where $j = \sqrt{-1}$ and ω is the radian frequency. In comparing (2.3) with (2.2), it is clear that the T-network circuit of mutual inductances acts as a K-inverter network with

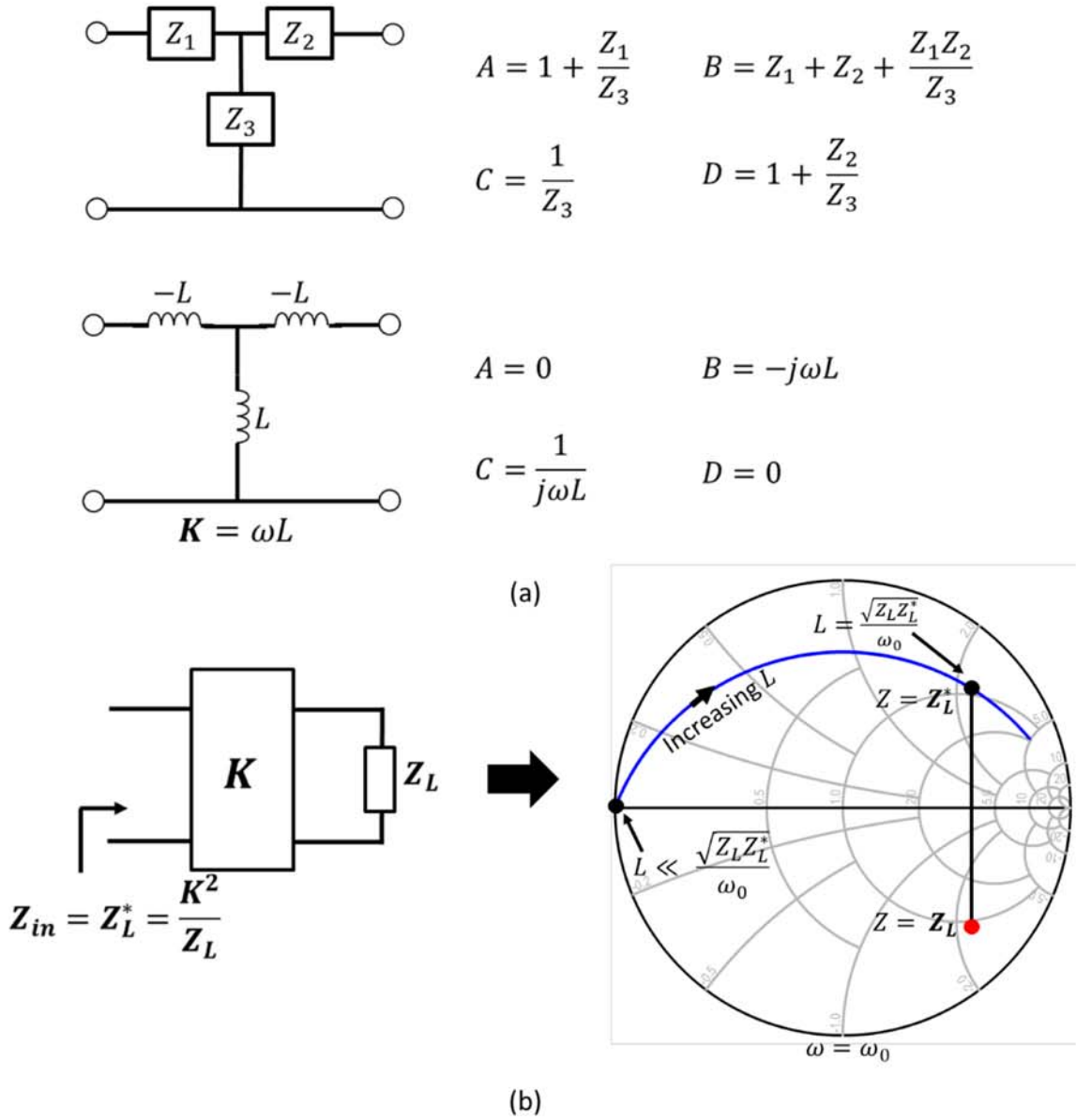

Figure 2.4 Example of an *ABCD* network parameter derivation for a K-inverter formed of a T-network of inductors. (a) Equivalent two-port network derivation. (b) Impedance tracking of input impedance (blue line in smith chart) as a function of inductance, L, at $\omega = \omega_0$. At $L = \frac{\sqrt{Z_L Z_L^*}}{\omega_0}$ the input impedance is inverted across the real axis and is equivalent to the complex conjugate of load impedance Z_L.

$K = \omega L$. It is important to note that the T-network circuit of mutual inductances represents one kind of many different lumped element K-inverter networks. Figure 2.4(b)

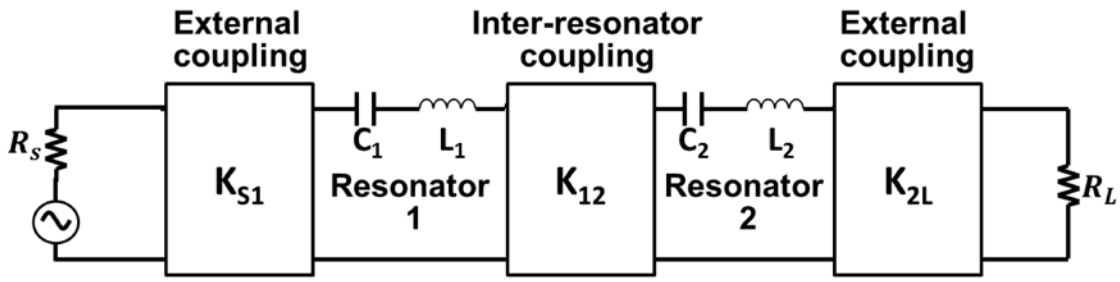

Figure 2.5 BPF network formed of K-inverters and series resonators

illustrates the impedance inversion process of the K-inverter network. When L exhibits a value of $L = \frac{\sqrt{Z_L Z_L^*}}{\omega_0}$, the impedance looking into the K-inverter is inverted across the real axis and is transformed into the complex conjugate of load impedance Z_L.

Since the T-network of mutual inductances are equivalent to a K-inverter network, Figure 2.2 is generalized into the system shown in Figure 2.5, a generic BPF model with series resonators. It is important to note that external coupling K-inverters, K_{S1} and K_{2L}, were generalized in the manner shown in Figure 2.6, to delete the source (L_s) and load (L_L) inductances, respectively, and to form inductors L_1 and L_2. In doing so, the BPF is generalized into a more practical form exhibiting three key features: 1.) the system does not require source or load coupling coils for system excitation and power transfer to a load, respectively, 2.) the system can be optimized and tuned through the external coupling K-inverter networks, and 3.) external coupling can be achieved using any type of lumped element network so long as the network is designed to act as a K-inverter. To the extent that the lumped element K-inverter network can be physically implemented is dependent on the resulting lumped element values which must remain positive and real in value.

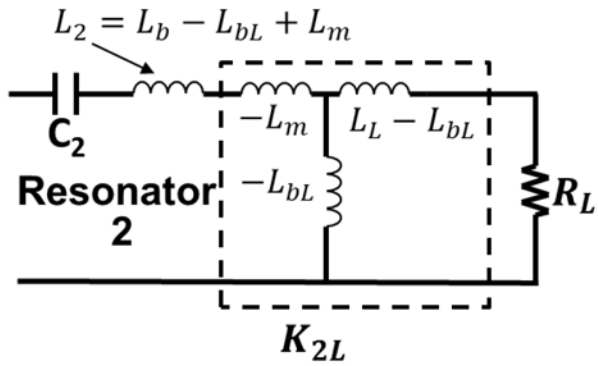

Figure 2.6 External coupling K-inverter generalization method for resonator 2 and load. K-inverter K_{2L} is formed from the absorption of load coil L_L and formation of L_2. The generalization procedure is applied to the source side.

Since K-inverter, K_{12}, is a virtualization of inter-resonator coupling representing the WPT mechanism, the creation of a lumped element inter-resonator coupling K-inverter network is not necessary. Therefore, it is not shown in the generic BPF model in Figure 2.5. The result is Figure 2.7, the generic BPF model for a coupled resonator WPT system. Note that inter-resonator coupling is now represented as magnetic coupling coefficient, k_{12}. This generic BPF model of coupled resonator WPT is representative of standard microwave BPF models. Similar to standard BPF systems, proper external coupling tuning is essential for achieving desired filter characteristics such as roll-off rates, bandwidths, ripple, and insertion loss [64]. However, in optimizing WPT performance, the only feature of importance is insertion loss and determining the external coupling characteristics necessary for its minimization. Additional modifications to Figure 2.7 are necessary for modeling practical design considerations including finite resonator unloaded quality factors, Q_0, and accommodation for complex source/load impedances.

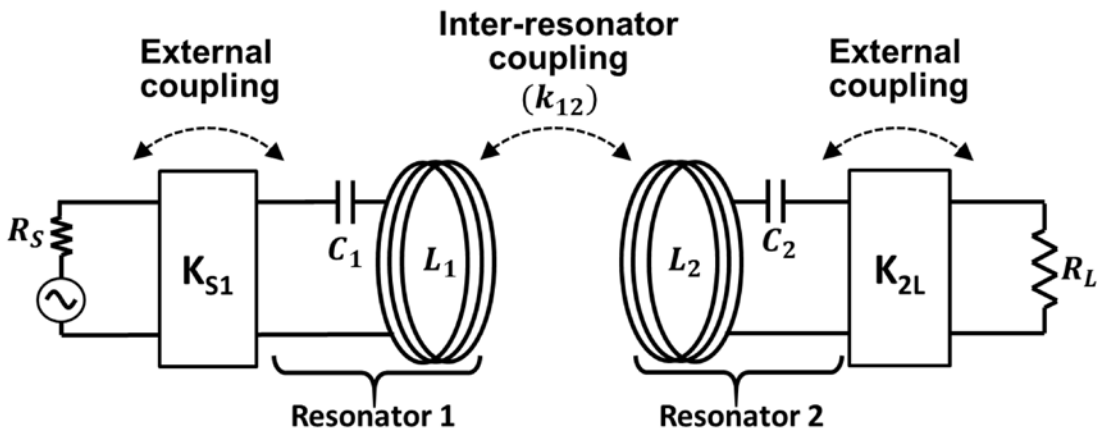

Figure 2.7 Generic BPF model for a 2 resonator MRC WPT system.

2.2.2 Model Modification to Account for Lossy Resonators

To account for resonator losses, a frequency dependent parasitic series resistance, R_{pi}, is placed in series with the resonator inductor, L_i, where i represents the ith resonator for an MRC system with n resonators ($i = 1,2, \dots, n$). Figure 2.8 shows the modified resonator system. By incorporating R_{pi}, the resonators are modeled to accurately exhibit a finite unloaded quality factor, Q_{0i}. As will be shown, Q_{0i} is a major parameter influencing maximum achievable power transfer efficiency, PTE response control, and optimal external coupling characteristic impedances. Its inclusion in the BPF model is essential for predicting and realizing optimal PTE responses.

For a series resonator, Q_{0i} has the relationship given by [61]

$$Q_{0i} = \frac{\omega L_i}{R_{Pi}} \tag{2.4}$$

which is a ratio of average stored magnetic energy to the energy dissipated in frequency dependent loss parameters. In MRC WPT systems, R_{pi} is primarily due to DC and AC

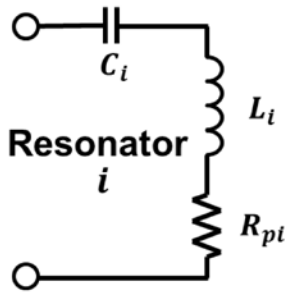

Figure 2.8 Series resonator modified to exhibit finite Q_{0i}.

dependent losses in the coil inductors. For example, in planar printed spiral coils, R_{pi} is a function of the DC resistance of the traces, frequency (ω) of operation, skin depth (δ), inter-winding capacitance, skin effect winding repulsion, and dielectric losses [73]. In wearable and implanted environments, additional frequency dependent losses are incurred from magnetic field interactions with biological tissue, which are electrically lossy and dispersive in nature [36]. Consequently, the resonator inductors and resonant frequency, ω_0, must be designed carefully so as to minimize DC and AC losses and maximize Q_{0i}.

2.2.3 Model Modification to Accommodate Detuning Effects of Complex Port Impedances

Figure 2.9 describes the complex load accommodation BPF design approach. The purpose of complex port (source and/or load) impedance accommodation is to remove the necessity for extra IM networks placed between the port (source or load) and BPF. Commonly implemented extraneous IM networks add additional loss, complexity in design, and require additional board space for implementation [65, 70, 74]. By

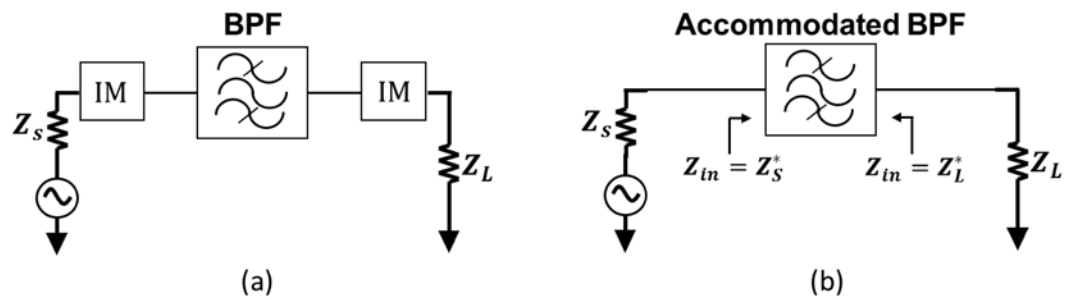

Figure 2.9 Complex load accommodation. (a) Unaccommodated BPF requiring extraneous IM networks for complex port impedance matching. (b) Accommodated BPF inherently matched to complex port impedances. Complex impedance accommodation removes the need for extra IM networks.

accommodating the BPF for a complex port impedance, the input/output impedances of the filter are configured to the complex conjugate of the port. As a result, the filter becomes inherently impedance matched. Thus, direct connection of the BPF to a complex load will not distort a pre-described PTE or frequency response of the BPF modeled MRC system. Additionally, as the IM network is inherent to the BPF system, its effects on WPT performance can be derived and controlled.

To achieve complex port impedance accommodation, the BPF structure requires 1.) a modified resonator model to account for extraneous reactance and 2.) the determination of optimal external coupling K-inverters characteristic impedances. The focus of this section is on the modified resonator model to account for extraneous reactance. K-inverter optimization will be described in Section 2.4. Recall in Section 2.2 that the characteristic impedance of a K-inverter is real. Thus, K-inverter networks serve as useful IM networks for matching purely real/imaginary source impedances to purely real/imaginary port impedances. K-inverter networks, however, are unable to match non-equivalent complex sources to complex port impedances which include both resistance

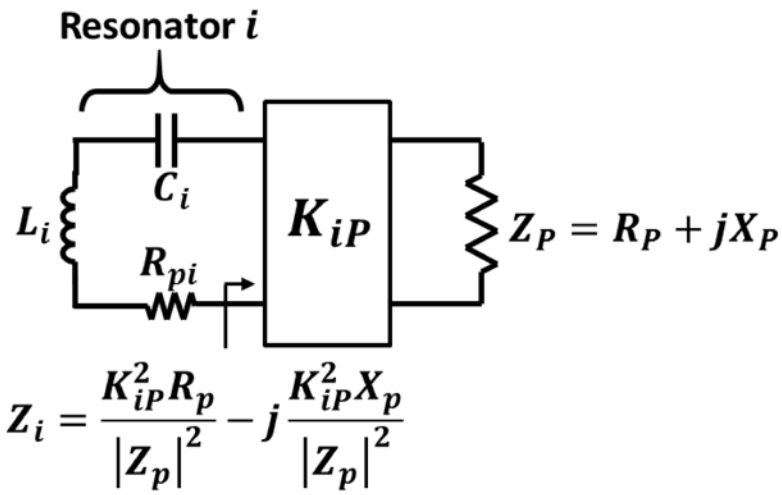

Figure 2.10 Impedance, Z_i, seen by resonator i, when connected to external coupling K-inverter, K_{iP}, terminated with port impedance, Z_P.

and reactance terms. As a result, the input impedance looking into a K-inverter network terminated onto a complex port impedance, Z_P, will typically remain complex. Figure 2.10 shows the impedance, Z_i, seen by resonator i, when connected to external coupling K-inverter, K_{Pi}. When Z_P is complex, Z_i is resultantly

$$Z_i = \frac{K_{iP}^2 R_p}{|Z_p|^2} - j\frac{K_{iP}^2 X_p}{|Z_p|^2} \tag{2.5}$$

where $|Z_p| = \sqrt{{R_p}^2 + {X_p}^2}$. The resonant frequency, ω_{0i}, of resonator i is given by

$$\omega_{0i} = \frac{1}{\sqrt{L_i C_i}} \tag{2.6}$$

As shown in (2.6), ω_{0i} is only a function of the complementary reactive elements of the resonator. Consequently, any reactance from Z_i loads the resonator with additional reactance and will detune it away from ω_{0i}. Without compensating for this additional

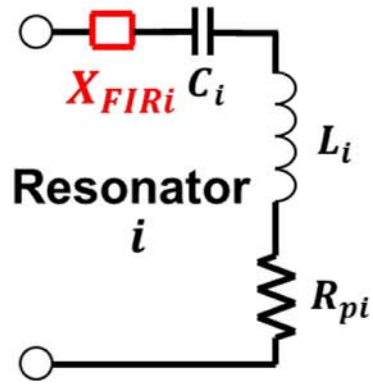

Figure 2.11 Modified resonator network incorporating a frequency invariant reactance element.

reactance, the resonators of the BPF would act in an asynchronous ($\omega_{0i} \neq \omega_0$) state resulting in drastically reduced PTEs.

To compensate for the added reactance due to a complex port impedance, a frequency invariant reactance (FIR) element, X_{FIRi}, is added in series to the resonator and defined exclusively to exhibit a value satisfying the condition defined as

$$X_{FIRi} = -Im(Z_i) = \frac{K_{iP}^2 X_p}{|Z_p|^2} \tag{2.7}$$

As shown in (2.7), the X_{FIRi} value that neutralizes a detuning reactance is calculated from the port impedance and external coupling characteristic impedance, K_{iP}. FIR elements are commonly employed in BPF structures to represent asymmetric or asynchronous characteristics [64]. Figure 2.11 shows the updated resonator i structure. In this work, I set K_{iP} as the optimizable design parameter. By implementing an X_{FIRi} element, which exhibits a value satisfying (2.7), the resonator will maintain operation at the designed resonant frequency even in the presence of detuning reactance.

2.2.4 Final Generalized BPF Model for MRC WPT System

Figure 2.12 shows the final generalized 2-resonator BPF modeled MRC WPT system. This model is strategically designed to account for resonators which exhibit finite Q_{0i} (incorporation of R_{pi}) and a FIR element to neutralize resonator detuning effects (incorporation of X_{FIRi}) due to complex port impedances. These modifications are especially crucial for optimizing WPT in wearable or implantable medical applications where resonator Q_{0i} and inter-resonator coupling are low (due to small coil sizes and field-tissue interactions) and load impedances, such as the input impedance of a rectifier system, are complex. In the following sections, I formulate the representative impedance matrix for Figure 2.12 from which the generalize coupling matrix is derived, utilize network analysis to predict system behavior, and derive an optimization procedure to maximize power transfer efficiency responses.

2.3 Synthesis and Derivation of the Generalized Coupling Matrix

The generalized coupling matrix is a useful and commonly employed tool in coupled resonator filter design. Its utility stems from its simple synthesis, which requires only knowledge of filter coupling coefficients, resonator parameters, and port impedances, from which useful and generalized formulas for analyzing and optimizing complex coupled resonator filter behavior are derived [64, 75]. In this work, I derive and modify the general coupling matrix, $[m]$, to incorporate the novel resonator modifications presented in the final generalized BPF modeled MRC WPT system shown in Figure 2.12.

The derivation of $[m]$, begins first with the synthesis of the equivalent source and load included impedance matrix $[Z]$ representation of Figure 2.12. Figure 2.13(a) shows

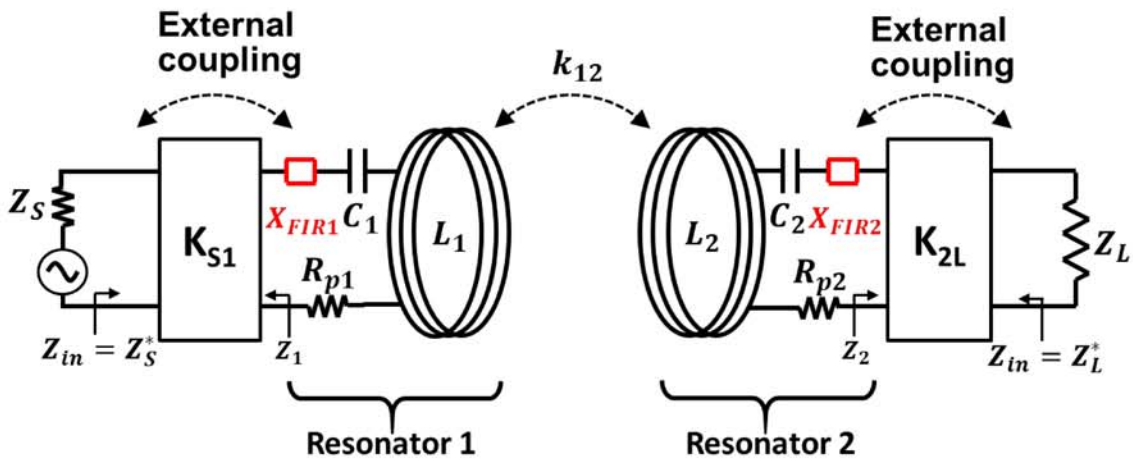

Figure 2.12 Final Generalized BPF model for MRC WPT

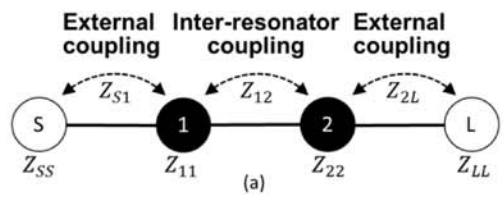

$$
\begin{array}{c}
 \\ S \\ 1 \\ 2 \\ L
\end{array}
\begin{array}{c}
\begin{array}{cccc} S & 1 & 2 & L \end{array} \\
\begin{bmatrix}
R_s + jX_s & jK_{S1} & 0 & 0 \\
jK_{S1} & R_{p1} + jX_{FIR1} + j\omega L_1 - {}^{j}/_{\omega C_1} & j\omega_0 L_{12} & 0 \\
0 & j\omega_0 L_{12} & R_{p2} + X_{FIR2} + j\omega L_2 - {}^{j}/_{\omega C_2} & jK_{2L} \\
0 & 0 & jK_{2L} & Z_{LL} = R_L + jX_L
\end{bmatrix}
\end{array}
$$

(b)

Figure 2.13 (a) Coupling map for 2 resonator BPF modeled MRC WPT system and (b) equivalent impedance matrix $[Z]$ representation

the coupling map representation of the final generalized BPF modeled system and Figure 2.13(b) shows the representative $[Z]$ matrix. The source and load included $[Z]$ matrix is a $n + 2$ sized matrix where n represents the total number of resonators in the system. In this application n is set to 2 (n = 2). However, n can be expanded to include greater than 2 resonators, see Figure 2.30. Matrix $[Z]$ is derived from the loop equation formulation of

$$
\begin{array}{cc}
 & \begin{array}{cccc} \times\left(\sqrt{R_S}\right)^{-1} & \times\left(\sqrt{\omega_0 L_1}\right)^{-1} & \times\left(\sqrt{\omega_0 L_2}\right)^{-1} & \times\left(\sqrt{R_L}\right)^{-1} \\ \downarrow & \downarrow & \downarrow & \downarrow \end{array} \\
\begin{array}{c} \times\left(\sqrt{R_S}\right)^{-1} \rightarrow \\ \times\left(\sqrt{\omega_0 L_1}\right)^{-1} \rightarrow \\ \times\left(\sqrt{\omega_0 L_2}\right)^{-1} \rightarrow \\ \times\left(\sqrt{R_L}\right)^{-1} \rightarrow \end{array} &
\begin{bmatrix} Z_{SS} & Z_{S1} & 0 & 0 \\ Z_{S1} & Z_{11} & Z_{S1} & Z_{S1} \\ 0 & Z_{S1} & Z_{22} & Z_{2L} \\ 0 & 0 & Z_{2L} & Z_{LL} \end{bmatrix}
\end{array}
$$

Figure 2.14 Impedance matrix normalization procedure using impedance ($1/\sqrt{R_P}$)and resonator ($1/\sqrt{\omega_0 L_i}$) scaling factors.

the source and load, external and inter-resonator couplings, and resonator impedances. An impedance scaling factor, $1/\sqrt{R_P}$, where P represents the port (P = S, L), and a resonator scaling factor, $1/\sqrt{\omega_0 L_i}$, are implemented in the manner described in Figure 2.14, to generalize matrix $[Z]$ such that the resultant matrix can be normalized in terms of couplings and port impedances only. The resultant matrix is the normalized impedance matrix, $[\tilde{Z}]$, provided in Figure 2.15. Using algebraic manipulation, $[\tilde{Z}]$ is separated into constitutive components into the form given by

$$[\tilde{Z}] = j[m] + j\Omega[R] + [P] \tag{2.8}$$

where Ω is the standard bandpass filter frequency transform variable given by

$$\Omega = \left(\frac{\omega}{\omega_0} - \frac{\omega_0}{\omega}\right) \tag{2.9}$$

In BPF design, Ω is the frequency transform variable utilized for transforming the lowpass filter prototype into a filter with a BPF response [62]. For the purposes of WPT optimization, this variable simply reflects the frequency dependency of the BPF modeled

$$[\tilde{Z}] = \begin{bmatrix} 1 + j\frac{X_s}{R_s} & j\frac{K_{S1}}{\omega_0 R_s L_1} & 0 & 0 \\ j\frac{K_{S1}}{\omega_0 R_s L_1} & \frac{1}{Q_{01}} + j\frac{X_{FIR1}}{\omega_0 L_1} + j\left[\frac{\omega}{\omega_0} - \frac{\omega_0}{\omega}\right] & j\frac{L_{12}}{\sqrt{L_2 L_2}} & 0 \\ 0 & j\frac{L_{12}}{\sqrt{L_2 L_2}} & \frac{1}{Q_{01}} + j\frac{X_{FIR2}}{\omega_0 L_2} + j\left[\frac{\omega}{\omega_0} - \frac{\omega_0}{\omega}\right] & j\frac{K_{2L}}{\omega_0 R_L L_2} \\ 0 & 0 & j\frac{K_{2L}}{\omega_0 R_L L_2} & 1 + j\frac{X_L}{R_L} \end{bmatrix}$$

Figure 2.15 Normalized impedance matrix for 2 resonator BPF modeled MRC WPT System.

MRC WPT frequency response. Matrices $[m]$, $[R]$, and $[P]$, are the source and load impedance included coupling matrix, identity matrix denoting the existence of a resonator network, and normalized port impedance matrix, respectively. They are expressed by

$$[m] = \begin{bmatrix} M_{SS} & M_{S1} & 0 & 0 \\ M_{S1} & M_{11} & M_{12} & 0 \\ 0 & M_{12} & M_{22} & M_{2L} \\ 0 & 0 & M_{2L} & M_{LL} \end{bmatrix} \tag{2.10}$$

and

$$[R] = \begin{bmatrix} 0 & 0 & 0 & 0 \\ 0 & 1 & 0 & 0 \\ 0 & 0 & 1 & 0 \\ 0 & 0 & 0 & 0 \end{bmatrix}, [P] = \begin{bmatrix} 1 & 0 & 0 & 0 \\ 0 & 0 & 0 & 0 \\ 0 & 0 & 0 & 0 \\ 0 & 0 & 0 & 1 \end{bmatrix} \tag{2.11), (2.12}$$

In (2.10), M_{SS} and M_{LL}, generalized as M_{PP}, represents the normalized port impedances expressed as

$$M_{PP} = \frac{X_P}{R_P} \tag{2.13}$$

where X_P and R_P are the port reactance and resistance, respectively. Coefficient M_{12}, represents the inter-resonator coupling coefficient given by

$$M_{12} = k_{12} = \frac{L_{12}}{\sqrt{L_1 L_2}}, 0 \leq k_{12} \leq 1 \tag{2.14}$$

This inter-resonator coupling coefficient, k_{12}, represents the magnetic coupling coefficient between magnetic field generating sources, such as coil inductors, and ranges in value between 0 and 1. The maximum achievable value of k_{12} between coil inductors in MRC systems is dependent on the relative physical dimensions, separation gap, and angular misalignment between coils. In MRC WPT systems, the maximum value k_{12} is typically much less than 1.

Coefficients M_{S1} and M_{2L}, generalized as M_{iP}, represents the normalized external coupling characteristic impedances and is given by

$$M_{iP} = \frac{K_{iP}}{\sqrt{\omega_0 R_P L_i}} \tag{2.15}$$

The main diagonal entries of self-coupling coefficients, M_{11} and M_{22}, generalized as M_{ii}, represents the normalized impedance of the resonator. Since the resonators are modeled to exhibit finite Q_{0i} and include an FIR element for maintaining system synchronicity in the presence of complex port impedances, M_{ii} is non-zero and expressed as

$$M_{ii} = \frac{-j}{Q_{0i}} + \frac{X_{FIRi}}{\omega_0 L_i} \tag{2.16}$$

Using the reactance neutralization condition described by equation (2.7) and the external coupling coefficient relation described by equation (2.15), (2.16) is re-expressed as

$$M_{ii} = \frac{-j}{Q_{0i}} + \frac{M_{iP}^2 R_P X_P}{|Z_P|^2} \tag{2.17}$$

Coefficient M_{ii} is expressed in this manner to ensure that the derivation and calculation of optimal external coupling characteristic impedances, K_{iP}, are independent of FIR element, X_{FIRi}. Among the corresponding parameters defining each entry in $[m]$, K_{iP} is defined as the optimizable design parameter for minimizing insertion loss (maximizing PTE). The derivation and calculation for determining optimal values of K_{iP} is determined from analysis of the system transfer response.

2.4 Determination of System Transfer Response and Derivation of Optimal K_{iP}

The filter response, from source to load, for the generalized BPF modeled MRC WPT system is determined from matrix $[\tilde{Z}]$ in terms of scattering parameters by [62]

$$S_{21} = 2[\tilde{Z}]^{-1}_{n+2,1} \tag{2.18}$$

$$S_{11} = 1 - 2[\tilde{Z}]^{-1}_{1,1} \tag{2.19}$$

$$S_{22} = 1 - 2[\tilde{Z}]^{-1}_{n+2,n+2} \tag{2.20}$$

where S_{21}, S_{11}, and S_{22} are the transfer response, return loss at port 1, and return loss at port 2, respectively. The transfer response, S_{21}, represents the PTE delivered to the load by

$$PTE = |S_{21}|^2 \times 100 \tag{2.21}$$

Using (2.18), the S_{21} response at the designed resonant frequency i.e. $\omega = \omega_0$ ($\Omega = 0$) is:

$$S_{21}|_{\omega=\omega_0} = \frac{2jM_{12}M_{2L}M_{S1}}{-M_{12}^2(-j+M_{LL})(-j+M_{SS}) + (M_{2L}^2 - M_{22}(-j+M_{LL}))(M_{S1}^2 - M_{11}(-j+M_{SS}))} \tag{2.22}$$

A cursory analysis on the form of (2.22) provides little intuition on system behavior as a function of the external coupling coefficient optimization parameters. However, the magnitude of $S_{21}|_{\omega=\omega_0}$ plotted as a function of external coupling coefficients M_{S1} and M_{2L}, and by virtue of (2.15), external coupling characteristic impedances, K_{S1} and K_{2L}, for a given set of initial design parameters ($f_0, k_{12}, L_i, C_i, Q_{0i}, Z_S, Z_L$) reveals optimal values of K_{S1} and K_{2L} at which the magnitude of $S_{21}|_{\omega=\omega_0}$ will be a global maximum. It is important to note that in practical MRC system design, parameters f_0 and k_{12} are defined by the user, whereas L_n and Q_{0i} are fixed based on the coil design and coil environment, and Z_S and Z_L are fixed by design. Design parameter C_n is simply calculated using (2.6) based on the user defined resonant frequency and associated resonator coil inductance.

Figure 2.16 shows predicted $|S_{21}|^2_{\omega=\omega_0}$ as a function of K_{S1} and K_{2L} for an example set of design parameters summarized in the same Figure. Note that the brackets denote magnitude. As shown in Figure 2.16, a global maximum PTE exists at $K_{S1} = K_{S1opt}$ and $K_{2L} = K_{2Lopt}$. Thus, optimal PTE for a given set of system design parameters is achieved only at unique external coupling characteristic impedances termed as K_{S1opt} and K_{2Lopt}.

Analytically, K_{S1opt} and K_{2Lopt} are determined by taking the partial derivative of $S_{21}|_{\omega=\omega_0}$ with respect to (w.r.t.) K_{S1} and K_{2L} and setting both functions to zero ($\frac{\partial S_{21}|_{\omega=\omega_0}}{\partial K_{S1}} = 0$ and $\frac{\partial S_{21}|_{\omega=\omega_0}}{\partial K_{2L}} = 0$) indicating a global maximum. Solving the set of simultaneous equations and taking only real and positive solutions, K_{S1opt} and K_{2Lopt} are derived as

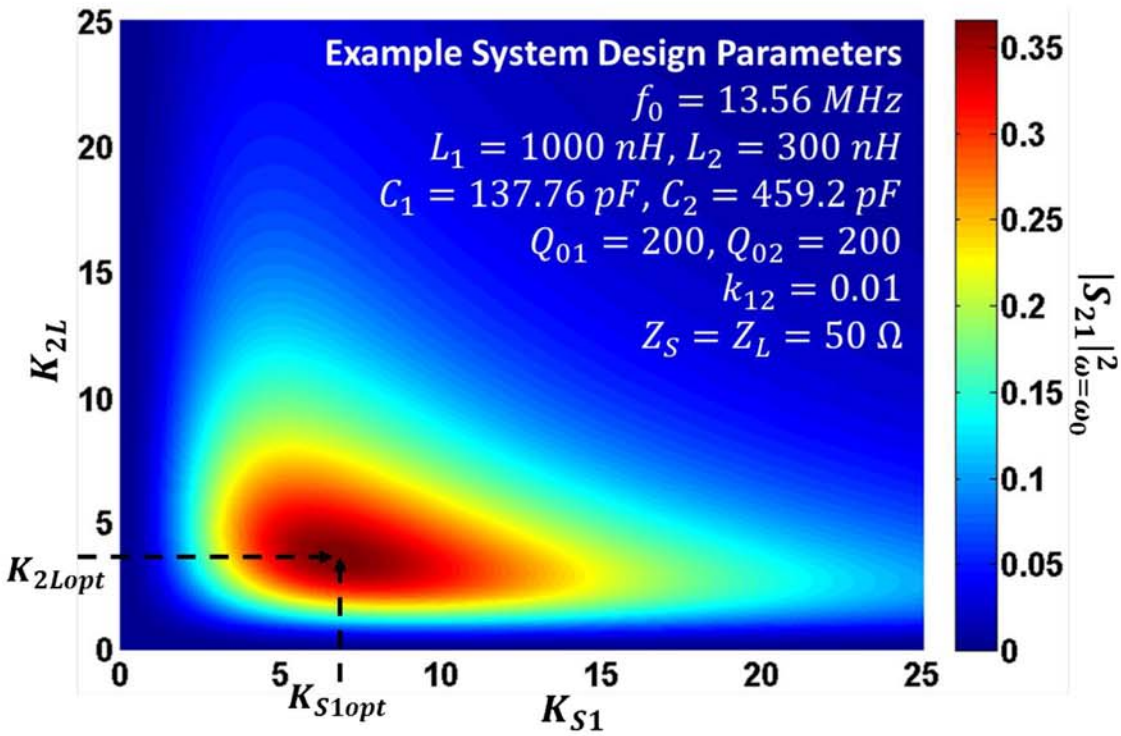

Figure 2.16 Map of $|S_{21}|^2_{\omega=\omega_0}$ (PTE at $\omega = \omega_0$) as a function of external coupling characteristic impedances K_{S1} and K_{2L}. Note the locations of maximum power transfer at K_{S1opt} and K_{2Lopt}. The example system design parameters are given.

$$K_{S1opt} = \left(1 + k_{12opt}^2 Q_{01} Q_{02}\right)^{1/4} |Z_S| \sqrt{\frac{R_{p1}}{R_S}} \tag{2.23}$$

$$K_{2Lopt} = \left(1 + k_{12opt}^2 Q_{01} Q_{02}\right)^{1/4} |Z_L| \sqrt{\frac{R_{p2}}{R_L}} \tag{2.24}$$

where k_{12opt} is the k_{12} location for which optimal K_{S1opt} and K_{2Lopt} are determined. In practical MRC system design, especially in wearable and implantable medical device applications, source impedance, load impedance, and resonator Q_{0i} are typically fixed. In contrast, the inter-resonator coupling location at which optimal PTE is desired to occur,

k_{12opt}, can be changed based on the system designers discretion. The specific value of k_{12opt}, however, will drastically change the optimized PTE response over an expected coil separation distance or angular misalignment. Thus, the value of k_{12opt} must be carefully chosen to maximize an optimal PTE response for a given application.

2.5 Investigation of Optimal PTE Responses and PTE Control Through k_{12opt}

The optimal PTE response of the 2 resonator BPF modeled MRC WPT system is determined analytically by substituting (2.23) and (2.24) into the filter transfer function equation described by (2.18). Figure 2.17 shows the predicted $|S_{21}|^2_{opt}$ as a function of frequency and inter-resonator coupling, k_{12}, for a given set of system design parameters. Note that subscript opt is used to indicate the substitution of K_{S1opt} and K_{2Lopt} into the S_{21} function. As shown, depending on the inter-resonator coupling value, three distinct PTE regions exists: under-coupling, critical coupling, and over-coupling. This predicted optimal PTE response of the 2 resonator BPF modeled MRC WPT system is unique to resonantly coupled systems seen in both resonantly coupled filters and traditional MRC WPT systems [50, 61, 62, 76]. Indeed, the 2 resonator BPF modeled MRC WPT system is a resonantly coupled system. The three regions are distinguished by

1.) Under-coupling: $k_{12} < k_{12crit}$
2.) Critical-coupling: $k_{12} = k_{12crit}$
3.) Over-coupling: $k_{12} > k_{12crit}$

The critical coupling point (CCP) is defined as the k_{12} point at which peak PTE is achieved at the designed resonant frequency ($f/f_0 = 1$). The region of $k_{12} > k_{12crit}$ is

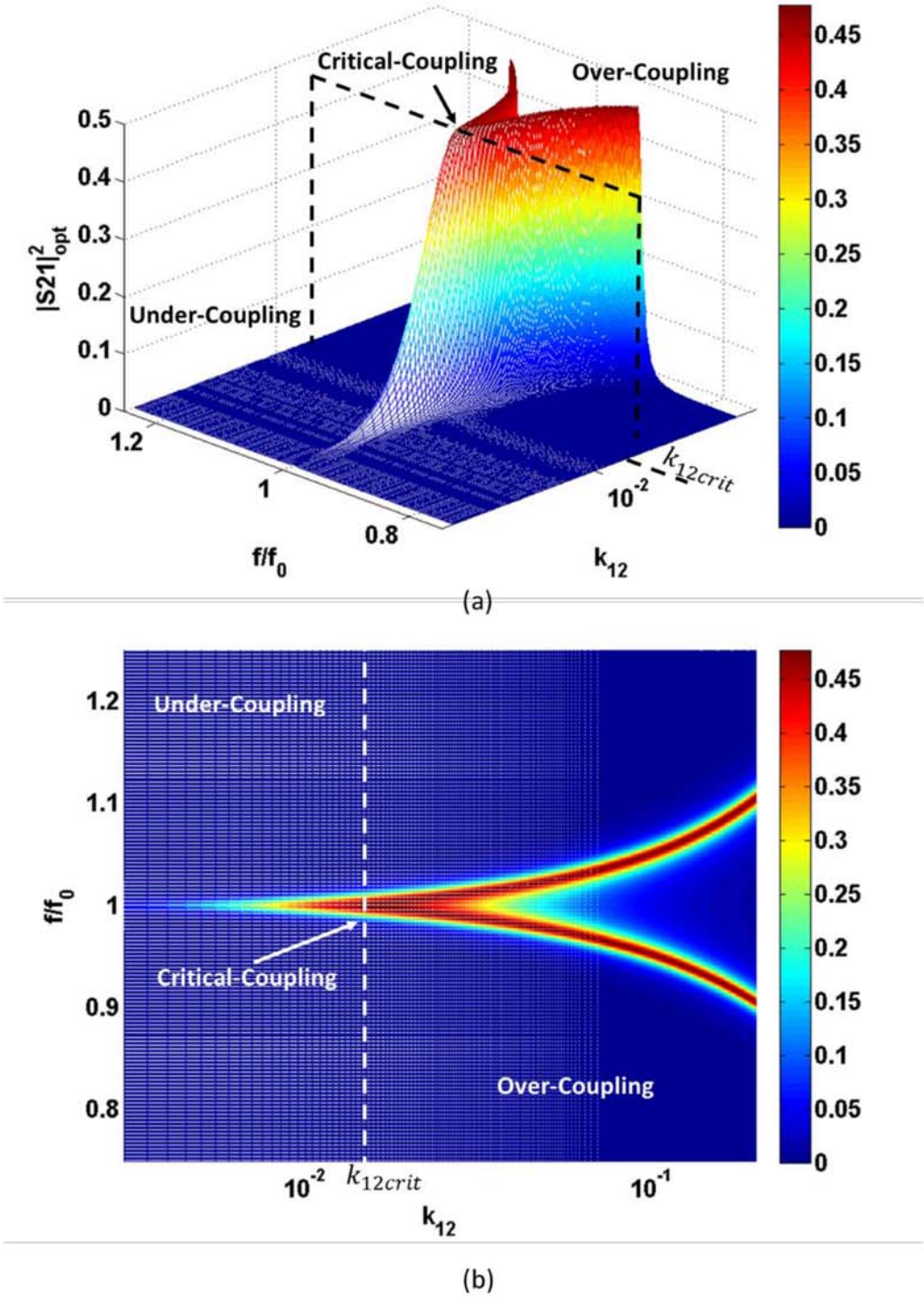

Figure 2.17 Plot of theoretically predicted $|S_{21}|^2_{opt}$ as a function k_{12} and frequency ratio, f/f_0, with clearly defined under, critical, and over-coupling PTE regions. Plot was created using the same example system design parameters used to generate Figure 2.16 (a) Full-view and (b) Top down view.

known as the over-coupled region and is distinguished by the frequency splitting phenomenon. In this region, peak PTE can be maintained through frequency following even if k_{12} varies [50]. In this region stronger coupling results in wider frequency separation and decreased PTE at the resonant frequency. Although not shown in Figure 2.17, but commonly predicted in coupled resonator BPF systems [62], each resonant peak is characterized by an out of phase response. The region of $k_{12} < k_{12crit}$ is known as the under-coupled region and is distinguished by a rapid decline in PTE at the designed resonant frequency as inter-resonator coupling decreases away from the CCP.

The location of CCP can be varied and must be carefully chosen so as to control the ideal PTE response. In this work, the CCP is uniquely controlled by varying the value of k_{12opt} and creating K-inverter networks which exhibit the resulting values of K_{S1opt} and K_{2Lopt} , calculated from (2.23) and (2.24), respectively, in the circuit. This directly contrasts with traditional MRC WPT systems which control the CCP by manipulating external coupling coefficient values between drive/source and resonator coils [53] and switching resonator coils [52]. Figure 2.18 illustrates the effect varying k_{12opt}, as predicted by the theoretical analysis derived here, will have on the resonant frequency PTE response as a function of inter-resonator coupling for an example set of system design parameters. Three distinct results from varying k_{12opt} on the optimal PTE response can be deduced from Figure 2.18. These are: 1.) the location of the CCP will follow the chosen value of k_{12opt} but a discrepancy will exist between k_{12opt} and k_{12crit} i.e. $k_{12opt} \neq k_{12crit}$, 2.) Increasing the value of k_{12opt} has the effect of

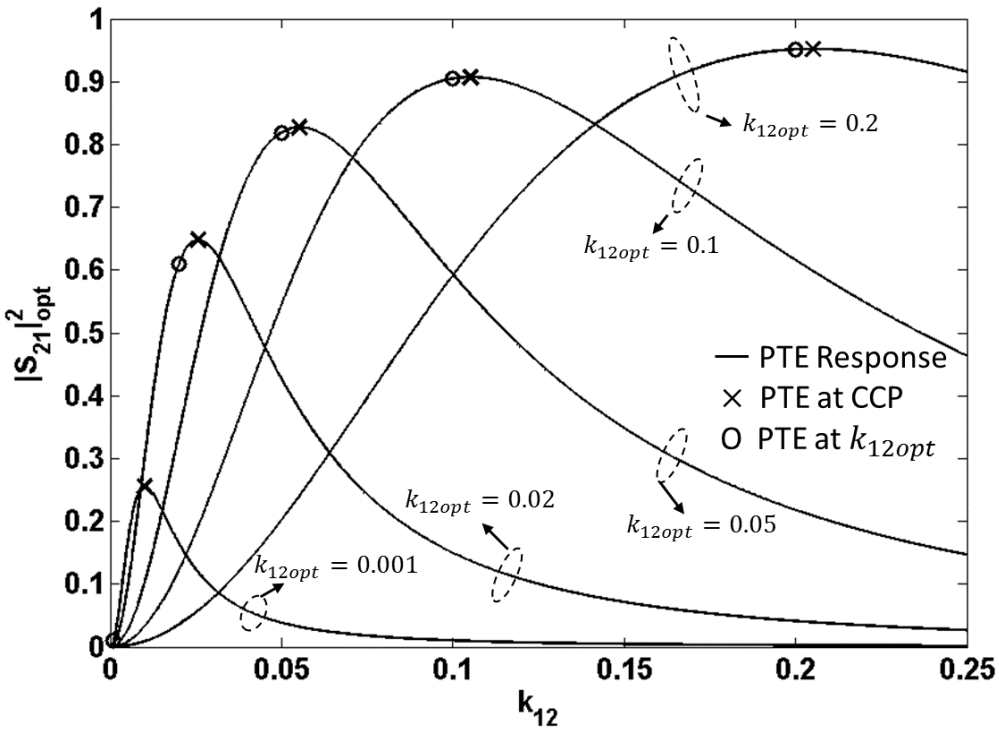

Figure 2.18 Plot of theoretically predicted $|S_{21}|^2_{opt}$ as a function k_{12} for varying values of k_{12opt}. The PTE at the CCP and k_{12opt} for each curve is given. Except for design parameter k_{12opt}, the example design parameters for generating each curve is given in Figure 2.16.

increasing the PTE at the CCP, and 3.) decreasing the value of k_{12opt} has the effect of maximizing range (increasing PTE at lower k_{12} values), but at the expense of maximum achievable PTE at the CCP. Note, the predicted responses in Figure 2.18 were generated by substituting (2.23) and (2.24) into the expanded function of (2.18), setting $\omega = \omega_0$ ($\Omega = 0$), and varying k_{12opt} by the five values shown. Indeed, the chosen value of k_{12opt} is critical for maximizing the PTE response in a given application and expected inter-resonator coupling range.

Analytically, the relationship between k_{12opt} and k_{12crit} is derived by substituting (2.23) and (2.24) into the expanded function of (2.18) and setting the derivative of $|S_{21}|^2_{opt}$ at $\omega = \omega_0$ w.r.t k_{12}, to zero ($\frac{\partial S_{21}|_{opt,\omega=\omega_0}}{\partial k_{12}} = 0$), and solving for k_{12}, now re-termed k_{12crit}. The resulting relationship is:

$$k_{12crit} = \frac{1}{\sqrt{Q_{01}Q_{02}}} + \sqrt{\frac{1}{Q_{01}Q_{02}} + k^2_{12opt}} \tag{2.25}$$

This result indicates that CCP control is a function of both the k_{12opt} value and resonator quality factors. Importantly, CCP control is not a function of source or load impedances. This is a particularly important result as it indicates that with proper source and load impedance accommodation, source and load impedance will not affect optimally designed responses of the BPF modeled MRC WPT system. The corresponding CCP value of $|S_{21}|_{crit}$ is determined by substituting (2.25), along with (2.23) and (2.24), into (2.18). The resulting function is:

$$|S_{21}|_{crit} = 1 - \frac{1}{k_{12crit}\sqrt{Q_{01}Q_{02}}} = 1 - \frac{1}{1 + \sqrt{1 + k^2_{12opt}Q_{01}Q_{02}}} \tag{2.26}$$

From (2.25), as $k_{12opt} \to 0$, k_{12crit} becomes a function of only resonator Q_{0i}. This minimum value of k_{12crit}, re-termed $k_{12crit,min}$, represents the minimum critical coupling point a given system can achieve and represents the condition at which range is fully maximized. Specifically, $k_{12crit,min}$ is calculated by

$$k_{12crit,min} = \frac{2}{\sqrt{Q_{01}Q_{02}}}, when\ k_{12opt} = 0 \tag{2.27}$$

Additionally, from (2.26), when $k_{12opt} = 0$, the value of $|S_{21}|_{crit}$ at $k_{12crit,min}$ will always exhibit a value of 0.5 (PTE = 25%), independent of the resonator quality factor. Indeed, the relationship described by (2.25) – (2.27) indicates that k_{12opt} and resonator Q_{0i} influence CCP control. For a given value of k_{12opt}, maximizing Q_{0i} has the effect of both maximizing $|S_{21}|_{crit}$ and increasing CCP control i.e. bringing $k_{12opt} \rightarrow k_{12crit}$. PTE response and CCP control are especially important considerations in MRC applications where the maximum possible value of k_{12} is << 1. Based on the results presented here, both Q_{0i} and k_{12opt} are vitally important for achieving a desired and maximized performance. Indeed, as Q_{0i} is driven low due to environmental conditions (lossy materials, biological tissue, etc.), sub-optimal coil design, and/or improper choice on frequency of operation, the ability to achieve critical coupling may become impossible, even if k_{12opt} were set to a value below the maximum inter-resonator coupling value, $k_{12,max}$, between resonators. In other words, if resonator Q_{0i} is too low, then $k_{12crit,min} > k_{12,max}$. As discovered from this analysis, designing for high resonator unloaded Q-factors is important for both maximizing PTE and for maximizing CCP control. Analytically, CCP control is defined by the figure of merit (FOM) developed here as

$$FOM = \frac{k_{12opt}}{k_{12crit}} = \frac{k_{12tgt}\sqrt{Q_{01}Q_{02}}}{1 + \sqrt{1 + k_{12tgt}^2 Q_{01}Q_{02}}} \tag{2.28}$$

which describes the ratio of k_{12opt} to k_{12crit}. A FOM = 1 indicates that the desired CCP, set by k_{12opt} will be k_{12crit}.

Up until this point, all theoretically predicated responses were determined by using an example set of system design parameters and evaluating the effect of integrating K_{S1opt} and K_{2Lopt}, from (2.23) and (2.24), respectively, into the system transfer function calculated using (2.18). However, in practical implementation, K_{S1opt} and K_{2Lopt} must be configured in a network that can be integrated into a real circuit . As described earlier, one form of K-inverter network is the quarter-wave transmission line, which represents a distributed element. However, for MRC WPT applications, distributed elements would be too large as the designed operating frequencies of MRC systems are typically in the low MHZ (< 30 MHz) frequency ranges. Thus, lumped element K-inverter networks present the best path for practical implementation and integration with medical electronics.

2.6 Lumped element K-Inverter Design to Exhibit K_{S1opt}, K_{2Lopt}, and X_{FIRi}

As shown previously in Figure 2.5, an example lumped element K-inverter network could be formed by a T-network of lumped element inductors. However, discrete inductors, such as surface mount device (SMD) chip inductors are lossy in MHz frequency ranges. Additionally, the negative inductance could only be achieved in a real system by absorption into the inductance of the coil resonator. This requires reshaping or redesigning the coil inductor, which is entirely impractical for implanted bioelectronics applications. To circumvent these issues, a capacitive lumped element K-inverter network would be much more practical. Figure 2.19 shows the L-network formed of capacitors $-C_{si}$ and C_{pi}, to that can be configured to exhibit an optimal K-inverter characteristic impedance. Series capacitor, $-C_{si}$, is made negative such that the lumped element

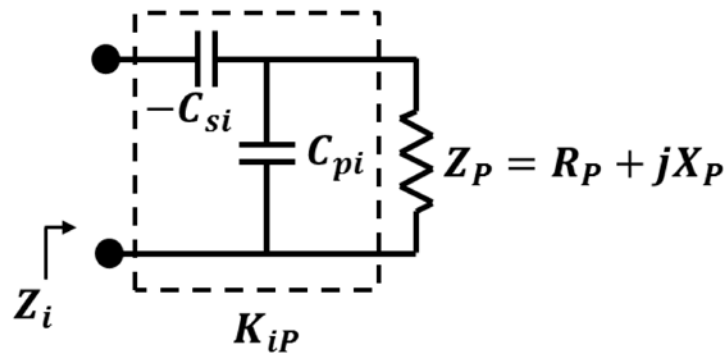

Figure 2.19 Capacitive K-inverter network connected to port impedance Z_P.

network exhibits the properties of K-inverters, previously described in Section 2.2 [57, 63].

The input impedance, Z_i, of the network shown in Figure 2.19 is given by

$$Z_i = \left(\frac{1}{Z_P} + j\omega_0 C_{pi}\right)^{-1} + \frac{1}{j\omega_0(-C_{si})} = \frac{K_{iP}^2}{R_P + jX_P} \tag{2.29}$$

The right hand side of (2.29) is the K-inverter inversion relationship for the external coupling K-inverter networks. The $-C_{si}$ and C_{pi} value for exhibiting a desired external coupling characteristic impedance, K_{iP}, is derived by setting $Re(Z_i) = Re[K_{iP}^2/(R_P + jX_P)]$ and $Im(Z_i) = Im[K_{iP}^2/(R_P + jX_P)]$. This provides a set of simultaneous equations which are used to solve $-C_{si}$ and C_{pi}. Recall that the characteristic impedance of K-inverters are real valued. The resulting expressions for $-C_{si}$ and C_{pi} are solved as

$$-C_{si} = \frac{|Z_P|^2}{\omega_0 K_{iP}\left(\sqrt{|Z_P|^4 - K_{iP}^2 {R_P}^2} - K_{iP}X_P\right)} \tag{2.30}$$

$$C_{pn} = \frac{K_{iP}X_P + \sqrt{|Z_P|^4 - K_{iP}^2 {R_P}^2}}{\omega_0 K_{iP}|Z_P|^2} \tag{2.31}$$

To calculate the optimal capacitance values for CCP and PTE response control, K_{ipopt}, is substituted into (2.30) and (2.31). Based on (2.30) and (2.31), it is clear that the physical limit on external coupling K-inverter characteristic impedance this lumped element K-inverter network can exhibit is enforced by

$$\frac{|Z_P|^2}{R_P} \geq K_{iP} \tag{2.32}$$

Condition (2.32) must be satisfied to ensure that the calculated capacitances values stay real in value.

Although the resistance and reactance of port impedance is accounted for in the calculations of $-C_{si}$ and C_{pi}, complex port accommodation is not fully achieved. Recall in Section 2.2.2 that a complex port impedance will result in resonator detuning due to a resonator still "seeing" extraneous reactance. A series FIR element, X_{FIRi}, with a value calculated using (2.7), however will neutralize the loading reactance due to complex port impedance. To physically implement X_{FIRi} in the resonators, X_{FIRi} is treated as a capacitive reactance expressed by

$$C_{FIRi} = -\frac{1}{\omega_0 X_{FIRi}} = -\frac{|Z_P|^2}{\omega_0 K_{iP}^2 X_P} \tag{2.33}$$

FIR element, X_{FIRi}, could have been treated as a series inductor. However, similar to the reason for not using lumped element K-inverter made of inductors, absorption of a series inductor into the resonator coil inductor is impractical. Capacitor C_{FIRi} represents the

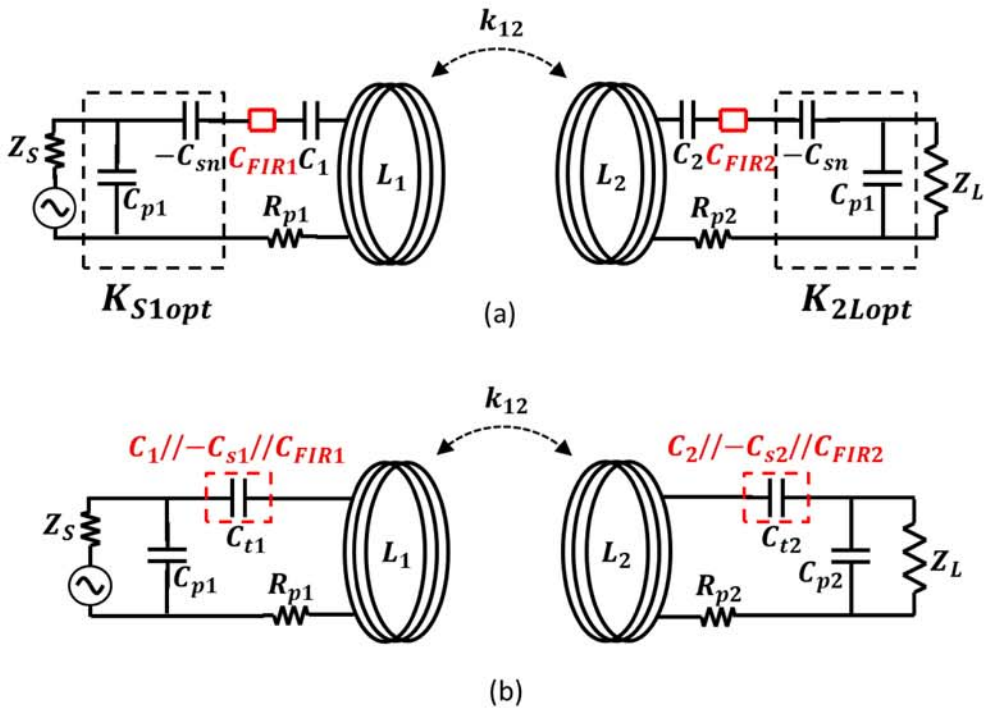

Figure 2.20 Simple and practically realizable 2 resonator BPF modeled MRC WPT system. (a) all individual lumped element components and (b) all lumped components with total series capacitor, C_{ti}, representing the total absorbed capacitance.

additional resonator series capacitor needed to achieve full complex load accommodation. Note, since C_{FIRi} is a series capacitor, its absorption into resonator capacitor, C_i, forces (2.33) to be in reciprocal form, thereby allowing for port reactance, X_P, to equal zero.

Figure 2.20 shows the simple and practically realizable 2 resonator BPF modeled MRC WPT system. FIR element series capacitance, C_{FIRi}, and K-inverter series capacitance, $-C_{si}$, are absorbed by series resonator capacitor, C_i, forming total series capacitor, C_{ti}, calculated by

$$C_{ti} = \left(\frac{1}{C_i} - \frac{1}{(-C_{si})} + \frac{1}{C_{FIRi}}\right)^{-1} \tag{2.34}$$

Indeed, PTE response control, CCP control, and complex port impedance accommodation is achieved by simply implementing optimally calculated capacitors. The use of capacitors for tuning is particularly advantageous due to small form factor and low loss characteristics of SMD components.

2.7 Experimental Results and Theory Validation

Measurement and circuit simulations are used to validate the theory, PTE response control, CCP control, and complex impedance accommodation. All S-parameters measurements come from standard 50 Ω one-port and two-port vector network analyzer (VNA) (Agilent E5072A) measurements. All circuit simulations were based on the system shown in Figure 2.20(b) and were performed with Agilent Advanced Design System (ADS©).

2.7.1 Experimental Design

Figure 2.21 shows the experimental set-up used for measurement. A linear guide rail system was implemented to enable precise resonator parameter and PTE measurements at incremental coil separations distances, d. Two WPT optimization scenarios were designed:

1.) Scenario 1 (Tx to Rx1): high transmit and receive resonator Q_0 with a large maximum achievable $k_{12} = 0.134$
2.) Scenario 2 (Tx to Rx2): high transmit and low receive resonator Q_0 with a low maximum achievable $k_{12} = 0.008$.

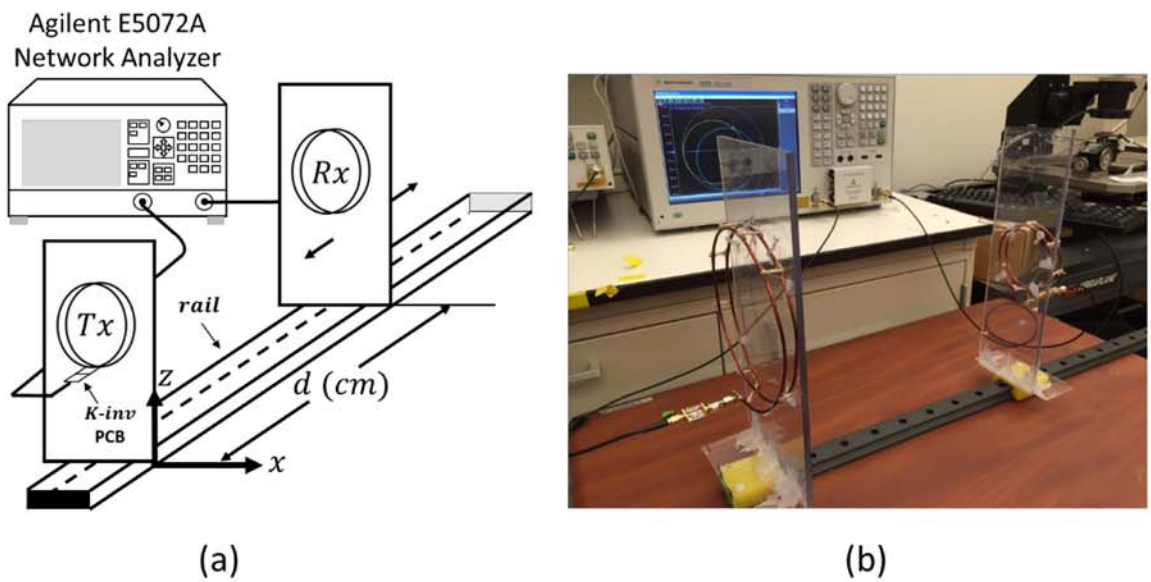

Figure 2.21 (a) Experimental Set-up between transmit (Tx) and receive (Rx) coils with linear guide rail and (b) photograph of experimental set-up

Scenario 1 was designed to reflect a WPT optimization case where critical coupling between resonators is achievable. This reflects WPT conditions where tight coupling and high Q resonators can be implemented. The results from optimization in Scenario 1 provide validation to the theory and optimization methodology. Scenario 2 was designed to reflect a WPT optimization case where critical coupling is not achievable (minimum possible value of k_{12crit} < maximum value of k_{12}). This reflects WPT conditions where inter-resonator coupling is low due either to large transmit (Tx) to receive (Rx) coil size mismatches, large separation distances, and/or large angular misalignments. The results from optimization in Scenario 2 provides the design procedure for maximizing PTE responses in systems such as miniature implanted bioelectronics.

Scenario 1 consists of transmit coil, Tx, fabricated using 10 American wire gauge (AWG) insulated copper magnet wire with a coil diameter of 16 cm, 2 turns, and an inter-

Table 2.1 Coil Design for coil Tx, Rx1, and Rx2

	Tx	**Rx1**	**Rx2**
Scenario 1	Wire Diameter: 10 AWG Coil Diameter: 7.5 cm Turns: 2 Inter-winding Spacing: 1 cm	Wire Diameter: 10 AWG Coil Diameter: 7.5 cm Turns: 2 Inter-winding Spacing: 1 cm	N/A
Scenario 2	Wire Diameter: 10 AWG Coil Diameter: 7.5 cm Turns: 2 Inter-winding Spacing: 1 cm	N/A	Wire Diameter: 24 AWG Coil Diameter: 1.5 cm Turns: 3 Tightly Wound

N/A = not applicable

winding spacing of 1 cm. Coil Tx was coupled to receive coil 1 (Rx1) which was fabricated using 10 AWG insulated copper magnet wire with a coil diameter of 7.5 cm, 2 turns, and inter-winding spacing of 1 cm. Scenario 2 consists of the same Tx coil used in Scenario 1 but coupled to receive coil 2 (Rx2) which was fabricated using 24 AWG copper magnet wire with a coil diameter of 1.5 cm and tightly wound with 3 turns. A summary of coil design specifications used in Scenario 1 and 2 are provided in Table 2.1.

2.7.2 Measurement of Resonator Parameters

As described in Section 2.2.2, resonator losses are predominately determined by the AC and DC losses in the coil. Thus, the unloaded Q of each resonator were determined by one-port VNA measurements of coil Tx, Rx1, and Rx2 directly. This

Table 2.2 Measured Resonator Parameters

Parameters	**Tx**	**Rx1**	**Rx2**
f_0	13.56 MHz	13.56 MHz	13.56 MHz
L_i	1259 nH	482 nH	171 nH
C_i	109.42 pF	285.87 pF	805.61 pF
Q_{0i}	430	300	85
k_{12} range (Tx to Rx1)	$0 \leq k_{12} \leq 0.134$		
k_{12} range (Tx to Rx2)	$0 \leq k_{12} \leq 0.00851$		

provided L_i and R_{pi} as a function of frequency. The operating frequency, f_0, was set to 13.56 MHz, a common Industrial, Scientific, and Medical (ISM) frequency band commonly used in MRC WPT systems. Q_{0i} was calculated using (2.4) and C_i was calculated using the rearranged form of (2.6). The k_{12} range for Tx to Rx1 and Tx to Rx2 as a function of d was measured using two-port VNA measurements between two coils directly. The measured two-port S-parameters were converted into Z-parameters and k_{12} was calculated by

$$k_{12} = \frac{L_{12}}{\sqrt{L_1 L_2}} = \frac{Im(Z_{12})}{\omega_0 \sqrt{L_1 L_2}} \tag{2.35}$$

Recall L_{12} is the mutual inductance between resonators. Figure 2.22 shows the measured range of k_{12} for Tx to Rx1 (scenario 1) and Tx to Rx2 (scenario 2). Table 2.2 provides a summary of measured resonator parameters.

Using the measured resonator parameters, K_{S1opt} and K_{2Lopt} were calculated by (2.23) and (2.24), respectively, at selected k_{12opt} points within the k_{12} range of resonator sets i.e. Tx-to-Rx1 and Tx-to-Rx2. Total series capacitance, C_{ti}, was calculated

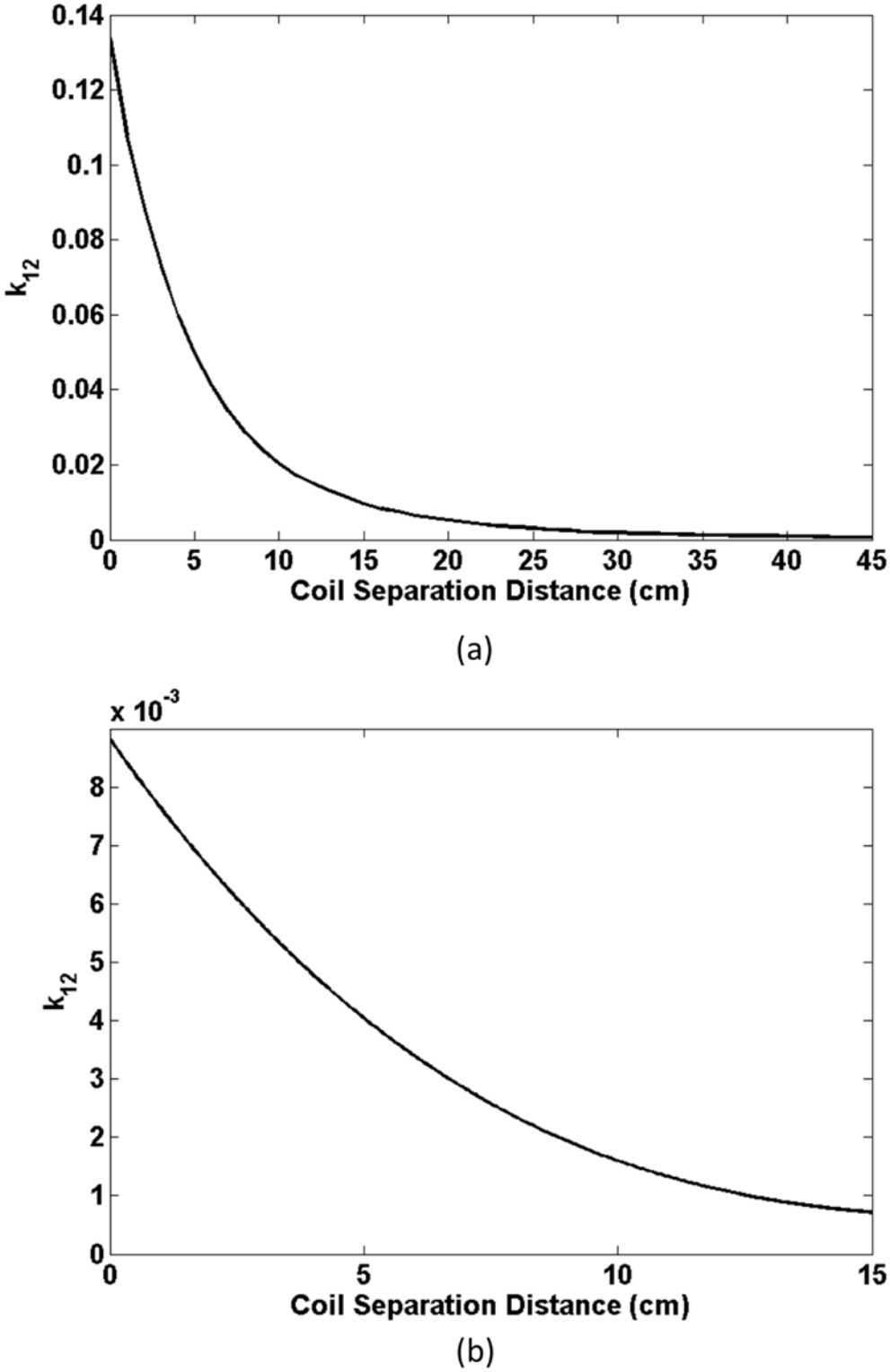

Figure 2.22 Measured k_{12} range for (a) Tx to Rx1 and (b) Tx to Rx2

using (2.34) and shunt capacitance, C_{pi}, was calculated using (2.31). SMD chip capacitors in 0402 or 0603 packages were used for tuning on a printed circuit board (PCB). Multiple capacitors in parallel were used in cases where there was not a single discrete capacitor value for the calculated total series or shunt capacitance values. Additionally, each SMD capacitor was measured using the VNA at f_0 to determine on-PCB capacitance. This was necessary due to 5% - 10% manufacture variability of SMD capacitors.

2.7.3 CCP Control and PTE Response Optimization for Tx to Rx1 (Non-Complex Source and Load Impedance)

Figure 2.23 shows the measured and theory predicted PTE responses at $f_0 = 13.56$ MHz as a function of k_{12} for five k_{12opt} optimization points. A summary of the optimally calculated capacitance values for configuring the network to exhibit each optimal condition (K_{S1opt} and K_{2Lopt} values) is given in Table 2.3. As shown, the predicted and measured responses shows excellent agreement, indicating optimal PTE response can be controlled using the method developed in this work. Slight differences in PTE responses were likely due to PCB parasitic and slight deviation of on-board optimal capacitance values. Also, Figure 2.23 shows the predicted and measured discrepancy between k_{12opt} and k_{12crit} locations. Table 2.4 provides a summary of the predicted and measured FOM, Δ and Δ^*, respectively. The 5% - 10% discrepancy between predicted and measured FOM is most likely due to the slight deviation of on-board optimal capacitance values. Additionally, measured responses were only accurate to ± 5 mm in

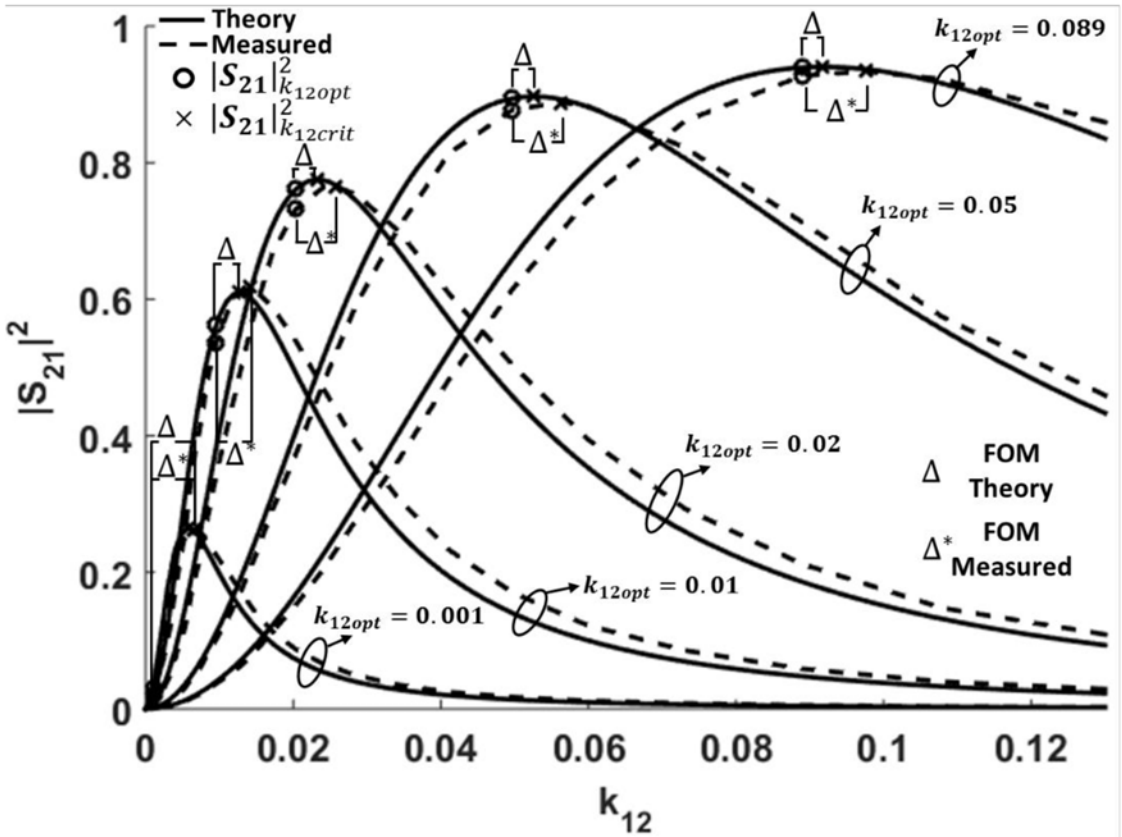

Figure 2.23 Measured and theory predicted PTE responses at $f_0 = 13.56$ MHz as a function of k_{12} as a result of five different k_{12opt} optimization points. The predicted and measured FOM are also given.

Table 2.3 Calculated Optimal Capacitance Values for Tx to Rx1

k_{12opt}	Tx		Rx1	
	C_{p1} (pF)	C_{t1} (pF) †	C_{p2} (pF)	C_{t2} (pF) †
0.09	535.17	132.06	753.25	437.05
0.05	747.64	126.24	1031.60	388.13
0.02	1211.51	119.85	1649.44	344.36
0.01	1705.09	116.77	2311.83	325.73
0.001	3215.50	113.253	4346.42	305.93

† $X_{FIRn} = 0$ since $Z_S = Z_L = 50\ \Omega$

Table 2.4 Predicted and Measured FOM for Tx to Rx1 Optimization Examples

k_{12opt}	**Predicted FOM** (Δ)	**Measured FOM** (Δ^*)
0.09	0.9677	0.9230
0.05	0.9434	0.8900
0.02	0.8734	0.7806
0.01	0.7634	0.7008
0.001	0.1742	0.1560

Figure 2.24 shows the measured, circuit simulated, and theory predicted $|S_{21}|$

coil separation distance, d. Inter-resonator coupling has a $1/d^3$ dependency. Thus, the ability to tease k_{12} differences of ± 0.001 was out of measurement capability. Nonetheless, both predicted and measured responses verify the unique behavior of CCP control in BPF modeled MRC WPT systems. As shown, for a given set of resonator quality factors, minimizing k_{12opt} has the effect of maximizing range but at the expense of both CCP control and maximum achievable PTE.

Figure 2.24 shows the measured, circuit simulated, and theory predicted $|S_{21}|$ frequency response for $k_{12opt} = 0.01$ optimization curve. Three k_{12} locations are shown to highlight over coupling (OC), critical coupling (CC), and under coupling (UC) responses. A close match between measured, circuit simulated, and theory predicted is shown. Frequency splitting is observed in the OC region. As k_{12} decreases to k_{12crit} the resonant peaks converge to the CC point. As k_{12} decreases further, the system enters

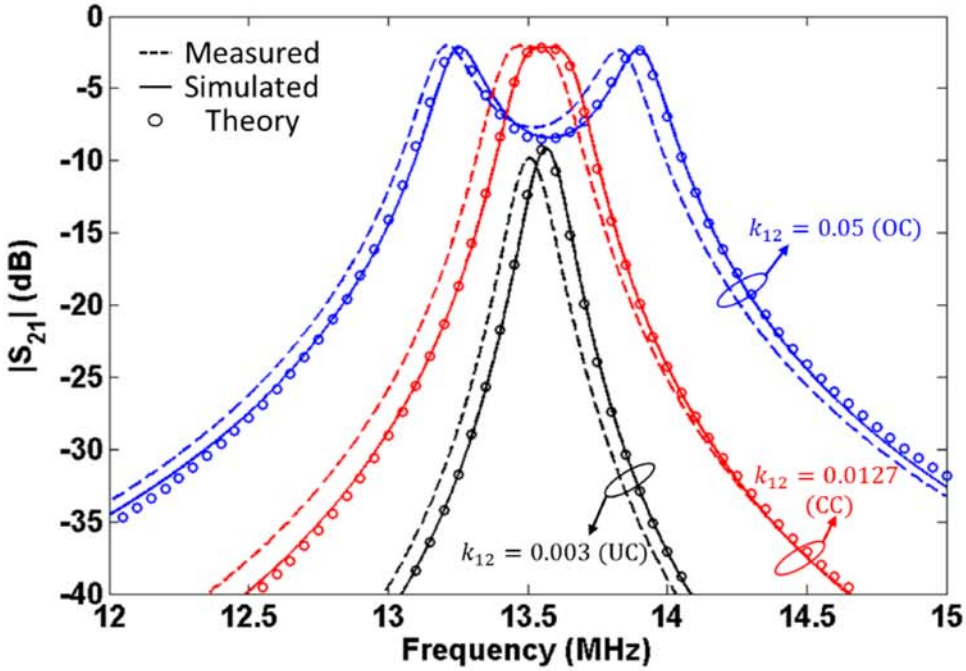

Figure 2.24 Example frequency response, at k_{12} locations representing UC, CC, and OC regions, for the $k_{12opt} = 0.01$ optimized Tx to Rx1 system

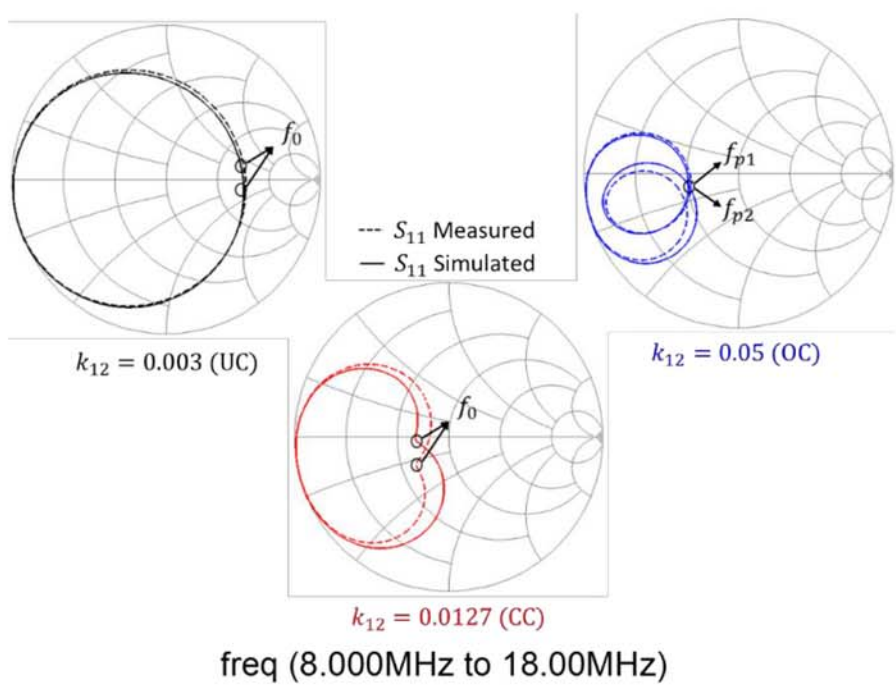

Figure 2.25 Example S_{11} responses at k_{12} locations representing UC, CC, and OC regions, for the $k_{12opt} = 0.01$ optimized Tx to Rx1 system

the UC region marked by a rapid decrease in PTE at the resonant frequency. Figure 2.25 shows the corresponding S_{11} response. The S_{22} response is not shown but it exhibits an analogous behavior to the S_{11} response. As shown, a unique impedance profile exists for each region of coupling depending on the inter-resonator coupling between resonators. The S_{11} response for the UC region is marked by a full resonant impedance circle where the 2nd resonator shows no influence on the S_{11} response. As the 2nd (Rx1) resonator is brought closer to the Tx resonator to where CC occurs, the S_{11} impedance profile responds to the presence of the Rx1 resonator and a dip, at the resonant frequency, occurs in the impedance circle. This change in the S_{11} impedance circle occurs because the mutual impedance between resonators becomes non-negligible and loads the primary (Tx) resonator. As far as the primary circuit is concerned, the presence of receive resonator, Rx1, is manifested simply as a mutual impedance that has been added in series with the Tx resonator [77]. As Rx1 resonator is brought even closer to the Tx resonator to where OC occurs, the S_{11} impedance profile responds dynamically as the resonant frequency dip becomes more pronounced depending on the value of the OC k_{12} value. Indeed, two frequency points intersect to form the dip. These two frequency points of intersection represent each resonant peak of the OC region. The responses described in Figures 2.24 and 2.25 are representative of the behavior for all of the k_{12opt} optimization responses. Clearly, the developed theory accurately predicts the PTE responses and CCP behavior of BPF modeled MRC systems.

2.7.4 CCP Control and PTE Response Optimization for Tx to Rx2 (Non-Complex Source and Load Impedance)

In the previous section, CCP control and the PTE response were demonstrated for a system in which CC was achievable i.e. $k_{12crit,min} < k_{12,max}$. In this section, PTE response control for a system which can never achieve CC is demonstrated. For Tx to Rx2 system, $k_{12crit,min} = 0.0105 > k_{12,max} = 0.008$. Thus, CC can never be achieved in this system.

Figure 2.26 shows a set of predicted PTE responses between Tx to Rx2 for $k_{12opt} = 0.03$ (optimization above $k_{12,max}$) and $k_{12opt} = 0.001$ (optimization below $k_{12,max}$). Clearly, CC can never be achieved in this system. However, choosing a k_{12opt} optimization point below $k_{12,max}$ maximized the PTE response within the achievable k_{12} range between resonators. As much as an 11% increase in PTE is achieved in comparison to the same system optimized at a k_{12opt} value of 0.03. In applications such a medical device powering, where systems may typically exhibit $k_{12cirt,min} < k_{12,max}$, an 11% increase in PTE may mean the difference between safe (output power level that maintains or is below government regulated biological tissue specific absorption rate (SAR) levels) and unsafe powering. Uniquely, this work presents the optimization and PTE control methodology for maximizing the PTE response.

2.7.5 Demonstration of Complex Load Impedance Accommodation (Tx to Rx1)

In many WPT scenarios, load impedances are not purely real, such as the input impedance of a rectifier and power management system which provides stable DC power

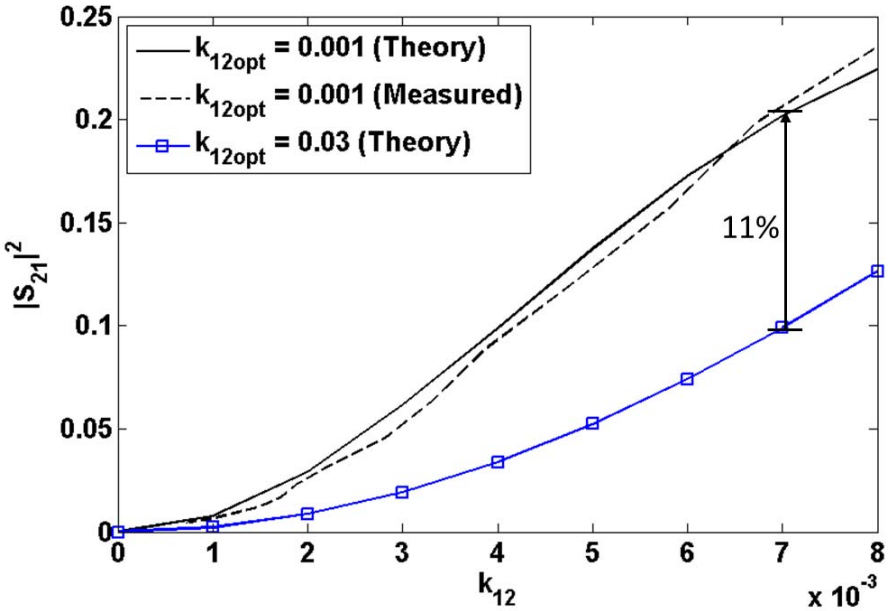

Figure 2.26 Measured (dotted line) and Simulated PTE responses for Tx to Rx2. Critical coupling can never be achieved in this system. However, as large as an 11% increase in PTE can be achieved by choosing an ideal k_{12opt} optimization point.

to an electronic device (e.g. the Bionode). As described in this work (see Figure 2.9), the BPF modeled MRC WPT system is developed to accommodate for complex impedances without distorting a pre-designed PTE/CCP response i.e. a particular k_{12opt} optimization response. Critically, this system removes the need for additional IM networks.

Figure 2.27(a) shows the input impedance of a voltage quadrupler rectifier and power management system. The rectifier was constructed on a PCB using 4 SMD capacitors in 0402 package (0.1 μF) and a single four diode package in SOT-363 package (HSMS-282R). The output of the rectifier was connected to a 1.8V LDO regulator in a 4-Ball WLCSP package (ADP150ACBZ-1.8-R7) to provide a stable 1.8V DC signal for operating the device electronics. The output of the regulator was connected to a custom designed implantable system, Bionode, developed at the Center for Implantable Devices,

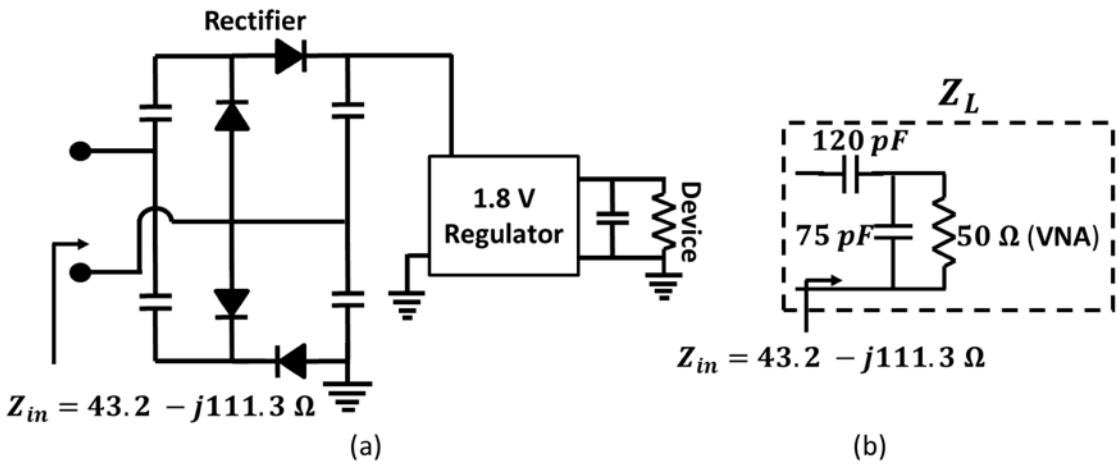

Figure 2.27 Measured input impedance (f_0=13.56 MHz, Pin = 15 dBm) for (a) rectifier and voltage regulator circuit connected to a custom designed medical device (Bionode) and (b) input impedance replication circuit for enabling 2-port VNA measurement.

Purdue University [78]. The input impedance of this system, measured using one-port VNA measurements, was $Z_{in} = 43.2 - j111.3\ \Omega$ at an input power (Pin) of 15 dBm (31.6 mW) and a frequency of 13.56 MHz.

Two-port VNA measurements of the Tx to Rx1 system were made to verify the impedance accommodation methodology. To enable two-port VNA measurements, the rectifier system input impedance was replicated on a separate PCB with the capacitive network shown in Figure 2.27(b) placed in front of the 50 Ω VNA port impedances. This circuit acted as the effective load seen by the output of the MRC system.

System Tx to Rx1, at the k_{12opt} design point of 0.01, was used for demonstration of complex load impedance accommodation. Figure 2.28 shows the theory predicted, measured at 50 Ω source and load impedance, and measured at 50 Ω source and $43.2 - j111.3\ \Omega$ load impedance responses. Since the source impedance was maintained at 50 Ω ($X_{FIR1} = 0$), the calculated optimal capacitance values of the Tx system was equivalent to

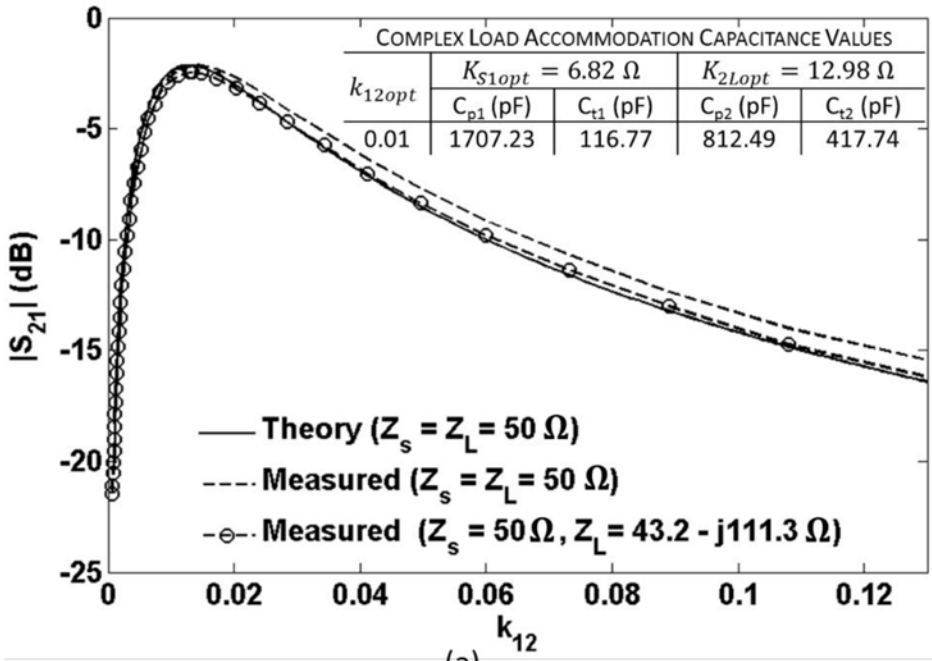

(a)

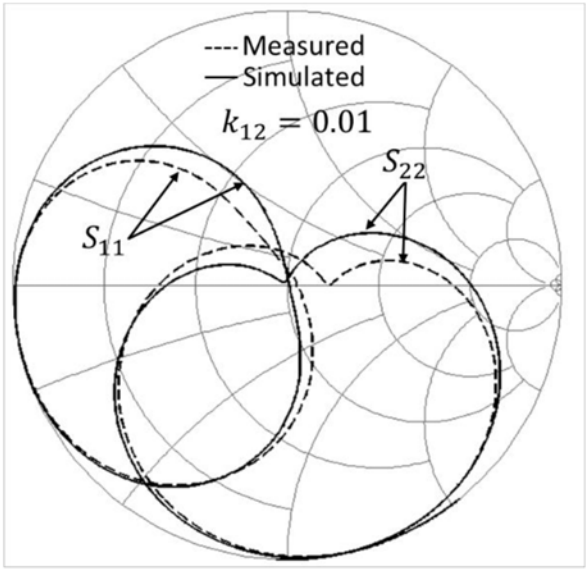

freq (8.000MHz to 18.00MHz)

(b)

Figure 2.28 Experimental validation of complex load impedance accommodation. (a) Comparison of Inter-resonator coupling PTE response for Tx to Rx1 optimized at $k_{12opt} = 0.01$. The complex load accommodated system achieves the same PTE response predicted and measured for a non-complex load impedance system. (b) Measured and circuit simulated S_{11} and S_{22} responses at inter-resonator coupling location $k_{12} = k_{12opt} = 0.01$.

those shown in Table 2.3 at the k_{12opt} design point of 0.01. However, due to the complex load impedance, the optimal calculated capacitance values on the Rx1 side were updated with the complex load accommodation values of K_{2Lopt} and X_{FIR2}. Total series capacitance was calculated using (2.34) and shunt capacitance was calculated using (2.31). A summary of the updated capacitance values for complex load impedance accommodation is given in the inset of Figure 2.28(a). As shown, the complex load accommodated PTE performance matches closely with the theory and measured PTE performance with purely real 50 Ω source and load impedances. Indeed, complex load impedance accommodation was achieved with no distortion to the pre-designed inter-resonator coupling PTE response. Figure 2.28(b) shows the circuit simulated and measured S_{11} and S_{22} responses of the complex load impedance accommodated response measured at the inter-resonator coupling location $k_{12} = 0.01$. As shown the resonance dip of the S_{22} response approaches the center of the Smith chart. This indicates that the output impedance of the $k_{12opt} = 0.01$ optimized system is the complex conjugate of $Z_{in} = 43.2 - j111.3\ \Omega$.

2.7.6 Summary of PTE/CCP Response Control and Optimization Methodology

Figure 2.29 provides a summary the generalized design procedure for optimizing and controlling PTE responses and CCP location for the BPF modeled MRC WPT system. In this work, the design procedure begins first with the measurement and determination of resonator and system design parameters including the selection of k_{12opt}. In systems with > 2 resonators, multiple k_{12opt} locations may exists with each

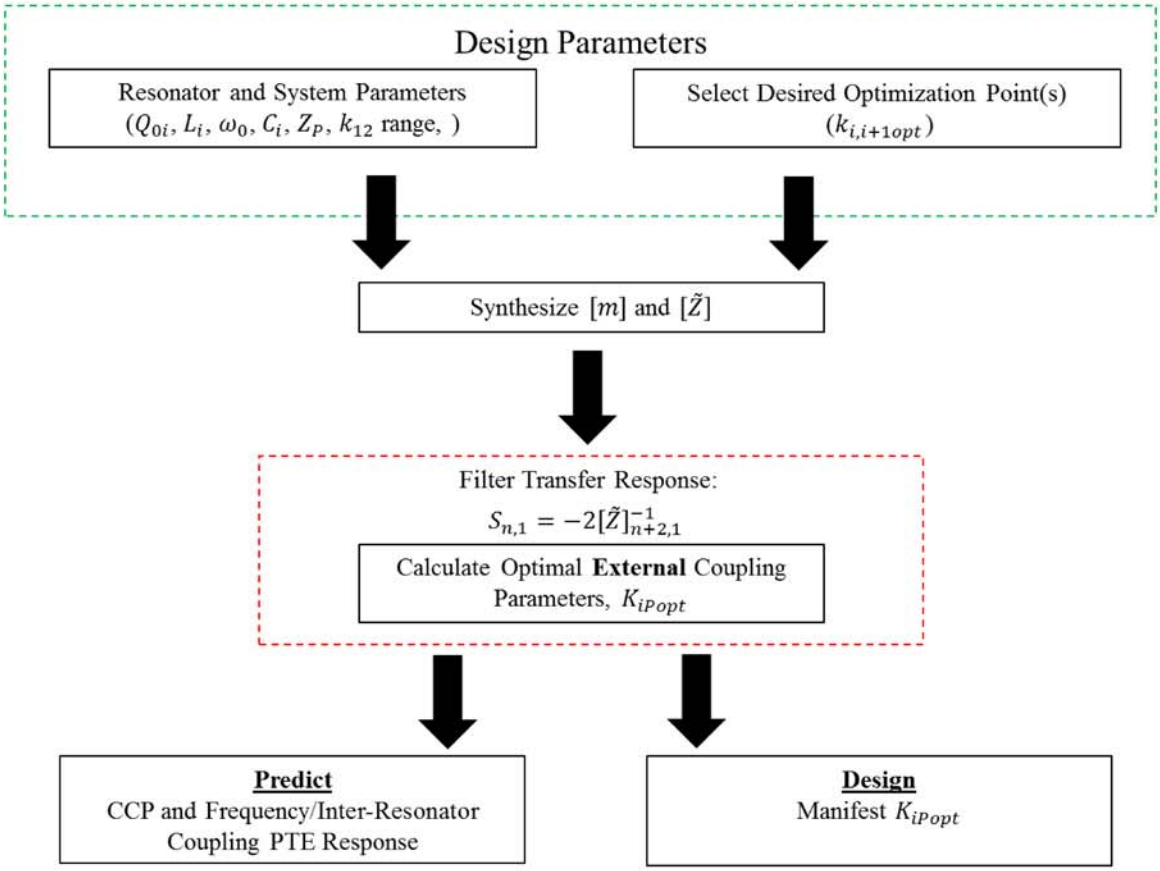

Figure 2.29 Generalized procedure for BPF modeled MRC WPT control and optimization.

representing the inter-resonator coupling locations at which optimization is desired to occur. These resonator and system design parameters are then utilized to from the generalized coupling matrix, $[m]$, and normalized impedance matrix, $[\tilde{Z}]$, from which the transfer function can be derived and the optimal external coupling characteristic impedances can be solved. Using these functions, the full PTE response of the system can be predicted and then designed by configuring K-inverter networks to exhibit optimal external coupling characteristic impedances calculated from the set of fixed system design parameters.

2.7.7 Additional Coupling Maps and Corresponding Coupling Matrices

The general coupling matrix synthesis and analysis method is versatile and can be expanded to represent myriad of filter coupling combinations. Using the generalized procedure outlined in Section 2.7.6, PTE response and optimization can be achieved for systems which may include additional resonators and multiple loads. These systems could have power relaying and selective powering capabilities exhibiting predictable, controllable, and optimizable PTE responses. In these multi-resonator and multi-load systems, numerical methods may be a better approach for optimization and system control. Nonetheless, the optimization procedure for these systems will still follow the general methodology summarized in Figure 2.29.

A few examples of useful BPF modeled MRC coupling topologies and associated general coupling matrices are shown in Figure 2.30. Figure 2.30(a) describes a serial resonator system with one source and one load. It is important to note that only port connected resonators (black circles) include an FIR element. Relay resonators (gray circle) are series RLC resonators and do not include series FIR. In MRC systems, relay resonators are used as power "hoppers" to extend WPT distance [79]. Thus, Figure 2.30(a) is a WPT system with power extending capability. The corresponding coupling matrix is given. Figure 2.30(b) describes a system utilizing a single source resonator (resonator 1) exciting a parallel set of cross-coupled relay resonators simultaneously. A single load resonator (resonator n) receives the coupled energy from the cross-coupled relay resonators to deliver power to a load. This type of BPF modeled MRC WPT system configuration has been utilized previously for the development of tri-axial small animal powering cage systems [80]. Finally, Figure 2.30(c) describes a system consisting of a

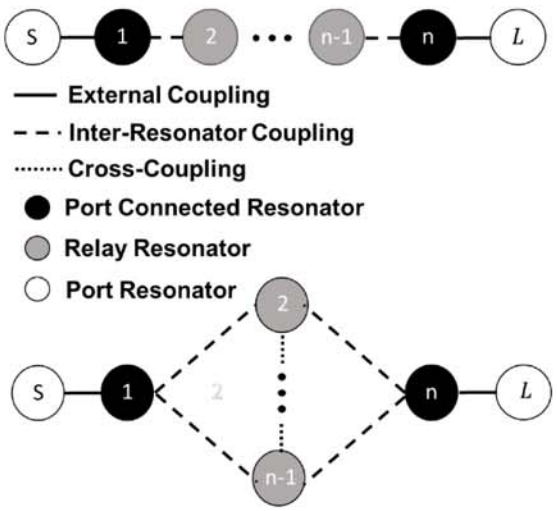

$$
\begin{array}{c|c}
 & \begin{matrix} S & 1 & 2 & \cdots & n-1 & n & L \end{matrix} \\
\begin{matrix} S \\ 1 \\ 2 \\ \vdots \\ n-1 \\ n \\ L \end{matrix} &
\begin{bmatrix}
M_{SS} & M_{S1} & 0 & \cdots & 0 & 0 & 0 \\
M_{S1} & M_{11} & M_{12} & \cdots & 0 & 0 & 0 \\
0 & M_{12} & M_{22} & \cdots & 0 & 0 & 0 \\
\vdots & \vdots & \vdots & \ddots & \vdots & \vdots & \vdots \\
0 & 0 & 0 & \cdots & M_{n-1,n-1} & M_{n-1,n} & 0 \\
0 & 0 & 0 & \cdots & M_{n-1,n} & M_{n,n} & M_{n,L} \\
0 & 0 & 0 & \cdots & 0 & M_{n,L} & M_{LL}
\end{bmatrix}
\end{array}
$$

(a)

$$
\begin{array}{c|c}
 & \begin{matrix} S & 1 & 2 & \cdots & n-1 & n & L \end{matrix} \\
\begin{matrix} S \\ 1 \\ 2 \\ \vdots \\ n-1 \\ n \\ L \end{matrix} &
\begin{bmatrix}
M_{SS} & M_{S1} & 0 & \cdots & 0 & 0 & 0 \\
M_{S1} & M_{11} & M_{12} & \cdots & M_{1,n-1} & 0 & 0 \\
0 & M_{12} & M_{22} & \cdots & M_{2,n-1} & M_{2,n} & 0 \\
\vdots & \vdots & \vdots & \ddots & \vdots & \vdots & \vdots \\
0 & M_{1,n-1} & M_{2,n-1} & \cdots & M_{n-1,n-1} & M_{n-1,n} & 0 \\
0 & 0 & M_{2,n} & \cdots & M_{n-1,n} & M_{n,n} & M_{n,L} \\
0 & 0 & 0 & \cdots & 0 & M_{n,L} & M_{LL}
\end{bmatrix}
\end{array}
$$

(b)

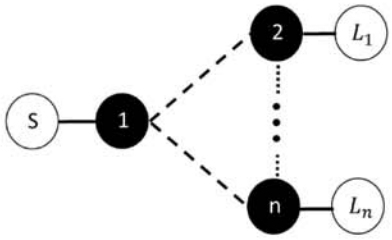

$$
\begin{array}{c|c}
 & \begin{matrix} S & 1 & 2 & L_1 & \cdots & n & L_n \end{matrix} \\
\begin{matrix} S \\ 1 \\ 2 \\ L_1 \\ \vdots \\ n \\ L_n \end{matrix} &
\begin{bmatrix}
M_{SS} & M_{S1} & 0 & 0 & \cdots & 0 & 0 \\
M_{S1} & M_{11} & M_{12} & 0 & \cdots & M_{1n} & 0 \\
0 & M_{12} & M_{22} & M_{2L_1} & \cdots & M_{2n} & 0 \\
0 & 0 & M_{2L_1} & M_{L_1L_1} & \cdots & 0 & 0 \\
\vdots & \vdots & \vdots & \vdots & \ddots & \vdots & \vdots \\
0 & M_{1n} & M_{2n} & 0 & \cdots & M_{nn} & M_{n,L_n} \\
0 & 0 & 0 & 0 & \cdots & M_{n,L_n} & M_{L_nL_n}
\end{bmatrix}
\end{array}
$$

(c)

Figure 2.30 Example BPF modeled MRC WPT coupling arrangements: (a) serial power "hopper", (b) cross-coupled parallel power "hopper", and (c) multi-load power distribution arrangement.

single source resonator coupling directly to an n number of load resonators. This system provides wireless power to multiple loads simultaneously. Such a powering arrangement may be useful for simultaneously wirelessly powering multiple externally worn or implanted medical devices.

2.8 Conclusion

A novel BPF modeled MRC WPT system, analysis methodology, and optimization procedure, for purely real and complex source and load impedances, has been developed and verified experimentally. A full analytical treatment of the transfer response and optimization methodology provided unique insight into the PTE response behavior and CCP control. To the author's knowledge, the first analytical method for describing and predicting CCP behavior and control in BPF modeled MRC WPT systems is presented. This analytical and optimization foundation acts as a useful platform for optimizing PTE responses based on expected wireless power conditions i.e. inter-resonator coupling range. The developed methodology is applicable with MRC systems designed with high quality factor resonators and high inter-resonator coupling capability and MRC systems with low quality factor resonators and low inter-resonator coupling capability. This provides the optimization strategy to enable effective wireless powering to small wearable or implantable medical devices.

CHAPTER 3. NOVEL MRC WPT ARRANGMENT FOR A MYOELECTRIC SENSING SYSTEM

The data and work in this chapter have been submitted for publication in the Journal of Neural Engineering. The citations can be found in the Publications section. This work was performed in collaboration with Rebecca A. Bercich and Zhi (Grant) Wang at the Center for Implantable Devices, Purdue University.

3.1 Introduction

Synergy between electromyography (EMG) sensing devices and myoelectric control systems have improved the performance of sophisticated electronic prosthetic systems [81, 82]. A major contributing factor to the improved synergy is the removal of the battery, thus enabling device miniaturization. Miniaturization minimizes the invasiveness of an implanted or externally applied EMG sensing device. Consequently, devices for upper-limb amputees, including those utilized in the first human trials, utilized inductive coupling WPT for operation [83, 84]. These systems, however, utilize only traditional coil design and lack PTE optimization. Traditional powering coils which consist of standard coil loops wrapped around a patient's limb, can only supply magnetic flux along the axis of the limb. Such a system could not be implemented, for example, to sensing devices which require magnetic flux permeating perpendicular to a limb. Additionally, without proper optimization, maximizing PTE to multiple devices may not

be achieved. In this work, I develop a novel MRC WPT arrangement, utilizing the optimization procedure developed in Chapter 2, to enable wireless operation of custom designed surface EMG (sEMG) sensing devices. An array of eight of these fully wireless devices, located circumferentially around an able-bodied subject's forearm, were simultaneously wirelessly powered generating eight channels of sEMG sensing providing the subsequent control of a virtual prosthetic arm. The novel contributions of this work are:

1. A new and easily worn anti-Helmholtz (AHH) arm-band power source coil
2. A BPF derived optimization methodology to power 8 sEMG sensing devices simultaneously
3. WPT demonstration, simultaneously operating 8 sEMG devices around an able-bodied subject's forearm (conducted at the Rehabilitation Institute of Chicago)

3.2 The MRC WPT Arrangement

The MRC WPT arrangement consists of a new and easily worn AHH arm-band coil and 8 thin and flexible receive coil resonator systems wrapped circumferentially around a subject's forearm. Figure 3.1 illustrates this novel MRC WPT arrangement. The system is fully optimized via the developed BPF model optimization strategy presented in Chapter 2.

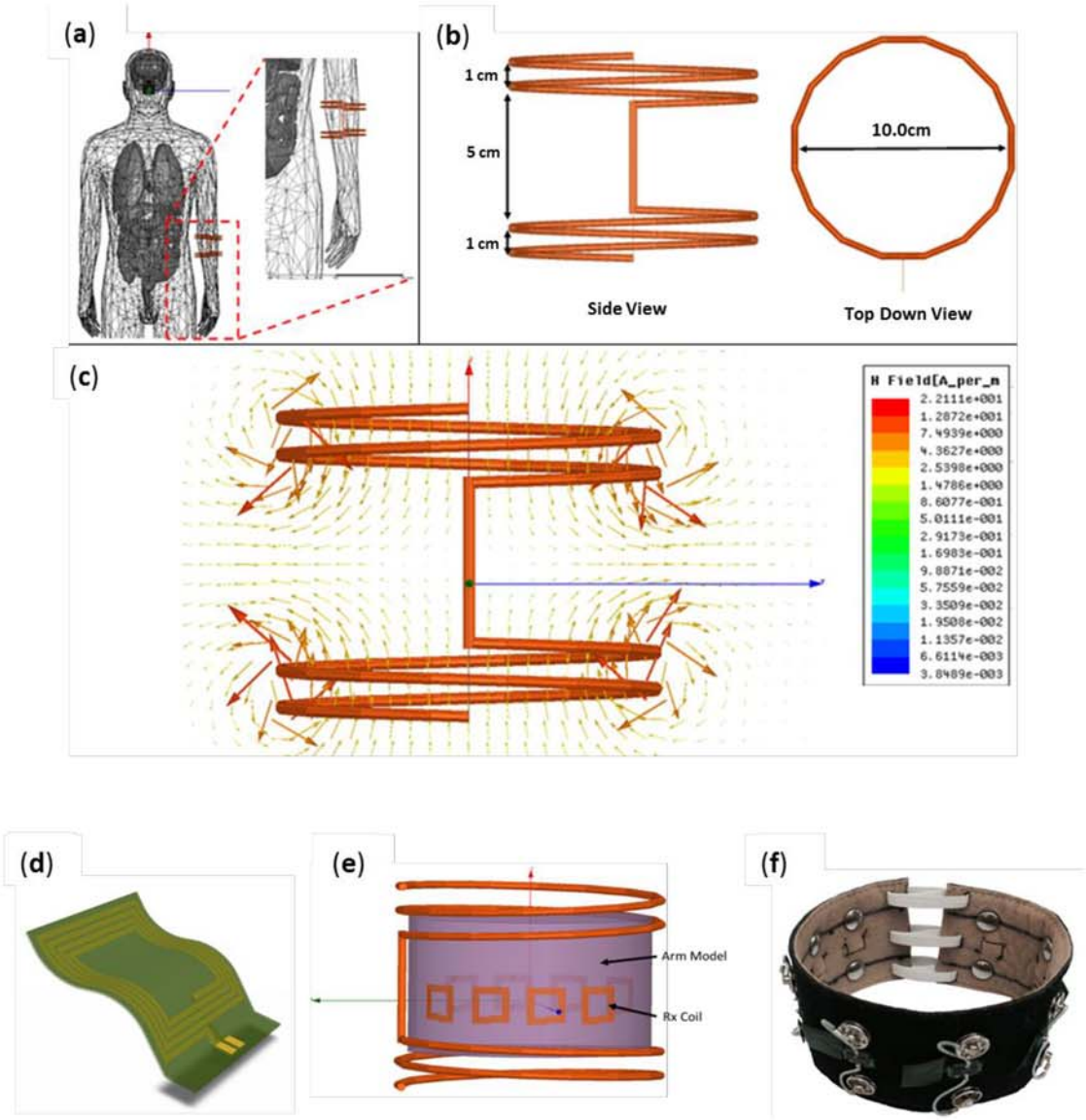

Figure 3.1 MRC WPT arrangement for operating multiple Myoelectric sensing devices. (a) Intended placement of the AHH arm band coil around a human body model in ANSYS HFSS®. (b) AHH coil dimensions. (c) Illustration of magnetic field vectors. (d) Rx coil fabricated on a flexible polyimide substrate with 2oz. copper deposition and insulting polyimide overlay. Coil footprint is 15 mm x 15 mm and a thickness of 0.13 mm. (e) HFSS® model of the AHH arm band coil and relative positioning of the 8 flexible printed Rx coils. Equal inter-resonator coupling is achieved to enable optimum simultaneous wireless power distribution to eight devices wrapped circumferentially around a subject's forearm. (f) Adjustable forearm cuff designed to house eight pairs of dry metal dome electrodes for sEMG recording on the interior lining. Electrode interface with the microelectronics platform on the exterior surface through snap joint and flexible extension spring leads.

3.2.1 Anti-Helmholtz Coil

An AHH coil is formed exactly as a normal Helmholtz coil system but with oppositely directed currents between top and bottom coils (Figure 3.2). Figure 3.3 shows the simulated magnetic field ($\vec{H}$-field) distribution for an AHH coil arrangement. An

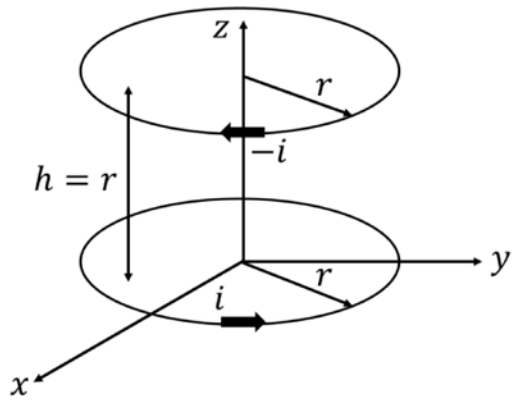

Figure 3.2 Anti-Helmholtz coil arrangement. Note the equal and opposite current, i, directions between top and bottom coils.

AHH coil produces a quadrupole field which has the critical feature of high density $\vec{H}$-fields directed radially (x-y components) from the cylindrical "window" formed between the coil pair. Consequently, an AHH coil placed around a subject's forearm will produce $\vec{H}$-fields directed perpendicular, instead of parallel or along, to the forearm. This provides the necessary flux and equivalent inter-resonator coupling to a set of Rx resonators wrapped circumferentially around the limb [Figure 3.1(e)].

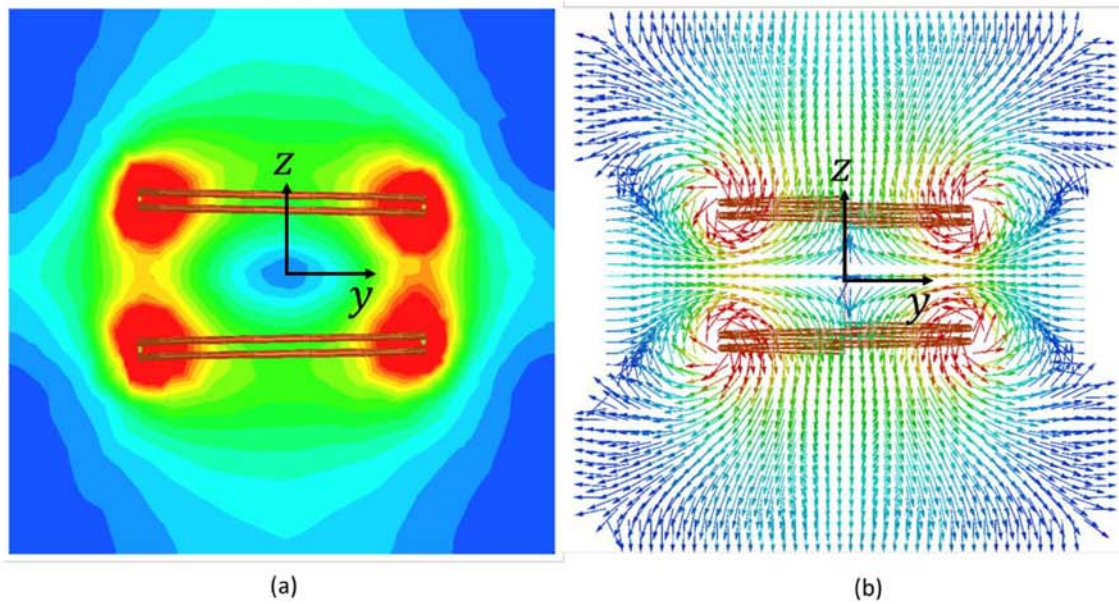

Figure 3.3 HFSS simulated $\vec{H}$-field distribution for an AHH arranged coil. Opposite currents are achieved by connecting oppositely wound coils. (a) magnitude of $\vec{H}$-field distribution. The AHH system produces a quadrupole field. (b) vector $\vec{H}$-field distribution. Note the high density of radially directed fields within the cylindrical window between coils. (Red, large magnitude; Blue, small magnitude)

3.2.2 Anti-Helmholtz Coil and Rx coil Fabrication

Figure 3.4 shows the fabricated AHH coil and placement on a forearm. The AHH coil was fabricated using 8 AWG copper magnet wire. Two coils were fabricated separately and strategically wound in opposite directions (right and left-handed winding) to form a system of oppositely directed currents. Each coil was fabricated with equivalent criteria and dimensions i.e. 2 turns, 1 cm inter-winding separation distance, and 10 cm diameter. Each coil was soldered together with a height separation of 5 cm (coil radius). The end points for each coil were connected to form a single excitation port. A summary

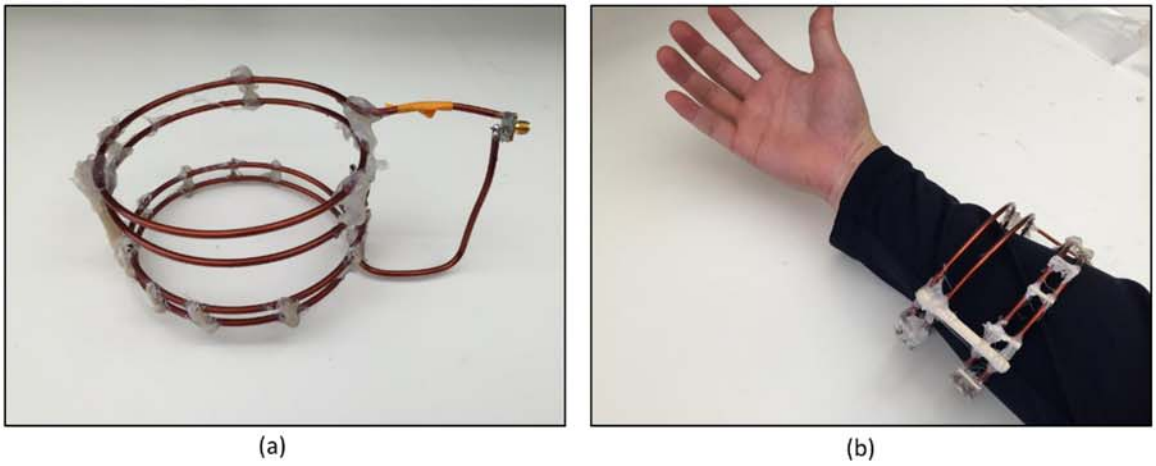

Figure 3.4 (a) Fabricated AHH arm coil and (b) placement on a subject's forearm.

of the AHH arranged coil dimensions are provided in Figure 3.1(b). It is important to note that the 1 cm inter-winding separation distance for each coil of the AHH pair was strategically implemented to reduce proximity effects and parasitic capacitance of the coil pair. As shown in Figure 3.5, an inductor with an inter-winding spacing of 1 cm achieves as much as a 272% increase in inductor Q (Q of 90 to 245 at 8 MHz) over an AHH system made of tightly wound coils of equivalent dimensions. As described in Chapter 2, improving Q, improves PTE and CCP control.

Each Rx coil was built on a thin, flexible FR4 substrate and designed to be easily mounted on the fabric cuff [Figure 3.1(d)-(f)]. Flexibility enhances conformity of the Rx coil to the body. The coil design criteria are given in Figure 3.6. Figure 3.7 shows the measured inductor Q for the Rx coil off and on the arm. At frequencies above 10 MHz, magnetic energy generated by the inductor is lost and absorbed into the biological tissue

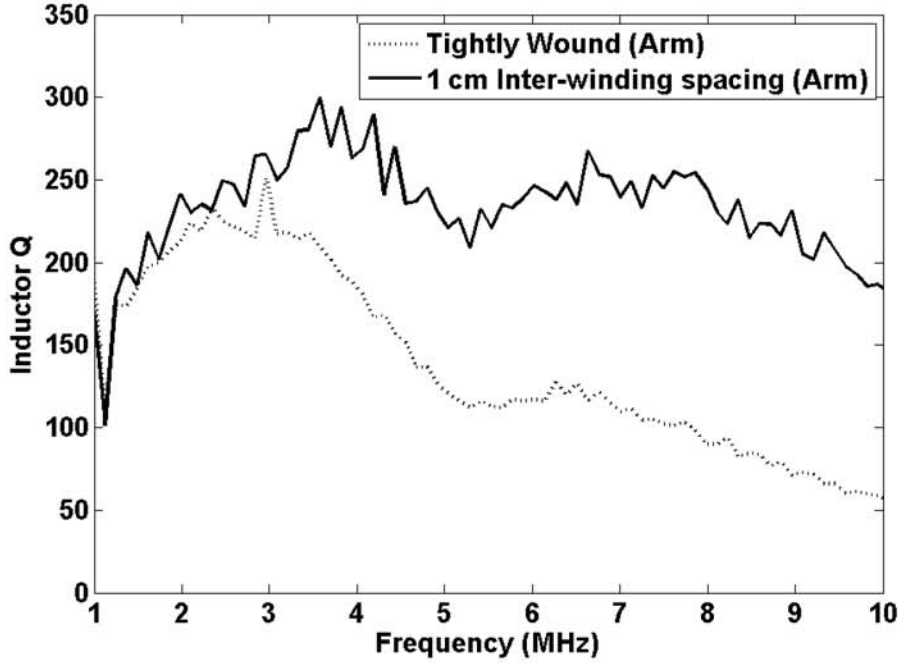

Figure 3.5 Measured AHH system inductor Q and comparison between an AHH system formed of top and bottom coils with 1 cm inter-winding spacing and an AHH system with top and bottom coils that were tightly wound. Inductor Q is improved by 272% (90 to 245 at 8 MHz) by implementing a 1 cm space in between windings in the top and bottom coils.

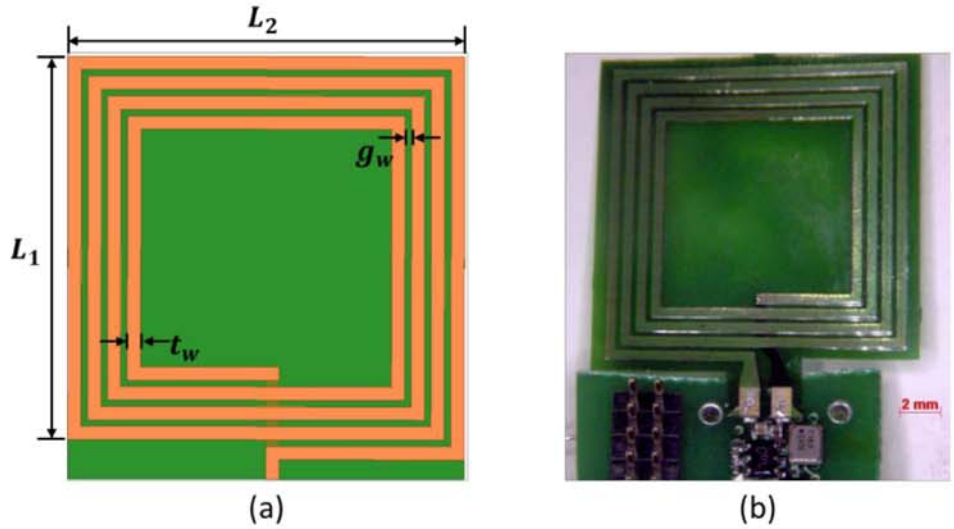

Figure 3.6 Individual flexible Rx coil (a) design: g_w = 0.25 mm, t_w = 0.35 mm, $L_1 = L_2 = 15$ mm, N = 4 turns. (b) Fabricated coil

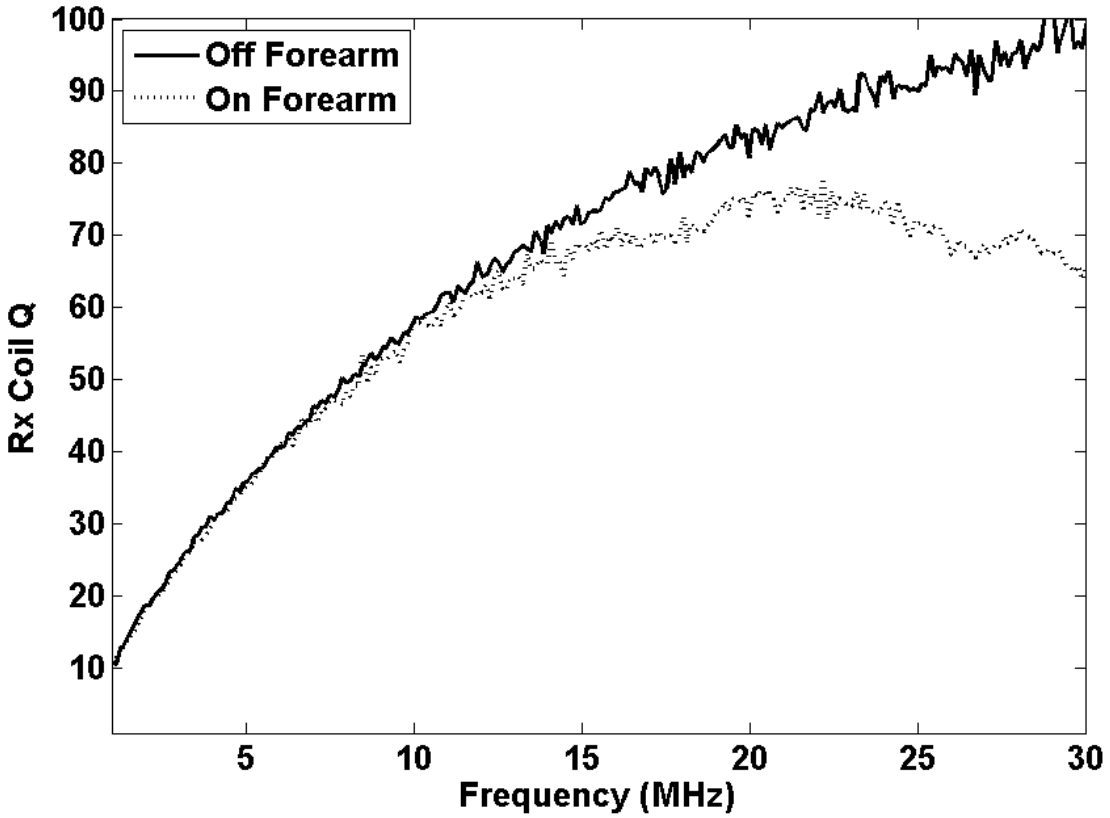

Figure 3.7 Measured Rx coil Q on and off the forearm.

(transformed into tissue heating). As a result, inductor Q begins to drop. At frequencies below 10 MHz, biological tissue is relatively transparent to the oscillating magnetic fields and thus Q does not change between being on or off the forearm. Thus, it is advantageous to design the resonant operation of the BPF modeled MRC WPT system at a frequency below 10 MHz. Consequently, an 8 MHz operating frequency was chosen for the AHH and Rx Coil MRC powering arrangement. At 8 MHz, peak inductor Q between the AHH and Rx coil was maximized. A summary of the measured resonator and design parameters for the AHH Tx coil and Rx coil, on a subject's forearm, are given in Table 3.1. The k_{12} range was measured in the position shown in Figure 3.1(e) and based on a

Table 3.1 Measured Resonator Parameters (forearm)

Parameters	**Tx (AHH Coil)**	**Rx Coil**
f_0	8.0 MHz	8.0 MHz
L_i	1533 nH	343 nH
C_i	109.42 pF	285.87 pF
Q_{0i}	245	49.6
k_{12} range †	$0.008 \leq k_{12} \leq 0.013$	

† dependent on the diameter of the subject's forearm

Tx and Rx coil separation distance of 1-2 cm, depending on diameter of the subject's forearm. Lumped element parameters are based on Figure 2.20(a).

3.2.3 Equal Power Distribution Optimization

Figure 3.8 shows the representative coupling topology and corresponding coupling matrix for the n = 9 resonator (1 source and 8 receive resonators) and P = 9 port (1 source and 8 loads) MRC power distribution arrangement. The corresponding coupling matrix is an 18 x 18 sized matrix. The optimization goal for this system is to 1.) achieve equivalent power distribution from the source resonator (resonator 1) to each of the receive resonators (resonators 2-9) and 2.) maximize the PTE to each resonator. The equivalent power distribution condition is given by

$$S_{21} = 2j[\tilde{Z}]_{4,1}^{-1} = S_{31} = 2j[\tilde{Z}]_{6,1}^{-1} = \cdots = S_{P1} = 2j[\tilde{Z}]_{P\times 2,1}^{-1}, \quad P = 2,3,\ldots,n \tag{3.1}$$

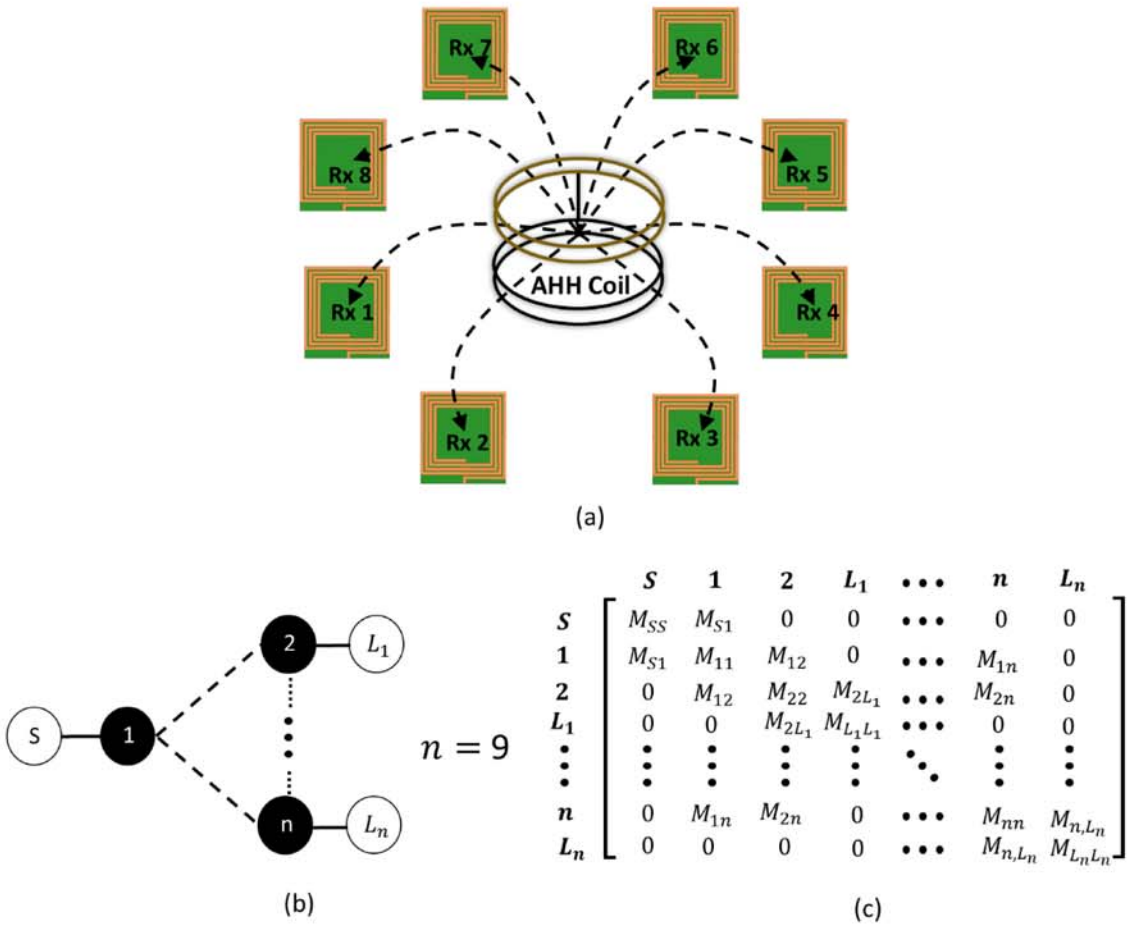

Figure 3.8 (a) Coupling configuration, (b) coupling map, and (c) general coupling matrix for the AHH MRC powering arrangement (1 source resonator and 8 receive resonators and loads). See Figure 2.29 for coupling map key.

The condition to achieve equivalent power distribution is derived as [56]

$$K_{2L} = K_{3L} = \cdots = K_{PL}, \qquad P = 2,3,\ldots,n \tag{3.2}$$

Therefore, the only external coupling characteristic impedance optimization variables in the PTE function are K_{S1} and K_{2L}. Also, each receive resonator and load are equivalent (equivalent coil, rectifier system, and device). Thus the coupling matrix is simplified by having only two external coupling M_{S1} and M_{2L} variables. Additionally, since the receive coils are small and spaced sufficiently apart, all cross-couplings can be approximated to

$$
m := \begin{pmatrix}
0 & MS1 & 0 & 0 & 0 & 0 & 0 & 0 & 0 & 0 & 0 & 0 & 0 & 0 & 0 & 0 & 0 & 0 \\
MS1 & M11 & M12 & 0 & M13 & 0 & M14 & 0 & M15 & 0 & M16 & 0 & M17 & 0 & M18 & 0 & M19 & 0 \\
0 & M12 & M22 & M2L & 0 & 0 & 0 & 0 & 0 & 0 & 0 & 0 & 0 & 0 & 0 & 0 & 0 & 0 \\
0 & 0 & M2L & 0 & 0 & 0 & 0 & 0 & 0 & 0 & 0 & 0 & 0 & 0 & 0 & 0 & 0 & 0 \\
0 & M13 & 0 & 0 & M33 & M3L & 0 & 0 & 0 & 0 & 0 & 0 & 0 & 0 & 0 & 0 & 0 & 0 \\
0 & 0 & 0 & 0 & M3L & 0 & 0 & 0 & 0 & 0 & 0 & 0 & 0 & 0 & 0 & 0 & 0 & 0 \\
0 & M14 & 0 & 0 & 0 & 0 & M44 & M4L & 0 & 0 & 0 & 0 & 0 & 0 & 0 & 0 & 0 & 0 \\
0 & 0 & 0 & 0 & 0 & 0 & M4L & 0 & 0 & 0 & 0 & 0 & 0 & 0 & 0 & 0 & 0 & 0 \\
0 & M15 & 0 & 0 & 0 & 0 & 0 & 0 & M55 & M5L & 0 & 0 & 0 & 0 & 0 & 0 & 0 & 0 \\
0 & 0 & 0 & 0 & 0 & 0 & 0 & 0 & M5L & 0 & 0 & 0 & 0 & 0 & 0 & 0 & 0 & 0 \\
0 & M16 & 0 & 0 & 0 & 0 & 0 & 0 & 0 & 0 & M66 & M6L & 0 & 0 & 0 & 0 & 0 & 0 \\
0 & 0 & 0 & 0 & 0 & 0 & 0 & 0 & 0 & 0 & M6L & 0 & 0 & 0 & 0 & 0 & 0 & 0 \\
0 & M17 & 0 & 0 & 0 & 0 & 0 & 0 & 0 & 0 & 0 & 0 & M77 & M7L & 0 & 0 & 0 & 0 \\
0 & 0 & 0 & 0 & 0 & 0 & 0 & 0 & 0 & 0 & 0 & 0 & M7L & 0 & 0 & 0 & 0 & 0 \\
0 & M18 & 0 & 0 & 0 & 0 & 0 & 0 & 0 & 0 & 0 & 0 & 0 & 0 & M88 & M8L & 0 & 0 \\
0 & 0 & 0 & 0 & 0 & 0 & 0 & 0 & 0 & 0 & 0 & 0 & 0 & 0 & M8L & 0 & 0 & 0 \\
0 & M19 & 0 & 0 & 0 & 0 & 0 & 0 & 0 & 0 & 0 & 0 & 0 & 0 & 0 & 0 & M99 & M9L \\
0 & 0 & 0 & 0 & 0 & 0 & 0 & 0 & 0 & 0 & 0 & 0 & 0 & 0 & 0 & 0 & M9L & 0
\end{pmatrix};
$$

Figure 3.9 Coupling matrix for the single source and 8 resonator/load AHH MRC powering arrangement.

zero. Figure 3.9 shows the constructed coupling matrix. Using this matrix and the analysis and optimization procedure developed in Chapter 2, the K_{S1opt} and K_{2Lopt} values for the source and each receive resonator were derived as

$$K_{S1opt} = \left(1 + Q_{01}Q_{02}\sum_{i=2}^{n} k_{1,i,opt}^2\right)^{1/4} |Z_S|\sqrt{\frac{R_{p1}}{R_S}} \tag{3.3}$$

$$K_{2Lopt} = \left(1 + Q_{01}Q_{02}\sum_{i=2}^{n} k_{1,i,opt}^2\right)^{1/4} |Z_L|\sqrt{\frac{R_{p2}}{R_L}} \tag{3.4}$$

where $k_{1,i,opt}$ represents the desired source to receive resonator inter-resonator coupling value at which optimal PTE is desired to occur for each system. A significant advantage of the AHH arm band coil system is that the inter-resonator coupling between the AHH Tx coil and each receive resonator can be assumed to be fixed (fixed forearm diameter) and equivalent in value. Based on the k_{12} range shown in Table 3.1, a $k_{1,i,opt}$ value of 0.1 was chosen. This balances the variability that may be seen due to differing forearm

diameters and ensures that operation in the over-coupling (frequency splitting) regime does not occur. Note that K_{2Lopt} represents the optimal external coupling characteristic impedance for each of the 8 receive systems. Additionally, R_{p2} is equivalent for each receive resonator since each coil is equivalent in design.

Figure 3.10 shows the circuit diagram for an individual receive resonator and power management system. The power management system consists of a full bridge voltage doubler rectifier and downstream LDO voltage rectifier. A Zener diode ($V_Z =$ 5.1V) is implemented for over-voltage protection to the voltage regulator. The measured input impedance of the power management system is approximately 50 Ohms at an input power of 20 dBm (100 mW) and a frequency of 8 MHz. The source impedance of the system is also 50 Ohms (50 Ohm signal generator and power amplifier). Using the source and load impedances, resonator parameters summarized in Table 3.1, and $k_{1,i,opt} = 0.01$, K_{S1opt} and K_{2Lopt} for an 8 receive resonator system were calculated to be 7.176 Ω and 7.54 Ω, respectively. The corresponding capacitance values for configuring the K-inverter network to exhibit K_{S1opt} and K_{2Lopt} were calculated using (2.31) and (2.34). Figure 3.11 shows the simulated and predicted frequency response between each receive resonator and the AHH arm band coil at the inter-resonator coupling location $k_{12} =$ k_{12opt}. As shown, power is distributed equally from the AHH arm band coil to each of the 8 receive systems. A peak and optimal PTE of 6.65% is achieved at the designed resonant frequency of 8 MHz. It is important to note this optimal PTE can only be achieved given the condition of 8 equivalent receive resonators coupled equivalently to the AHH arm band coil. For other coupling scenarios, K_{S1opt} and K_{2Lopt} must be updated

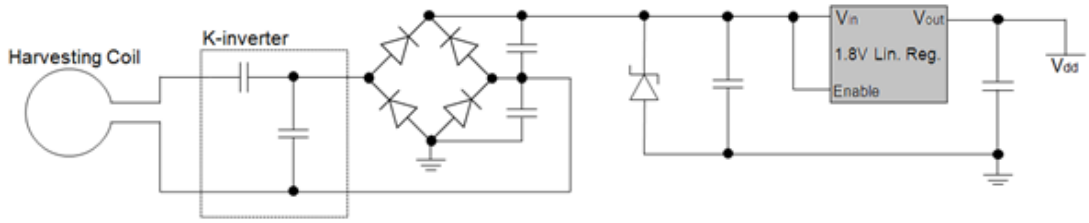

Figure 3.10 Individual receive resonator and power management system.

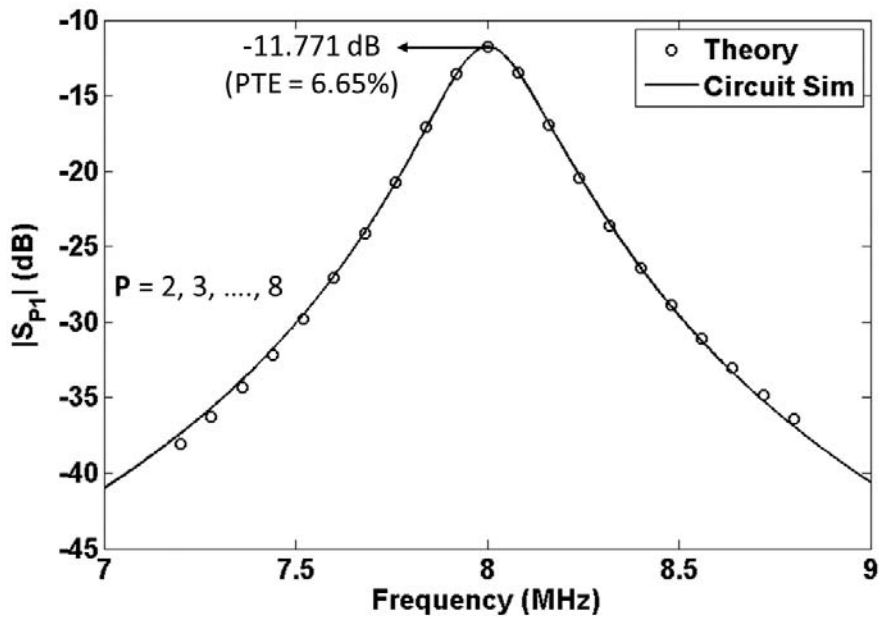

Figure 3.11 Predicted (theory) and circuit simulated PTE response between each receive system and the AHH arm band coil coupled to 8 receive systems. At $k_{12} = k_{12opt}$, equal power distribution and optimal PTE is achieved.

accordingly (configured by the capacitive network) to achieve optimal PTE. For example, if only 1 receive resonator is coupled to the system originally optimized for 8 receive resonators, the achievable PTE is 13.72%. However, if K_{S1opt} and K_{2Lopt} are updated for a single receive system, the achievable PTE increases to 19.63%. Indeed, configuring the K-inverter network to exhibit K_{S1opt} and K_{2Lopt} correctly for a given condition maximizes the achievable PTE.

3.3 Human sEMG Acquisition

The optimized WPT system was utilized to demonstrate simultaneous powering of 8 sEMG recording devices connected to an able-bodied subject. System demonstration was conducted at Northwestern University at the Rehabilitation Institute of Chicago. All experiments involving human subjects were approved by the Northwestern University Institutional Review Board.

Figure 3.12 shows the experimental set-up. Eight, fully wireless (power and telemetry) sEMG recording devices were mounted on a forearm cuff [Figure 3.1(f)] which was secured around the subject's forearm—approximately one-third the length of the forearm from the elbow—with the eight devices equally spaced circumferentially. An elastic bandage was wrapped around the cuff and forearm to protect the microelectronics. The arm band coil was slipped over the top of the cuff such that the separation between the AHH Tx coil and each Rx coil was 1-2cm (depending on the diameter of the subject's forearm).

A pattern recognition system was used to correlate the streaming sEMG from the wirelessly powered device array to the intended motion of the user. During wireless powering, the user was able to train the system by providing four repetitions of training contractions, which were comprised of three-second contractions for each of the following seven motion classes: no motion, pronation, supination, wrist flexion, wrist extension, hand open, and hand close. A set of time domain features (the Hudgins set, which includes: mean absolute value, waveform length, number of slope sign changes, and number of zero crossings [85] and sixth order autoregressive features were calculated

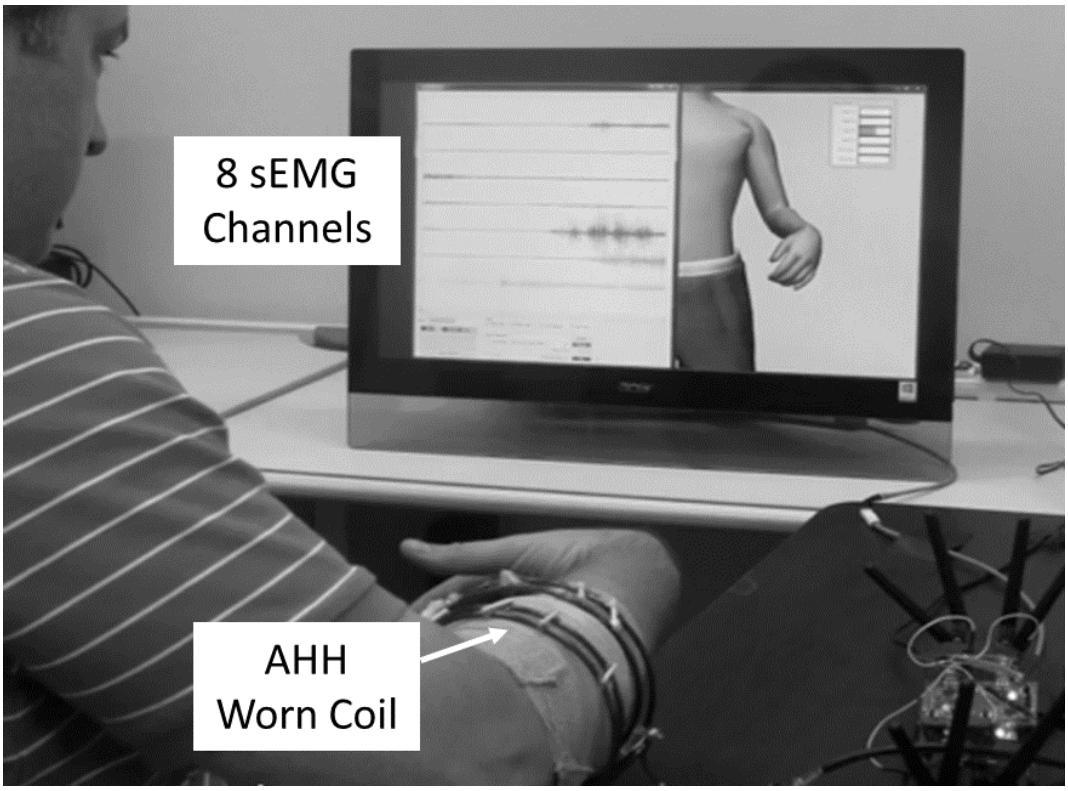

Figure 3.12 Demonstration of the novel MRC arrangement integrated around the arm of an able-bodied subject. Eight devices, wrapped circumferentially around the arm, were simultaneously wirelessly powered enabling the control of a virtual arm.

for each channel from 250 ms sliding windows with a 50 ms frame increment. An LDA classifier was trained using features extracted from the training contractions. The user then employed this classifier and the 8 simultaneously wireless powered devices to move a virtual reality prosthetic arm.

The fully wireless and custom designed sEMG device operates with an average power consumption of 2.9 mW. Simultaneous operation of the 8 devices required a minimum of 800 mW of transmit power to the AHH coil. The bridge rectifier exhibits a rectifier conversion efficiency (RCE) of approximately 50%, where RCE is defined as

$$RCE = \frac{P_{in,AC}}{P_{out,DC}} \tag{3.5}$$

Table 3.2 Implemented K-inverter Capacitance Values and Power Budget

$k_{1,i,opt} = 0.01$	$\boldsymbol{K_{S1opt} = 4.84\ \Omega}$		$\boldsymbol{K_{2Lopt} = 5.09\ \Omega}$	
	C_{p1} (pF)	C_{t1} (pF)	C_{p2} (pF)	C_{t2} (pF)
	4082.6 pF	275.43 pF	3899.83 pF	1631.72 pF
Peak PTE/Device (Theory for 8 Devices)			**6.65 %**	
RCE (Measured)			50 %	
Avg. Device Power Consumption			2.9 mW	
Minimum Tx Power (8 simultaneous device operation)			800 mW	
Peak PTE/Device (Achieved to 8 devices) †			**6.0%**	

† Achieved PTE/Device = $\frac{2.9\ mW*8}{0.5*800\ mW} \times 100$

where $P_{in,AC}$ is the AC power at the input of the rectifier and $P_{out,DC}$ is the DC power at the rectifier output. Table 3.2 summarizes the implemented K-inverter capacitance values and power budget values. Using the RCE, minimum transmit power, and average device power consumption, the PTE achieved to each device was approximately 6%, matching closely with the optimally predicted value of 6.65% determined in Section 3.2.3.

3.4 Safety Considerations

Regulatory agencies such as the Federal Communications Committee (FCC) [86, 87], Institute of Electrical and Electronic Engineers (IEEE) [88], and the International Commission on Non-Ionizing Radiation Protection (ICNIRP) [89] have provided established guidelines for the allowable levels of electromagnetic field (EMF) exposure to biological tissue. From extensive analysis and experimental studies, these agencies have concluded that, in general, human exposure to radiofrequency (RF) electromagnetic (EM)

Table 3.3 RF Exposure Limits by ICNIRP and FCC (100 kHz – 10 MHz)

Agency	**SAR [W/kg] (Whole Body Avg.)**	**SAR [W/kg] (Head/Trunk)**	**SAR [W/kg] (Limbs)**
FCC	0.08	2 (10-g)	4 (10-g)
ICNIRP (2010)	0.08	1.6 (1-g)	4 (10-g)

fields at sub millimeter wave frequencies are non-ionizing and thus do not induce the formation of cancer [89]. However, tissue heating is an established concern, as exposure to EM fields can cause local increases in body temperature. Consequently, regulatory agencies limit the amount of EM energy absorbed by the body that is converted into heat. The most utilized parameter for quantifying EM absorption is specific absorption rate (SAR). Table 3.3 summarizes the RF exposure limits for the general population in the frequency range of 100 kHz to 10 MHz. In this work, EM simulations (HFSS) were utilized to assess the compliance of the developed AHH arm band coil MRC power arrangement to the restrictions summarized in Table 3.3.

Figure 3.13 shows the simulated average SAR distribution (averaged over 1 g) in an HFSS arm model. The arm model is built from ANSYS HFSS human body model and consists of human fat, skin, muscle, blood, neural tissue, and bone. At 8 MHz and an input power of 1 W, the peak value of whole body average SAR is simulated to be 0.0005 W/kg. When averaged over 10 g of tissue, the peak average SAR is 0.3 W/kg. Indeed, these values are well below the limits imposed by the FCC and ICNIRP. Recall that 800 mW of Tx power was necessary to wirelessly power 8 devices simultaneously. Thus, it can be

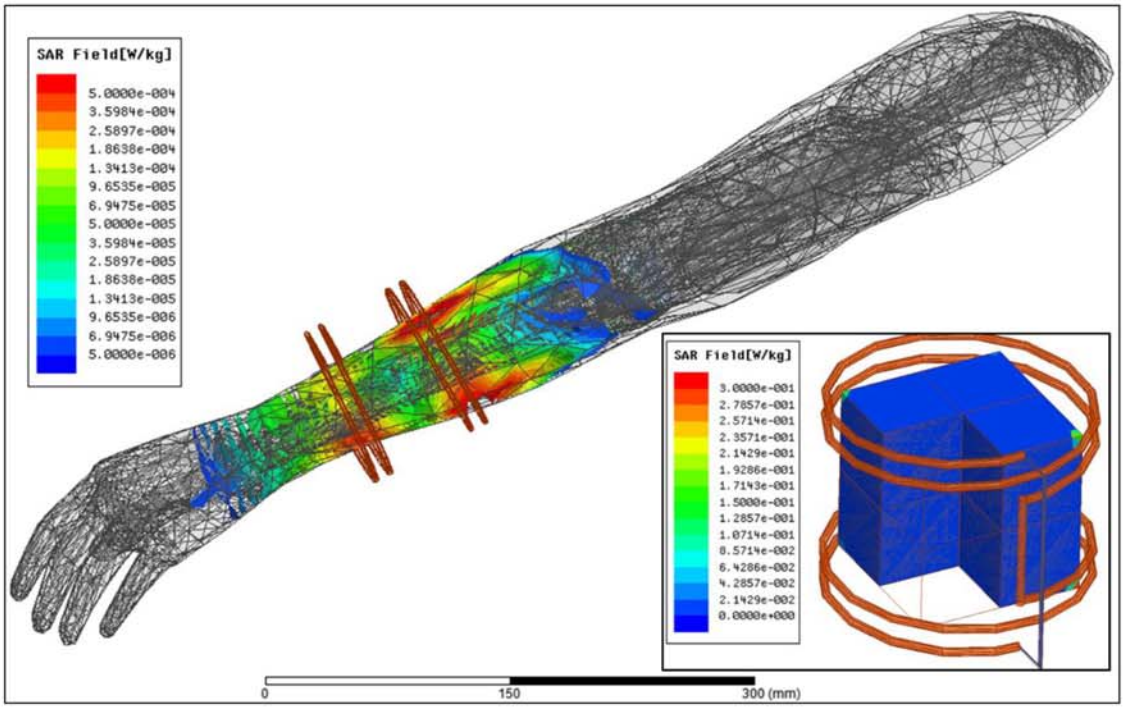

Figure 3.13 HFSS simulated SAR distribution for the forearm with AHH armband coil excited with 1 W power and 8 MHz operation. A peak value of 0.0005 W/kg whole body average. Inset shows peak SAR of 0.3 W/kg averaged over 10 g of tissue.

concluded that the MRC powering arrangement and optimization method are likely operating under the guidelines for safe of EM tissue exposure.

3.5 Conclusion

A novel MRC powering arrangement and optimization method was designed for simultaneously powering 8 sEMG sensing devices placed circumferentially around a subject's forearm. The MRC powering arrangement consisted of a novel AHH arm band coil and the optimization method resulted in equivalent power distribution with optimal PTE. The WPT system was demonstrated at the Rehabilitation Institute of Chicago and 8 sEMG sensing devices were wirelessly powered enabling the control of a virtual arm

system. The PTE achieved to each of the receive devices was measured to be 6.0%, a 0.65% decrease in the predicted and optimal value. Exploration on safety considerations were considered. Based on EM simulation, the MRC arrangement and optimization methodology resulted in average SAR levels well below the FCC and ICNIRP SAR safety guidelines.

CHAPTER 4. CAVITY RESONATOR BASED WIRELESS POWER TRANSFER SYSTEM

The data and work in this chapter is accepted for publication in the IEEE Antennas and Wireless Propagation Letters. The porcine eye data is accepted in 2015 BMES Conference (Tampa, FL) abstract. The citations can be found in the Publication section. This chapter is primarily a reproduction of the IEEE publication and BMES abstract. Both have been reformatted for this dissertation. This work was performed in collaboration with Kyle Thackston and Yu-Wen Huang at the Center for Implantable Devices, Purdue University.

4.1 Introduction

The unique near-field MRC WPT optimization procedures, analytical derivations, and PTE behaviors described in Chapters 2 and 3 descended from traditional analysis and optimization methods developed for microwave BPF systems of coupled resonators. Traditionally, microwave BPF structures operate in low GHz [71] to millimeter wave frequency ranges [90]. Consequently, these structures can be synthesized using distributed elements such as dielectric and air-filled coupled cavity resonators and various microstrip line configurations (hairpin, ring structures, pseudointerdigital microstrip lines, hairpin lines, etc.) [61, 62]. In these systems, magnetic and/or electric coupling are utilized to excite and configure the filter to achieve a specific response. Most importantly, however, is that these EM energy housing structures are electrical

resonators which, within some bandwidth of operation or design point, can be modeled simply as coupled RLC systems. It is natural then to pose the question: how can the coil to coil based coupled resonator based WPT system, developed in chapter 2, be physically represented in another form that may also prove useful for WPT applications? Here, it is shown that a large air-filled metallic cavity resonator, resonantly coupled through magnetic fields at mid-MHz frequencies (300-400 MHz) to a receive coil resonator system within, forms a unique and highly advantageous MRC structure which enables WPT within a large 3-D volumetric region. Additionally, an optimization methodology, analogous to the method described in Chapter 2, is developed to achieve high efficiency WPT to receive coils, as small as 2mm in diameter, located within a large cavity resonator volume. A potential bioelectronics application is WPT to miniatures devices implanted in small animals which can roam freely within the large open cavity resonator environment (Chapter 5). The novel contributions of this work are:

1. The development of a new cavity resonator based WPT system
2. The development of a corresponding WPT model and optimization method
3. Demonstration of high efficiency WPT to 2 mm diameter receive coils and in-vivo demonstration of powering within a Porcine Eye

4.2 General Overview of Cavity Resonator Structures

Simply stated, a cavity resonator is any air or dielectric filled closed conductor, that when excited properly, can give rise to modes of uniform electromagnetic (EM) standing waves reflecting back and forth between the cavity walls. Conceptually, this is not dissimilar to standing waves of acoustic pressure formed in musical instruments such as

the strings of a guitar, the pipe of a wind instrument, or the chamber of a drum. In this work, it is not acoustic, but EM standing waves oriented in specific modes conforming to EM boundary conditions, that are formed in a hollow conductor. By forming a carefully designed coupled resonator system, the resonant magnetic energy formed in the cavity can be efficiently transferred to a small receiver resonator within the cavity. It is important to note that the electric fields formed in the cavity can also be resonantly coupled (capacitive coupling) to a correctly designed receive resonator within. However, biological tissue is well known to have high relative electric permittivity's, high loss tangents, and non-zero conductivity that would make electric coupling an impractical form of WPT to devices implanted in biological tissue [91-93].

Figure 4.1 illustrates commonly shaped rectangular and cylindrical cavity resonator systems, along with the dominant mode (lowest resonant frequency) EM field distributions for each. Assuming z-directed propagation, the dominant mode transverse magnetic (TM) field distribution for the rectangular and cylindrical cavity are the TM_{110} and TM_{010} modes, respectively. As illustrated, a high spatial uniformity in the magnetic fields exist within the entire volume of the rectangular and cylindrical cavity. In the dominant TM mode for both cavities, the $\vec{H}$-field is rotational about the center of the cavity, increases in magnitude radially, and is not a function of height. Expressions for the field distributions of rectangular and cylindrical cavities are well defined and can be found in EM textbooks [41, 61, 94]. Additionally, as shown in Figure 4.1, areas of low $\vec{H}$-field magnitude exist at the center for each cavity and 4 corners for the rectangular cavity. These represent MRC WPT "blindspots" within the system and can be avoided by properly placed barriers within the cavity. However, higher order modes at higher

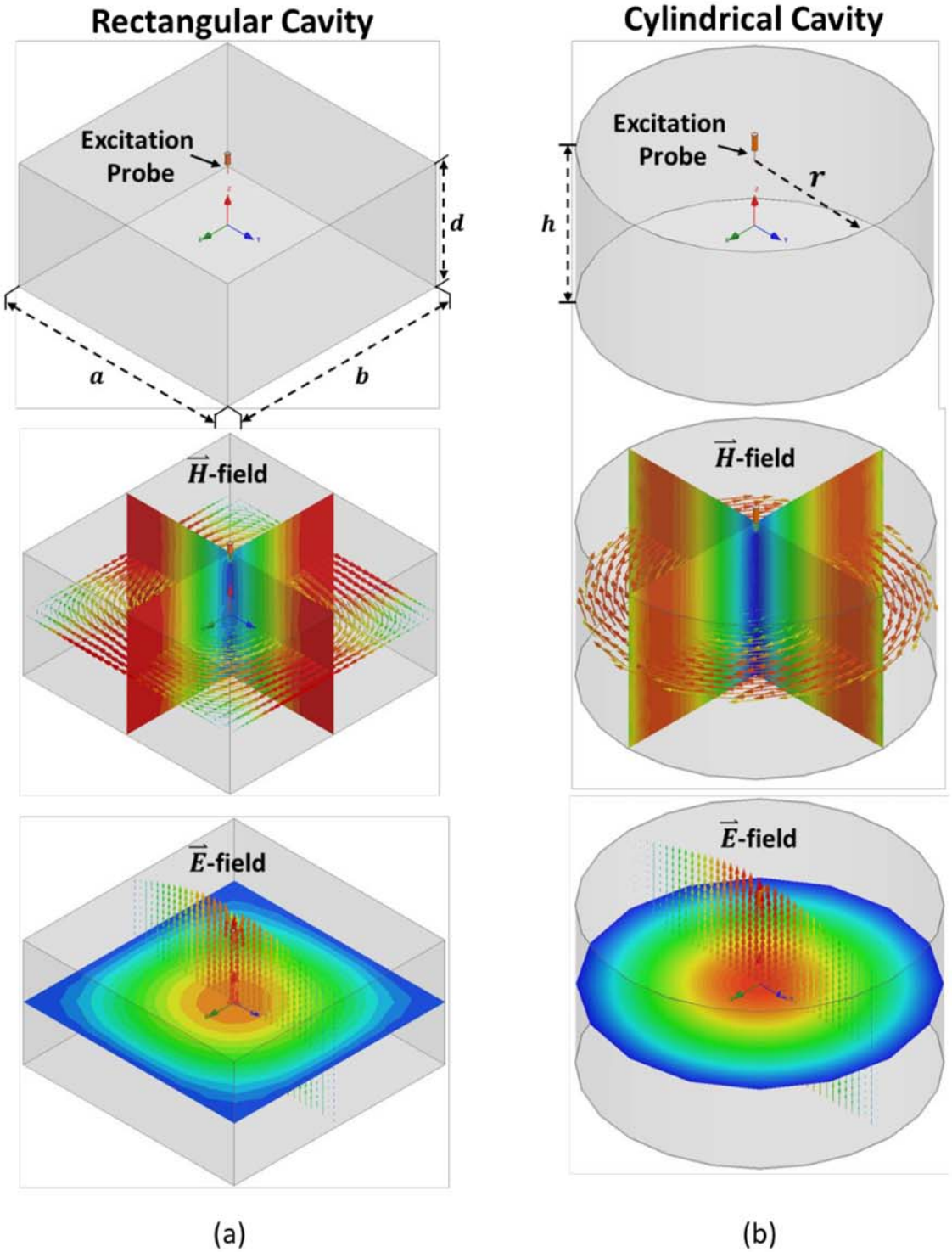

Figure 4.1 Illustration of commonly shaped EM cavity resonators. (a) Rectangular cavity resonator and associated dominant mode (TM_{110}) EM field distribution and (b) cylindrical cavity resonator and associated dominant mode (TM_{010}) EM field distribution.

resonant frequencies will exhibit increased number of these standing wave node locations. Thus, the dominant TM mode field of a cylindrical or rectangular cavity is ideal for WPT. Importantly, a receive resonator within must be oriented perpendicular to the circularly directed $\vec{H}$-fields to achieve proper coupling and WPT.

The resonant frequency of the TM_{110} mode for a rectangular cavity resonator is given by [61]

$$f_{110} = \frac{c}{2\pi\sqrt{\mu_r \varepsilon_r}} \sqrt{\left(\frac{\pi}{a}\right)^2 + \left(\frac{\pi}{b}\right)^2} \tag{4.1}$$

where c is the speed of light, μ_r and ε_r are the relative magnetic permeability and relative electric permittivity of material within cavity, respectively, and a and b are the cavity dimensions as shown in Figure 4.1(a). The resonant frequency of the TM_{010} mode for a cylindrical cavity resonator is given by [61]

$$f_{010} = \frac{c}{2\pi\sqrt{\mu_r \varepsilon_r}} \frac{P_{01}}{r} \tag{4.2}$$

where r is the radius of the cylinder and P_{01} is 2.405 (for the TM_{010} mode of a cylindrical cavity resonator, this P_{01} value represents the location of the first zero for the Bessel function of order zero i.e. $J_0(2.405)$). From (4.1) and (4.2), it is clear that the resonant frequency of an air-filled cavity resonator is dictated by the dimensions of the resonator. In fact, cavities resonators must be constructed with dimensions that are an integer multiple of a half-guide wavelength at the resonant frequency. Therefore, the operating frequency for a cavity resonator MRC WPT system is largely dictated by its physical dimensions.

In order to excite cavity resonators, external circuitry must be coupled to the cavity resonator. Depending on the cavity resonator structure and desired excitation mode transmission lines, waveguides, evanescent wave coupling, and probes can be used to externally couple to excite the cavity resonator. In this work, an easily configurable excitation probe was utilized to externally couple and excite rectangular and cylindrical cavity resonators. A depiction of the excitation probe is shown in Figure 4.1

As determined in Chapter 2, the fundamental parameters for resonant coupling and PTE optimization in the BPF modeled MRC system are: the unloaded resonator quality factors, resonant frequency, inter-resonator coupling, and optimal characteristic impedances/admittances of the immitance (impedance or admittance) inverter network. To determine these relationships for a cavity resonator MRC WPT system, a unique cavity resonator coupled BPF model, coupling matrix synthesis and analysis, and optimization method are developed.

4.3 Cavity Resonator MRC WPT BPF Model

Figure 4.2 illustrates the conceptual idea for the cavity resonator WPT system. An external signal generator feeds the excitation probe to excite a cylindrical (or rectangular) cavity in the TM_{010} mode at f_{010}. As will be shown, the external coupling between the probe and cavity is tuned by the length of the excitation probe. The generated magnetic fields within the cavity [shown in Figure 4.1(b)] are resonantly coupled to a receive (Rx) resonator within. The receive resonator is formed by a coil and shunt capacitor. In order

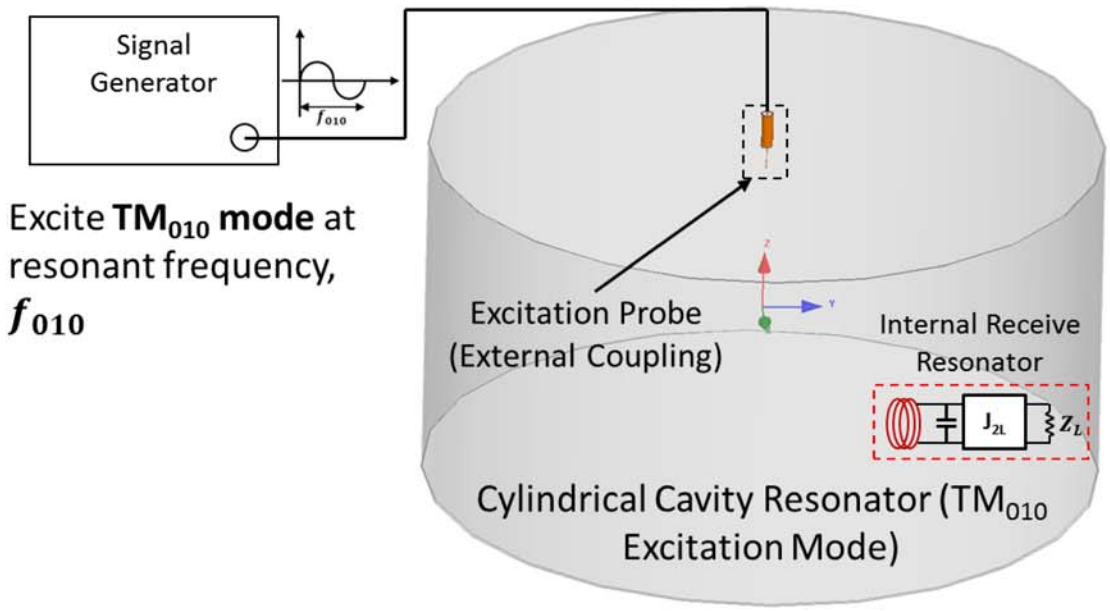

Figure 4.2 Illustration of a cavity resonator MRC WPT system concept. An excitation probe is fed by an external signal generator to excite the cavity at f_{010}. The induced fields are resonantly coupled to an internal receive resonator within. The internal receive resonator is formed by a coil and shunt capacitor. External coupling from the receive resonator to load is configured by an admittance inverter.

to maximize coupling, the coil should be oriented perpendicular to the circulating $\vec{H}$-fields. The Rx resonator is externally coupled to the load through an admittance inverter (the admittance analogue of an impedance inverter).

The circuit representation of Figure 4.2 and its transformation into an equivalent BPF circuit are shown in Figure 4.3. In Figure 4.3(a), an RF signal source, exhibiting a source impedance is connected to a shunt capacitor which is used to model the excitation probe. The coupling between the probe and cavity is electrical and represents the external coupling between the source to the cavity resonator. The cavity resonator (cylindrical or rectangular) excited the in its dominant TM mode can be modeled as a parallel RLC circuit. The magnetic fields generated within the cavity are coupled to the receive

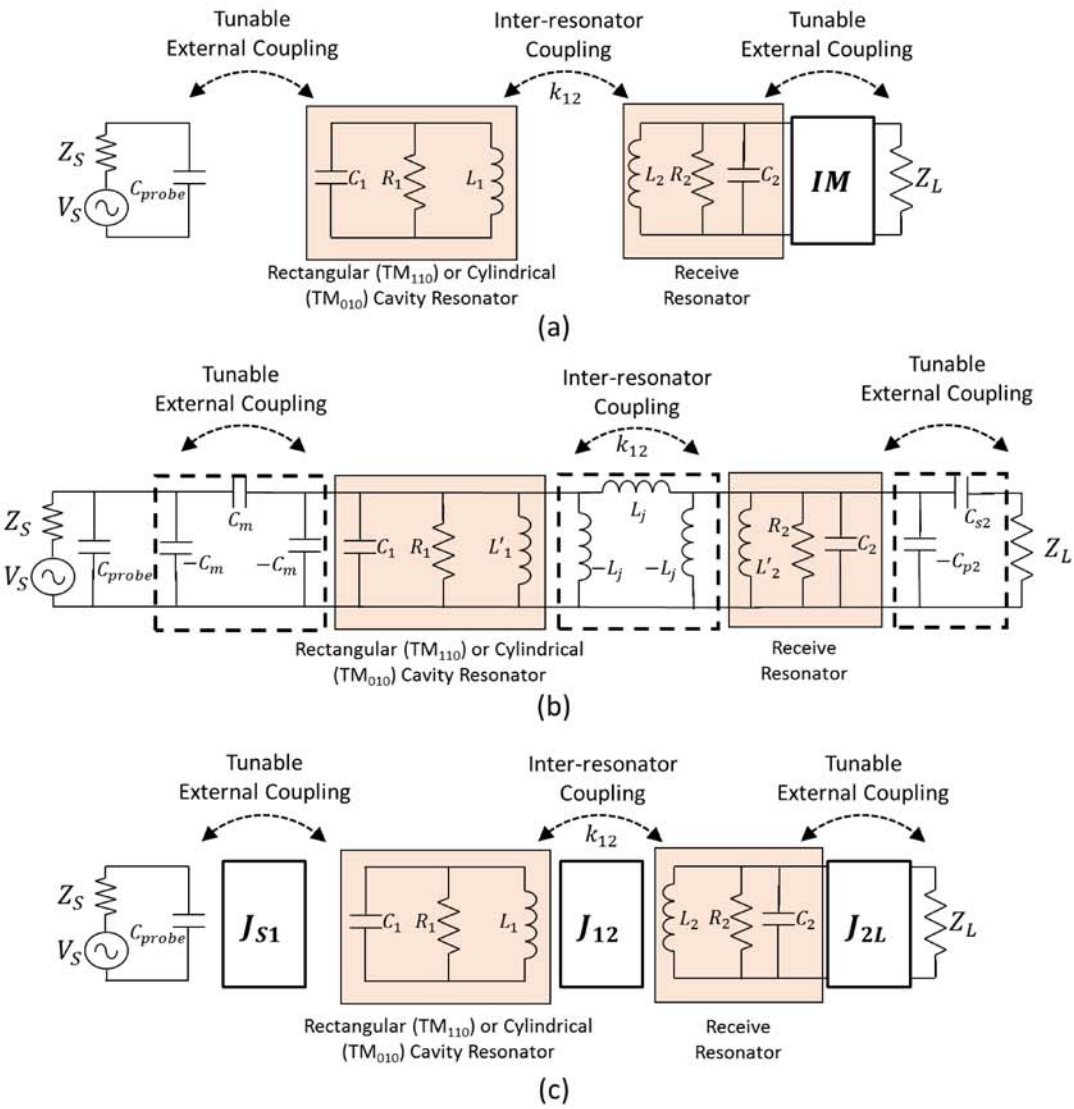

Figure 4.3 Circuit representation and BPF model transformation of the cavity resonator MRC WPT system. (a) standard circuit model, (b) standard circuit model with equivalent external and inter-resonator coupling networks, and (c) BPF model form.

resonator. This represents inter-resonator coupling, k_{12}. The receive system consists of a parallel RLC resonator and external coupling impedance matching (IM) circuitry which connects to a load.

Figure 4.3(b) shows the circuit model with equivalent lumped element network configurations for the external and inter-resonator couplings. The external coupling between the probe and cavity is electrical in nature and thus can be modeled by the simplified pi-network configuration of capacitors, C_m, which represents the mutual capacitance between the probe and cavity [62, 95]. The mutual capacitance is tunable by controlling the length of the excitation probe, l_{probe}. The inter-resonator coupling, which is magnetic in nature, can be replaced by its equivalent pi network with inductance of L_j and transformations of $L_1$and L_2 into L_1' and L_2', respectively. These relationships are

$$L_j = \frac{(1-k_{12}^2)\sqrt{L_1 L_2}}{k_{12}} \tag{4.3}$$

$$L_n' = L_n(1-k_{12}^2) \text{ for } n = 1,2 \tag{4.4}$$

$$k_{12} = \frac{L_m}{\sqrt{L_1 L_2}} \tag{4.5}$$

where L_m is the mutual inductance. These pi network configurations of mutual capacitive and mutually inductive couplings can be equivalently modeled as admittance inverters (J-inverters) exhibiting characteristic admittances J_{S1} and J_{12}, respectively, which are given by [62]

$$J_{S1} = \omega_0 C_m = 2\pi f_0 C_m \tag{4.6}$$

$$J_{12} = \frac{1}{\omega_0 L_j} = \frac{k_{12}}{(1-k_{12}^2)\omega_0\sqrt{L_1 L_2}} \approx k_{12}\omega_0\sqrt{C_1 C_2} \tag{4.7}$$

In (4.7), k_{12} represents the magnetic inter-resonator coupling coefficient and is << 1. Thus the $1-k_{12}^2$ term is approximately 1. The external coupling between the receive

resonator and load impedance is also formed as a J-inverter network, with characteristic admittance J_{2L}. The network is formed by a half pi network with a negative shunt capacitance $-C_{p2}$ and series capacitor C_{s2}. Figure 4.3(c) shows the cavity resonator WPT system circuit with J-inverter representations of the external and inter-resonator couplings. This circuit is a BPF made of coupled parallel RLC resonators. It is important to note that the resistance terms in each RLC resonator are placed into the model to account for finite unloaded resonator quality factors, Q_{0i}, where i represents the ith resonator. This cavity resonator WPT BPF model can also be modified to achieve the same complex port impedance accommodation capability developed in Chapter 2. For the cavity resonator WPT system, a parallel frequency invariant susceptance (FIS) element, B_{FISi}, is added into the parallel RLC resonators. The condition for neutralizing complex impedance is given by

$$B_{FISi} = -Im(Y_i) = \frac{J_{iP}^2 B_p}{\left|Y_p\right|^2} \tag{4.8}$$

where Y_i is the input admittance seen by the respective resonator , J_{iP} is the characteristic impedances of the respective external coupling J-inverter, B_p is the port impedance susceptance, and Y_p is the port admittance given by

$$Y_p = \frac{1}{Z_P} = \frac{R_P}{R_P^2 + X_P^2} + j\frac{-X_P}{R_P^2 + X_P^2} = G_P + jB_p \tag{4.9}$$

where R_P and X_P are the port resistance and reactance respectively, and G_P is the port conductance. Note that subscript $P = S$ or L denote source or load impedance ports. Figure 4.4 shows the generalized form of the BPF modeled cavity resonator WPT system.

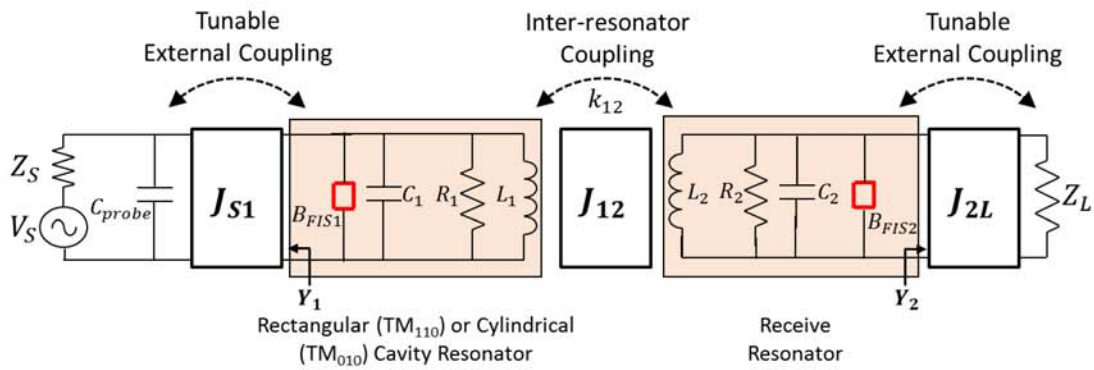

Figure 4.4 Generalized cavity resonator BPF model, with complex port admittance (impedance) accommodation, for a rectangular or cylindrical cavity resonator (excited in the dominant TM mode) WPT system.

4.4 Synthesis of Cavity Resonator WPT System Coupling Matrix

Figure 4.5 shows the equivalent source and load included admittance matrix, $[Y]$, for the 2 resonator (n = 2) generalized BPF model of the cavity resonator WPT system. Resonator and impedance scaling factors, $\sqrt{\omega_0 C_i}^{-1}$ and $\sqrt{G_s}^{-1}$, respectively, are used to generalize $[Y]$ such that the resultant matrix is normalized in terms of couplings and port impedances. The resultant matrix is the normalized admittance matrix, $[\tilde{Y}]$, provided in Figure 4.6. The Q_{0i} for a parallel resonator is given by

$$Q_{0i} = \omega_0 R_i C_i = \frac{R}{\omega_0 L_i} \tag{4.10}$$

Through algebraic manipulation, $[\tilde{Y}]$ is separated into constitutive matricies into the form

$$[\tilde{Y}] = j[m] + j\Omega[R] + [P] \tag{4.11}$$

$$
\begin{array}{c}
\\ \times(\sqrt{G_S})^{-1} \rightarrow \boldsymbol{S} \\ \times(\sqrt{\omega_0 C_1})^{-1} \rightarrow \boldsymbol{1} \\ \times(\sqrt{\omega_0 C_2})^{-1} \rightarrow \boldsymbol{2} \\ \times(\sqrt{G_L})^{-1} \rightarrow \boldsymbol{L}
\end{array}
\begin{array}{c}
\begin{array}{cccc}
\times(\sqrt{G_S})^{-1} & \times(\sqrt{\omega_0 C_1})^{-1} & \times(\sqrt{\omega_0 C_2})^{-1} & \times(\sqrt{G_L})^{-1} \\
\downarrow & \downarrow & \downarrow & \downarrow \\
\boldsymbol{S} & \boldsymbol{1} & \boldsymbol{2} & \boldsymbol{L}
\end{array} \\
\begin{bmatrix}
G_s + jB_s & jJ_{S1} & 0 & 0 \\
jJ_{S1} & G_1 + jB_{FIR1} + {}^{1}/_{j\omega L_1} + j\omega C_1 & jJ_{12} & 0 \\
0 & jJ_{12} & G_2 + jB_{FIR2} + {}^{1}/_{j\omega L_2} + j\omega C_2 & jJ_{2L} \\
0 & 0 & jJ_{2L} & G_L + jB_L
\end{bmatrix}
\end{array}
$$

Figure 4.5 Representative $[Y]$ for the BPF modeled cavity resonator WPT system. Resonator and impedance scaling factors are shown.

$$
[\tilde{Y}] = \begin{bmatrix}
1 + j\dfrac{B_s}{G_s} & j\dfrac{J_{S1}}{\omega_0 G_s C_1} & 0 & 0 \\
j\dfrac{J_{S1}}{\omega_0 G_s C_1} & \dfrac{1}{Q_{01}} + j\dfrac{B_{FIS1}}{\omega_0 C_1} + j\left[\dfrac{\omega}{\omega_0} - \dfrac{\omega_0}{\omega}\right] & jk_{12} & 0 \\
0 & jk_{12} & \dfrac{1}{Q_{01}} + j\dfrac{B_{FIS2}}{\omega_0 C_2} + j\left[\dfrac{\omega}{\omega_0} - \dfrac{\omega_0}{\omega}\right] & j\dfrac{J_{2L}}{\omega_0 G_L C_2} \\
0 & 0 & j\dfrac{J_{2L}}{\omega_0 G_L C_2} & 1 + j\dfrac{B_L}{G_L}
\end{bmatrix}
$$

Figure 4.6 Normalized admittance matrix

Notice that (4.11) is in the exact same form as (2.10), developed previously in Chapter 2. Instead of impedances, matrices $[m]$, $[R]$, and $[P]$, are the source and load admittance included coupling matrix, identity matrix denoting the existence of a resonator network, and normalized port admittance matrix, respectively. In similar form to Chapter 2, these matrices are expressed as

$$
[m] = \begin{bmatrix}
M_{SS} & M_{S1} & 0 & 0 \\
M_{S1} & M_{11} & M_{12} & 0 \\
0 & M_{12} & M_{22} & M_{2L} \\
0 & 0 & M_{2L} & M_{LL}
\end{bmatrix} \tag{4.12}
$$

and

$$[R] = \begin{bmatrix} 0 & 0 & 0 & 0 \\ 0 & 1 & 0 & 0 \\ 0 & 0 & 1 & 0 \\ 0 & 0 & 0 & 0 \end{bmatrix}, [P] = \begin{bmatrix} 1 & 0 & 0 & 0 \\ 0 & 0 & 0 & 0 \\ 0 & 0 & 0 & 0 \\ 0 & 0 & 0 & 1 \end{bmatrix} \quad (4.13), (4.14)$$

In (4.12), M_{SS} and M_{LL}, generalized as M_{PP}, represents the normalized port admittances expressed as expressed as

$$M_{PP} = \frac{B_P}{G_P} \quad (4.15)$$

Coefficient M_{12} is the magnetic inter-resonator coupling coefficient given in (4.5). Coefficients M_{S1} and M_{2L}, generalized as M_{iP}, represents the normalized external coupling characteristic admittances and are given by

$$M_{iP} = \frac{J_{iP}}{\sqrt{\omega_0 G_P C_i}} \quad (4.16)$$

The main diagonal entries of self-coupling coefficients, M_{11} and M_{22}, generalized as M_{ii}, represents the normalized admittance of the resonator and are given by

$$M_{ii} = \frac{-j}{Q_{0i}} + \frac{B_{FISi}}{\omega_0 C_i} = \frac{-j}{Q_{0i}} + \frac{M_{iP}^2 G_P B_P}{|Y_P|^2} \quad (4.17)$$

where $\frac{B_{FISi}}{\omega_0 C_i}$ is rearranged into the form of $\frac{M_{iP}^2 G_P B_P}{|Y_P|^2}$ by substitution of (4.8) into (4.16). Indeed, the developed coupling matrix for the BPF modeled cavity resonator WPT system is simply the admittance analogue of the MRC system developed in Chapter 2.

4.5 Determination of System Transfer Response and Derivation of Optimal J_{iP}

The filter response, from source to load, for the generalized BPF modeled cavity resonator WPT system is determined from matrix $[\tilde{Y}]$ in terms of scattering parameters by [62]

$$S_{21} = 2[\tilde{Y}]^{-1}_{n+2,1} \tag{4.18}$$

$$S_{11} = 1 - 2[\tilde{Y}]^{-1}_{1,1} \tag{4.19}$$

$$S_{22} = 1 - 2[\tilde{Y}]^{-1}_{n+2,n+2} \tag{4.20}$$

Indeed, (4.18) – (4.20) are the admittance analogue to (2.19) – (2.21). By way of symmetry, the analytical expressions for the determination of J_{iPopt} are derived using the same process described in Chapter 2 (Section 2.4). These expressions are given by

$$J_{S1opt} = \left(1 + k^2_{12opt} Q_{01} Q_{02}\right)^{1/4} |Y_S| \sqrt{\frac{G_1}{G_S}} \tag{4.21}$$

$$J_{2Lopt} = \left(1 + k^2_{12opt} Q_{01} Q_{02}\right)^{1/4} |Y_L| \sqrt{\frac{G_2}{G_L}} \tag{4.22}$$

4.6 Symmetry of PTE Response and Behavior

As demonstrated in the previous sections, the admittance matrix, transfer response, and analytical formulation for J_{S1opt} and J_{2Lopt} are simply the admittance analogue of the impedance formulations derived in Chapter 2. Consequently, the PTE response and behavior of the BPF modeled cavity resonator WPT system is symmetric to that of the series resonator system developed in Chapter 2. As can be verified using the same

methodology developed in Section 2.5, critical coupling behavior and relationships for the cavity resonator WPT system are derived as

$$k_{12crit} = \frac{1}{\sqrt{Q_{01}Q_{02}}} + \sqrt{\frac{1}{Q_{01}Q_{02}} + k_{12opt}^2} \tag{4.23}$$

$$|S_{21}|_{crit} = 1 - \frac{1}{k_{12crit}\sqrt{Q_{01}Q_{02}}} = 1 - \frac{1}{1 + \sqrt{1 + k_{12opt}^2 Q_{01}Q_{02}}} \tag{4.24}$$

Indeed, (4.23) and (4.24) are equivalent to (2.25) and (2.26), respectively. Thus, it can be concluded, that the analytical expressions for predicting PTE behavior developed in Chapter 2, in admittance form, can also be applied to the BPF modeled cavity resonator WPT system. However, it is important to note, that although the analytical expressions for PTE are symmetric, the differences in physical WPT environment between the two systems will incur differences in WPT behavior. For the cavity resonator WPT system, things to consider include: presence of strong electric field within the cavity, high operating frequency (> 100 MHz), and magnetic field distribution.

4.7 Network Configuration for J_{iPopt} and B_{FISi}

Figure 4.7 shows the lumped element representation of external coupling J-inverters, J_{S1} and J_{2L}. The mutual capacitance, C_m, in Figure 4.7(a), can be determined from the rearranged form of (4.6) and is given as

$$C_m = \frac{J_{S1}}{\omega_0} \tag{4.25}$$

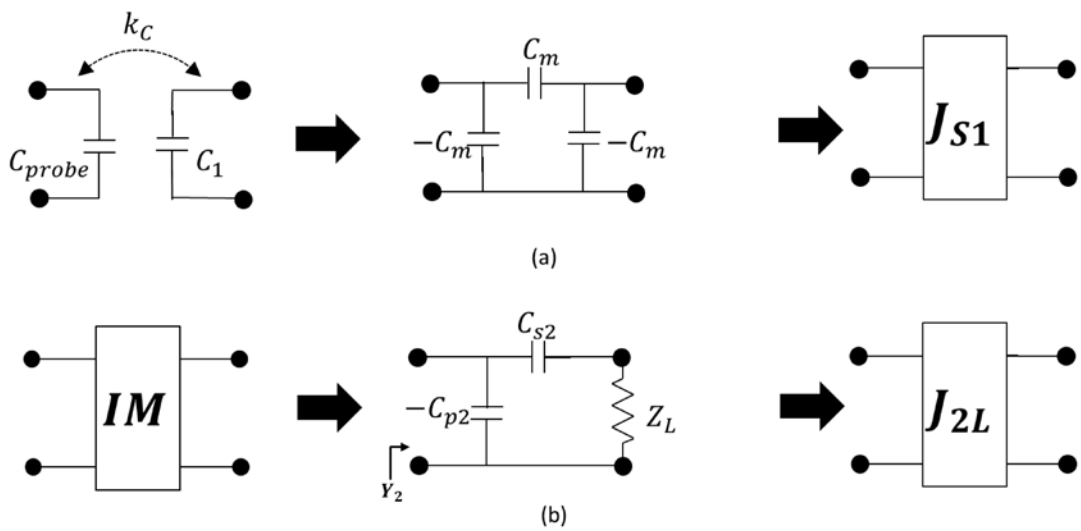

Figure 4.7 Lumped element representation of external coupling J-inverters. (a) Capacitive coupling between excitation probe and cavity resonator. (b) half-pi J-inverter network.

where the value of C_m, which represents external coupling tuning for the source, is configured by the length of the excitation probe. The half pi network formed of a shunt and series capacitor, which represents the external coupling tuning for the load, are shown in Figure 4.7(b). The input admittance, of the half pi network is given by

$$Y_2 = \frac{J_{2L}^2}{Y_L} = j\omega\left(-C_{p2}\right) + \left(\frac{1}{j\omega C_{s2}} + \frac{1}{Y_L}\right)^{-1} \tag{4.26}$$

where $Y_L = G_L + jB_L$. Capacitors, $-C_{p2}$ and C_{s2} can then be solved by setting the real and imaginary parts of the right-hand and left-hand side of the equation (4.26), respectively. Capacitors, $-C_{p2}$ and C_{s2} are derived as

$$C_{s2} = \frac{B_L J_{2L}^2 + J_{2L}\sqrt{B_L^4 + 2B_L^2 G_L^2 + G_L^4 - G_L^2 J_{2L}^2}}{\omega_o(B_L^2 + G_L^2 - J_{2L}^2)} \tag{4.27}$$

$$-C_{p2} = -\frac{C_{s2}B_L^4\omega_0 + C_{s2}G_L^4\omega_0 + 2C_{s2}B_L^2(G_L^2 + J_{2L}^2)\omega_0 + B_L^3(J_{2L}^2 + C_{s2}^2\omega_0^2) + B_L\left(C_{s2}^2J_{2L}^2\omega_0^2 + G_L^2(J_{2L}^2 + C_{s2}^2\omega_0^2)\right)}{(B_L^2 + G_L^2)\omega_0(B_L^2 + G_L^2 + 2C_{s2}B_L\omega_0 + C_{s2}^2\omega_0^2)} \quad (4.28)$$

The optimal mutual capacitance, C_m, is determined by substitution of (4.21) into (4.25). Optimal pi-network capacitance values C_{s2} and $-C_{p2}$ are determined by substitution of (4.22) into (4.27) and (4.28). To physically implement B_{FISi} in the parallel resonators, it is treated as a capacitive susceptance expressed by

$$C_{FISi} = \frac{B_{FISi}}{\omega_0} = \frac{J_{iP}^2 B_P}{|Y_P|^2} \quad (4.29)$$

The total parallel capacitance of the Rx resonator is thus the parallel combination of capacitors C_2, $-C_{p2}$, and C_{FIS2}. On the transmit side, the probe capacitance and source admittance act as a complex source admittance. Consequently, C_{FIS1} is non-zero. However, its typical value, as it will be shown, is much less than the capacitance of the cavity, C_1, and thus its effect on the transmit side is negligible. Figure 4.8 shows the simplified form of the generalized BPF modeled cavity resonator WPT system. Note that capacitor C_{pt} is the total parallel capacitance for the receive resonator system and is calculated by

$$C_{pt} = C_2 - C_{p2} + C_{FIS2} \quad (4.30)$$

where C_2 is determined from the resonant frequency, dictated by the cavity resonator, and the inductance of the receive coil. In the cavity resonator WPT system, PTE response optimization and control and complex load impedance is achieved by implementing an optimal excitation probe length and optimally calculated capacitors.

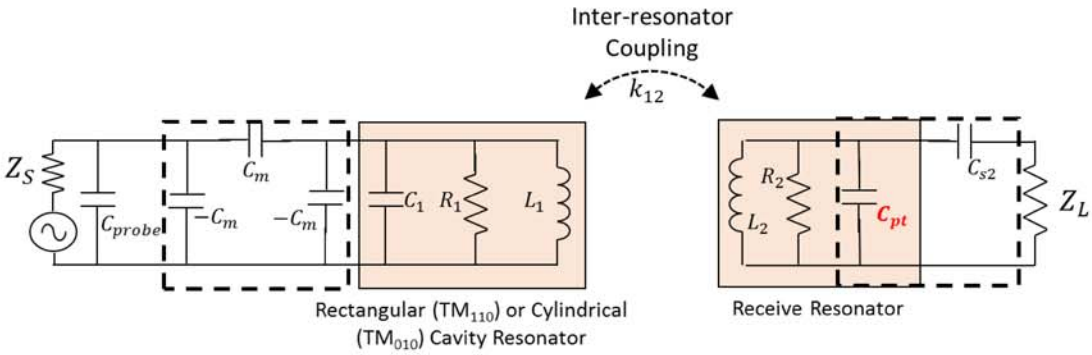

Figure 4.8 Simplified and generalized cavity resonator BPF model. Capacitor C_{FIS1} is small relative to C_1 and is thus removed from the transmit side. The parallel combination C_2, $-C_{p2}$, and C_{FIS2} forms a single parallel capacitor, C_{pt}, on the receive resonator system.

4.8 Experimental Validation

All S-parameter measurements were conducted using standard 50 Ω one-port and two-port vector network analyzer (VNA) (Agilent E5071B) measurements. Circuit simulations were based on Figure 4.8 and performed with Agilent Advanced Design System (ADS©).

4.8.1 Cavity and Receive Resonator Construction

Figure 4.9 shows the constructed cylindrical cavity and receive resonator system. The cylindrical cavity was constructed with a diameter of 60.96 cm (2 ft.) using two single sided copper clad FR4 boards (2 ft. base and cavity lid). Copper sheet foil was rolled and adhered to the entire cavity interior to form the conductive wall. An excitation probe with length, l_{probe}, was soldered to a centrally located SMA connector on the cavity lid. Copper tape (conductive adhesive) was used to electrically connect the interior

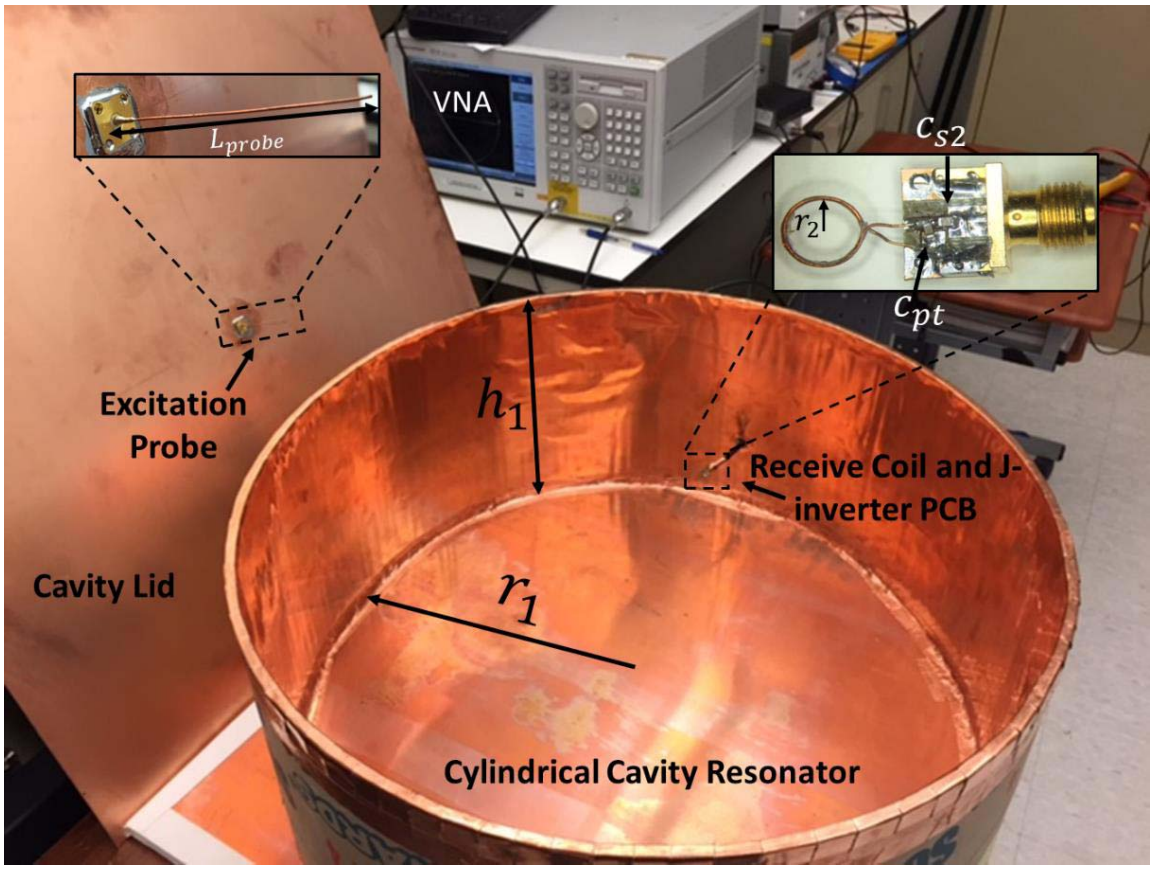

Figure 4.9 Image of the constructed cylindrical cavity and receive resonator WPT system. Physical dimensions: $r_1 = 30$ cm, $h_1 = 25.4$ cm, $L_{probe} = 5.76$ cm, $r_2 = 2.5$ mm, receive coil thickness = 0.70 mm. Cavity volume = 0.072 m^3; Receive coil volume = 13.75 mm^3.

to the copper base. The copper cavity was constructed with a height of 30 cm. An access hole (2 cm in diameter) was drilled at a height of 15 cm to allow placement of the receive resonator within. The receive resonator system was constructed of a receive coil (2 turn, 5 mm diameter, 30 AWG copper magnet wire) connected to the impedance matching (IM) tuning PCB. Recall that to achieve optimal coupling, the receive coil must be oriented perpendicular to the circularly directed $\vec{H}$-fields in the TM_{010} excitation mode. Using the cavity dimensions and (4.2), the predicted resonant frequency of the system, f_{010}, is

375.50 MHz. A summary of the cavity and receive resonator dimensions are given in Figure 4.8. For this cavity resonator WPT system, the 5 mm diameter coil occupies a volume that is $\approx 5.23 \times 10^6$ times smaller than the volume of the cylindrical cavity resonator.

4.8.2 Extraction of Resonator Parameters

The cavity resonator WPT model and transfer function analysis methods provides a useful methodology for WPT optimization. Namely the configuration of networks to exhibit calculated values of J_{S1opt} and J_{2Lopt} [see (4.21) and (4.22)]. However, these analytical expressions are expressed in terms of Q_{0i}, Y_S, Y_L and k_{12opt}. Note that Y_S is the combined admittance between the admittance of the source and shunt probe capacitance, C_{probe}. Section 4.8.2.1 and 4.8.2.2 describe the measurement techniques used to independently determine the parameters of the cavity and receive resonators. For the cavity resonator WPT system, the unloaded quality factors and inter-resonator couplings are not directly measurable. However, through standard RF and microwave engineering resonator measurement techniques utilizing VNA measurements and circuit simulation, algorithms and curve fitting can be employed.

4.8.2.1 Extraction of Cavity Resonator Parameters

The VNA is used to measure the S_{11} parameter of the cavity resonator independently. Since the cavity resonator is measured using a single excitation port, the measurement of Q_{01} is conducted through the one-port reflection measurement method [96]. Figure 4.10 shows the one-port VNA measurement set-up, equivalent circuit, and

S_{11} measurement results (L_{probe} = 57.6 cm). The equivalent circuit of the one-port reflection measurement set-up consists of the VNA source and 50 Ω source impedance. The measurement consists of a 1601-point frequency sweep centered at 375.0 MHz with a frequency span shown in Figure 4.10(c). The VNA port (port 1) is connected to a transmission line of length, l, directly to the excitation port (port 2) of the cavity resonator. It is important to note that the transmission line exhibits a characteristic impedance, Z_0, of 50 Ω. Thus, the impedance seen at port 2 toward the VNA is simply the 50 Ω VNA port impedance. The impedance of the excitation probe, which is a function of l_{probe}, is modeled with a shunt probe capacitance and a series resistance, R_s. This impedance represents the external coupling mechanism. Indeed, the cavity resonator system, at port 3, will see the external coupling circuit and VNA port impedance. The effect of this is twofold: first, the reactance (susceptance) of the external coupling probe will load the cavity resonator causing a small frequency shift of the natural TM_{010} resonant frequency. Second, the unloaded quality factor of the cavity resonator cannot be measured directly since it is loaded by the source impedance of the VNA and the impedance of the excitation probe. However, Q_{01} can be determined indirectly using the measured input reflection coefficient of the copper cavity resonator shown in Figure 4.10(c). The resonance or Q circle, shown in Figure 4.10(c), is characteristic of resonant circuits and its diameter and frequency characteristics can be utilized to determine Q_{01}. The center of the circle is rotated by an angle θ with respect to the real axis of the Smith chart. The cause of this rotation is due to the reactance of the excitation probe. This, however, bears no importance in the determination of Q_{01}. Indeed, the reactance due to the coupling probe simply acts as a complex source admittance. As determined in

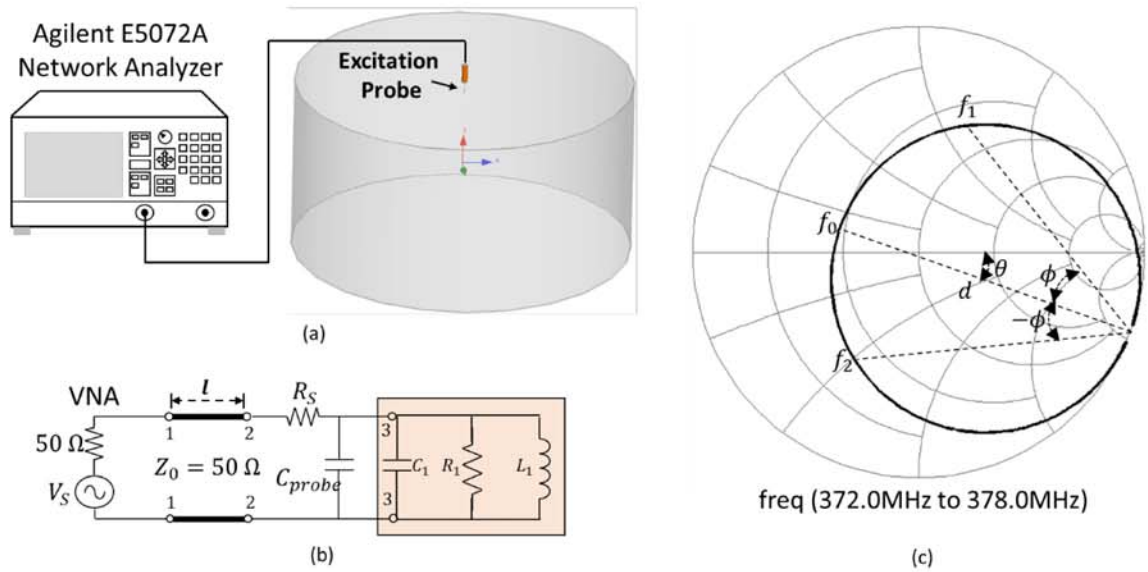

Figure 4.10 One port reflection cavity resonator measurement. (a) Illustration of one-port measurement set-up. (b) Equivalent circuit. (c) Measured S_{11} response of copper cylindrical cavity. The excitation probe length was set to 57.6 cm

Chapter 2 and analogously the work in this chapter, source and load impedances (admittances), when properly accommodated for, do not effect a desired optimal PTE response. From the resonant circle, two important quantities can be determined: the loaded Q, Q_L, and the external coupling coefficient, κ. The unloaded Q-factor of the cavity resonator, Q_0, can be obtained from the relationship

$$Q_0 = Q_L(1 + \kappa) \tag{4.31}$$

The value of Q_L can be determined by [96]

$$Q_L = \frac{f_0}{f_2 - f_1} \tag{4.32}$$

where f_0 is the center frequency and f_1 and f_2 are the frequency points inclined by $\pm\phi = 45^{\circ}$ on each side of the center diameter line of length d. The external coupling coefficient κ is calculated from the value of d by [97]

$$\kappa = \frac{d}{2-d} = \frac{Q_0}{Q_{ex}} \tag{4.33}$$

On the right hand side of (4.33), Q_{ex} is defined as the external quality factor given by

$$\frac{1}{Q_{ex}} = \frac{1}{Q_L} - \frac{1}{Q_0} \tag{4.34}$$

In this work, d is controlled and tuned by l_{probe}. As described in Section 4.7, an optimal value of l_{probe} is necessary to exhibit a calculated value of J_{S1opt} through C_m. Three external coupling conditions can be distinguished: when $\kappa = 1$, the resonator is critically coupled to the feedline, when $\kappa < 1$ the resonator is undercoupled to the feedline, and when $\kappa > 1$ the resonator is over-coupled to the feedline. It will be shown that the optimal calculated value of J_{S1opt} and C_m to achieve optimal PTE will require l_{probe} to be a length such that the cavity will exhibit $\kappa = 1$ when the receive resonator is located at the pre-determined inter-resonator coupling optimization point, k_{12opt}. Based on the measured S_{11} response of the constructed cavity resonator with $l_{probe} = 57.6$ cm, f_{010} was measured to be 375.32 MHz, d was measured to be 1.362, κ was measured to be 2.1361, and Q_L was measured to be 1974.0. Using (4.31), the Q_0 of the constructed copper cavity was 6193. Notice that the measured f_{010} of 325.32 MHz matches closely to the predicted frequency of 375.50 MHz.

4.8.2.1.1 Comment on Measured versus Theoretically Predicted Quality Factor

The unloaded quality factor for an air-filled cylindrical cavity resonator excited in the TM_{010} mode, where $h/r < 2$, is given by [98]

$$Q_{010}^{TM} = \frac{k\eta r h}{2R_{sCu}(r+h)} \tag{4.35}$$

where $k = \omega_0\sqrt{\mu_0\varepsilon_0}$, $\eta = \sqrt{\frac{\mu_0}{\varepsilon_0}} = 377\ \Omega$, and $R_{sCu} = 0.005\ \Omega$, the surface resistivity of copper at 375.5 MHz. Given the dimensions of the constructed cavity (Figure 4.8), the theoretically calculated cavity Q_{010}^{TM} is 44,964. This is approximately 7.2 times higher than the measured Q_0 of 6193. This discrepancy is due to the fact that the theoretical formulation shown in (4.35) does not account for the extraneous losses of the constructed cavity; mainly the imperfect electrical connections between the cavity lid (weight contact) and cavity base (copper tape and adhesive). These imperfect electrical connections may drastically increase system resistance thus significantly lowering actual cavity resonator quality factor. Other unaccounted losses associated with the constructed cavity may include large uneven surface roughness, radiation, imperfect solder connections (lid and excitation probe), and imperfect cavity shape. Small inaccuracies in the determination of these parameters will cause significant variation in the predicted resonator quality factor. Therefore, empirically measured cavity and receive resonator parameter values hold high merit and are relied upon for comparing the theoretically predicted PTE responses and measured results.

4.8.2.1.2 Determination of Cavity R, L, C

The cavity parameters determined from the one-port reflection measurement method include Q_{ex}, Q_L, Q_0 (Q_{010}^{TM}), κ, and f_{010}. From these parameters, the representative lumped element cavity resonator parameters, R, L, C (valid near the resonant frequency for the cavity operating in the TM_{010} excitation mode) can be determined. These are given by [97]

$$C_1 = \frac{Q_{ex}}{50\omega_{010}} \tag{4.36}$$

$$L_1 = \frac{1}{\omega_{010}^2 C_1} \tag{4.37}$$

$$R_1 = \frac{Q}{\omega_{010} C_1} \tag{4.38}$$

It is important to note that the values of cavity parameters R, L, C are lumped element circuit representation of the cavities measured response i.e. measured unloaded quality factor and TM_{010} resonant frequency.

4.8.2.1.3 Determination of C_m and C_{probe} Corresponding to l_{probe}

Recall that the optimal value of C_m is calculated from (4.25) where J_{S1} is substituted with J_{S1opt}, calculated from (4.21). The excitation probe length is varied (external coupling tuning) to physically configure the optimal value of C_m. The values of C_m and C_{probe}, corresponding to a particular l_{probe}, is determined by curve fitting circuit simulations of the model shown in Figure 4.11(a) to the measured S_{11} parameters, where Q_{01}, f_{010}, R_1, C_1, L_1 are known and Z_s=50 Ohms. Figure 4.11(b) presents the curve fitted

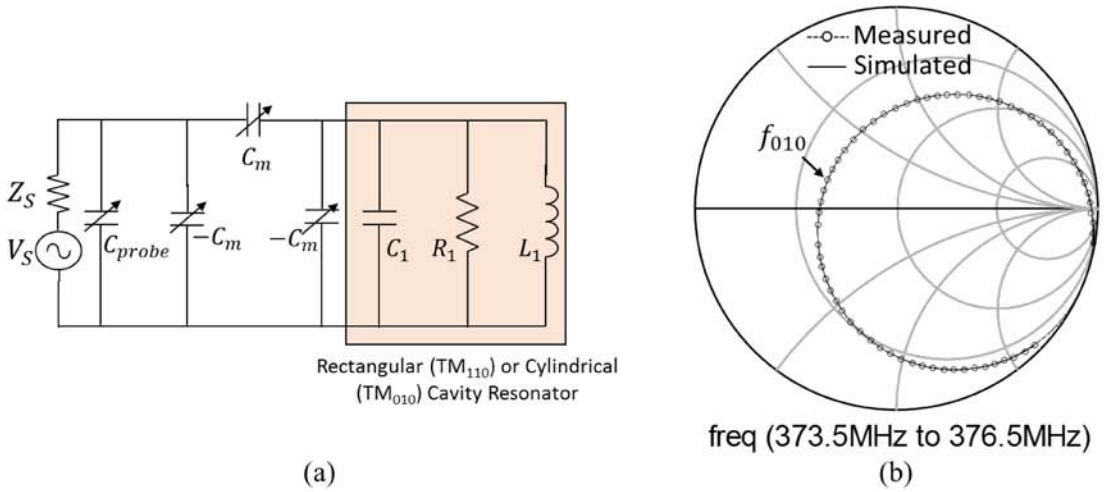

Figure 4.11 Curve fitting method to determine C_m and C_{probe} for a corresponding excitation probe, l_{probe} (a) Circuit simulation set-up, C_m and C_{probe} are varied in circuit simulation until the simulated S_{11} response matches the measured response. (b) circuit simulation shows close match to the measured response ($l_{probe} = 57.6$ cm) when C_m and C_{probe} are tuned to 8.65 pF and 1.6 pF, respectively.

match between circuit simulation and the measured response for $l_{probe} = 57.6$ cm. At this probe length, circuit simulation tuned values of $C_m = 8.65$ pF and $C_{probe} = 1.6$ pF result in a close match to the measured S_{11} cavity resonator response.

4.8.2.2 Extraction of Receive Resonator Parameters and k_{12}

The resonator parameters for the receive system were measured using the same methodology described in Chapter 2, Section 2.7.2. All receive resonator parameters were measured at f_{010}. Briefly, the receive resonator parameters were determined by one-port VNA measurements of the receive coil directly. This provides the measured parameters L_2 and Q_{02}. Parameters R_2 and C_2 are then calculated from L_2 and Q_{02}.

The value of k_{12} between the receive resonator and cavity resonator was determined using 2-port EM simulations (HFSS). Due to the miniature size of the receive coil (5 mm diameter), the estimated k_{12} range, with the coil oriented perpendicular to the circulating magnetic fields of the TM_{010} field distribution at a height of 15 cm, varies from 0 (center of the cavity) to a maximum of 0.004 (at the cavity wall). Note that k_{12} is not a function of height due to the TM_{010} field distribution characteristics of the cavity resonator.

Table 4.1 provides a summary of the measured cavity and receive resonator parameters.

Table 4.1 Measured Resonator Parameters

Parameters	**Cavity Resonator**	**Receive Resonator**
f_{010}	375.32 MHz	375.32 MHz
L_i	0.0074 nH	80 nH
C_i	24300 pF	2.25 pF
Q_{0i}	6191	100
C_{probe}*	1.6 pF	n/a
C_m*	8.65 pF	n/a
k_{12} range **	$0 \leq k_{12} \leq 0.004$	

* Corresponds to a probe length of 5.76 cm; ** estimated from HFSS simulation

Table 4.2 Summary of J_{S1opt}, J_{2Lopt}, and Corresponding Optimal and Actual Capacitance Values at $\omega = \omega_0$ and $k_{12opt} = 0.0025$

	$\boldsymbol{J_{S1opt} = 0.0206}$	$\boldsymbol{J_{2Lopt} = 0.0015}$	
	C_m (pF)	C_{pt} (pF)	C_{s2} (pF)
Optimal (Theory Derived)	8.66	1.605	0.652
Actual (Implemented)*	8.65	2.2	0.8

* Corresponds to a probe length of 5.76 cm

4.8.3 Measured, Circuit Simulated and Theory Predicted Optimal PTE Response

Table 4.2 provides a summary of the optimally determined J_{S1opt} and J_{2Lopt} values and optimally calculated capacitance values to achieve optimal PTE at $k_{12opt} = 0.0025$. The source and load impedances were set to the VNA port impedance of 50 Ω. Larger actual C_{pt} and C_{s2} values were used in measurement to account for the manufacture and high frequency variabilities associated with the surface mount 0603 capacitors implemented on the receive resonator PCB. The probe length is set to 5.76 cm so that the actual C_m matches closely with the optimally calculated value. Figure 4.12(a) shows the optimal theoretically predicted, simulated, and measured $|S_{21}|$ responses when the receive resonator is placed 10 cm ($k_{12} \approx 0.0025$) within the cavity. The optimal theoretical $|S_{21}|$ response was determined by substituting the source and load impedances, measured resonator parameters, $k_{12opt} = 0.0025$, and calculated J_{S1opt} and J_{2Lopt} into (4.18). For comparison, Figure 4.12(a) also shows the measured response of the same coil tuned on a separate PCB consisting without an optimal J-inverter network. Instead, the receive coil is tuned only with a single shunt resonant capacitor (2.25 pF). As shown, the system that is optimally tuned achieved a peak PTE of 33.88%. This is 4 times greater than the 7.68% PTE that would be achieved without optimized tuning. Also, the measured results matched closely to the optimal response predicted by the theory and circuit simulated cavity resonator BPF system; deviating by only 3.45% from the theoretically predicted and circuit simulated maximum achievable PTE. This deviation may be due to PCB parasitic impedances. As shown in Figure 4.12(a), the PTE decreases by as much as 13.18 dB at 0.5 MHz away from f_{010}. This sensitivity is due to

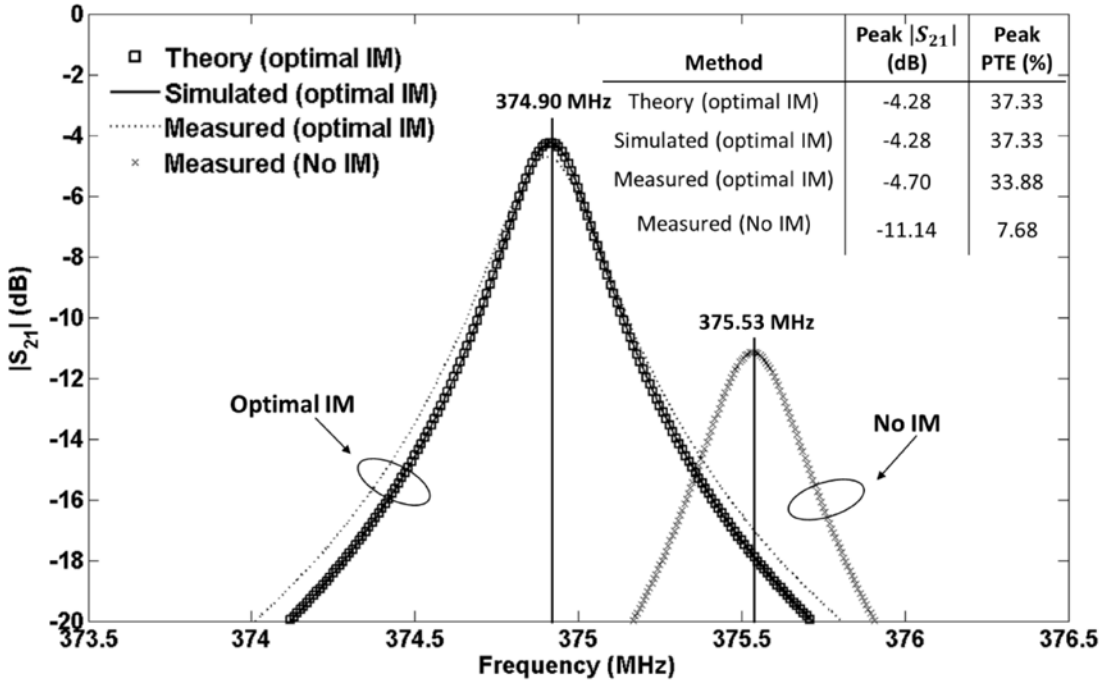

Method	Peak $\lvert S_{21}\rvert$ (dB)	Peak PTE (%)
Theory (optimal IM)	-4.28	37.33
Simulated (optimal IM)	-4.28	37.33
Measured (optimal IM)	-4.70	33.88
Measured (No IM)	-11.14	7.68

(a)

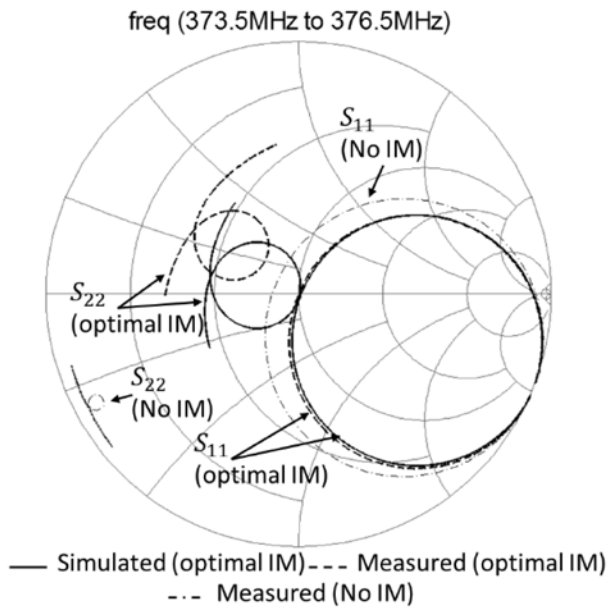

(b)

Figure 4.12 (a) Theoretically predicted, circuit simulated, and measured $|S_{21}|^2$ responses (measured includes optimal IM and non-optimal IM results). Inset shows a comparison of peak PTE. (b) Measured (optimal and no IM) and circuit simulated S_{11} and S_{22} responses. The receive resonator was oriented perpendicular to the TM_{010} distributed magnetic fields located 10 cm within the cavity and a height of 15 cm.

the extremely high Q_{01} of the constructed copper cylindrical cavity resonator. Figure 4.12(b) shows the measured and circuit simulated S_{11} and S_{22} responses of the optimized system. Indeed, the measured resonant S_{11} and S_{22} behaviors from the optimized system closely matches to the simulated responses. Figure 4.12(b) also includes the measured S_{11} and S_{22} responses of the system without the optimized network. As shown, a system with no IM deviates significantly from the optimal S_{11} and S_{22} responses.

4.9 In-Vivo Experiment with Porcine Ocular Tissue

Here, I present an in-vivo experiment demonstrating WPT to biological tissue within the cylindrical copper cavity environment. To demonstrate ultra-miniaturization, a 2 mm diameter receive coil was fabricated and utilized as the power receive coil. Two-port VNA measurements were utilized to measure PTE within the anterior chamber of a porcine eye (all housed within the cavity). An application demonstration for the wireless operation of a miniature LED device implanted in the porcine eye is presented. The results of this experiment validate the WPT capability of the cavity resonator WPT system for implantable or wearable bioelectronics applications. To the best knowledge of the author, this experiment demonstrates the first 2 mm diameter receive device with a measured in-vivo PTE of > 1%.

4.9.1 Experimental Design and Measured PTE

Figure 4.13 shows the experimental set-up. A single porcine eye was placed within the cavity resonator against the wall (location of maximum $\vec{H}$-filed intensity). A 2 mm diameter coil (2 tightly wound turns with 30 AWG copper magnet wire) was

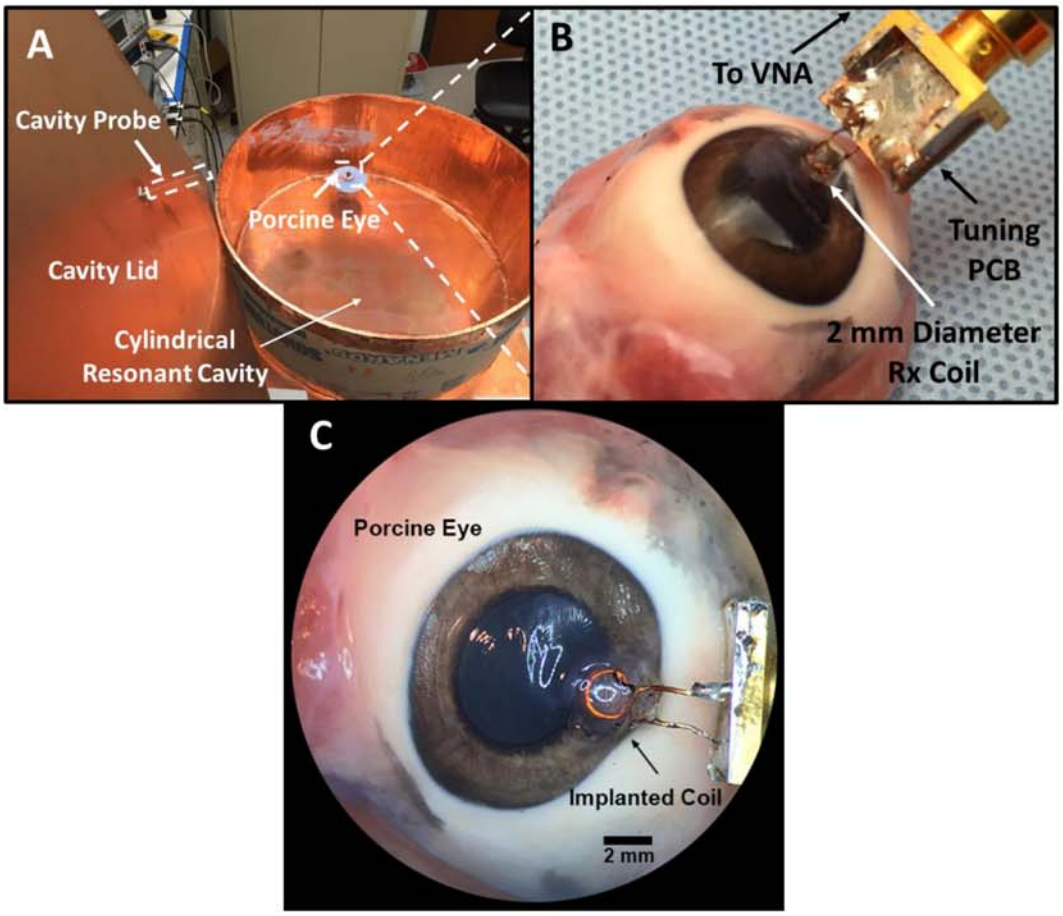

Figure 4.13 Experimental set-up to measure optimal cavity resonator WPT with porcine eye tissue. (A) shows location of porcine eye tissue and cavity resonator system. (B) shows the coil located in the eye for two-port VNA measurements. (C) shows a close up view of the porcine eye with embedded silicone epoxied 2 mm diameter receive resonator coil.

fabricated and packaged with Silicone epoxy. Table 4.3 summarizes the measured resonator parameters in the presence of the porcine eye i.e. porcine eye in cavity and silicone epoxied coil within anterior chamber of porcine eye. The presence of the porcine tissue within the cavity has a two-fold effect: 1.) decreases the unloaded resonator quality factor and 2.) lowers the resonant frequency. This is due to the high electric permittivity of ocular tissue. From the widely used Gabriel et al. biological tissue electrical properties

database [91-93], human ocular tissue (which is very near equivalent to porcine ocular tissue) exhibits $\varepsilon_r = 69.005$, $\mu_r = 1$, and $\sigma = 1.53\ S/m$, where σ is conductivity, μ_r is relative magnetic permeability, and ε_r is the relative permittivity. Due to the high relative permittivity, the ocular tissue will interact strongly with the electric field. Additionally, the non-zero conductivity of the ocular tissue acts to reduce the unloaded quality factor of cavity resonator. Based on the field distribution of the TM_{010} mode field distribution, ocular tissue placed nearest the edges of the wall should reduce the field interaction. In general, the presence of the ocular tissue acts to perturb the cavity resonator behavior acting to both lower resonant frequency and unloaded quality factor. However, due to the small size of tissue relative to the size of the cavity, the field distribution can be assumed similar. Although a full analytical exploration of this perturbation would be ideal to account for biological tissue within the cavity, the success of this work shows it is not necessary for a functional experiment for demonstrating the wireless powering capability of the optimized cavity resonator WPT system. To

Table 4.3 Measured Resonator Parameters with Porcine Eye

Parameters	**Cavity Resonator**	**Receive Resonator (2 mm Diameter)**
f_{010}	375.1 MHz	375.1 MHz
L_i	0.0059 nH	16.9 nH
C_i	24300 pF	10.65 pF
Q_{0i}	4024	50
C_{probe}*	1.6 pF	n/a
C_m*	8.65pF	n/a
k_{12opt}	0.0015	

* Corresponds to a probe length of 5.76 cm;

compensate for the reduced cavity Q, the excitation probe is elongated to a length of 60 cm.

Using the same procedure described in the previous section (Section 4.8.3), the optimal J-inverter conditions are calculated and the representative lumped element networks configured accordingly. Table 4.4 provides a summary of the optimally calculated and actually implemented capacitance values for experiments involving the porcine ocular tissue. Figure 4.14 shows the measured two port VNA $|S_{21}|$ results with

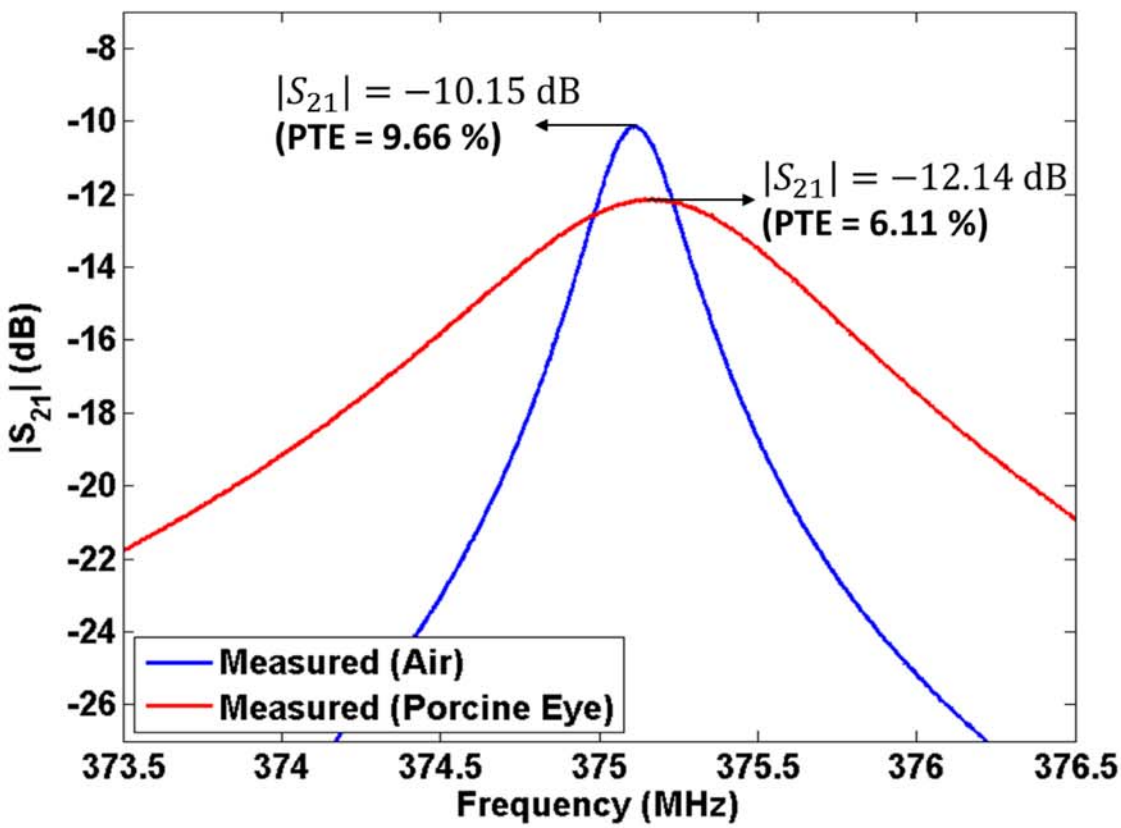

Figure 4.14 Measured PTE between the optimally tuned 2 mm diameter coil made resonator and cavity resonator system in air and in the anterior chamber of the Porcine Eye. In the eye tissue, the 2 mm diameter receive coil achieved a peak PTE of 6.11%

Table 4.4 Summary of J_{S1opt}, J_{2Lopt}, and Corresponding Optimal and Actual Capacitance Values at $\omega = \omega_0$ and $k_{12opt} = 0.0015$ (For Porcine Eye Experiment, 50 Ohm source and load)

	$\boldsymbol{J_{S1opt} = 0.0206}$	$\boldsymbol{J_{2Lopt} = 0.00347}$	
	C_m (pF)	C_{pt} (pF)	C_{s2} (pF)
Optimal (Theory Derived)	8.756	9.21	1.5
Actual (Implemented)*	8.65	11.1	1.2

* Corresponds to a probe length of 5.76 cm

Table 4.5 Wireless PTE Comparison to Biologically Implanted Systems with 2 mm diameter receive coils

Reference	**WPT Modality**	**Location**	**PTE (2 mm Diameter coil)**
Ho et al. 2014 [35]	Mid-Field	Rabbit Chest	0.036 %
Montgomery et al. 2015 [39]	Mid-Field	Subcutaneous in a Mouse	0.125 %
This Work	**Cavity Resonator**	**Porcine Eye**	**6.11%**

and without porcine ocular tissue. Indeed, the presence of the ocular tissue results in a 3.55% decrease in the optimal achievable PTE. However, the peak PTE of 6.11% is achieved to a receive resonator made of a 2 mm diameter coil. Table 4.5 provides a comparison this work to prior state of the art wireless PTEs to 2 mm diameter coils within biological tissue. As shown, this work achieves the highest biological tissue implanted PTE using 2 mm diameter receive coils.

4.9.2 Application Demonstration

Here, the optimized cavity resonator wireless powering methodology is utilized to power a miniaturized functional LED device implanted in porcine ocular tissue within. Figure 4.15 shows the fully implantable device circuit schematic. The device consists of a 2 mm diameter receive coil and optimizable tuning network connected to a voltage doubling rectifier and LED. This simple and passive device has been utilized for wirelessly powered optogenetic neurostimulation [39]. However, in this work, I add an optimized tuning network to maximize wireless PTE.

The input impedance of the combined rectifier and LED system, load impedance from the perspective of the receive resonator, was measured to be $Z_L = 75\ \Omega - j238.0\ \Omega$ at an input power of 10 dBm at 375.0 MHz. Consequently, the optimal capacitance values, C_{pt} and C_{s2}, shown in Table 4.4 were updated accordingly. Using the procedure developed in Section 4.7 (demonstrated in Chapter 2), the updated C_{pt} and C_{s2} values for accommodating the complex impedance of the rectifier/LED device were calculated to be 9.477 pF ($C_2 = 10.655$ pF, $C_{FIS2} = 0.815$ pF, $-C_{p2} =$ -1.993 pF) and 4.0 pF, respectively. These capacitance values were implemented on the fully fabricated and packaged device. To maintain miniaturization, capacitors in 0201 package size were used for the optimized tuning network and rectifier. Individual Schottky diodes (SMS-7630-061) in 0201 package size were utilized for the rectifier. A blue LED in 0402 package size was tied to the DC output of the voltage doubler rectifier.

Figure 4.16 shows the fabricated ultra-miniaturized device, packaged in silicone epoxy, and implanted in the anterior chamber of the porcine eye. The ocular tissue and implanted device were placed into the cavity resonator. Figure 4.17 shows the implanted

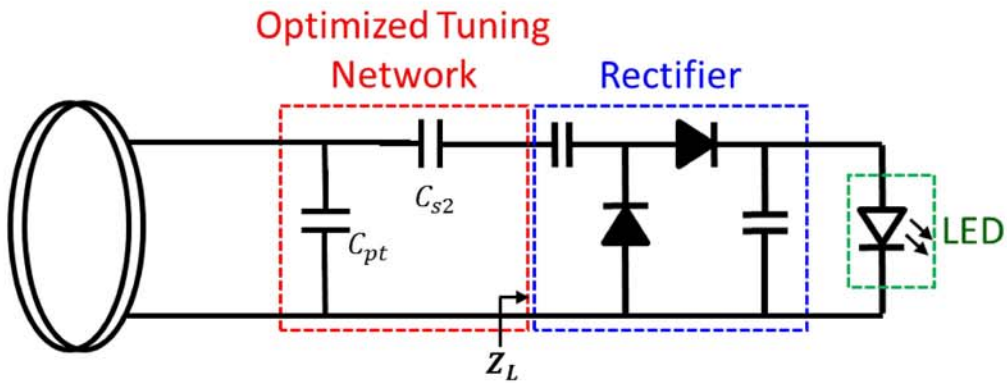

Figure 4.15 Ultra-miniature device circuit schematic. The fabricated device was implanted into porcine eye tissue.

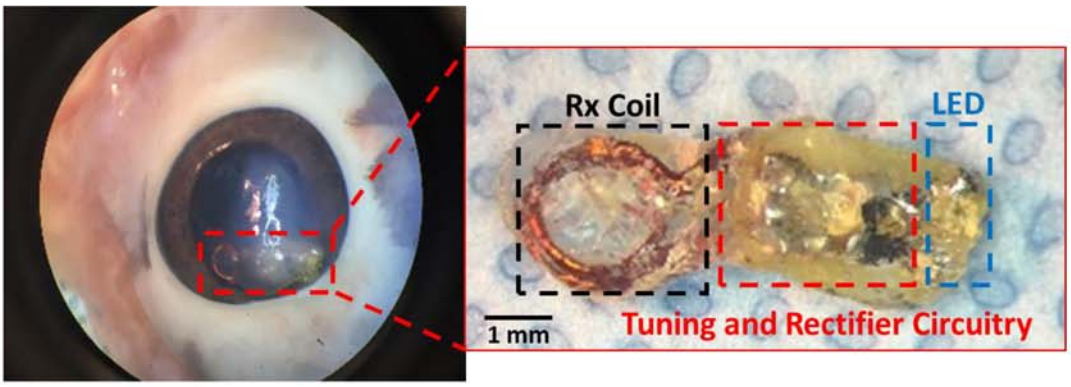

Figure 4.16 Fabricated miniature LED device. Left: Device fully implanted in the anterior chamber of the ocular tissue and right: zoomed in view of the optimally tuned miniature device. The device was packaged in silicone epoxy to isolate the electronics from the biological tissue.

device being successfully wirelessly powered within the cavity resonator. The device was wirelessly powered with 1 W input power to the cavity at 375.1 MHz. This application experiment has demonstrated two key important capabilities of the optimized cavity resonator WPT system: 1.) wireless powering to ultra-miniature sized devices, in-vivo, within he cavity resonator is feasible and 2.) complex load impedance accommodation

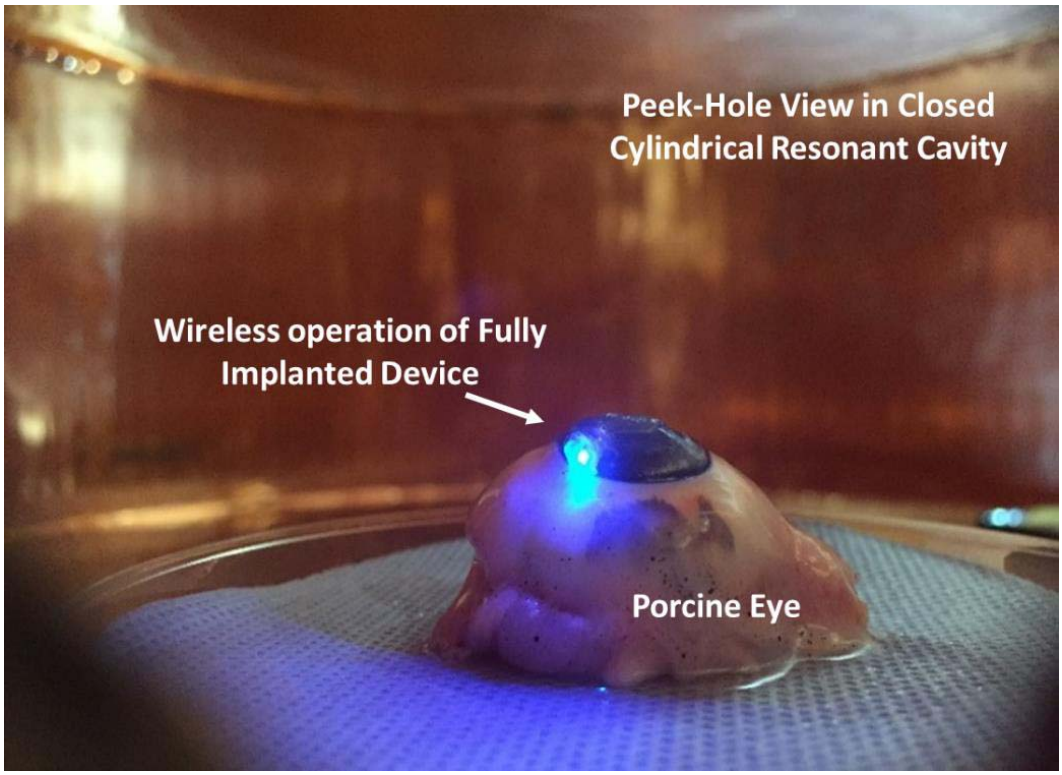

Figure 4.17 Peek-hold view inside the cavity resonator demonstrating wireless powering to the miniature LED device operating within the implant environment.

can be achieved for optimizing wireless powering to an implantable device within the cavity resonator.

4.10 Conclusion

A novel cavity resonator MRC WPT system, representative model, and optimization methodology has been presented. Coupling matrix synthesis and analysis was utilized to derive system transfer response and analytical expressions for optimal J-inverter conditions. A 60.96 cm (2 ft.) diameter cylindrical copper cavity resonator was constructed and the procedure for extracting resonator parameters was described. The optimization methodology was validated experimentally and a PTE of 33.88% was

demonstrated to a 5 mm diameter receive coil. The optimization method was then translated to an in-vivo experiment in which a PTE of 6.11% was demonstrated to a receive system made of a 2 mm diameter coil implanted in porcine ocular tissue. To the best knowledge of the author, this was the highest measured PTE, in-vivo, using a 2 mm diameter receive coil. Finally, an ultra-miniature rectifier/LED device was designed, fabricated, implanted in ocular tissue, and wirelessly powered within the cavity. Consequently, this experiment demonstrated the feasibility for complex load impedance accommodation and wireless powering miniature devices implanted in biological tissue within a cavity resonator.

CHAPTER 5. SMALL ANIMAL CAVITY RESOANTOR WIRELESS POWER TRANSFER SYSTEM

The data and work in this chapter has been submitted for publication in the IEEE Transactions on Biomedical Engineering. The citation can be found in the Publications section. This work was performed in collaboration with Kyle Thackston and Rebecca A. Bercich at the Center for Implantable Devices, Purdue University.

5.1 Introduction

Integration of wireless electronics with physiology has long been a goal of researchers to increase the clinical impact of animal experiments. Already, many implantable devices have been effectively integrated with wireless communication, offering bi-directional telemetry, remote control of stimulus parameters, and information processing capabilities [34, 45, 99, 100]. In contrast, practical and efficient integration of wireless powering remains a key challenge. Many conventional devices rely on batteries [99, 101, 102]. A major drawback of these systems, however, is the limited life-span (typically ranging in minutes to hours) of the battery making animal studies requiring continuous device operation, in time spans ranging from days to months, nearly impossible. This is especially true for sophisticated implantable devices with increased power consumption and functionality such as multiple recording channels, wireless telemetry, optical and/or electrical stimulation, and feedback. High capacity batteries are

typically too large for safe implantation in an animal [101, 103]. For these reasons, wireless power offers an attractive alternative to battery power. Toward this end, several groups have developed wireless powering arenas and enclosures for small animal studies [38, 47, 104-108]. These systems can be divided into those that operate using near-field induction and the recently developed mid-field method [35].

Near-field WPT systems are capable of delivering the necessary power that may be required by sophisticated implantable devices, but because of the $1/r^3$ behavior of magnetic field strength, power transfer efficiency (PTE) decreases dramatically from small variations in coil-to-coil misalignment and separation distance. Near-field WPT systems, therefore, require large receive coils (typically > 1 cm), making implementation a challenge. A variety of methods have been proposed to mitigate these shortcomings including closed-loop animal tracking algorithms [104], configurable and stackable coil arrays [47], phase delay power modulation [47, 104], mechanical armatures for animal tracking [107],columnar designed coil cages [106], and coil designed optimization [46, 73]. Although these highly engineered systems provide some level of improvement they cannot overcome the fundamental 2-dimensional nature of inductive coupling and the necessity for large (> 1 cm coil diameters) and often un-implantable receive coils operating in small areas around the field source.

More recently, a mid-field based WPT arena for mice was proposed [39]. In that work, the researchers demonstrated the operation of an optogenetic stimulator implanted in mice by coupling evanescent fields generated on the surface of a slotted cavity resonator. Due to the low power consumption (minimum of 5.6 mW), simple design (rectifier and LED), and unsafe input power (peak input power of 16 W at 1.6 GHz), the

researchers were able to utilize a 2 mm diameter receive coil for power receive, the smallest of its kind for an optogenetic device. Nevertheless, that WPT system does not resolve the persisting need for a miniaturization strategy which maintains an ability to continuously wirelessly power more sophisticated and power-hungry devices. Moreover, the energy coupling was confined to an enclosure for mice which employed a working height of 3 cm and a circuit surface of 21 cm in diameter. That system is unsuitable as a non-restrictive environment for larger rodents such as rats.

In this work, I introduce a new WPT arena for longitudinal studies involving freely-behaving small animals. This system achieves effective wireless powering to miniature receive coils for powering sophisticated implantable devices in large volumes. Figure 5.1 provides a summarized illustration of our WPT approach. The ability to operate with small receive coils, within the large volume (108,050 cm^3), is due to two critical reasons: 1.) I utilize the equivalent bandpass filter (BPF) circuit model and optimization methodology developed in Chapter 4 to predict and attain maximum achievable PTE's [109] and 2.) the unloaded Q-factor (Q_0) of the cavity resonator is naturally high, which maximizes the systems attainable PTE.

I achieve suitable orientation insensitivity of the WPT receiver by implementing a uniquely designed biaxial receive resonator system in which each axis can be tuned individually using the developed optimization methodology. Previously developed cavity resonator WPT system utilize the excitation of higher order modes to achieve orientation insensitivity [110]. Excitation of higher order resonant modes, however, may result in the degradation of cavity Q_0 and requires excitation at multiple frequencies. Currently, adaptability to higher order excitation mode would require changing on-board impedance

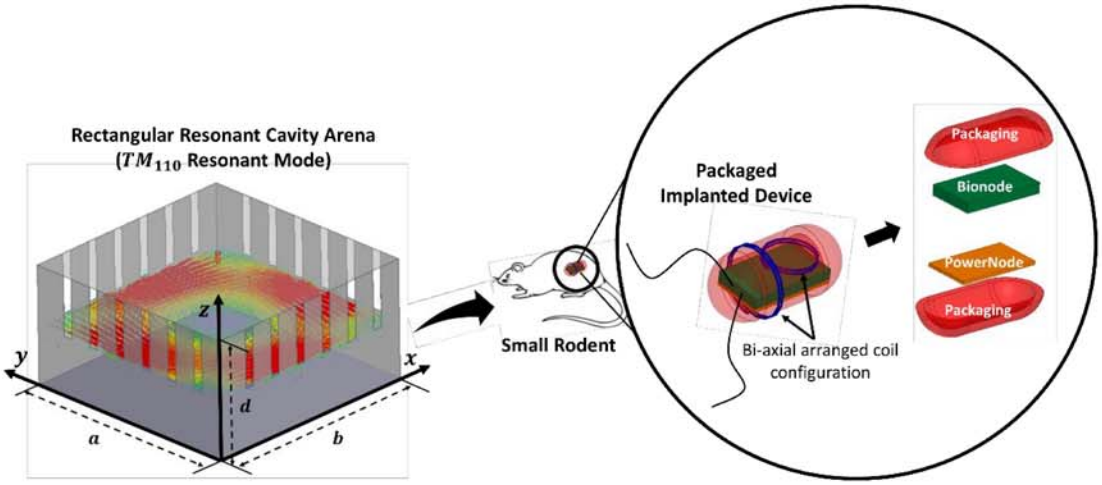

Figure 5.1 Summarized illustration of a cavity resonator WPT arena. The magnetic field density of the TM_{110} resonant mode is illustrated (Magnitude legend: Red, large; Blue, small). A small animal with a packaged implanted device is housed within the cavity resonator volume. A biaxial arranged power receive resonator system is used to promote orientation insensitivity. The in package bioelectric system consists of a custom designed "Powernode" and "Bionode" system.

matching, which is impractical for an implanted device. Thus, multi-mode excitation is not utilized in this application.

To demonstrate the functionality of the cavity resonator WPT method, a set of chronic in-vivo experiments involving freely behaving rats implanted with a custom designed multi-channel bioelectric recording devices measuring ECG signals was conducted. Overall, the novel contributions of this work are:

1. Development and construction of an animal housing based cavity resonator structure. To the best knowledge of the author, this is the largest WPT arena volume for small animal studies
2. Development of a novel packaging and miniature bi-axial receive resonator system (receive coils of 7 mm and 5 mm diameters).

3. Chronic in-vivo demonstration of a wirelessly powered and implanted device in a freely behaving rat within the cavity (> 90% average powering fidelity to a freely behaving small animal).

5.2 Cavity Resonator Design and Construction

Figure 5.2 shows the constructed and custom designed rectangular cavity resonator and Table 5.1 provides a summary of relevant dimensions. The cavity resonator structure and construction are designed such that the EM behavior of the cavity is maintained while its utility as a long-term small animal monitoring and care structure is maximized. Specialized cavity resonator design features included large physical dimensions, viewing/ventilation slots, and an easily removable lid. Consequently, this system was approved for use by the Purdue Animal Care and Use Committee (PACUC) at Purdue University and is compliant with the UK Animals (Scientific Procedures) Act of 1986 and approved for use at the University of Oxford.

5.2.1 Material Selection

A cavity can be constructed out of any conductive material. High conductivity material, however, is critical for maximizing cavity unloaded quality factor, Q_0; the ratio of stored energy over energy loss per cycle [61]. In constructed cavity resonator structures, losses are due to conductor loss, presence of an electrically lossy object, radiation, and imperfect electrical connectivity between structure connections. Importantly, high Q_0 is essential to maximizing the systems attainable PTE (see Chapter 4). To enable practical adoption by the scientific community, the cavity was constructed

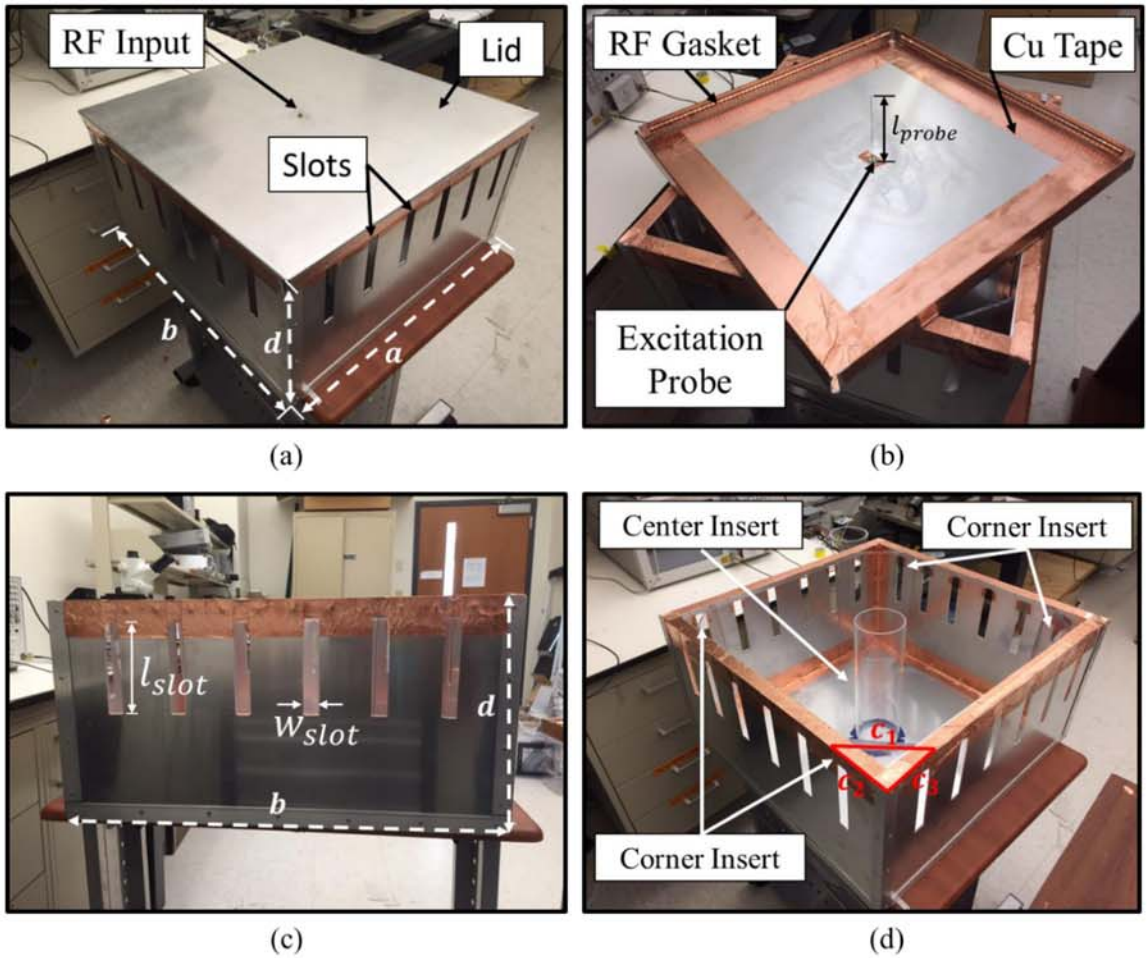

Figure 5.2 Photograph of the constructed cavity resonator small animal housing unit. (a) Full perspective view with lid attached. (b) Underside of lid unattached to cavity. The excitation probe with length, l_{probe}, is located at the center of the lid. The lips of the lid are lined with Copper Beryllium RF gasket. This provides electrical connection and minimizes field leakage. Copper tape is utilized to reinforce electrical connections. (c) Side view of cavity resonator with detail view of the cut out slots. (d) full perspective view without lid. Interior magnetic field "blind-spot" barriers (center and four corners) are shown.

in rectangular form using aluminum alloy 1100 (99% aluminum content). A copper cavity of equivalent dimensions using super-conductive 101 copper (99.99% copper content) was also constructed to explore WPT performance gains. However, due to the

Table 5.1 Relevant Dimensions of the Constructed Animal Housing Cavity Resonator Structure

Dimension	**Value**
a	60.96 cm
b	60.96 cm
d	30 cm
l_{slot}	15 cm
w_{slot}*	2.1 cm
Center Barrier Radius	5 cm
Corner Barrier (c_1, c_2, c_3)	5 cm, 3.54 cm, 3.54 cm

accessibility, safety, mechanical strength, and good corrosion resistance of aluminum, all functional in-vivo experiments were conducted using the aluminum constructed cavity.

5.2.2 Cavity Dimensions and Resonant Frequency

The cavity resonator acts as the primary small animal housing enclosure. The cavity was designed with dimensions of $a = 60.96$ cm, $b = 60.96$ cm, and $d = 30$ cm to maximize the physiological and behavioral needs of small animals. The large dimensions facilitate a large volume in which a freely behaving animal can conduct natural movement and postural adjustments. Additionally, bedding, absorbing mats, and food can be placed within the enclosure to enhance animal welfare.

The resonant frequency, f_{110}, of a rectangular cavity, where the height is less than the length and width, excited in the TM_{110} mode is calculated by

$$f_{110} = \frac{c}{2\pi\sqrt{\mu_r \varepsilon_r}} \sqrt{\left(\frac{\pi}{a}\right)^2 + \left(\frac{\pi}{b}\right)^2} \qquad 5.1$$

where c, μ_r, and ε_r are the speed of light, relative magnetic permeability and relative dielectric permittivity of a material within the cavity, respectively [61]. Using (1), the constructed cavity has a predicted f_{110} of 347.99 MHz. This is below the GHz frequencies at which EM fields are attenuated and reflected to a level making WPT impractical for powering sophisticated implantable bioelectronics.

5.2.3 $\vec{H}$-field Distribution in the TM_{110} Excitation Mode

Figure 5.3 shows the simulated magnetic field ($\vec{H}$-field) distribution for the rectangular cavity excited in the TM_{110} mode. Figure 5.4 shows the corresponding surface current density distribution. All EM simulations were conducted using ANSYS High Frequency Structural Simulator (HFSS®). The $\vec{H}$-field is rotational about the center of the cavity, increases in magnitude radially, and is not a function of height. A biaxial receive is developed to capture the circulating $\vec{H}$-field components in two axes, enabling adequate orientation insensitivity for a device implanted in a freely-behaving animal. As shown in Figure 5.3, five distinct locations (center and four corners) exhibit low-field strength. Placing EM transparent barriers in these areas restricts a freely-behaving animal from entering WPT "blind-spots". See Table 5.1 for a summary of barrier dimensions.

5.2.4 Cavity Slots and Animal Viewing

Cutting out six slots on the top of each wall of the cavity enables ease of animal viewing, permits air flow within the cavity (to maintain humidity and temperature), and water access. From an EM performance standpoint, the width of the slots were chosen to

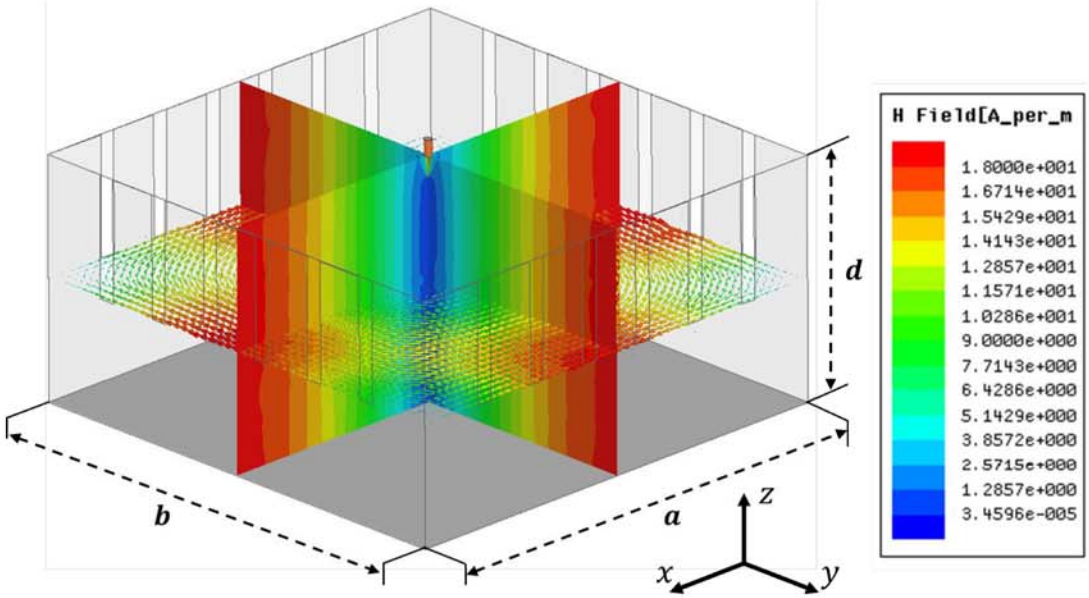

Figure 5.3 Simulated $\vec{H}$-field distribution in the TM_{110} excitation mode.

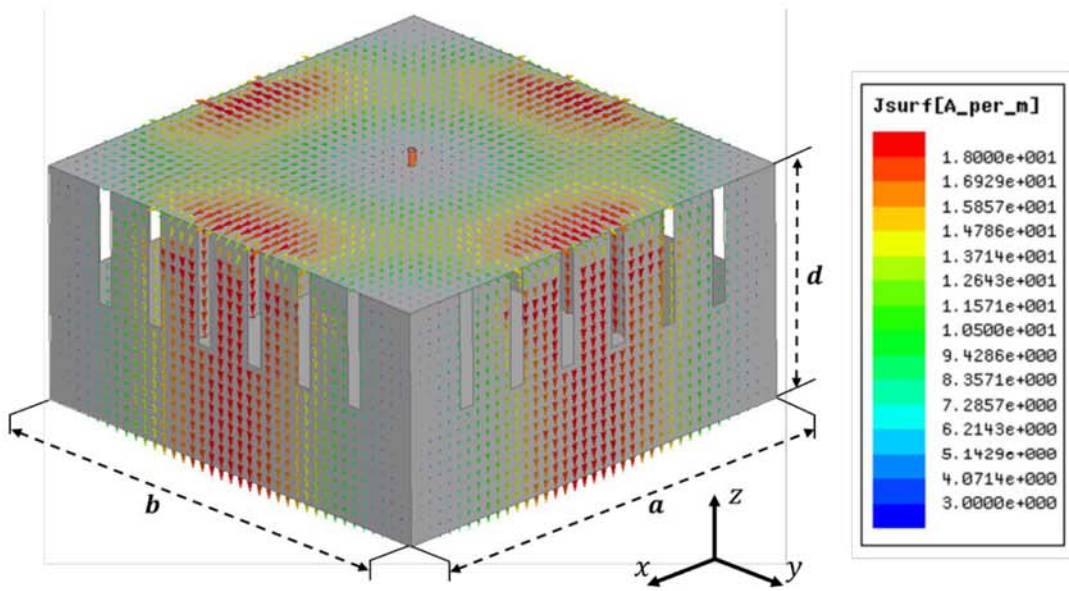

Figure 5.4 Simulated surface $\vec{J}$-field distribution in the TM_{110} excitation mode.

be $w_{slot} = 2.1$ cm. This dimension is $<< \lambda_{110}$, where λ_{110} is the wavelength at the TM_{110} frequency ($\approx$ 86.5 cm), thereby minimizing radiative losses. Slots are oriented vertically

(15 cm length) to minimize alteration of the surface current density ($\vec{J}$-field), shown in Figure 5.4, to maintain proper excitation of the TM_{110} field distribution.

5.2.5 Removable Lid Design and Excitation Probe

Featuring a removable lid eases placement of a small animal into the cavity and permits housing maintenance i.e. cleaning, water and food refills, environment sanitization. Robust electrical connectivity between the lid and cavity walls are facilitated by the placement of copper beryllium metal RF gaskets at the lips of the lid. A coaxial probe with a length, l_{probe}, electrically couples (capacitive coupling) RF energy to excite the cavity resonator and connects to the lid via a subminiture type-A (SMA) connector, where RF ground is soldered directly to the cavity. The excitation probe is protected by the center barrier. As described in Chapter 4, the length of the probe is critical for optimal tuning and attaining maximum achievable PTE.

5.3 Animal Housing Cavity Resonator WPT Optimization and Characterization

The BPF model and WPT optimization procedure, developed and demonstrated in Chapter 4 for rectangular or cylindrical cavity resonators excited in the respective TM dominant mode, was applied to the small animal housing cavity resonator WPT system developed in this chapter. Thus, the reader is directed to Chapter 4 (Sections 4.4 - 4.9) for relevant design and optimization equations. Here, the main focus is on the experimental method and characterization of the small animal housing cavity resonator structure and the design considerations necessary for achieving a functional chronic small animal experiment. All S-parameter measurements come from standard 50 Ω one-port and two-

port VNA (Agilent E5072A) measurements. All circuit simulations were performed with Agilent Advanced Design System (ADS©).

5.3.1 Characterization of l_{probe} to C_{probe} and C_m

As was described in Chapter 4 (Section 4.8.2.1.3), the relationship between the physical excitation probe length, l_{probe}, to source and external coupling model capacitances C_{probe} and C_m, were determined by curve fitting circuit simulations of the circuit model shown in Figure 5.5(a) to measured S_{11} parameters of the cavity resonator given a specific probe length. Figure 5.5(b) and Figure 5.5(c) shows the relationship determined between l_{probe} and capacitances, C_{probe} and C_m, for the air-filled cavity with cavity barriers within. As expected, increasing the excitation probe length will increase C_{probe} and C_m. Critical external coupling between the feed and cavity was achieved at an l_{probe} of approximately 80 mm.

5.3.2 PTE Measurements (Aluminum Cavity, No Animal)

PTE measurements were conducted between the cavity resonator structure and a receive resonator made of a 7 mm diameter, two turn (tightly wound) receive coil made of 22 AWG Cu magnet wire. Table 5.2 provides a summary of the resonator design parameters used to determine the optimization conditions. Note that the resonator parameters (cavity and receive resonator) were determined using the methodology described in Chapter 4, Section 4.8.2. The estimated k_{12} values (determined from HFSS simulations) between the cavity resonator and 7 mm diameter coil ranged from 0, near

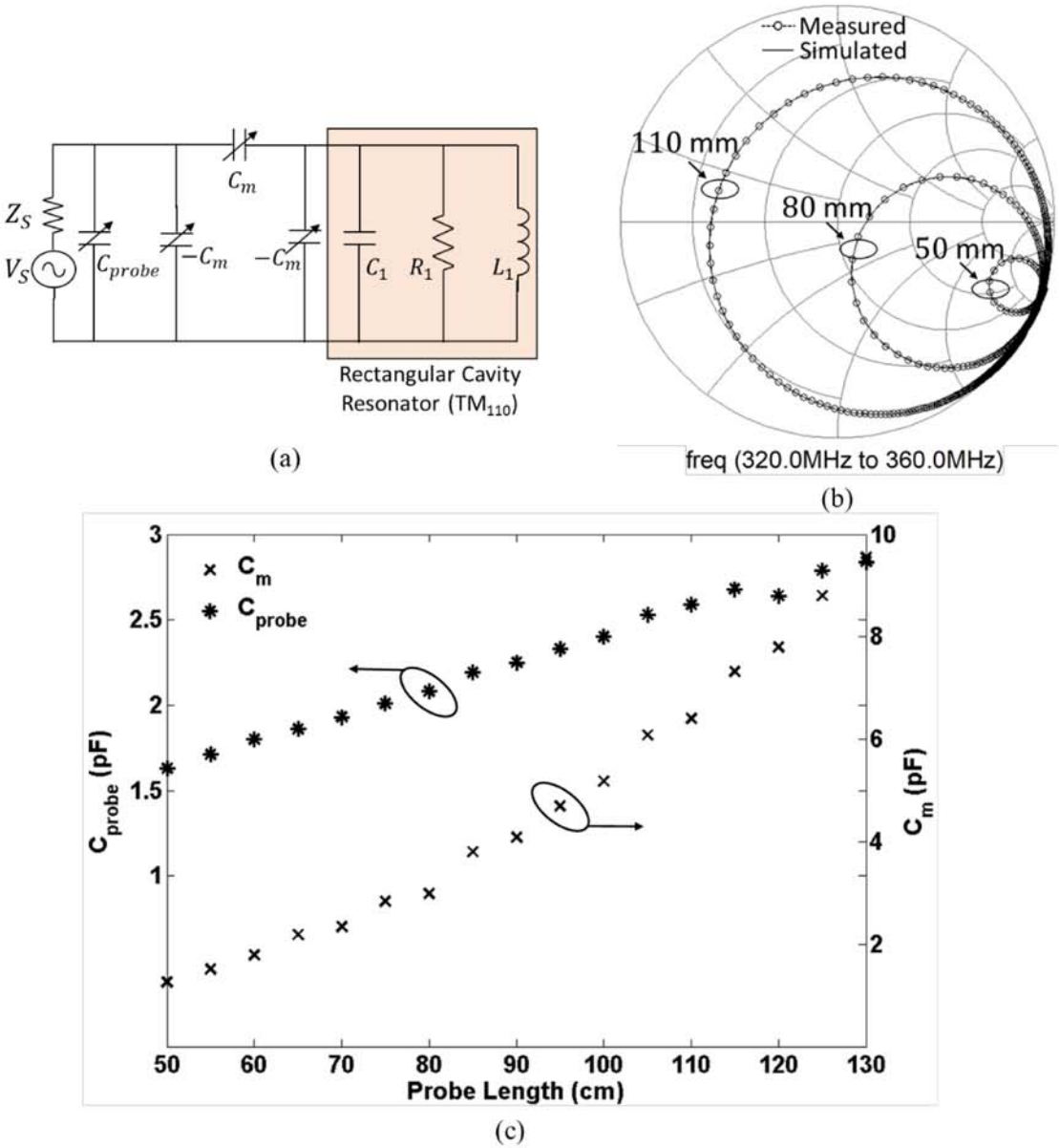

Figure 5.5 Relationship between l_{probe} and model capacitances C_{probe} and C_m. (a) Circuit model used for circuit simulation. C_{probe} and C_m were dynamically tuned in simulation until the simulated S_{11} response matched to the measured response. (b) example of circuit simulation matching for measured responses with l_{probe} at 110 mm, 80 mm, and 50 mm. (c) Plot of C_{probe} and C_m as a function of l_{probe} from 50mm to 130 mm for the small animal housing constructed rectangular cavity resonator structure.

Table 5.2 Measured Resonator Parameters

Parameters	**Cavity Resonator**	**Receive Resonator**
f_{010}	346.6 MHz	346.6 MHz
L_i	0.19455 nH	68 nH
C_i	1083.8 pF	67.48 pF
Q_{0i}	1027	67.0
C_{probe}*	1.6 pF	n/a
C_m*	8.65 pF	n/a
k_{12opt}	0.002	

* Corresponds to a probe length of 84.0 mm

the center of the cavity, to a maximum of 0.004 at the walls of the cavity (coil oriented perpendicular to the magnetic fields). For the remainder of this work, the k_{12opt} point was chosen to be 0.002. This provided a buffer of maximized PTE between the higher k_{12} values near the cavity walls and the lower k_{12} values near the cavity center.

Table 5.3 summarizes the calculated J_{S1opt}, J_{2Lopt} and corresponding capacitance values needed for achieving the optimal tuning conditions given the initial design parameters summarized in Table 5.2. Large C_{p2} values in actual implementation were used to account for the high frequency variation associated with surface mount 0201 capacitors (Johansson Technology, Inc.) implemented on the printed circuit board (PCB). Setting l_{probe} to 84 mm made C_m match closely with the optimally calculated value.

Figure 5.6 shows the 2-port VNA experimental set-up used for measuring S_{21} (PTE by $|S_{21}|^2 \times 100$) as a function of radial position. Moving the receive resonator [Figure 5.6(c)] through a plastic guide tube allowed for accurate PTE measurement control as a

Table 5.3 Summary of J_{S1opt}, J_{2Lopt}, and Corresponding Optimal and Actual Capacitance Values at $\omega = \omega_0$ and $k_{12opt} = 0.002$

	$J_{S1opt} = 0.0073$	$J_{2Lopt} = 0.0015$	
	C_m (pF)	C_{pt} (pF)	C_{s2} (pF)
Optimal (Theory Derived)	3.35	2.41	0.69
Actual (Implemented)	3.55*	2.7	0.7

* Corresponds to a probe length of 84.0 mm

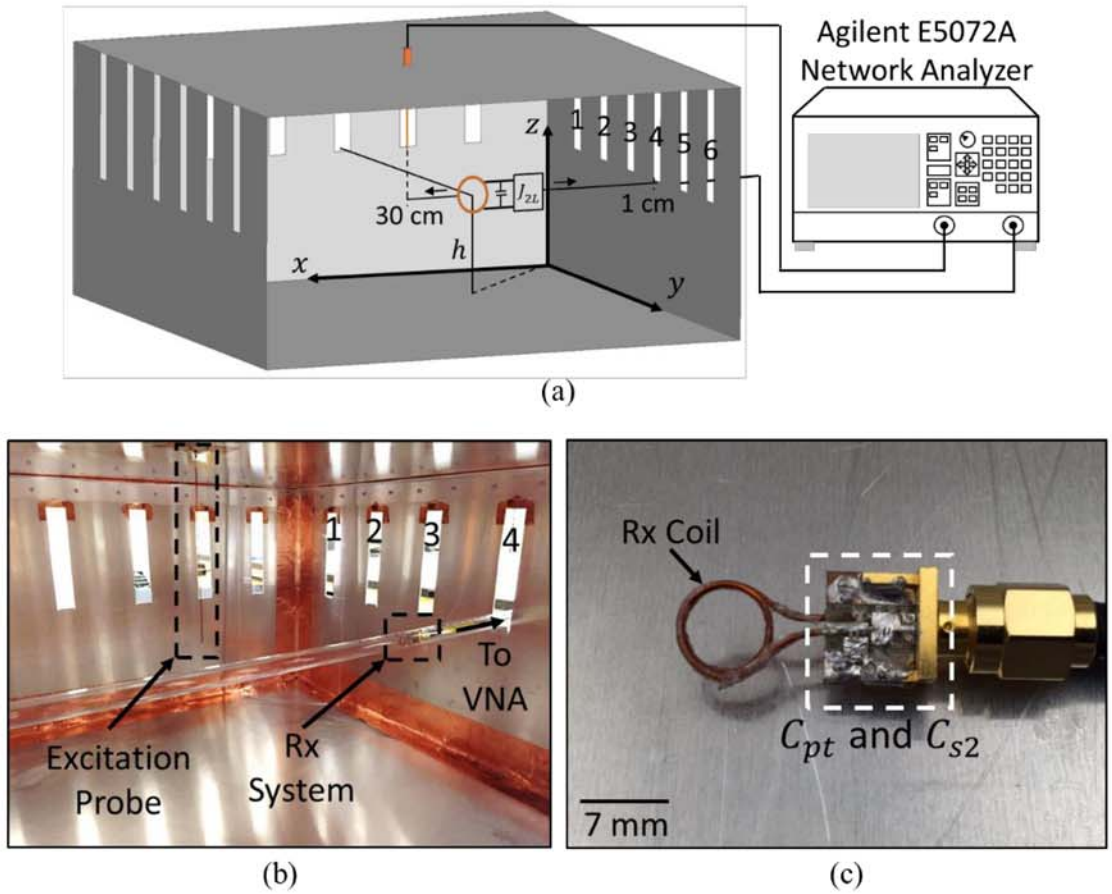

Figure 5.6 Experimental set-up of cavity resonator WPT characterization. (a) Diagram illustration of measurement set-up and labeled positions. The receive resonator is placed through slot 4 and moved in the x-direction. (b) Closed lid inside view highlighting excitation probe and receive resonator system within the plastic guide tube. (c) 7 mm diameter receive coil connected to optimized tuning PCB for measurement.

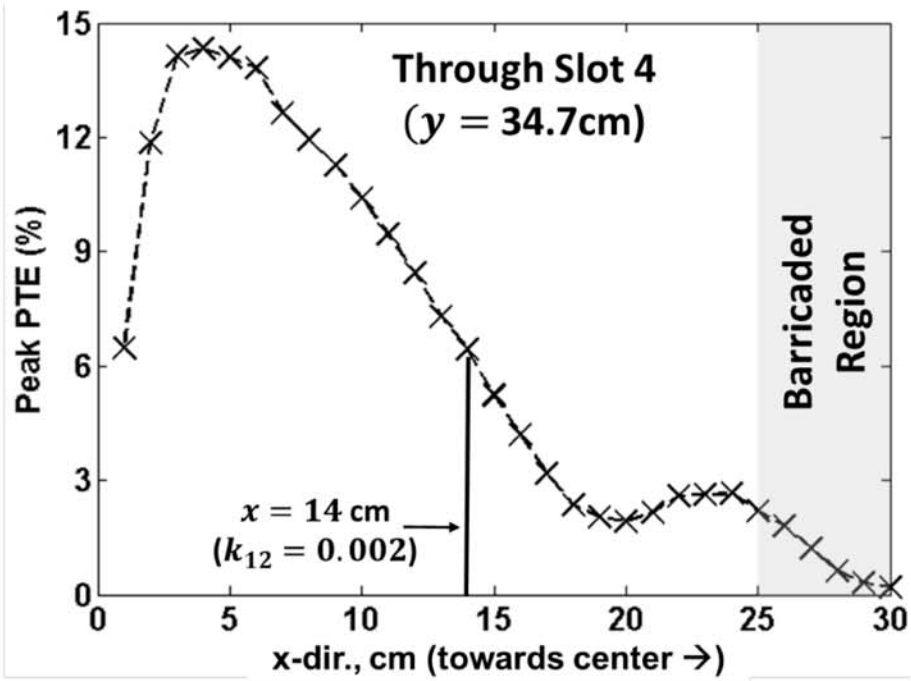

(a)

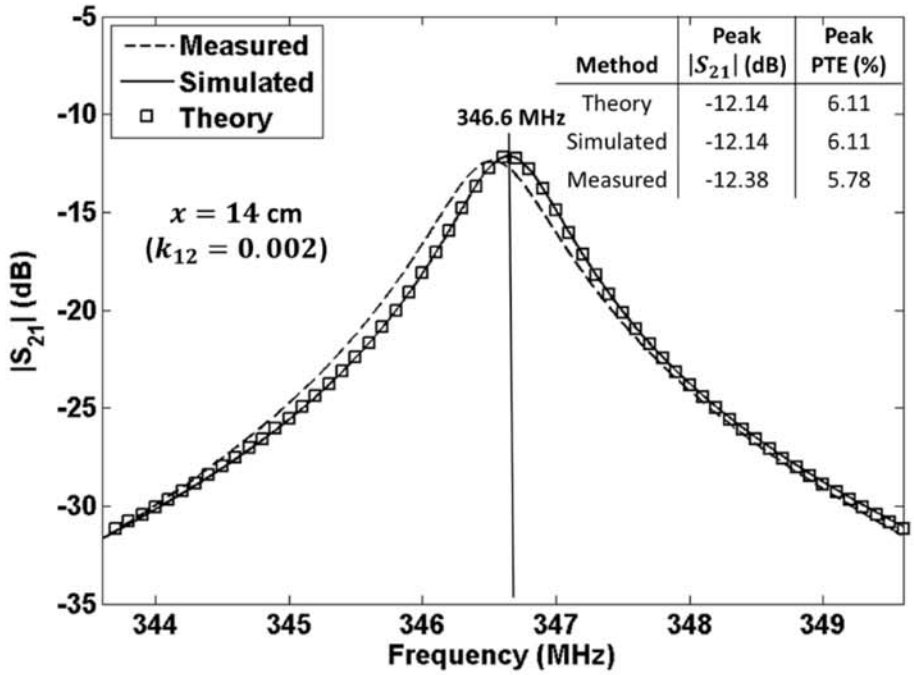

Method	Peak $\lvert S_{21}\rvert$ (dB)	Peak PTE (%)
Theory	-12.14	6.11
Simulated	-12.14	6.11
Measured	-12.38	5.78

(b)

Figure 5.7 Summary of measured PTE response within the cavity. Location of measurements are in reference to the coordinates provided in Figure 5.6. (a) Peak PTE as a function of x-direction position. (b) Measured, circuit simulated, and theoretically predicted frequency response at $k_{12} = k_{12opt} = 0.002$.

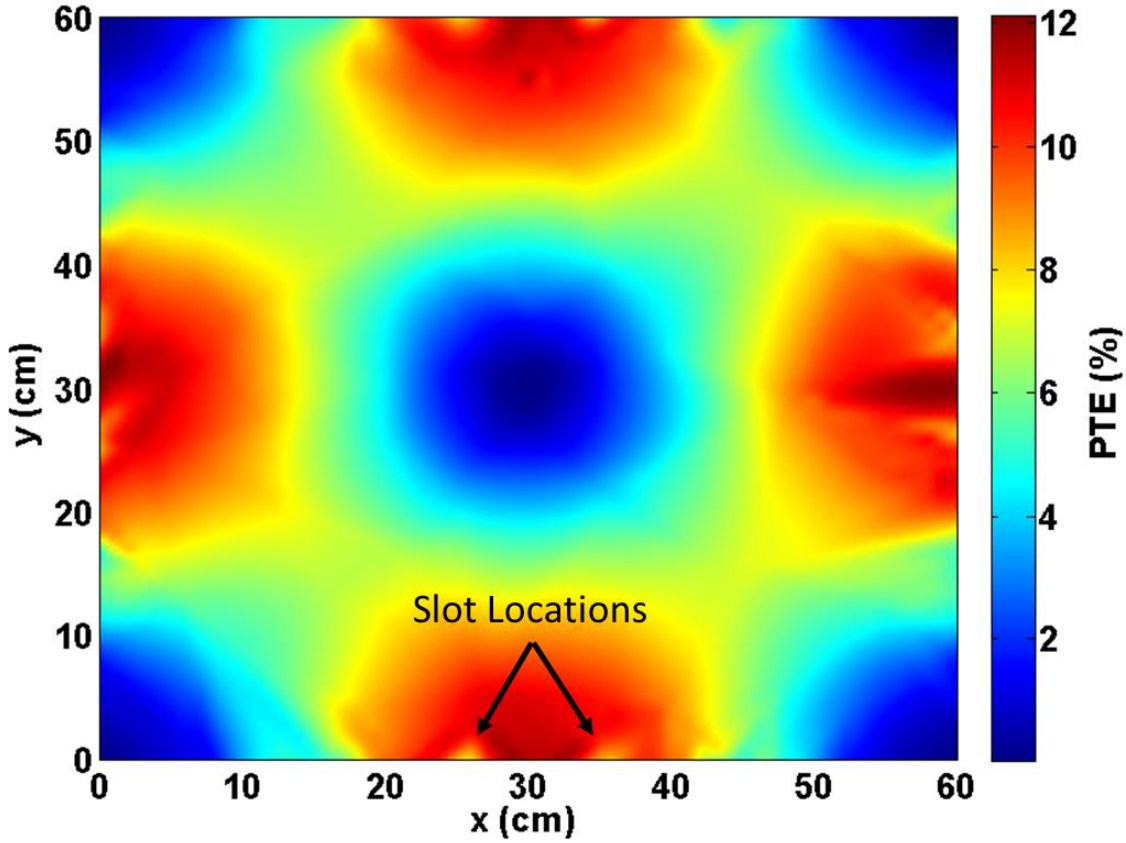

Figure 5.8 Estimated peak obtainable PTE (inferred from measured data) in the x-y plane at a height of 15 cm. Note the lower values of PTE at the slot locations.

function of location. Shown in Figure 5.7(a), a peak PTE of 14.32% was achieved when the receiver was placed at coordinate locations of $x = 4$ cm, $y = 34.7$ cm [slot 4 in reference to Figure 5.6(a)]. The peak PTE decreases as the receiver approaches the center of the cavity, verifying the TM_{110} $\vec{H}$-field behavior of the cavity. Radiative losses from the slots cause the initial low value of PTE at the coil entry location (x = 1 cm). Figure 5.7(b) illustrates the measured, circuit simulated, and theoretically predicted frequency response of the optimally tuned cavity resonator WPT system at the designed optimization point, $k_{12opt} = 0.002$. Figure 5.8 shows a more comprehensive view of an estimated account of theoretical peak obtainable PTE in the x-y plane (height at 15 cm). The plot was created

by assuming that the estimated k_{12} range (0 at center to 0.004 at cavity wall at slot 4 and inferred from the measured data) and simulated x-y plane distribution of magnetic field magnitude (Hmag) share a constant proportionality value, estimated roughly as 0.5 m/A. This proportionality value was then multiplied to the simulated Hmag distribution to provide a corresponding estimated x-y map of peak k_{12} that was plugged back into the transfer function (Chapter 4, Section 4.5). The result was the calculated predicted peak obtainable PTE throughout the x-y plane. Interesting to note are location of slots and the decreased PTE. Indeed, this matches with the measured results.

5.3.3 Copper Cavity PTE Capability (No Animal)

Due to its superior conductivity, the copper cavity achieves a measured Q_0 of 12,157, which is ~ 12 times the measured unloaded quality factor of the aluminum cavity. Figure 5.9 shows the resulting WPT performance capability of the copper cavity using smaller 5 mm diameter and 2 mm diameter coils. Using the same experimental procedure described above, a maximum peak PTE of 51% and 7.7% to the 5 mm diameter and 2 mm diameter receive coils, respectively. This performance enhancement may justify the increased cost for researchers with greater design constraints, such as the need to wirelessly power ultra-miniaturized systems implanted in mice.

5.3.4 Accounting for the Presence of the Small Animal and PTE Measurements

An important consideration when using the cavity resonator WPT system is how the presence of objects will perturb the system. The resonant frequency and Q_0 of a

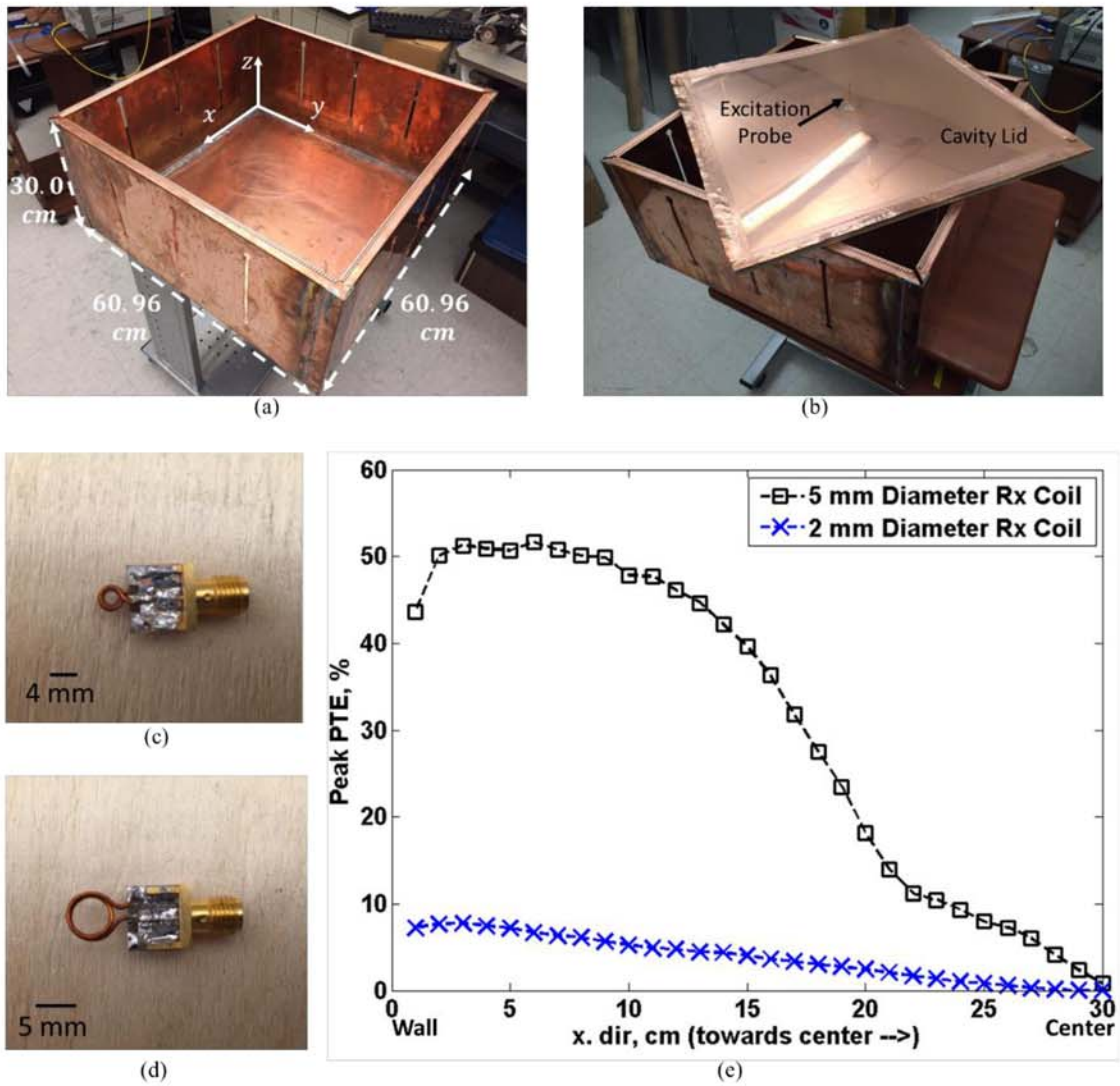

Figure 5.9 Copper cavity resonator provides drastic improvement in WPT performance. (a) Full perspective view of the constructed rectangular copper cavity with dimensions of 60.96 cm x 60.96 cm x 30.0 cm (L x W x H). (b) Full perspective view of the copper cavity lid and attached excitation probe (l_{probe} = 50 mm). The copper cavity exhibits a measured Q_0 of 12,157 and f_{110} = 344.60 MHz. (c) 2 mm diameter receive coil coil (L = 16.73 nH at f_{110}) connected to tuning circuit PCB (C_{s2} = 1.8 pF, $-C_{p2}$+C_2 = 12.4 pF). (d) 5 mm diameter receive coil (L = 48.23 nH at f_{110}) connected to tuning circuit PCB (C_{s2} = 1.2 pF, $-C_{p2}$+C_2 = 4.1 pF). (e) Measured peak PTE as a function of radial position within the cavity. The measurement set-up and coil locations were conducted identically with the experimental set-up shown in Fig. 8(a). Constructing the cavity out of copper and utilizing our optimal IM methodology, we achieve a maximum peak PTE of 51% for a 5 mm diameter receive coil and a maximum peak PTE of 7.7% with a 2 mm diameter coil. In comparison, a maximum PTE of 14% is achieved with a 7 mm diameter coil in the aluminum cavity of same dimensions.

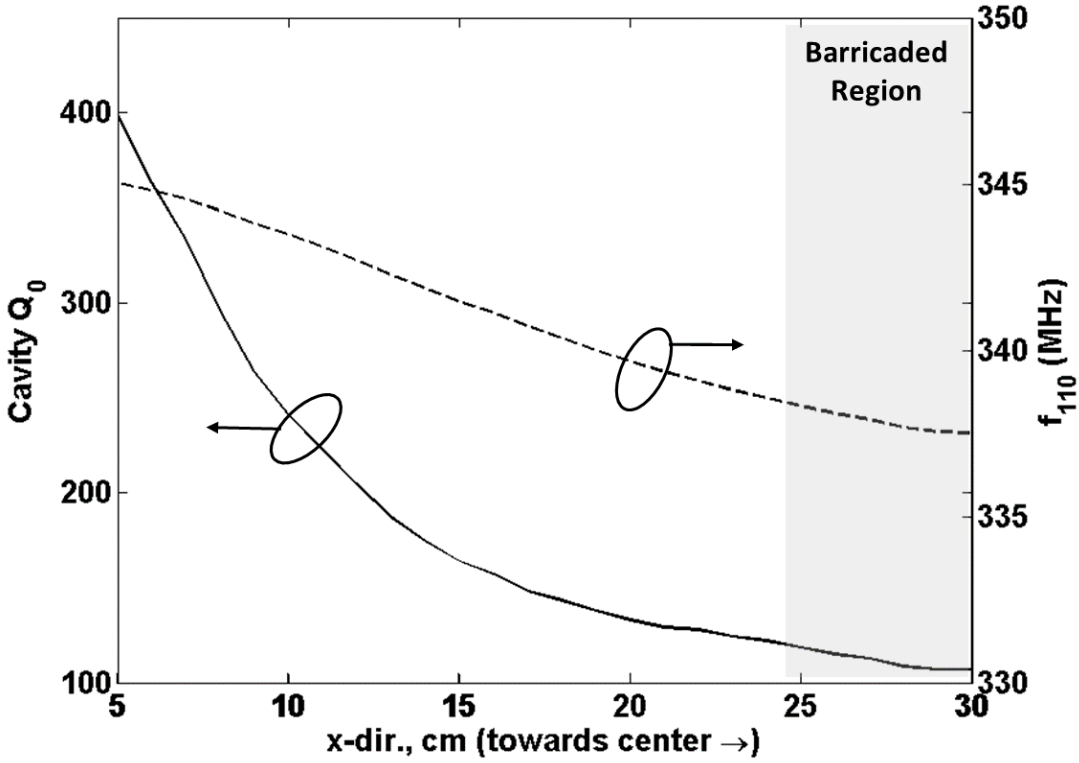

Figure 5.10 Cavity Q_0 and f_{110} as a function of rat position within the cavity (moved incrementally through center of cavity). Note that the excitation probe length was 84.0 mm.

resonant cavity are very sensitive to the EM properties of its contents. It is for this reason resonant cavities are often used to measure the EM properties of materials [61]. In this application, the contents of the cavity will be a moving animal. At the operating frequency of the cavity resonator WPT system (~ 346 MHz), biological tissue will appear as a lossy dielectric [92]. Consequently, a downward shift in resonator frequency and a drop in Q-factor is expected. The magnitude of these changes will depend on the location of the rat inside of the cavity. Figure 5.10 shows the measured effects the body of a rat will have on cavity Q_0 and resonant frequency as a function of radial position through the center of the cavity. Additionally, the quality factor and inductance of the receive

resonator will also change; from measured the 7 mm diameter receive coil decreased in Q_{02} (68.48 to 30.0 in animal) and a light increase in L_2 (68 nH to 69 nH). All of these changes result in alterations to the circuit model, meaning that optimal PTE can still be achieved in implementation as long as measurements are made to account for the change in resonator f_{110}, L_i, , and Q_{0i} and system re-tuning is accomplished. Figure 5.11 shows the measured peak PTE (cavity resonator to 7 mm diameter coil) for various animal accounting based re-tuning conditions. It is important to note that frequency tracking was necessary to obtain peak PTE. Table 5.4 summarizes the changes that were made for each re-tuning condition. In each re-tuning condition, either the probe length and/or receive resonator capacitors were re-tuned. Condition 1 was the control representing the optimized PTE response shown in Figure 5.7(a). Condition 2 represents the change due to the inclusion of the rat body placed within the cavity and the receive resonator implanted within. As shown, the PTE response simply shifts downward as would be expected due to the decrease in both cavity and resonator Q_{0i}. Condition 3 represents a de-tuning state in which the probe length is increased from 84 to 128 mm. At an l_{probe} of 128 mm, critical external coupling occurs when the rat is located at 10 cm within the cavity. In this case, peak PTE decreases dramatically. Condition 4 represents the retuned scenario of condition 3 where the capacitance values on the receive resonator are modified slightly. In this case, peak PTE approaches 11% and can be maintained from 15 cm to 20 cm within the cavity. Finally, condition 5 represents the condition of an extended probe length such that critical external coupling occurs when the rat is placed 14 cm within the cavity with tuned receive resonator capacitors. In this case, a peak PTE was achieved matching closely to the peak PTE of the control state (condition 1) but at a position of 23

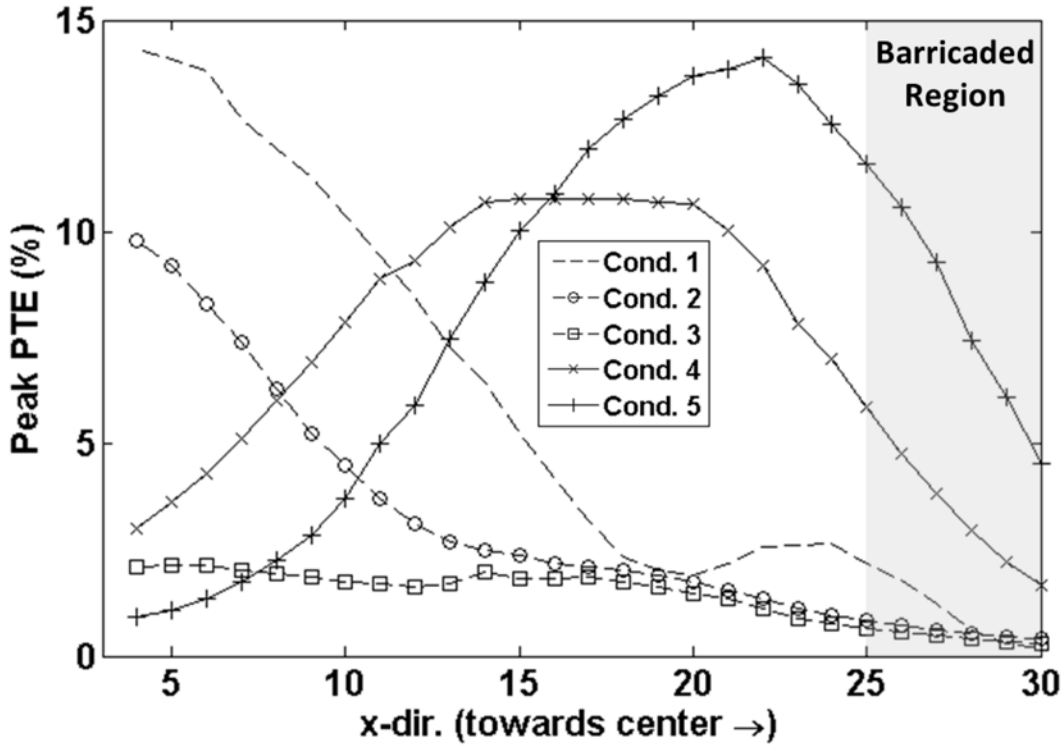

Figure 5.11 Measured peak PTE (frequency tracked) as a function of radial position (through Slot 4) for various re-tuning conditions (summarized in Table 5.4).

Table 5.4 Rat Tuning Conditions for Figure 5.11

Condition	l_{probe} **(mm)**	C_{pt} **(pF) and** C_{s2} **(pF)**
1*	84	2.7 and 0.7
2	84	2.7 and 0.7
3	128	2.7 and 0.7
4	128	2.5 and 1.0
5	143	2.8 and 0.9

*No Rat [same PTE response as shown in Figure 5.7(a)].

cm instead of 1 cm. What these results indicate are two-fold: 1.) the introduction of the small animal requires proper re-tuning of the system. Importantly, retuning for different

animal locations can have dramatic effects on the PTE response. Condition 4, for example is a retuned example for a rat body that was placed approximately 10 cm within the cavity. On the other hand, condition 5 is a retuned example for a rat body placed approximately 14 cm within the cavity. 2.) small capacitance changes on the receive resonator (on the order of 100's of femtofarads) may be the difference between adequate and inadequate PTE behavior. Since a freely moving animal will explore primarily between the center barrier and cavity wall, Condition 4 is chosen as the optimization condition for the chronic animal experiments. It is important to note that only a single operating frequency of 335.0 MHz was utilized for the chronic animal experiments. Figure 5.12 shows the updated PTE response of condition 4 at single the operating frequency of 335.0 MHz. Although a dynamic tuning solution of the cavity probe, on-board tuning capacitor, and frequency would be ideal to account for a moving small animal within, the success of this work shows it is not necessary for a functional experiment.

Finally, a careful observer may analyze the PTE results of condition 5 and wonder how the peak PTE value at 23 cm, where cavity resonator Q_0 drops dramatically to approximately 120 and magnetic fields are approaching their weakest in the TM_{110} excitation, can match closely with the peak PTE of the control condition (condition 1). Recall that the electric field intensity is strongest toward the center of the rectangular cavity excited in the TM_{110} mode. These high intensity electric fields are significantly distorted by the presence of high relative permittivity of the biological tissues. Consequently, it is hypothesized that the high interaction between the biological tissue and high intensity electric fields results in locally increased inter-resonator coupling

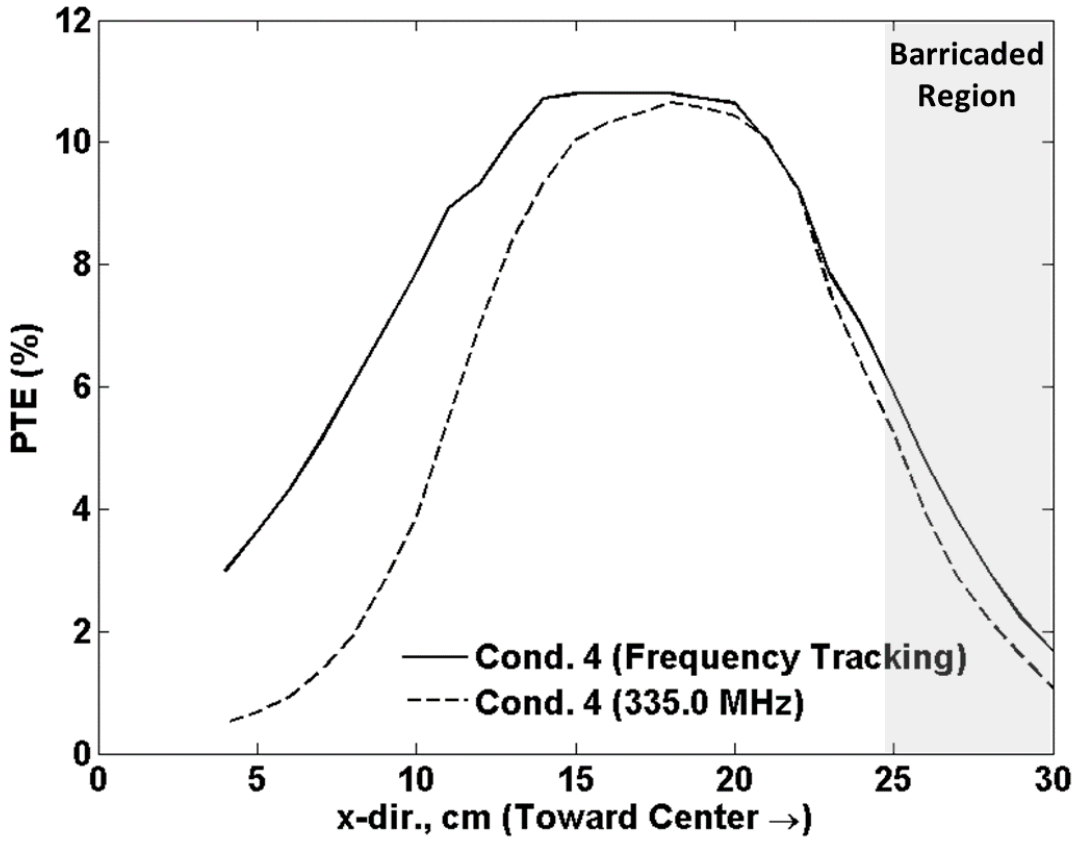

Figure 5.12 Measured peak PTE (frequency tracked) as a function of radial position (through Slot 4) for various re-tuning conditions (summarized in Table 5.4).

within the implant environment. Previous literature exploiting this behavior provides evidence for this phenomenon [40]. Experimental exploration of this phenomenon, however, is beyond the scope of this work.

5.4 Custom Designed Implantable Device for the Chronic *In-Vivo* Experiment

A custom designed fully wireless implantable device was used for the chronic *in-vivo* small animal experiments conducted within the cavity. The fully wireless implantable device consists of three main parts: 1.) the bioelectric recording and

stimulating device (Bionode), the power receive/management device (Powernode), and the packaging solution.

5.4.1 The Bionode

The Bionode is a highly sophisticated bioelectronic device and its development has been a true collaborative effort between members at the Center for Implantable Devices at Purdue University. Its ongoing development is led by Professor Pedro P. Irazoqui. Key engineering members include Rebecca A. Bercich, Dr. Steven Lee, Muhammad Arafat, Zhi Wang, Dan Pederson, Jesse Somann, Gabriel Albors, and Chris Quinkert.

The ability to wirelessly observe and collect electrophysiological data from rodents is a sizeable advantage for certain types of studies–namely those that require long-term or 24-hour monitoring. The implantable electronics were designed with a high level of functionality and flexibility since investigators would need these devices to perform a variety of tasks. Each device includes two integrated analog front-end channels for filtering and amplifying bioelectric signals and two optional data inputs that feed directly to the analog-to-digital converter (ADC). A temperature sensing circuit is included to evaluate device heating and prevent thermal damage to tissue. The additional ability to stimulate bioelectric activity is granted through a current-controlled stimulator with 10.5V headroom. The 10.5V supply for the stimulator circuit along with the 1.8V main power supply needed for operation of the recording device microelectronics are supplied by a supplementary power receive and management board (Powernode) that is responsible for converting the incident electromagnetic fields into stable, DC voltages. In this work, only biosignal acquisition, for real-time ECG capture, is utilized.

Device tasks are directed by an nRF51822 (Nordic Semiconductor) system-on-chip (SoC) which includes an ARM® Cortex™ M0 microcontroller and 2.4 GHz transceiver. The device is capable of bi-directional communication with a base station using a wireless protocol from Nordic Semiconductor. Forward telemetry is used to make changes to the on-board firmware or update operating parameters including: sampling rate, ADC resolution, number of recording channels, and stimulus conditions (frequency, duty cycle, and amplitude). Reverse telemetry is used to send packets of data to the base station, which relay the data to a custom software/graphical user interface (GUI) for real-time illustration and or storage. The functional elements of the system are summarized in Figure 5.13.

All of the microelectronics used to achieve the various device capabilities commercially available for off-the-shelf purchase. The power consumption of the device varies with the system's total sampling rate from 6.1 mW (total sampling rate = 5 kHz) to 13 mW (total sampling rate = 25 kHz). This high power demand paired with the full system performance in the resonant cavity serves to demonstrate the efficacy of the cavity resonator based WPT system.

5.4.2 Biaxial Powernode System

Figure 5.14 shows a schematic diagram and photograph of the biaxial tunable Powernode system. This custom designed circuit board converts the captured RF energy generated within the cavity into a usable and stable DC supply for operation of the Bionode. Importantly, this device is designed using two receive coils oriented

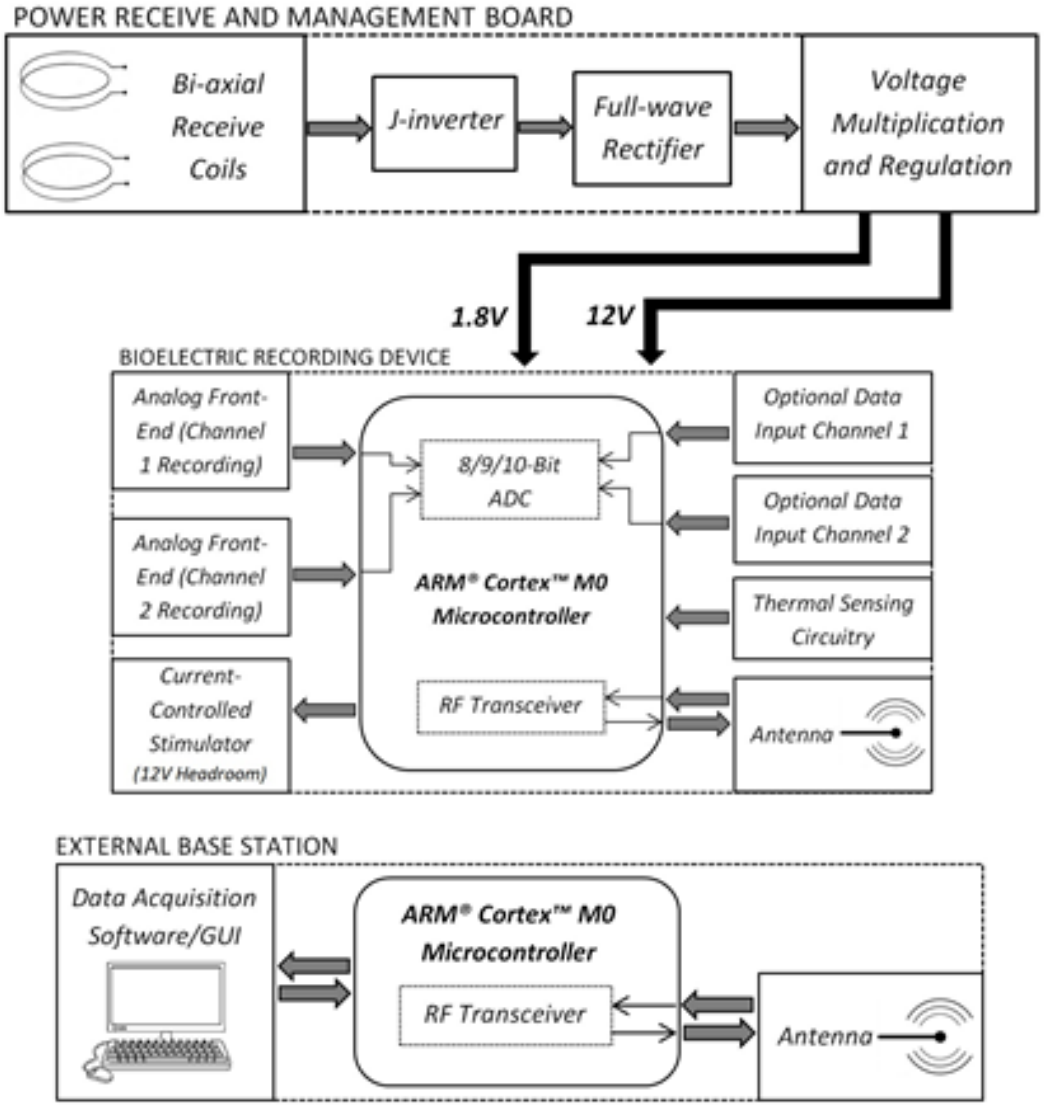

Figure 5.13 Block diagram of implantable microelectronics and external base station used to record bioelectric events in untethered, freely behaving animals within the cavity resonator. The bioelectric recording device utilizes all COTS integrated circuits and incorporates two analog front-end channels having a combined peak sample rate of 25 kHz and a current-controlled stimulating output channel having a voltage headroom of 10.5 V. Device logic and tasks are facilitated by a SoC with an integrated 2.4 GHz transceiver. The power needed to run the microelectronics come from the Powernode, which coupled and rectifies RF energy and supplies regulated DC voltages to the bioelectric recording device.

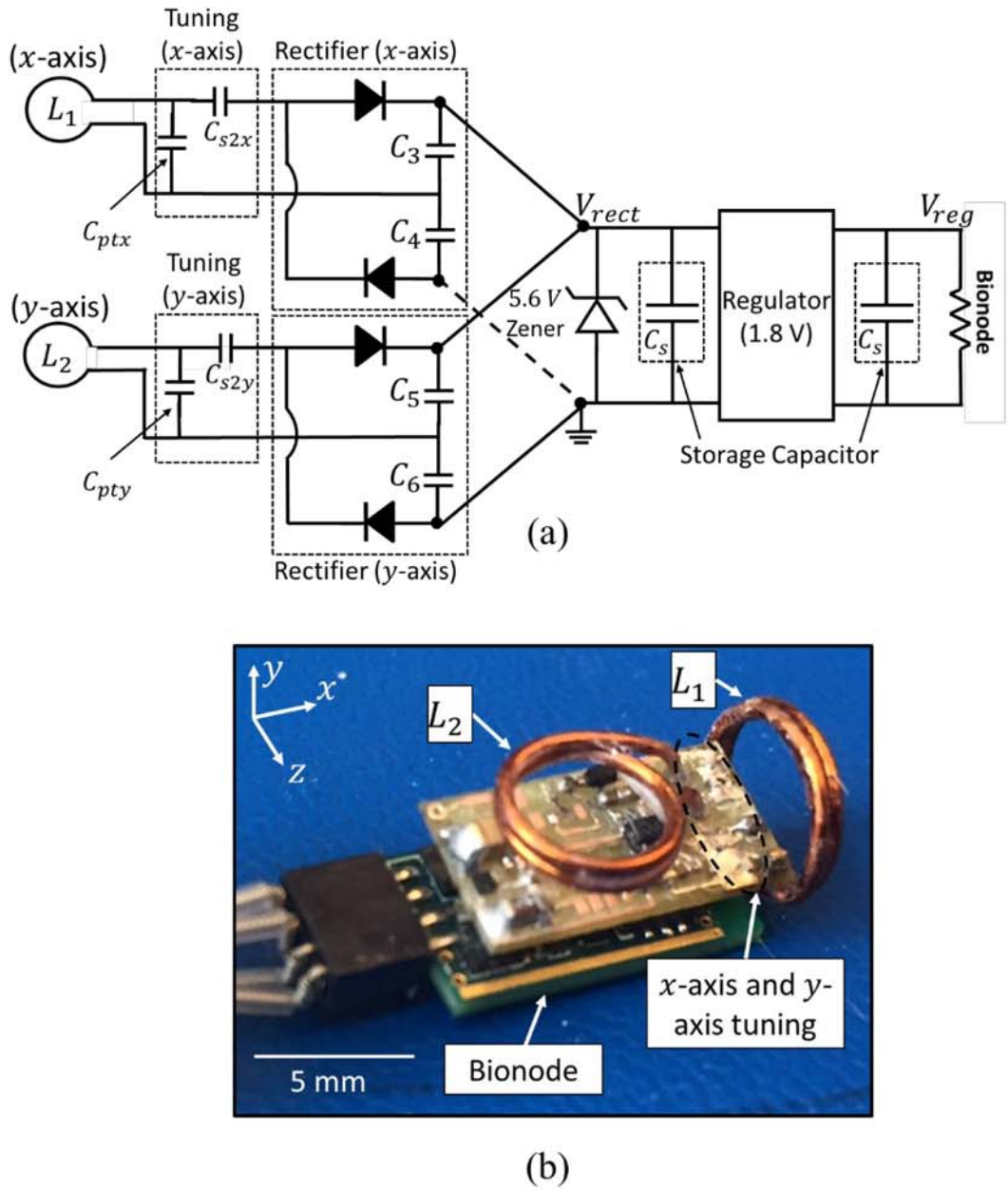

Figure 5.14 Biaxial Powernode System. (a) Schematic diagram of biaxial RF-to-DC conversion circuitry. (b) Photograph of fabricated Powernode device PCB. The Powernode is stacked on top of and electrically connected to the Bionode.

perpendicular to each other to achieve bidirectional coupling: a 7 mm diameter coil oriented in the x-axis and a 5 mm diameter coil oriented in the y-axis. Additionally, each

coil is connected to its own optimal tuning and rectifier voltage doubler circuit to enable independent resonator tuning. A third axis coil (z-axis), optimal tuning, and rectifier could easily be added to achieve truly omnidirectional powering. However, a third axis was omitted to maintain total system miniaturization and simplicity of the packaged system.

As shown in Figure 5.14(a), the output of each optimal tuning network is connected to a voltage doubling rectifier circuit using Schottky diodes. A single SOT-363 bridge quad diode package (HSMS-282P) is used for both rectifiers to ensure small size and ease of fabrication. The rectified DC output voltage, V_{rect}, of each rectifier are tied together to a Zener diode (Mfg. part no. BZT585B5V6T-7, 5.6 V_Z), which provides overvoltage protection to the voltage regulator (Mfg. part no. ADP150ACBZ-1.8-R7CT). The voltage regulator provides a stable 1.8 V for Bionode system. Storage capacitors (10 μF) buffer the power supply and minimize ripple on the DC supply lines.

Figure 5.15 shows the normalized (from 0 to 1) simulated PTE performance of the biaxial coil system as a function of angular rotation (theta and phi). The data was acquired through an angular parametric sweep in HFSS. Indeed, only 4 angular conditions (phi = 0°, theta = 90°; phi = 180°, theta = 90°; phi = 0°, theta = 270°; phi = 180°, theta = 270°) result in significant PTE degradation (normalized PTE < 0.3). Consequently, the biaxial system should be implanted in an advantageous orientation to maximize orientation insensitivity when implanted in a freely behaving animal. The normal behavior of a freely moving rodent is characterized by resting or locomotion while on all four limbs. Consequently, a biaxial system implanted in the animal should have the x-axis and associated coil

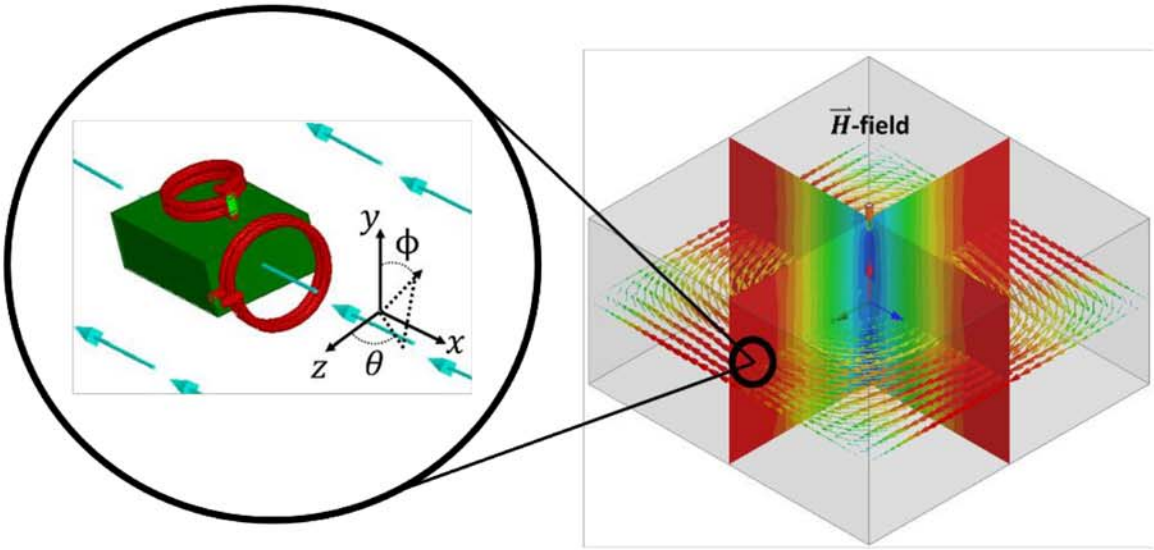

(a)

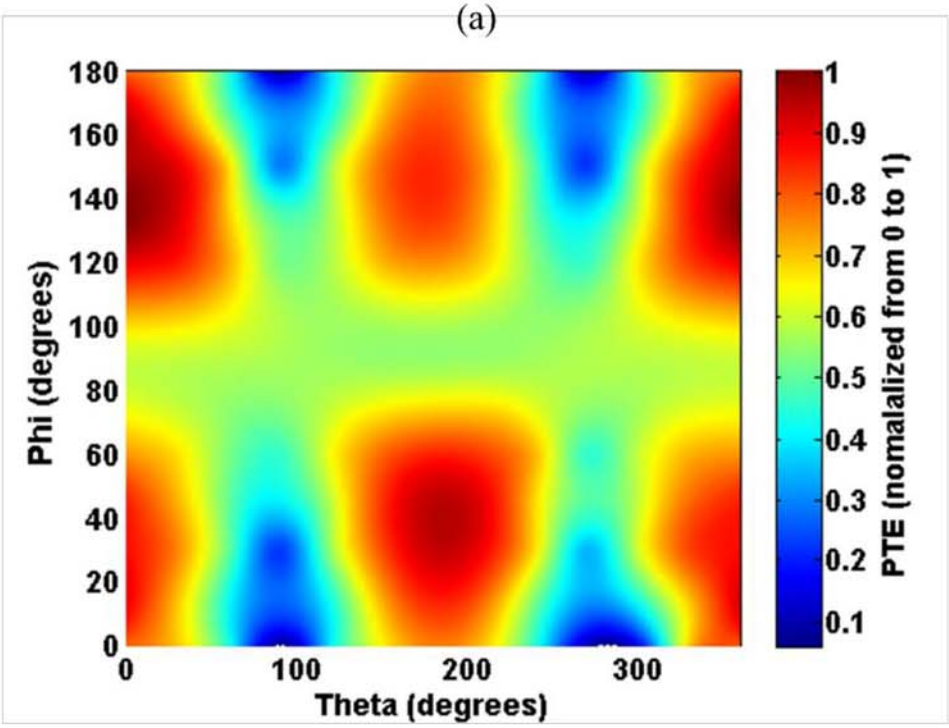

(b)

Figure 5.15 Simulated power receive performance as a function of angular performance of the biaxial arranged Powernode system. (a) Orientation and coordinate reference. (b) Normalized (0 to 1) simulated PTE as a function of angular rotation (theta and phi).

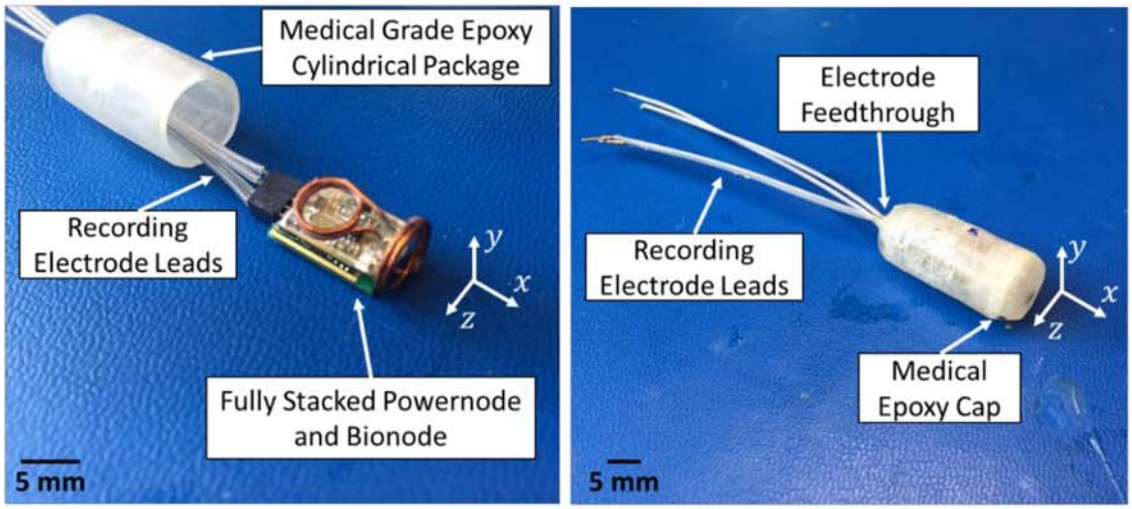

(a) (b)

Figure 5.16 Full system and packaging. (a) Pre-packaged and (b) fully packaged wireless implantable device with biaxial powering capability.

[referenced to coordinate system in Figure 5.15(a)] oriented along the length of the rodent body and the y-axis and associated coil oriented perpendicular to the rodent.

5.4.3 Packaging Design

Figure 5.16 shows the pre-packaged and fully packaged system. A hollow cylinder was formed of biocompatible medical grade epoxy (Loctite® EA M-31CL Adhesive). The cylindrical form factor is advantageous in two respects: it minimizes sharp corners that may injure the animal and it helps ease surgical implantation. The package was designed with an inner diameter (ID) of 10.5 mm (to account for device sticking), an outer diameter (OD) of 14 mm, and a length of 25 mm. The fully stacked Powernode and Bionode system were placed within the epoxy made cylindrical contained and sealed with a medical epoxy lid. An electrode feedthrough was created at the end of the package and sealed with medical grade epoxy.

5.5 Chronic *In-Vivo* Experiment

The functional utility of the cavity resonator WPT system is demonstrated through chronic *in-vivo* experiments involving freely behaving rats. Wireless collection of ECG recordings in a freely behaving animal within the cavity is demonstrated. A powering fidelity metric is introduced to quantify the continuous powering capability of the cavity resonator WPT system.

5.5.1 Surgical Procedure

Two rats, identified as R200 and ER34, weighing 197 g and 263 g, respectively were used in the *in-vivo* experiments. All procedures were approved by the Purdue Animal Care and Use Committee (PACUC) at Purdue University. Aseptic surgical technique was performed prior to and after each rat was anesthetized with isoflurane (0.5% - 3% in 2 L/min O_2) A small incision was made on one side of the animal for device insertion and followed by tunneling to the lateral side for electrode placement (ECG lead II configuration). To ensure adequate orientation insensitivity, the implanted device was anchored to the tissue such that the biaxial coils would be perpendicular to the x and y axes of the cavity (referenced to Figure 5.6) while the animal was in normal or standing position. Following implantation, the animals were sutured accordingly.

5.5.2 *In-vivo* Experimental Setup and Validation

Figure 5.17(a) shows the external view of the *in-vivo* experimental setup. A 335.0 MHz RF signal from a signal generator (Agilent EXG Vector Signal Generator N5172B), was fed into a power amplifier (PA, Mini-Circuits® ZHL-1-2W) connected directly to the

excitation probe of the cavity. The high electric permittivity of biological tissues act to decrease the resonant frequency of the cavity (see Figure 5.9). Thus, to compensate for the animal, the cavity was excited at 335.0 MHz, instead of the calculated and measured frequency of 346.6 MHz. To promote continuous powering, all *in-vivo* experiments were conducted at 2 W input power into the cavity, the maximum rated power output of the PA. In order to robustly capture the telemetered data, the receive antenna of the external base station was placed directly into the cavity. Figure 5.17(b) shows an inside view of the cavity containing rat ER34 (post-operative day 43). Figure 5.18 provides a snapshot of the acquired ECG signal (sampling rate of 2.5 kHz).

5.5.3 Evaluation of Powering Fidelity

A power fidelity metric was developed to evaluate the practical performance capability of the cavity resonator WPT system. The power fidelity metric is given by

$$\%\,On = \frac{no.\,of\ samples\ recieved}{no.\,of\ samples\ expected} \times 100 \qquad 5.2$$

Where the no. of samples expected is determined by the length of the recording session multiplied by the sampling frequency. Since (5.2) is purely a powering fidelity metric, all received samples, including erroneous samples, were included in the calculation.

Figure 5.19 shows the powering fidelity for rat R200 over nine separate recording sessions of varying length up to post-operative day 64. All recording sessions began directly after animal placement and closure of the cavity. This ensured that all powering all powering fidelity measurements captured active, pre-acclimation, exploration

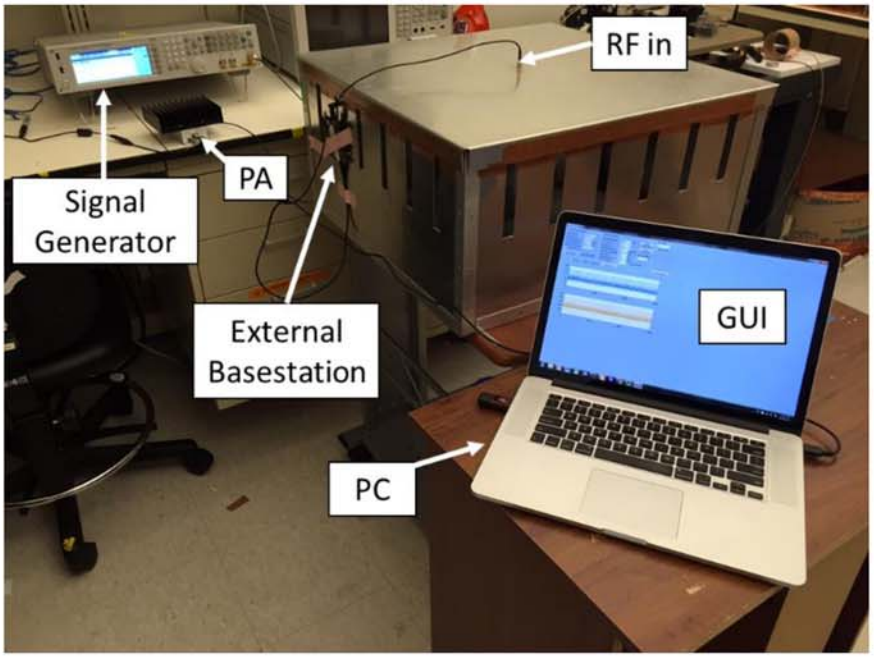

(a)

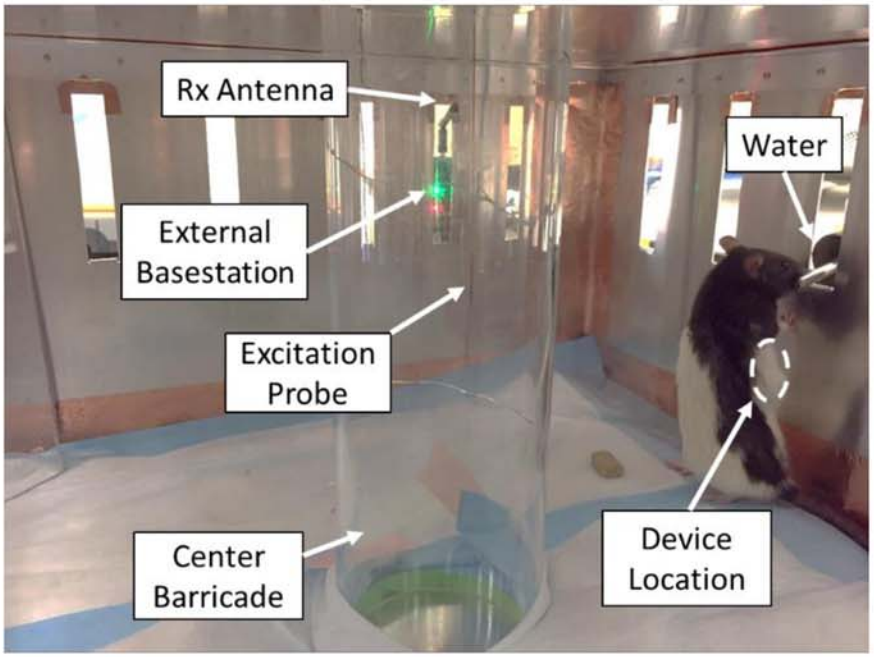

(b)

Figure 5.17 *In-vivo* experimental setup. (a) An external view showing the signal generator, PA, cavity resonator, external base station, and corresponding PC. (b) Inside view of the cavity with a freely behaving rat within (post-operative day 43). The green light on the external base station indicates that the implanted device is on and transmitting data.

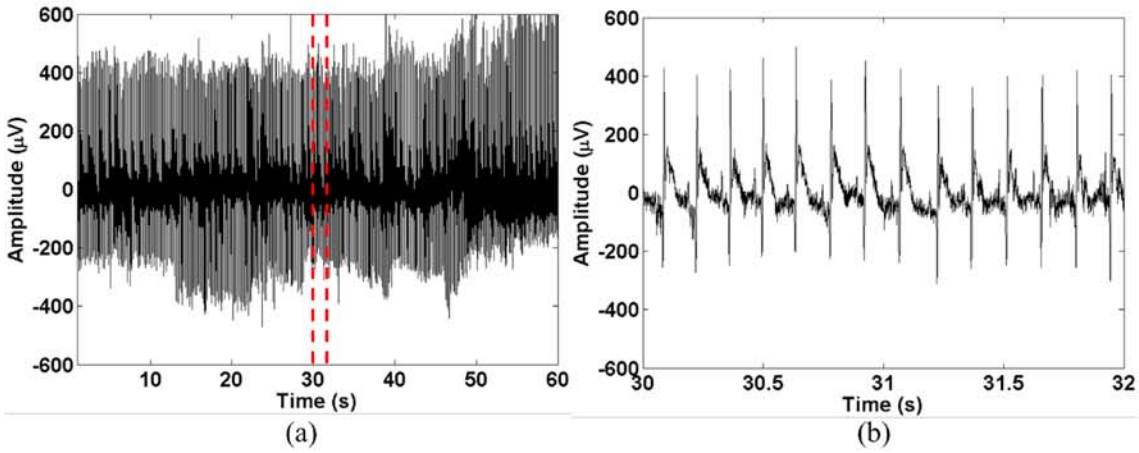

Figure 5.18 Wirelessly acquired rat ECG signal from within the cavity. (a) 60 s window and (b) 2 second zoomed in view (segment between dashed lines).

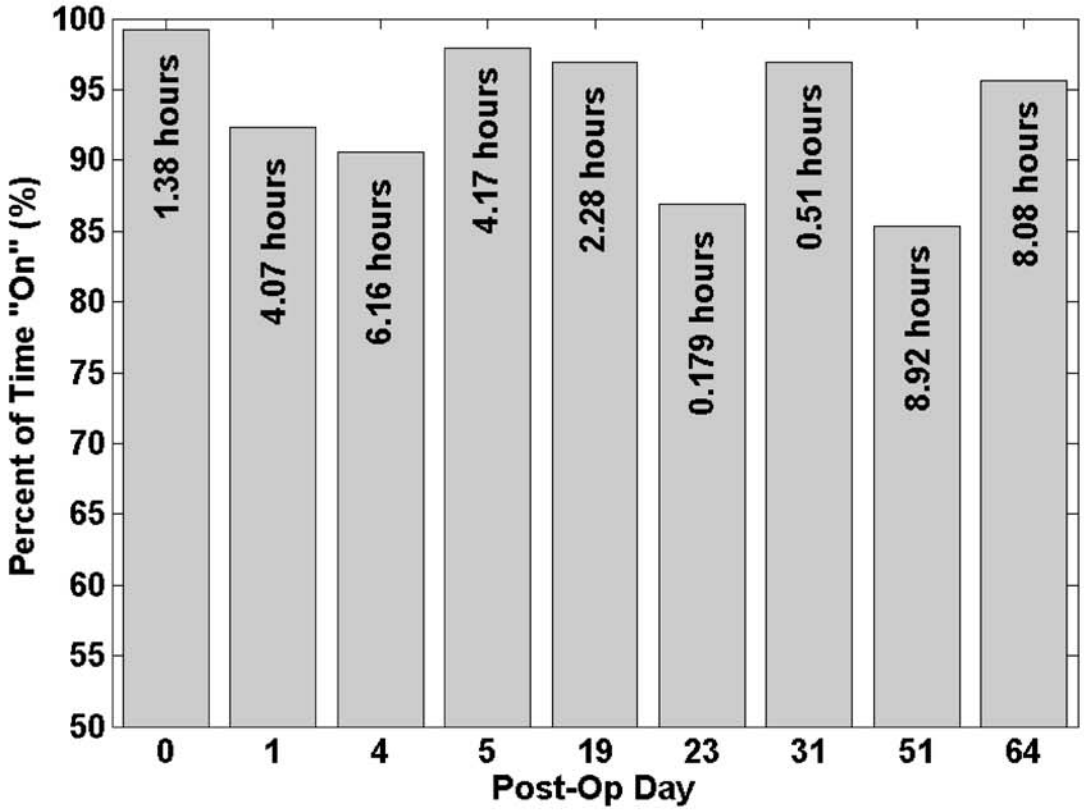

Figure 5.19 Power fidelity distribution for rat R200 over nine separate recording sessions taken over a period of nine weeks. The recording session length is provided in each bar.

behaviors which included standing, walking, and running. During long recording sessions (> 2 hours), where acclimation to the cavity was achieved, animal activities were observed to also include resting behavior which included eating, drinking, grooming, and sleeping. As shown in Figure 5.19, we achieved a maximum powering fidelity of 99.24% for a 1.38-hour recording session. For the longer 8.92-hour and 8.08-hour recording sessions, we achieved a powering fidelity of 85.35% and 95.63%, respectively. Power drop outs were observed to occur when the animal stood at angled positions against the side walls and center barrier where the biaxial system became ineffective at capturing the $\vec{H}$-field of the TM_{110} resonant mode. Overall, across 9 recording sessions, with observed natural exploration and resting behaviors, we achieved an average powering fidelity of 93.53%. Indeed, the biaxial and optimally tuned receive resonator system is sufficient for nearly continuous device operation.

5.5.4 Specific Absorption Rate Considerations

Regulatory agencies such as the FCC measure tissue exposure to RF energy by the specific absorption rate (SAR). Although multiple standards exist, the limits imposed to prevent damage to human tissue by IEEE is 10 W/kg (20 W/kg in extremities) averaged over 10 g of tissue [88]. Although non-human animals do not have such standards, any freely behaving animal environment should not include RF exposure that results in behavioral changes of the animal. Moreover, staying below SAR limits will ensure safety for the user and promote use across the scientific community.

In this work, the cavity was fed with 2 W at 335.0 MHz. This is well below the power and frequency levels associated with similar work which showed safe SAR

exposure as high as 4 W at 1.5 GHz [40]. As this study was operating with lower frequency and lower power with no observed behavioral changes during animal experiments, it is concluded that the animal subjects were within the safe RF exposure limits.

5.5.5 Electromagnetic Interference (EMI) Considerations

As the implanted device is saturated within a high frequency RF field, electromagnetic interference (EMI) may be a significant source of noise. This noise may couple directly onto the AFE resulting in significant signal distortion or complete signal saturation. Thus, proper EMI filtering, either external to the AFE or within the AFE integrated circuits (ICs), should be utilized. The Bionode AFE begins first with a set of instrumentation amplifier ICs (Texas Instruments, INA333). Within the INA333 are built in radio-frequency interference filters (RFI) to minimize susceptibility to RFI. To test the effectiveness of the RFI filters, an experiment was conducted to examine the quality of a known signal input in three testing environments: in cavity, with an external coil outside the cavity, and DC powered outside the cavity. Figure 5.20(a) shows the reconstructed set of input signals (100 Hz, 2 mVpp, AFE gain = 100, sampled at 1kHz) and Figure 5.20(b) shows the corresponding fast Fourier transforms (FFTs). Note that the discontinuities of the signal are due to packet loss. Indeed, signal integrity is maintained when the system is powered on within the cavity, powered wirelessly external from the cavity, and DC powered outside the cavity. Based on these results, it can be concluded that the EMI rejection of the Bionode is sufficient for maintaining signal integrity within the cavity resonator system.

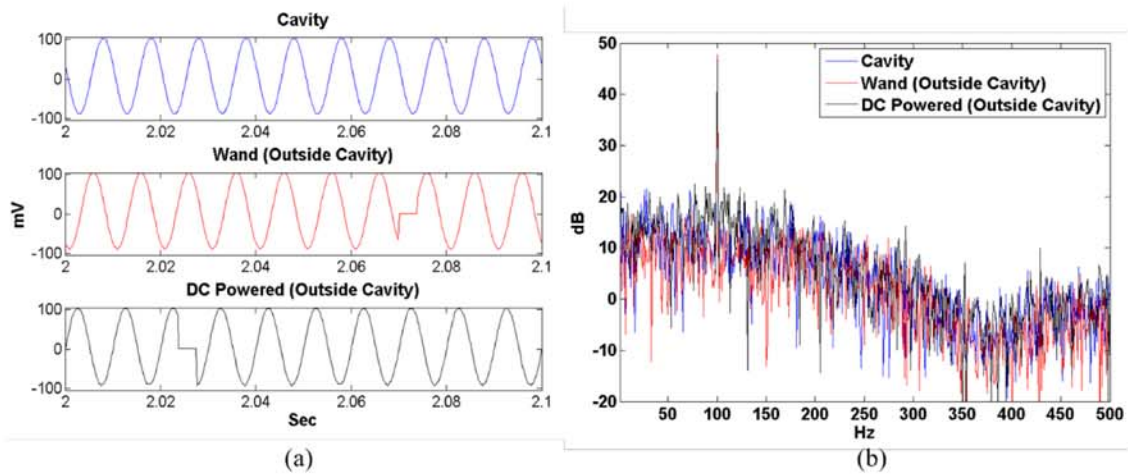

Figure 5.20 EMI testing results. (a) Reconstructed signal (from ADC input, AFE output) under 3 powering and operating conditions. Input signal (into AFE) = 100 Hz sin wave, 2 mVpp, AFE gain = 100. (b) FFT of the 3 powering and operating conditions.

5.6 Conclusion

A novel cavity resonator based WPT system for long-term studies involving freely behaving rats has been presented. Strategic cavity design and construction techniques were presented which maximized its utility as a large, safe, and engaging small animal housing environment while simultaneously maintaining its EM performance for WPT. Maximized WPT performance was achieved by utilizing the optimization methodology developed in Chapter 4. A miniaturized and tunable biaxial receive resonator system, with 7 mm and 5 mm diameter coils was designed to improve orientation insensitivity. As a result, an average powering fidelity of 93.54% to a freely behaving animal, implanted with the Bionode system, within the cavity was achieved. Finally, this chapter is concluded with Figure 5.21, a comparison of this work to prior state-of-the-art WPT

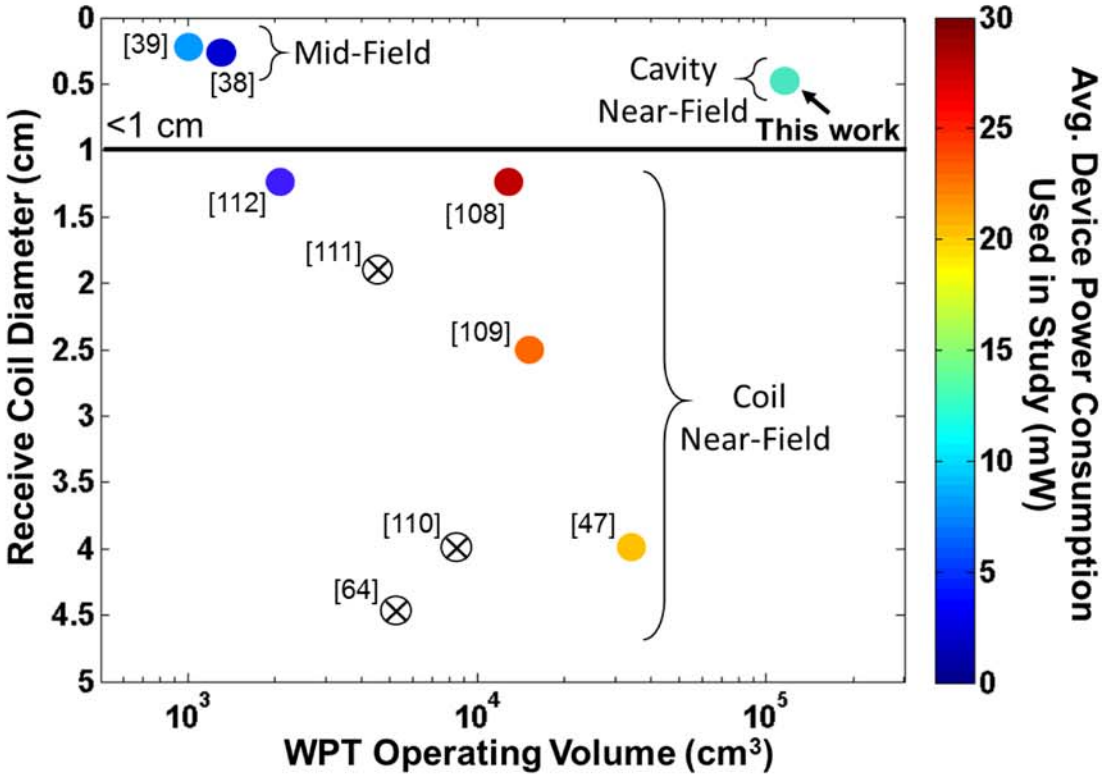

Figure 5.21 Comparison of this work to prior state-of-the-art WPT systems used for small animal experiments. WPT system approaching the upper right corner exhibit the largest operating volume with greatest device miniaturization capability. See Table 5.5 for a description of arena volume calculations for each reference. Circles with an "X" represent references which did not describe or demonstrate wireless powering of a bioelectronics device.

arenas. Table 5.5 summarizes the arena volume calculation for each reference cited in Figure 5.21.

Table 5.5 Calculation of WPT arena volumes shown in Figure 5.21

Reference	Arena Enclosure Shape	Volume Calculation (Cylindrical: $\pi \times r^2 \times h$; Rectangular: $L \times w \times h$)
[103] (Chang et al.)*	Cylindrical	$\pi \times 12.7^2 \times 25.4 = 12870$ cm^3
[47] (Jow et al.)†	Rectangular	$58 \times 61 \times 12 = 42456$ cm^3
[104] (Lee et al.)†	Rectangular	$30 \times 30 \times 17 = 15300$ cm^3
[38] (Yeh et al.)§	Cylindrical	$\pi \times 9^2 \times 5 =$1272.3 cm^3
[105] (Soltani et al.)†	Rectangular	$45 \times 26 \times 7.3 = 8541$ cm^3
[106] (Eom et al.)†	Rectangular	$15 \times 20 \times 15 = 4500$ cm^3
[107] (Kilinc et al.)†	Rectangular	$20 \times 35 \times 3 = 2100$ cm^3
[39] (Montgomery et al.)§	Cylindrical	$\pi \times 10.5^2 \times 3 =$1039.1 cm^3
[111] (Mirbozorgi et al.)†	Rectangular	$30 \times 30 \times 8 = 7200$ cm^3
This Work	Rectangular	$(60.96 \times 60.96 \times 30) -$ Barricaded Volume = 108050 cm^3

*Estimated dimensions based on relative scale between the rat used in study and photograph of WPT enclosure

† Explicitly provided arena dimensions

§ Height dimension determined by the reference's specified maximum height for achieving minimum required WPT performance

CHAPTER 6. CONCLUSION AND FUTURE WORK

6.1 Conclusion

WPT technologies aim to obviate the need for large on-board energy storage elements, or remove them altogether, and help usher in a new era of miniaturization capability for sophisticated bioelectronics. In human clinical applications, device miniaturization means minimized invasiveness, minimized disruption, and maximum therapeutic utility. In scientific based discovery applications, device miniaturization means enabling complex neuroscientific studies involving small animals without the confounding variables introduced by the device or environment itself.

Consequently, this dissertation presented a platform methodology for WPT performance control and optimization in filter synthesized coupled resonator based WPT systems and introduced a new platform cavity resonator WPT technology for freely behaving small animal based wireless power transfer experiments.

Chapter 2 presented an exhaustive analytical understanding for predicting and enabling WPT performance optimization and control in filter synthesized coupled resonator based WPT systems. A new figure of merit and new insight into critical coupling control unique to the developed optimization method were developed. The foundation developed in Chapter 2 provided the performance optimization methodology for enabling safe and efficient powering to a myoelectric sensing system which was

presented in Chapter 3. In Chapter 3, a novel anti-Helmholtz arm band coil and requisite optimization methodology to wirelessly power eight surface EMG sensing devices wrapped circumferentially around a patient's arm were presented. The system was demonstrated on an able-bodied subject, enabling the fully wireless operation of a virtual prosthetic arm.

Transitioning from coil to coil based coupled resonator WPT systems, Chapter 4 presented the first filter model, optimization methodology, and design of a cavity resonator based WPT system for bioelectronics. The theory and optimization methodology were experimentally verified using a cylindrical cavity resonator constructed out of copper foil (diameter = 60.96 cm, height = 30 cm) and a 5 cm diameter power receive coil. As a consequence of the developed optimization methodology, a peak PTE of 33.88% was achieved within the cavity. This was approximately 4.4 times greater than what would be achieved without the optimization methodologies developed in this work. An experiment involving porcine ocular tissue and custom designed ultra-miniature rectifier/LED device with a 2 mm diameter receive coil was presented to verify *in-vivo* cavity resonator wireless powering capabilities. A peak PTE of 6.11% was achieved within the porcine eye, representing the highest PTE capability to a 2 mm diameter coil in comparison with reported performances in mid-field WPT technologies. Chapter 5 presented the first small animal housing cavity resonator WPT system for freely-behaving small rodent animal experiments. The small animal housing cavity resonator arena was designed to be cost-effective, achieve practical utility as a small animal housing structure, and achieve sufficient EM performance for WPT applications. Key design considerations included its rectangular shape, aluminum construction, large

physical size (60.96 cm x 60.96 cm x 30.0 cm), viewing/ventilation/water slots, and a removable lid. Additionally, a novel biaxial arranged receive coil (7 mm and 5 mm diameter coils), power management, and biocompatible packaging system were presented. As a result, a successful chronic *in-vivo* experiment involving a rat implanted with the Bionode and biaxial Powernode system was demonstrated. An average powering fidelity of 93.53% was achieved over 9 recording session of varying length. As compared to prior state of the art WPT arenas, this small animal housing cavity resonator WPT system demonstrated the largest freely behaving WPT small animal arena with nearly the smallest receive coils. Thus enabling an entirely new and effective WPT capability for scientific discovery applications involving miniature and sophisticated bioelectronics.

In summary, the work in this dissertation has provided the foundational premise for designing, optimizing, and controlling filter synthesized coupled resonator based WPT systems. Indeed, coupled resonator WPT systems can be formed using coils or cavities. Figure 6.1 provides a graphic summary of the major contributions of this dissertation. Overall, it is the hope of the author that this work will help promote the use and continued exploration of coupled resonator based WPT systems for the advancement of sophisticated bioelectronics miniaturization and the betterment of clinical and scientific based applications.

6.2 Future Work

6.2.1 Cavity Resonator WPT Systems for Freely-Behaving Small Animal Experiments

To further advance the cavity resonator WPT platform, future work should focus on enabling dynamic tuning and frequency tracking capabilities. Dynamic tuning, both on

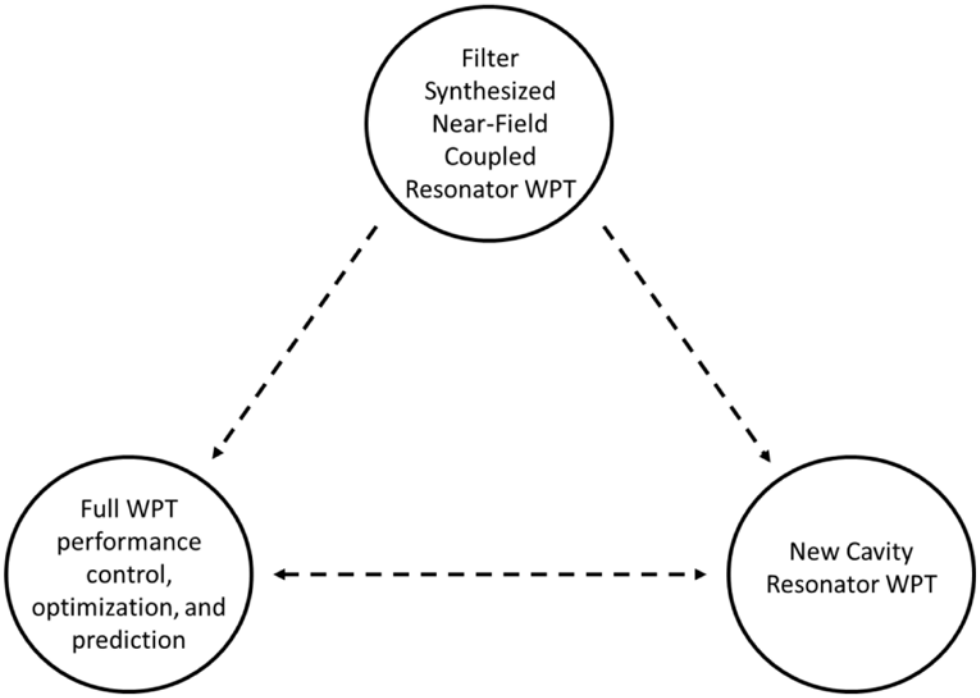

Figure 6.1 Key contribution framework of this research. This research provides a robust and new analytical understanding and optimization methodology of filter synthesized coupled resonator WPT system. The same framework can be extended to cavity resonator WPT systems which were also developed within this research.

board and the cavity, should be designed to maintain maximum achievable PTE a freely behaving animal placed within the cavity. This would improve the freely behaving experiments by enabling further miniaturization of the receive coils. Consequently, a tri-axial receive coil design would be physically practical and may push powering fidelity towards 100%. A tri-axial receive coil system would also greatly simplify the implantation procedure. On board dynamic tuning could be implemented with a miniature on-board capacitor bank while dynamic tuning of the cavity could be implemented with a dynamically varying excitation probe length.

6.2.2 Cavity Resonator WPT System for Potential Human Clinical Applications

The analysis, design, and optimization methodologies for coupled resonator based WPT systems developed in this dissertation were applied to coil to coil and cavity to coil based resonator systems. Indeed, other electrical resonator structures exist, including dielectric resonators. Given that biological tissue exhibits high dielectric constants, it is natural to pose a couple of questions: can the human body, or parts of the human body such as the limbs, be modeled and utilized as a dielectric resonator or waveguide such that EM energy from an external source could couple into it? And, can we leverage the optimization methodology developed in this work to efficiently extract that coupled EM energy into an ultra-miniature implanted receiver? Here, it is shown with preliminary simulations that propagating modes of EM energy can be induced into a simulated human arm model. Using these simulations as a guide, a preliminary experiment, which leveraged the cavity resonator WPT optimization methodology developed in this work, was conducted to demonstrate energy transfer enhancement to a 2 mm diameter receive coil positioned near a liquid tissue phantom representing muscle. An application demonstration was also conducted to demonstrate energy propagation through an able-bodied subjects arm.

6.2.2.1 Evanescent Coupling into Biological Tissue

Figure 6.2 shows the HFSS simulation setup and simulation results demonstrating evanescent field coupling into a simplified human arm model (consisting of only muscle and bone). To the best knowledge of the author, this is the first exploration of evanescent

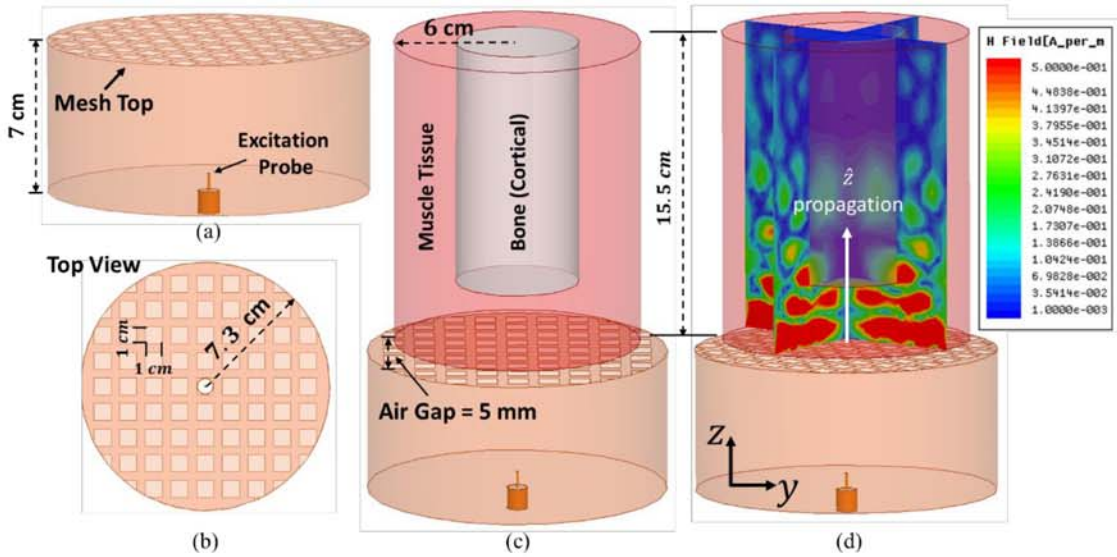

Figure 6.2 Simulations of evanescent field coupling into biological tissue. (a) side view of cavity resonator structure with meshed top. (b) top view showing mesh top. With a radius of 7.3 cm, the dominant mode excitation frequency is 1.57 GHz. (c) Simulation model with cylindrical muscle tissue and bone. A 5 mm air gap exists between the tissue model and cavity mesh. (d) Simulated $\vec{H}$-field distribution within the human arm model. The simulation results indicate that a z-dir. propagating mode can be induced into tissue at 1.57 GHz by evanescent field coupling. Note the attenuation of $\vec{H}$-field in the cortical bone structure.

field coupling into human tissue using a cylindrical cavity resonator structure. This result is critical because it demonstrates that this form of induced energy transfer could be modeled as a system of coupled resonator structures. Consequently, the analysis and optimization methodologies developed in this dissertation could be utilized to maximize the wireless energy transfer. In the simulation model, the cavity resonator structure was designed to with a radius of 7.3 cm resulting in a dominant mode excitation frequency of 1.57 GHz. To generate an evanescent field, the top of the cavity was designed with a mesh consisting of sub-wavelength sized (to minimize radiative losses) 1 cm x 1 cm square slots. This method of evanescent field generation is similar to what has been done previously [40]. As shown in Figure 6.2(d), a propagating mode of EM energy was

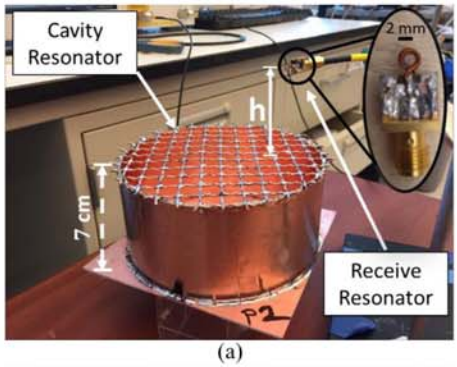

(a)

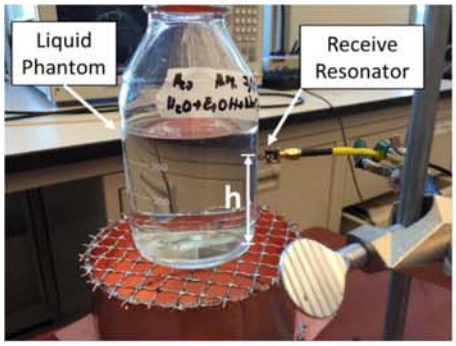

(b)

Condition	Peak $\lvert S_{21} \rvert$ (dB)	Peak PTE (%)
h = 6 cm, no phantom	-33.50	0.0447
h = 6 cm, w/ phantom	-26.051	0.2483
h = 3 cm, no phantom	-29.88	0.1028
h = 3 cm, w/ phantom	-25.74	0.2667

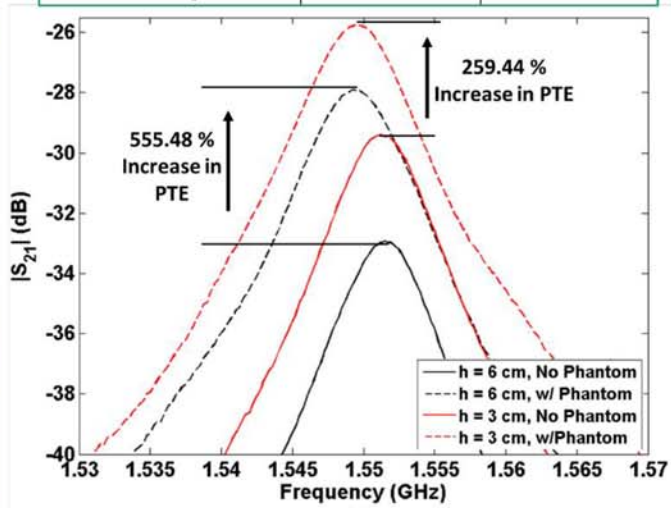

(c)

Figure 6.3 Experimental Demonstration. (a) Experimental setup with constructed cavity resonator structure and receive resonator system (2 mm diameter coil connected to tuning PCB, $C_{pt} = 0.2$ pF, $C_{s2} = 0.2$ pF) located at a height, h, above the surface of the cavity mesh. (b) Experimental setup with a liquid tissue phantom (replicating electrical properties of muscle at 1.6 GHz) on the surface of the mesh. (c) Measured PTE results at h = 6 cm and h = 3 cm with and without the liquid tissue phantom.

induced into the simplified human arm model. Indeed, at 1.57 GHz, the human arm appeared as dielectric waveguide. This conforms to the literature which have shown that propagating modes of energy within biological tissue occurs in the 1.5 GHz to 1.6 GHz frequency ranges [35, 36, 112].

6.2.2.2 Experimental Demonstration

Figure 6.3 shows the constructed cylindrical cavity resonator structure, receive resonator structure, and measured PTE results with and without the presence of liquid

tissue phantom at a height, h, of 3 cm and 6 cm above the cavity resonator. The body of the cavity resonator was constructed out of copper tape, the base was made of a copper cladded FR4 board, and copper wire mesh was utilized to construct the top. The base, body, and mesh were soldered together to help maximize the cavity Q_0, measured to be 884 at 1.55 GHz. The cavity was constructed with the same dimensions described in Figure 6.2(a) and Figure 6.2(b). Leveraging the optimization strategies developed in this dissertation (Chapters 4 and 5), the excitation probe length and receive resonator PCB capacitors were tuned accordingly. The excitation probe length (not shown) was set to a length of 20 cm to ensure that the system became critically coupled with the presence of tissue phantom resting on the mesh. The tuning board PCB was set with a shunt and series capacitance of $C_{pt} = 0.2$ pF and $C_{s2} = 0.2$ pF, respectively. The liquid tissue phantom, exhibiting a complex permittivity (55.1 + 13.5j) mimicking muscle at 1.6 GHz, was formed of 59.30% H_2O, 40.55% Ethanol, and 0.15% NaCl [113].

As shown in Figure 6.3(c), the presence of the liquid tissue phantom drastically improved the measured PTE between the cavity resonator and the tuned receiver constructed with a 2 mm diameter receive coil. At a separation height of 3 cm and 6 cm, PTE was increased by 259.44% and 555.48%, respectively, with the addition of the liquid tissue phantom placed on top of the mesh. These measured results corroborate the EM phenomenon predicted by the simulations. Indeed, EM energy is coupled into the tissue phantom creating a dielectric waveguide resonator from which energy can be extracted and PTEs increased. It is important to note that the measurements with the liquid phantom were taken with the receive coil placed next to the tissue phantom glass container but not inside it. Although a majority of the EM fields are confined within the

Table 6.1 Wireless PTE Comparison using 2 mm diameter receive coils

Reference	**WPT Modality**	**Optimization Methodology**	**Location**	**PTE (2 mm Diameter coil)**
Coil to Coil	Near-field	Coupled resonator developed in this work	5 cm from source in air*	0.0039%
Ho et al. 2014 [35]	Mid-Field	None	5 cm from source into biological tissue	0.036 %
This Work	**Coupled Resonator**	**Coupled resonator developed in this work**	**6 cm from source into liquid tissue phantom**	**0.2483%**

* 14 cm diameter transmit coil, optimized at 6.78 MHz

dielectric waveguide, field components leak from the imperfect conducting boundary of the dielectric liquid and air boundary. Consequently, it is hypothesized that a carefully isolated receive coil placed within the phantom would exhibit improved energy transfer performance as compared to being outside it. Nonetheless, the peak PTE at separation heights of 3 cm and 6 cm were measured to 0.2667% and 0.2483%. Table 6.1 provides a comparison of the achieved result with standard coil to coil and mid-field based methods. Indeed, leveraging the cavity resonator based optimization methodology developed in this dissertation enabled an achieved peak PTE that was approximately two orders of magnitude more efficient than the capability of optimized standard coil to coil based

systems (Tx coil of same size as the cavity resonator and a 2 mm diameter receive coil) and an order of magnitude more efficient than reported in mid-field based technologies.

6.2.2.3 Qualitative Demonstration using a Human Arm

Figure 6.4 shows the experimental method used to qualitatively demonstrate energy coupling into a human arm. The tuned receive resonator, made of a 2 mm diameter coil and tuning PCB, was connected to a voltage doubler rectifier which provided DC power to operate a green LED. As shown in Figure 6.4(a), without the human arm, the LED was non-operational (off) at a separation height of 6.0 cm. However, as shown in Figure 6.4(b), with the human arm, the separation height at which the LED was operational (on) was extended over 3 times. Indeed, energy was coupled into the human arm. Further work is necessary to test the powering capability to safely operate a bioelctronic device implanted within tissue. Nevertheless, these initial results demonstrate the feasibility for optimizing a coupled resonator WPT system formed of a cavity resonator source coupled to a human limb, which in itself can be modeled as a dielectric waveguide resonator. Such a system may enable the feasibility to safely power sophisticated bioelectronics, in ultra-miniaturized form factors, deep within biological tissue.

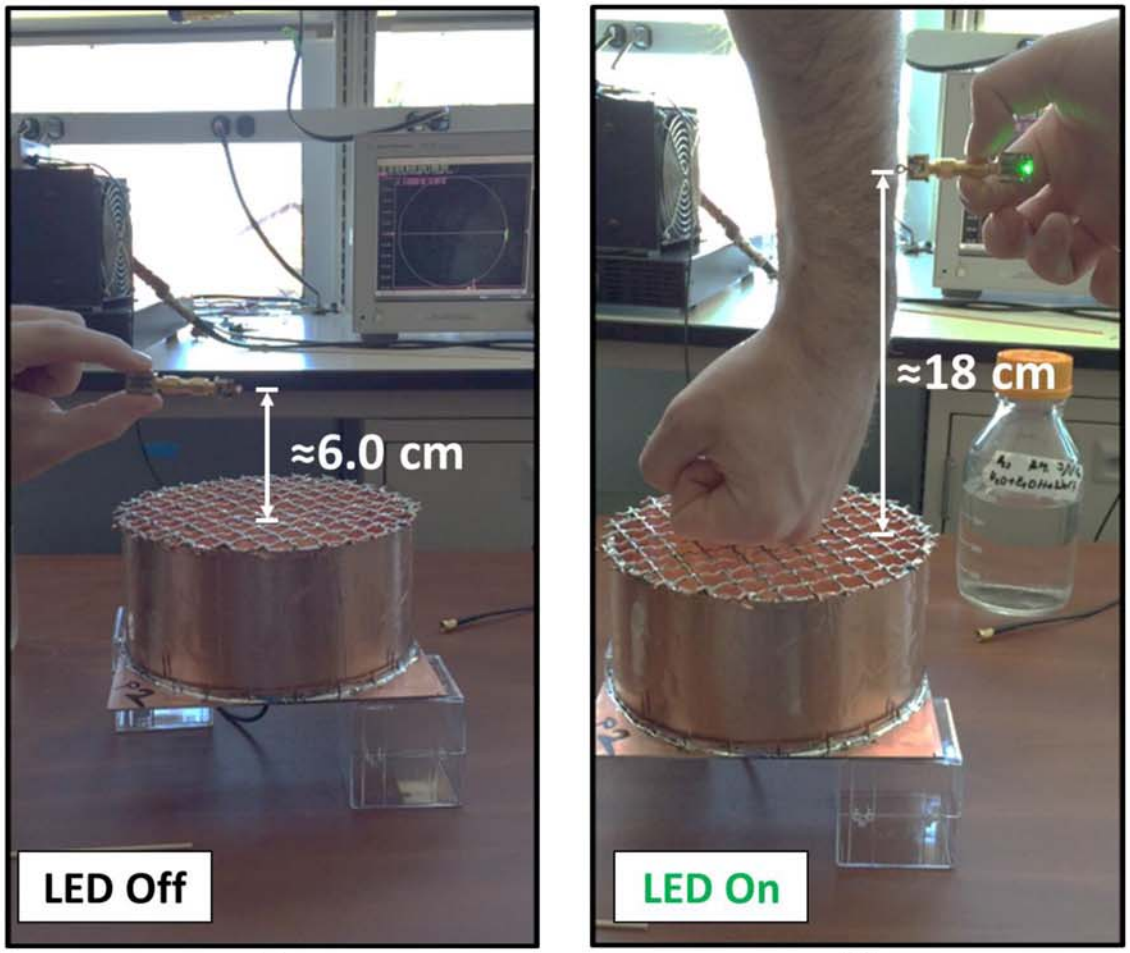

(a) (b)

Figure 6.4 Evanescent field coupling demonstration with and without coupling into a human arm. In both experiments, the input power to the cavity was 6 W at 1.55 GHz. (a) Without the presence of a human arm, wireless power transfer efficiency decays rapidly resulting in the LED being off at a height of approximately 6.0 cm. (b) Acting as a dielectric waveguide, energy is coupled into the human arm and wireless power transfer efficiencies are maintained at a level high enough to operate the LED at > 3 times the height.

LIST OF REFERENCES

LIST OF REFERENCES

[1] J. C. Maxwell, "A Dynamical Theory of the Electromagnetic Field," R. Society, Ed., ed. Philosophical Transactions of the Royal Society, 1865, pp. 459 - 512.

[2] N. Tesla, "Experiments with alternate currents of high potential and high frequency," *Electrical Engineers, Journal of the Institution of,* vol. 21, 1892.

[3] N. Tesla, "The Transmission of Electrical Energy Without Wires as a Means for Furthering Peace ", ed. Electrical World and Engineer: Electrical World and Engineer, 1905, p. 21.

[4] W. C. Brown, "The technology and application of free-space power transmission by microwave beam," *Proceedings of the IEEE,* vol. 62, pp. 11-25, 1974.

[5] W. C. Brown, "Optimization of the Efficiency and Other Properties of the Rectenna Element," *Microwave Symposium, 1976 IEEE-MTT-S International,* pp. 142-144, 1976.

[6] W. C. Brown, "Adapting Microwave Techniques to Help Solve Future Energy Problems," *IEEE Transactions on Microwave Theory and Techniques,* vol. MT21, pp. 753-763, 1973 1973.

[7] H. Beck, W. E. Boden, S. Patibandla, D. Kireyev, V. Gupta, F. Campagna*, et al.*, "50th Anniversary of the First Successful Permanent Pacemaker Implantation in the United States: Historical Review and Future Directions," *American Journal of Cardiology,* vol. 106, pp. 810-818, Sep 2010.

[8] S. Reardon, "Electroceuticals spark interest," *Nature,* vol. 511, pp. 18-18, Jul 2014.

[9] K. Famm, B. Litt, K. J. Tracey, E. S. Boyden, and M. Slaoui, "A jump-start for electroceuticals," *Nature,* vol. 496, pp. 159-161, Apr 2013.

[10] H. Mei and P. P. Irazoqui, "Miniaturizing wireless implants," *Nature Biotechnology,* vol. 32, pp. 1008-1010, Oct 2014.

[11] C. Dagdeviren, B. D. Yang, Y. Su, P. L. Tran, P. Joe, E. Anderson*, et al.*, "Conformal piezoelectric energy harvesting and storage from motions of the heart, lung, and diaphragm," *Proceedings of the National Academy of Sciences of the United States of America,* vol. 111, pp. 1927-1932, Feb 4 2014.

[12] C. A. Balanis, *Antenna Theory: Analysis and Design*, Third ed.: John Wiley & Sons, Inc., 2005.

[13] J. L. Volakis, C.-C. Chen, and K. Fujimoto, *Small Antennas: Miniaturization Techniques & Applications*: McGraw-Hill Companies, 2010.

[14] A. V. Vorst, A. Rosen, and Y. Kotsuka, *RF/Microwave Interaction Mechanisms in Biological Materials*, John Wiley & Sons, Inc., 2006.

[15] L. J. Chu, "Physical limitations of omni-directional antennas," *J. Appl. Phys,* vol. 19, pp. 1163-1175, 1948.

[16] H. A. Wheeler, "Fundamental limitations of small antennas," *Proceedings of the Institute of Radio Engineers,* vol. 35, pp. 1479-1484, 1947 1947.

[17] J. S. McLean, "A re-examination of the fundamental limits on the radiation Q of electrically small antennas," *IEEE Transactions on Antennas and Propagation,* vol. 44, pp. 672-676, May 1996.

[18] J. J. Adams, E. B. Duoss, T. F. Malkowski, M. J. Motala, B. Y. Ahn, R. G. Nuzzo*, et al.*, "Conformal Printing of Electrically Small Antennas on Three-Dimensional Surfaces," *Advanced Materials,* vol. 23, pp. 1335-1340, Mar 2011.

[19] J. J. Adams, S. C. Slimmer, T. F. Malkowski, E. B. Duoss, J. A. Lewis, and J. T. Bernhard, "Comparison of Spherical Antennas Fabricated via Conformal Printing: Helix, Meanderline, and Hybrid Designs," *IEEE Antennas and Wireless Propagation Letters,* vol. 10, pp. 1425-1428, 2011 2011.

[20] C. Pfeiffer, X. Xu, S. R. Forrest, and A. Grbic, "Direct Transfer Patterning of Electrically Small Antennas onto Three-Dimensionally Contoured Substrates," *Advanced Materials,* vol. 24, pp. 1166-1170, Mar 2 2012.

[21] P. M. Izdebski, H. Rajagopalan, and Y. Rahmat-Samii, "Conformal Ingestible Capsule Antenna: A Novel Chandelier Meandered Design," *IEEE Transactions on Antennas and Propagation,* vol. 57, pp. 900-909, Apr 2009.

[22] J. Abadia, F. Merli, J.-F. Zuercher, J. R. Mosig, A. K. Skrivervik, and IEEE, "3D-Spiral Small Antenna for Biomedical Transmission operating within the MICS band," *2009 3rd European Conference on Antennas and Propagation, Vols 1-6,* pp. 1765-1769, 2009 2009.

[23] T. Karacolak, A. Z. Hood, and E. Topsakal, "Design of a dual-band implantable antenna and development of skin mimicking gels for continuous glucose monitoring," *IEEE Transactions on Microwave Theory and Techniques,* vol. 56, pp. 1001-1008, Apr 2008.

[24] P. Soontornpipit, C. M. Furse, and Y. C. Chung, "Design of implantable microstrip antenna for communication with medical implants," *IEEE Transactions on Microwave Theory and Techniques,* vol. 52, pp. 1944-1951, Aug 2004.

[25] F. Merli, L. Bolomey, J.-F. Zuercher, G. Corradini, E. Meurville, and A. K. Skrivervik, "Design, Realization and Measurements of a Miniature Antenna for Implantable Wireless Communication Systems," *IEEE Transactions on Antennas and Propagation,* vol. 59, pp. 3544-3555, Oct 2011.

[26] T.-F. Chien, H.-C. Yang, C.-M. Cheng, and C.-H. Luo, "Develop CPW-Fed Monopole Broadband Implantable Antennas on the High Dielectric Constant Ceramic Substrates," *Microwave and Optical Technology Letters,* vol. 52, pp. 2136-2139, Sep 2010.

[27] C.-L. Yang, C.-L. Tsai, and S.-H. Chen, "Implantable High-Gain Dental Antennas for Minimally Invasive Biomedical Devices," *IEEE Transactions on Antennas and Propagation,* vol. 61, pp. 2380-2387, May 2013.

[28] C. M. Lee, T. C. Yo, C. H. Luo, C. H. Tu, and Y. Z. Juang, "Compact broadband stacked implantable antenna for biotelemetry with medical devices," *Electronics Letters,* vol. 43, pp. 660-662, Jun 7 2007.

[29] K. Gosalia, G. Lazzi, and M. Humayun, "Investigation of a microwave data telemetry link for a retinal prosthesis," *IEEE Transactions on Microwave Theory and Techniques,* vol. 52, pp. 1925-1933, Aug 2004.

[30] R. A. Bercich, D. R. Duffy, and P. P. Irazoqui, "Far-Field RF Powering of Implantable Devices: Safety Considerations," *IEEE Transactions on Biomedical Engineering,* vol. 60, pp. 2107-2112, Aug 2013.

[31] J. Pandey, Y.-T. Liao, A. Lingley, R. Mirjalili, B. Parviz, and B. P. Otis, "A Fully Integrated RF-Powered Contact Lens With a Single Element Display," *IEEE Transactions on Biomedical Circuits and Systems,* vol. 4, pp. 454-461, Dec 2010.

[32] E. Y. Chow, A. L. Chlebowski, and P. P. Irazoqui, "A Miniature-Implantable RF-Wireless Active Glaucoma Intraocular Pressure Monitor," *IEEE Transactions on Biomedical Circuits and Systems,* vol. 4, pp. 340-349, Dec 2010.

[33] C. Dagdeviren, Y. Su, P. Joe, R. Yona, Y. Liu, Y.-S. Kim*, et al.*, "Conformable amplified lead zirconate titanate sensors with enhanced piezoelectric response for cutaneous pressure monitoring," *Nature Communications,* vol. 5, Aug 2014.

[34] H. Bhamra, Y. Kim, J. Joseph, J. Lynch, O. Z. Gall, H. Mei*, et al.*, "A 24 µW, Batteryless, Crystal-free, Multinode Synchronized SoC "Bionode" for Wireless Prosthesis Control (Accepted)," *IEEE Journal of Solid-State Circuits,* 2015.

[35] J. S. Ho, A. J. Yeh, E. Neofytou, S. Kim, Y. Tanabe, B. Patlolla*, et al.*, "Wireless power transfer to deep-tissue microimplants," *Proceedings of the National Academy of Sciences of the United States of America,* vol. 111, pp. 7974-7979, Jun 2014.

[36] A. S. Y. Poon, S. O'Driscoll, and T. H. Meng, "Optimal Frequency for Wireless Power Transmission Into Dispersive Tissue," *IEEE Transactions on Antennas and Propagation,* vol. 58, pp. 1739-1750, May 2010.

[37] S. Kim, J. S. Ho, and A. S. Y. Poon, "Midfield Wireless Powering of Subwavelength Autonomous Devices," *Physical Review Letters,* vol. 110, May 17 2013.

[38] A. J. Yeh, J. S. Ho, Y. Tanabe, E. Neofytou, R. E. Beygui, and A. S. Y. Poon, "Wirelessly powering miniature implants for optogenetic stimulation," *Applied Physics Letters,* vol. 103, Oct 14 2013.

[39] K. L. Montgomery, A. J. Yeh, J. S. Ho, V. Tsao, S. Mohan Iyer, L. Grosenick*, et al.*, "Wirelessly powered, fully internal optogenetics for brain, spinal and peripheral circuits in mice," *Nat Meth,* vol. 12, pp. 969-974, 10//print 2015.

[40] J. S. Ho, Y. Tanabe, S. M. Iyer, A. J. Christensen, L. Grosenick, K. Deisseroth*, et al.*, "Self-Tracking Energy Transfer for Neural Stimulation in Untethered Mice," *Physical Review Applied,* vol. 4, Aug 2015.

[41] M. N. O. Sadiku, *Elements of Electromagnetics*, 5th ed.: Oxford University Press, 2010.

[42] B. W. Flynn and K. Fotopoulou, "Rectifying Loose Coils," *IEEE Microwave Magazine,* vol. 14, pp. 48-54, Mar-Apr 2013.

[43] T. H. Lee, *Planar Microwave Engineering A Practical Guide to Theory, Measurements, and Circuits*: Cambridge University Press, 2004.

[44] B. H. Waters, A. P. Sample, P. Bonde, and J. R. Smith, "Powering a Ventricular Assist Device (VAD) With the Free-Range Resonant Electrical Energy Delivery (FREE-D) System," *Proceedings of the IEEE,* vol. 100, pp. 138-149, Jan 2012.

[45] S. B. Lee, H. M. Lee, M. Kiani, U. M. Jow, and M. Ghovanloo, "An Inductively Powered Scalable 32-Channel Wireless Neural Recording System-on-a-Chip for Neuroscience Applications," *IEEE Transactions on Biomedical Circuits and Systems,* vol. 4, pp. 360-371, Dec 2010.

[46] U. M. Jow and M. Ghovanloo, "Geometrical Design of a Scalable Overlapping Planar Spiral Coil Array to Generate a Homogeneous Magnetic Field," *IEEE Transactions on Magnetics,* vol. 49, pp. 2933-2945, Jun 2013.

[47] U.-M. Jow, P. McMenamin, M. Kiani, J. R. Manns, and M. Ghovanloo, "EnerCage: A Smart Experimental Arena With Scalable Architecture for Behavioral Experiments," *IEEE Transactions on Biomedical Engineering,* vol. 61, pp. 139-148, Jan 2014.

[48] D. S. Ricketts, M. J. Chabalko, and A. Hillenius, "Experimental demonstration of the equivalence of inductive and strongly coupled magnetic resonance wireless power transfer," *Applied Physics Letters,* vol. 102, Feb 4 2013.

[49] A. Kurs, A. Karalis, R. Moffatt, J. D. Joannopoulos, P. Fisher, and M. Soljacic, "Wireless power transfer via strongly coupled magnetic resonances," *Science,* vol. 317, pp. 83-86, Jul 6 2007.

[50] A. P. Sample, D. A. Meyer, and J. R. Smith, "Analysis, Experimental Results, and Range Adaptation of Magnetically Coupled Resonators for Wireless Power Transfer," *IEEE Transactions on Industrial Electronics,* vol. 58, pp. 544-554, Feb 2011.

[51] S. Cheon, Y. H. Kim, S. Y. Kang, M. L. Lee, J. M. Lee, and T. Zyung, "Circuit-Model-Based Analysis of a Wireless Energy-Transfer System via Coupled Magnetic Resonances," *IEEE Transactions on Industrial Electronics,* vol. 58, pp. 2906-2914, Jul 2011.

[52] J. Kim, W. S. Choi, and J. Jeong, "Loop Switching Technique for Wireless Power Transfer Using Magnetic Resonance Coupling," *Progress in Electromagnetics Research-Pier,* vol. 138, pp. 197-209, 2013.

[53] D. Thuc Phi and J.-W. Lee, "Experimental Results of High-Efficiency Resonant Coupling Wireless Power Transfer Using a Variable Coupling Method," *IEEE Microwave and Wireless Components Letters,* vol. 21, pp. 442-444, Aug 2011.

[54] I. Awai and T. Ishizaki, "Superiority of BPF theory for design of coupled resonator WPT systems," in *Microwave Conference Proceedings (APMC)*, Asia-Pacific, 2011, pp. 1889-1892.

[55] I. Awai and T. Ishizaki, "Design of "Magnetic Resonance Type" WPT Systems Based on Filter Theory," *Electronics and Communications in Japan,* vol. 96, pp. 1-11, Oct 2013.

[56] D. Ha, T.-C. Lee, D. J. Weber, and W. J. Chappell, "Power distribution to multiple implanted sensor devices using a multiport bandpass filter (BPF) approach," presented at the Microwave Symposium (IMS), 2014 IEEE MTT-S International, Tampa, FL, 2014.

[57] J. Lee, Y. S. Lim, W. J. Yang, and S. O. Lim, "Wireless Power Transfer System Adaptive to Change in Coil Separation," *IEEE Transactions on Antennas and Propagation,* vol. 62, pp. 889-897, Feb 2014.

[58] J. Lee, Y. Lim, H. Ahn, J.-D. Yu, and S.-O. Lim, "Impedance-Matched Wireless Power Transfer Systems Using an Arbitrary Number of Coils With Flexible Coil Positioning," *IEEE Antennas and Wireless Propagation Letters,* vol. 13, pp. 1207-1210, 2014 2014.

[59] D. Ha, "Harmonic-Based Wireless Pressure Sensor and Wireless Power Transfer System for Implantable Wireless Sensor Networks," Ph.D., ECE, Purdue University, 2014.

[60] K. K. Ean, B. T. Chuan, T. Imura, and Y. Hori, "Novel band-pass filter model for multi-receiver wireless power transfer via magnetic resonance coupling and power division," presented at the Wireless and Microwave Technology Conference (WAMI-CON), 2012 IEEE 13th Annual, 2012.

[61] D. M. Pozar, *Microwave Engineering*, 4 ed.: John Wiley & Sons, Inc., 2012.

[62] J.-S. Hong, *Microstrip Filters for RF/Microwave Applications*, 2nd ed.: John Wiley & Sons, Inc., 2011.

[63] T. C. Lee, J. Lee, and D. Peroulis, "Dynamic Bandpass Filter Shape and Interference Cancellation Control Utilizing Bandpass-Bandstop Filter Cascade," *IEEE Transactions on Microwave Theory and Techniques,* vol. 63, pp. 2526-2539, Aug 2015.

[64] R. J. Cameron, C. M. Kudsia, and R. R. Mansour, *Microwave Filters for Communication Systems: Fundamentals, Design, and Application*: Wiley-Interscience, 2007.

[65] T. C. Beh, M. Kato, T. Imura, S. Oh, and Y. Hori, "Automated Impedance Matching System for Robust Wireless Power Transfer via Magnetic Resonance Coupling," *IEEE Transactions on Industrial Electronics,* vol. 60, pp. 3689-3698, Sep 2013.

[66] W. S. Lee, H. L. Lee, K. S. Oh, and J. W. Yu, "Switchable Distance-Based Impedance Matching Networks for Tunable HF System," *Progress in Electromagnetics Research-Pier,* vol. 128, pp. 19-34, 2012.

[67] B. H. Waters, A. P. Sample, and J. R. Smith, "Adaptive Impedance Matching for Magnetically Coupled Resonators," *Piers 2012 Moscow: Progress in Electromagnetics Research Symposium,* pp. 694-701, 2012 2012.

[68] A. P. Sample, B. H. Waters, S. T. Wisdom, and J. R. Smith, "Enabling Seamless Wireless Power Delivery in Dynamic Environments," *Proceedings of the IEEE,* vol. 101, pp. 1343-1358, Jun 2013.

[69] Y. Lim, H. Tang, S. Lim, and J. Park, "An Adaptive Impedance-Matching Network Based on a Novel Capacitor Matrix for Wireless Power Transfer," *IEEE Transactions on Power Electronics,* vol. 29, pp. 4403-4413, Aug 2014.

[70] J. Kim, D.-H. Kim, and Y.-J. Park, "Analysis of Capacitive Impedance Matching Networks for Simultaneous Wireless Power Transfer to Multiple Devices," *IEEE Transactions on Industrial Electronics,* vol. 62, pp. 2807-2813, May 2015 2015.

[71] X. Liu, L. P. B. Katehi, W. J. Chappell, and D. Peroulis, "High-Q Tunable Microwave Cavity Resonators and Filters Using SOI-Based RF MEMS Tuners," *Journal of Microelectromechanical Systems,* vol. 19, pp. 774-784, Aug 2010.

[72] H. Joshi, H. H. Sigmarsson, D. Peroulis, W. J. Chappell, and IEEE, "Highly loaded evanescent cavities for widely tunable high-Q filters," *2007 IEEE/Mtt-S International Microwave Symposium Digest, Vols 1-6,* pp. 2124-2127, 2007 2007.

[73] U.-M. Jow and M. Ghovanloo, "Modeling and Optimization of Printed Spiral Coils in Air, Saline, and Muscle Tissue Environments," *IEEE Transactions on Biomedical Circuits and Systems,* vol. 3, pp. 339-347, Oct 2009.

[74] T. C. Beh, T. Imura, M. Kato, Y. Hori, and IEEE, "Basic Study of Improving Efficiency of Wireless Power Transfer via Magnetic Resonance Coupling Based on Impedance Matching," *IEEE International Symposium on Industrial Electronics (Isie 2010),* pp. 2011-2016, 2010.

[75] R. J. Cameron, "General coupling matrix synthesis methods for Chebyshev filtering functions," *IEEE Transactions on Microwave Theory and Techniques,* vol. 47, pp. 433-442, Apr 1999.

[76] B. L. Cannon, J. F. Hoburg, D. D. Stancil, and S. C. Goldstein, "Magnetic Resonant Coupling As a Potential Means for Wireless Power Transfer to Multiple Small Receivers," *IEEE Transactions on Power Electronics,* vol. 24, pp. 1819-1825, Jul 2009.

[77] F. E. Terman, *Radio Engineers' Handbook*, 1st ed.: McGraw-Hill Book Company, Inc., 1943.

[78] R. A. Bercich, S. T. Lee, D. J. Pederson, Z. Wang, M. A. Arafat, H. Mei*, et al.*, "Bionode for Fully Wireless Recording and Stimulating of Bioelectric Events in Rodents within a Large Volume Cavity Resonator (Submitted)," *IEEE Transactions on Biomedical Engineering,* 2016.

[79] W. Zhong, C. K. Lee, and S. Y. R. Hui, "General Analysis on the Use of Tesla's Resonators in Domino Forms for Wireless Power Transfer," *IEEE Transactions on Industrial Electronics,* vol. 60, pp. 261-270, Jan 2013.

[80] S. T. Lee, "Wireless Tools for Neuromodulation," Doctor of Philosophy, Biomedical Engineering, Purdue University, 2015.

[81] M. Ortiz-Catalan, B. Hakansson, and R. Branemark, "An osseointegrated human-machine gateway for long-term sensory feedback and motor control of artificial limbs," *Science Translational Medicine,* vol. 6, Oct 8 2014.

[82] P. F. Pasquina, M. Evangelista, A. J. Carvalho, J. Lockhart, S. Griffin, G. Nanos*, et al.*, "First-in-man demonstration of a fully implanted myoelectric sensors system to control an advanced electromechanical prosthetic hand," *Journal of Neuroscience Methods,* vol. 244, pp. 85-93, Apr 15 2015.

[83] M. Soma, D. C. Galbraith, and R. L. White, "Radiofrequency Coils in Implantable Devices - Misalignment Analysis and Design Procedure," *IEEE Transactions on Biomedical Engineering,* vol. 34, pp. 276-282, Apr 1987.

[84] G. Vandevoorde and R. Puers, "Wireless energy transfer for stand-alone systems: a comparison between low and high power applicability," *Sensors and Actuators a-Physical,* vol. 92, pp. 305-311, Aug 1 2001.

[85] B. Hudgins, P. Parker, and R. N. Scott, "A New Strategy for Multifunction Myoelectric Control," *IEEE Transactions on Biomedical Engineering,* vol. 40, pp. 82-94, Jan 1993.

[86] D. L. Means, "Evaluating Compliance with FCC Guidelines for Human Exposure to Radiofrequency Electromagnetic Fields," K. W. Chan, Ed., 01-01 ed. Federal Communications Commission Office of Engineering and Technology, Tech. Rep.: Federal Communications Commission Office of Engineering and Technology, Tech. Rep., 2001.

[87] R. F. Cleveland and IEEE, "Compliance with FCC exposure guidelines for radiofrequency electromagnetic fields," *2004 International Symposium on Electromagnetic Compatibility, Symposium Record 1-3,* pp. 1030-1035, 2004 2004.

[88] I. S. C95.1, "IEEE Standard for Safety Levels with Respect to Human Exposure to Radio Frequency Electromagnetic Fields," ed, 2005.

[89] ICNIRP, "ICNIRP Guidelines for Limiting Exposure to Time-Varying Electric, Magnetic, and Electromagnetic Fields (up to 300 GHz)," ed, 1998.

[90] D. Psychogiou, D. Peroulis, Y. Li, and C. Hafner, "V-band bandpass filter with continuously variable centre frequency," *Iet Microwaves Antennas & Propagation,* vol. 7, pp. 701-707, Jun 5 2013.

[91] S. Gabriel, R. W. Lau, and C. Gabriel, "The dielectric properties of biological tissues .3. Parametric models for the dielectric spectrum of tissues," *Physics in Medicine and Biology,* vol. 41, pp. 2271-2293, Nov 1996.

[92] S. Gabriel, R. W. Lau, and C. Gabriel, "The dielectric properties of biological tissues .2. Measurements in the frequency range 10 Hz to 20 GHz," *Physics in Medicine and Biology,* vol. 41, pp. 2251-2269, Nov 1996.

[93] C. Gabriel, S. Gabriel, and E. Corthout, "The dielectric properties of biological tissues .1. Literature survey," *Physics in Medicine and Biology,* vol. 41, pp. 2231-2249, Nov 1996.

[94] S. Ramo, J. R. Whinnery, and T. Van Duzer, *Fields and Waves in Communication Electronics*, 3rd ed.: John Wiley & Sons, INC., 1965.

[95] P. Couffignal, J. Obregon, and H. Baudrand, "Equivalent-Circuit of a Cavity Coupled to a Feeding Line and its Dependence on the Electric or Magnetic Nature of Output Coupling Structure," *Iee Proceedings-H Microwaves Antennas and Propagation,* vol. 139, pp. 221-226, Jun 1992.

[96] D. Kajfez and E. J. Hwan, "Q-factor measurement with network analyzer," *IEEE Transactions on Microwave Theory and Techniques,* vol. 32, pp. 666-670, 1984.

[97] D. Kajfez, *Q Factor Measurements Using MATLAB*: Artech House, 2011.

[98] D. A. Hill, *Electromagnetic Fields in Cavities: Deterministic and Statistical Theories*: Wiley-IEEE Press, 2009.

[99] S. T. Lee, P. A. Williams, C. E. Braine, D.-T. Lin, S. W. M. John, and P. P. Irazoqui, "A Miniature, Fiber-Coupled, Wireless, Deep-Brain Optogenetic Stimulator," *IEEE Transactions on Neural Systems and Rehabilitation Engineering,* vol. 23, pp. 655-664, Jul 2015.

[100] Q. Xu, D. Hu, B. Duan, and J. He, "A Fully Implantable Stimulator With Wireless Power and Data Transmission for Experimental Investigation of Epidural Spinal Cord Stimulation," *IEEE Transactions on Neural Systems and Rehabilitation Engineering,* vol. 23, pp. 683-692, Jul 2015.

[101] T. A. Szuts, V. Fadeyev, S. Kachiguine, A. Sher, M. V. Grivich, M. Agrochao*, et al.*, "A wireless multi-channel neural amplifier for freely moving animals," *Nature Neuroscience,* vol. 14, pp. 263-U363, Feb 2011.

[102] D. Fan, D. Rich, T. Holtzman, P. Ruther, J. W. Dalley, A. Lopez*, et al.*, "A Wireless Multi-Channel Recording System for Freely Behaving Mice and Rats," *Plos One,* vol. 6, Jul 12 2011.

[103] C.-W. Chang and J.-C. Chiou, "A Wireless and Batteryless Microsystem with Implantable Grid Electrode/3-Dimensional Probe Array for ECoG and Extracellular Neural Recording in Rats," *Sensors,* vol. 13, pp. 4624-4639, Apr 2013.

[104] B. Lee, M. Kiani, and M. Ghovanloo, "A Smart Wirelessly Powered Homecage for Long-Term High-Throughput Behavioral Experiments," *IEEE Sensors Journal,* vol. 15, pp. 4905-4916, Sep 2015.

[105] N. Soltani, M. S. Aliroteh, R. Genov, and IEEE, "Cellular Inductive Powering System for Weakly-Linked Resonant Rodent Implants," in *IEEE Biomedical Circuits and Systems Conference (BioCAS)*, Rotterdam, Netherlands, 2013, pp. 350-353.

[106] K. Eom, J. Jeong, T. H. Lee, J. Kim, J. Kim, S. E. Lee*, et al.*, "A wireless power transmission system for implantable devices in freely moving rodents," *Medical & Biological Engineering & Computing,* vol. 52, pp. 639-651, Aug 2014.

[107] E. G. Kilinc, G. Conus, C. Weber, B. Kawkabani, F. Maloberti, and C. Dehollain, "A System for Wireless Power Transfer of Micro-Systems In-Vivo Implantable in Freely Moving Animals," *IEEE Sensors Journal,* vol. 14, pp. 522-531, Feb 2014.

[108] K. L. Montgomery, A. J. Yeh, J. S. Ho, V. Tsao, S. Mohan Iyer, L. Grosenick*, et al.*, "Wirelessly powered, fully internal optogenetics for brain, spinal and peripheral circuits in mice," *Nat Meth,* vol. advance online publication, 08/17/online 2015.

[109] H. Mei, Y. Huang, K. A. Thackston, and P. P. Irazoqui, "Optimal Wireless Power Transfer to Systems in an Enclosed Resonant Cavity (Accepted)," *IEEE Antennas and Wireless Propagation Letters,* 2015.

[110] M. J. Chabalko and A. P. Sample, "Three-Dimensional Charging via Multimode Resonant Cavity Enabled Wireless Power Transfer," *IEEE Transactions on Power Electronics,* vol. 30, pp. 6163-6173, Nov 2015.

[111] S. A. Mirbozorgi, H. Bahrami, M. Sawan, and B. Gosselin, "A Smart Multicoil Inductively Coupled Array for Wireless Power Transmission," *IEEE Transactions on Industrial Electronics,* vol. 61, pp. 6061-6070, Nov 2014.

[112] T. Thai, G. DeJean, and R. Gilad-Bachrach, "Confined Intra-Arm Communication for Medical Applications," ed. WH '12 Proceedings of the Conference on Wireless Health, 2012.

[113] A. J. Yeh, "Wireless Powering and Communications for mm-Sized Pacemakers, Sensors, Neuromodulators, and Optogenetics," Doctor of Philosophy, Electrical Engineering, Stanford University, 2014.

VITA

VITA

HIGHLIGHTS

- **Extensive experience in wireless power transfer (WPT) technology development and integration with medical electronics with published results.**
- **Created a new analytical method based on bandpass filter theory for examining magnetic resonance coupling WPT systems leading to more effective system optimization capability.**
- **Developed a new and need-driven based WPT tool for consumer, medical, and industrial based electronic systems.**
- **Established a core WPT technology and analysis technique which serves as the foundation for ongoing undergraduate, M.S., and PhD. student projects.**
- **Working experience in both industry and academia.**
- **Interdisciplinary: very wide research interests in technology and experience in electrical engineering (systems integration, circuit design, signal processing, and electromagnetics), neuroscience, and physiology.**

EDUCATION

Ph. D. Candidate, Biomedical Engineering Expected May 2016
Weldon School of Biomedical Engineering, Purdue University West Lafayette
Major Advisor: Professor Pedro P. Irazoqui
Dissertation Title: "Coupled Resonator Based Wireless Power Transfer Systems for Bioelectronics"

Bachelor of Science in Biomedical Engineering
Dec. 2010
Weldon School of Biomedical Engineering, Purdue University West Lafayette

RESEARCH EXPERIENCE

Graduate Research Assistant, Center for Implantable Devices Jan. 2011 - present
Purdue University-West Lafayette

- Development of microwave network models and analysis techniques for near-field magnetic resonantly coupled WPT systems
- Band-pass filter modeling of coupled resonator WPT systems
- Development of a cavity resonator based WPT system for experiments involving freely moving animals
- Development of electrically small antennas on flexible thin-film materials for the application of wearable far-field powered medical sensors

- Development of wireless energy harvesting and power conditioning/management circuitry
- Integration of WPT systems with implantable medical electronics

Graduate Research Assistant, Epilepsy Research Group May 2012 – Aug. 2012
University of Birmingham – Birmingham, United Kingdom

- Designed and conducted acute animal studies to study the effects of hippocampal electrical stimulation on cardiorespiratory function (Heart rate variability and respiratory rate variability)
- Developed extensive digital signal processing methodologies for data analysis and quantification
- Completed animal training and acquired animal experimentation certification in the United Kingdom

Undergraduate Research Assistant, Gralnick Lab May 2010 – Aug. 2010
University of Minnesota – Twin Cities

- Experimental studies on the functional comparison of glycerol metabolism in bacteria strains
- Genetically engineered novel strains of bacterium *Shewanella oneidensis* to metabolize Triose Phosphate Isomerase
- Performed extensive cell studies and enzymatic assay protocols for the evaluation of metabolite production

Undergraduate Research Assistant, Laboratory of Translational Neuroscience
Jan 2009 – Aug. 2009
Purdue University – West Lafayette

- Experimental analysis on the effects of acrolein concentration in animal tissue and cellular toxicity
- Extensive acute animal surgery, cell culture, and histology preparation

INDUSTRY EXPERIENCE

Graduate Intern, Software, Electronic, and Mechanical Systems (SEMS) Laboratory
May 2013-Aug. 2013
3M Company – St. Paul, MN

- Extensive development and successful demonstration of a device for passive sensing and imaging applications utilizing extremely high frequency (EHF) radio bands
- Conducted experimental studies and designed RF energy harvesting systems for applications in passive and semi-active RFID systems resulting in demonstration of feasibility
- Aided in the development and conducted extensive characterization of high frequency testing equipment (Network analyzer, anechoic chamber, etc.)
- Effective collaboration and communication of work with the SEMS team and across divisions within 3M
- Submitted an Intek report summarizing contributions and results

TEACHING EXPERIENCE|

Teaching Assistant, Undergraduate Level Course, Bioelectricity Aug. 2013 – May 2015
Weldon School of Biomedical Engineering, Purdue University- West Lafayette

- Aided in the development of course lectures
- Conducted office hours to help students in understanding lecture and homework material
- Prepared weekly homework questions, graded homework and quizzes, organized grading system for class
- Gave specialty lectures on op-amp circuits and electromagnetic theory

TECHNICAL CAPABILITIES

Electrical Engineering:

- RF engineering measurement and testing: spectrum analyzer, impedance matching, signal generators, power amplifiers, network analyzer, power meter, radiation measurements, anechoic chamber operation, waveguides, cavity resonator filters, microstrip filters etc.
- Near-field coil design: wire wound coils, printed spiral coils
- Far-field antenna design: phased arrays, patch, monopoles, dipoles, PIFA, printed
- Circuit Simulation: ADS, LTspice
- PCB Design: Altium, Osmond PCB, Ansoft Designer
- Electromagnetic field solvers: HFSS, ADS, Maxwell
- Analog Circuit Design and Testing: Filters, amplifiers
- Power conversion and management design: Rectifiers, DC-DC converters

Biomedical Engineering:

- Signal Processing: MATLAB, LabView (ECG, EEG, EMG signals)
- Small animal handling and surgical training (device implantation strategy)
- Implantable and Hermetic Packaging Design
- Biocompatibility Analysis
- Biological electrical systems Integration
- Electromagnetic-Biological Tissue Interaction simulation and testing.

PATENTS

- A Magnetic Resonance Coupling Arrangement
  Provisional Application Filed: June 2014

CONFERENCE POSTERS

- **H. Mei,** D. Jaroch, M.P. Ward, K. Qing, and P.P. Irazoqui, "Magnetically inserted thin flexible microelectrodes," presented at the American Epilepsy Society's Annual Meeting, Baltimore, MD, 2011.

- I. Dryg, H. Zhang**, H. Mei,** K. Qing, and P.P. Irazoqui, "Magnetically Inserted Microelectrode and Chronic Characterization in Vivo," presented at the American Epilepsy Society's Annual Meeting, San Diego, CA, 2012
- O. Newman, **H. Mei**, P.P. Irazoqui, Development of Far-Field RF Energy Harvesting Systems," presented at the IEEE Engineering in Medicine and Biology Society, Chicago, IL, 2014
- **H. Mei**, K.A. Thackston, and P.P. Irazoqui, "Design of a Highly Efficient Wireless Power Transfer System for Millimeter Sized Implantable Devices," presented at the Biomedical Engineering Society Conference, Tampa, FL, 2015.
- K.L. Seburn, R. Berchich, Z. Wang, D. Pederson, **H.Mei**, and P.P. Irazoqui, "Miniature wireless and batteryless device for longitudinal recording and stimulating of bioelectric events in small animals," presented at the Society for Neuroscience, Chicago, IL, 2015.

PROFESSIONAL MEMBERSHIPS

- Biomedical Engineering Graduate Student Association
  Aug. 2011- present

PUBLICATIONS

PUBLICATIONS

JOURNAL PUBLICATIONS

1. **Mei, H**., Huang, Y-W., Thackston, K.A., and Irazoqui, P.P., "Optimal Wireless Power Transfer to Systems in an Enclosed Resonant Cavity," *IEEE Antennas and Wireless Propagation Letters*, 2015 (*Accepted*)
2. **Mei, H**. Thackston, K.A., Bercich, R.A., Jefferys, John G. R., and Irazoqui, P.P. "Cavity Resonator Wireless Power Transfer System for Freely Moving Animal Experiments," *IEEE Transaction on Biomedical Engineering*. 2015, (*Resubmitted*)
3. **Mei, H**. Thackston, K.A., Irazoqui, P.P. "Critical Coupling Point Control in Magnetic Resonant Coupling Wireless Power Transfer Systems," *IEEE Transactions on Power Electronics*, 2015, (*In Preparation*)
4. Dryg, I.D., Ward, M.P., Qing, K.Y., **Mei, H**., Schaffer, J.E., Irazoqui, P.P., "Magnetically Inserted Neural Electrodes: Tissue Response and Functional Lifetime," *IEEE Transactions on Neural Systems and Rehabilitation Engineering*, vol. 23, no. 4, pp. 562-572, Feb. 2015 (*In Print*).
5. Bhamra, H., Kim, Y., Joseph, J., Lynch, J., Gall, O.Z., **Mei, H**., Meng, C., Tsai, J., and Irazoqui, P.P., "A 24 μW, Batteryless, Crystal-free, Multinode Synchronized SoC "Bionode" for Wireless Prosthesis Control," *IEEE Journal of Solid-State Circuits*, 2015 (*Accepted*).
6. Bercich, R.A., Wang, Z., **Mei, H**., Smith, L., Seburn, K., Hargrove, L., and Irazoqui, P.P., "Enhancing the Versatility of Wireless Biopotential Acquisition for Myoelectric Prosthetic Control", *Journal of Neural Engineering*, 2015 (*Major Revision*)
7. R. A. Bercich, S. T. Lee, D. J. Pederson, Z. Wang, M. A. Arafat, **H. Mei***, et al.*, "Bionode for Fully Wireless Recording and Stimulating of Bioelectric Events in Rodents within a Large Volume Cavity Resonator," *IEEE Transactions on Biomedical Engineering,* 2016 (*Submitted*).

COMMENTARY

1. **H. Mei**, P.P. Irazoqui, "Miniaturizing Wireless Implants," *Nature Biotechnology*, vol. 32, pp. 1008-1010, Oct. 2014.

BOOK CHAPTER

1. **H. Mei,** D. Ha, W.J. Chappell, P.P. Irazoqui, "*Design Analysis, and Optimization of Magnetic Resonant Coupling Wireless Power Transfer Systems using Bandpass Filter Theory*," Intelligent Wireless Power Transfer Systems Theory and Practice, River Publishers, Ch. 16, 2015.